FORMATION MECHANISMS OF LOW-DIMENSIONAL SEMICONDUCTOR NANOSTRUCTURES GROWN BY OMCVD ON NONPLANAR SUBSTRATES

THÈSE N^{O} 1859 (1998)

PRÉSENTÉE AU DÉPARTEMENT DE PHYSIQUE

ÉCOLE POLYTECHNIQUE FÉDÉRALE DE LAUSANNE

POUR L'OBTENTION DU GRADE DE DOCTEUR ÈS SCIENCES

PAR

Giorgio BIASIOL

laurea in fisica, Università degli Studi di Trieste, Italie
de nationalité italienne

acceptée sur proposition du jury:

Prof. E. Kapon, directeur de thèse
Prof. K. Kern, rapporteur
Dr P. Roentgen, rapporteur
Prof. M. Scheffler, rapporteur

Lausanne, EPFL
1998

Abstract

Semiconductor quantum wires (QWRs) are promising structures for optoelectronics applications, since they can provide quantum confinement for charge carriers in two dimensions. The advantage that they offer over conventional quantum wells (QWs) is due to the sharper density of states characteristic of these structures, yielding narrower spectral lines and higher optical gain. However, to exhibit clear confinement characteristics, QWRs must meet stringent requirements in terms of size, uniformity and interfacial quality.

Different methods have been explored for QWR fabrication. Techniques based on etching and regrowth suffer from defect incorporation into the lateral interfaces, since they are not formed *in situ*, and are limited in size by the lithographic features. On the other hand, growth of fractions of monolayers on vicinal substrates, although overcoming the above limitations, gives rise to size nonuniformities and graded interfaces. In this project, (In)GaAs/$Al_xGa_{1-x}As$ QWRs are obtained by organometallic chemical vapor deposition (OMCVD) growth of quantum wells on patterned, V-grooved substrates. In this way, the lithographically defined pattern serves as a *seed* for QWR formation. The self-ordering properties of OMCVD on nonplanar surfaces ensure the creation of *a self-limiting profile* at the bottom of the grooves, on which the wires are grown. This method overcomes the size limitations imposed by lithography, allows the *in situ* formation of interfaces and, thanks to the self-ordering mechanism, yields structures with high uniformity, whose characteristics are determined solely by the growth conditions.

Although nonplanar growth has been employed for more than ten years for QWR fabrication, the understanding of the self-ordering mechanisms originating the profiles at the bottom of the grooves has been until now only phenomenological. The attainment of self-limiting profiles takes place via transients of the growth rates at the bottom of the groove. Current models of nonplanar growth can predict the formation, evolution or disappearance of facets at the 100nm-μm size. However, they cannot describe the transient behaviors at the nm scale that lead to self-limiting growth. This thesis project has been aimed at elucidating the physical mechanisms of this self-organized growth.

A fundamental part of the project has been the creation of a wide experimental database to understand the dependence of the self-limiting profiles on the materials and growth conditions. The profiles at the bottom of the groove exhibit a *faceted structure*, consisting of a central (100) plane, surrounded by two {311}A ones. Cross-sectional transmission electron microscopy (TEM) shows that the bottom facets become wider as the growth temperature increases and as the Al mole fraction x of $Al_xGa_{1-x}As$ layers decreases. It appears therefore that surface diffusion is a key element in determining self-limiting growth. TEM cross sections show also that the establishment of self-limiting profiles takes place via *self-adjusting growth rates* on these facets.

Abstract

In addition to this *geometrical* self-ordering, $Al_xGa_{1-x}As$ alloys exhibit also a *compositional* self-ordering at the bottom of the groove. Due to the higher mobility of Ga species, with respect to the Al ones, the facets at the bottom of the groove are Ga rich, with respect to the sidewall planes, giving rise to so-called vertical quantum wells (VQWs). To determine the composition of the VQWs, we have developed a technique employing cross-sectional atomic force microscopy (AFM) in air. This method is based on the dependence of the $Al_xGa_{1-x}As$ oxidation rates on the Al content x. Through a calibration on a reference sample, we were able to measure compositions with an accuracy of ± 0.02. The enhanced Ga content of the VQWs follows classical models of segregation, and reaches a maximum of $\Delta x \cong 0.15$ for $x \cong 0.55$ at a growth temperature of 700°C.

We also studied the three dimensional structure of the self-limiting surface profiles by top-surface AFM in air of the nonplanar samples after cool-down and removal from the OMCVD reactor. Each of the planes composing the groove presents a monolayer step structure that reflects directly the morphology of surfaces of the same orientation found in planar epitaxy. However, on the facets forming on corrugated substrates the step structure exhibits a higher degree of ordering, with respect to planar epitaxy. This is due to a modification of surface diffusion, when the trench width becomes comparable to or lower than the adatom surface diffusion length.

In the last part of the project, we have developed a model ascribing the self-ordering phenomena observed above to local variations of the surface chemical potential μ. Since μ becomes lower as the concavity of the surface increases, it induces a curvature-dependent capillarity flux towards the bottom of the groove. In the absence of capillarity, if the growth rate is higher on the sidewall planes than on the bottom facets, the capillarity-enhanced growth rate at the bottom can balance exactly the sidewall growth rate, thus leading to self-limiting growth. The different behavior of nonplanar OMCVD (where self-ordering is usually observed at the bottom of the grooves) and molecular beam epitaxy (where self-ordering rather takes place at the top of the corrugations) can be explained by the different growth rate anisotropies of the two techniques. In a ternary alloy, the composition is locally different at the bottom of the groove, due to the different diffusion lengths of Ga and Al. The resulting entropy of mixing, which is lower than the one for a uniform composition, tends however to oppose this segregation, thus affecting the alloy self-limiting profiles.

The predictions of the model have been successfully verified on our OMCVD-grown profiles. They can be used to design and optimize a variety of nanostructures, including VQWs, QWRs and QWR superlattices in the GaAs/AlGaAs system, and can be further extended to the strained InGaAs/AlGaAs system.

Version abrégée

Les fils quantiques de semi-conducteurs sont des structures intéressantes pour les applications optoélectroniques puisqu'elles peuvent fournir un confinement quantique à deux dimensions pour les porteurs de charge. L'avantage qu'offre ces structures, par rapport aux puits quantiques conventionnels, est dû à leur densité d'états plus localisée, caractéristique de la réduction de dimensionalité, qui conduit à des lignes spectrales plus étroites et à un gain optique plus élevé. Toutefois, pour montrer des caractéristiques nettes de confinement, les fils doivent satisfaire à des critères tres exigeants en ce qui concerne leur dimension, la qualité de leur interfaces et leur uniformité

Différentes méthodes ont été utilisées pour la fabrication de fils quantiques. Les techniques d'attaque chimique suivie d'une recroissance donnent lieu à l'incorporation de défauts dans les interfaces latérales, et sont limitées en taille par les caractéristiques de la lithographie. Quant à la croissance de fractions de monocouches sur surfaces vicinales, celle ci est affectée par des problèmes d'uniformité et de définition d'interface. Dans ce projet, nous avons réalisé des fils quantiques de (In)GaAs/$Al_xGa_{1-x}As$ par déposition chimique en phase vapeur aux organométalliques (OMCVD) sur des substrats gravés en forme de V. Dans cette méthode, le réseau défini par lithographie est utilisé comme *germe* pour la formation des fils. Les propriétés d'auto-organisation de l'OMCVD assurent la création d'un *profil auto-limité* au fond des sillons, sur lequel sont déposés le fils. Cette technique s'affranchit des limitations de taille de la lithographie, permet la formation d'interfaces *in situ* et, grâce au mécanisme d'auto-organisation, fournit des structures de grande uniformité dont les caractéristiques sont déterminées uniquement par les conditions de croissance.

Bien que la croissance sur substrats non planaires soit employée depuis plus que dix ans pour la fabrication de fils quantiques, la connaissance des mécanismes d'auto-organisation qui sont à l'origine des profils au fond des sillons demeure pour l'instant phénoménologique. Les profils auto-limités sont formés par l'intermédiaire de transitoires des vitesses de croissance au fond des sillons. Les models actuels de croissance non planaire peuvent prédire la formation, l'évolution ou la disparition de facettes à l'échelle de 100nm. Toutefois, ils ne peuvent pas décrire les phénomènes transitoires à l'échelle du nanomètre qui conduisent à la croissance auto-limitée. Ce projet de thèse a eu pour objectif la compréhension des mécanismes physiques de cette croissance auto-organisée.

Une partie fondamentale du projet a été l'établissement d'une vaste base de données expérimentales afin de comprendre la dépendance des profils auto-limités des différents matériaux en fonction des conditions de croissance. Le fond des sillons est une *structure à facettes*, qui consiste en un plan central (100), entouré de deux facettes {311}A. Des images en section transverse au microscope électronique à transmission (TEM) montrent que les facettes

au fond du sillon deviennent plus large quand la température de croissance augmente et quand la composition en Al de l'$Al_xGa_{1-x}As$ diminue. Il semble donc que la diffusion en surface soit un élément essentiel de la croissance auto-organisée. Les sections TEM montrent aussi que les profils auto-limités sont atteints par *autoajustement des vitesses de croissance* sur ces facettes.

En plus de cette auto-organisation *géométrique*, les alliages $Al_xGa_{1-x}As$ présentent aussi une auto-organisation *chimique* au fond des sillons. Grâce à la mobilité plus élevée du Ga, par rapport à l'Al, les facettes du fond sont riches en Ga, par rapport aux parois du sillon, et forment ce que l'on nomme des puits quantiques verticaux (VQWs). Afin de déterminer la composition des VQWs, nous avons développé une technique qui utilise la microscopie à force atomique (AFM) à l'air de section. Cette technique est basée sur la dépendance en x de la vitesse d'oxydation de l'$Al_xGa_{1-x}As$. A l'aide d'un calibrage effectuée sur un échantillon de référence, nous pouvons mesurer des compositions avec une précision de ± 0.02. L'enrichissement en Ga dans le VQW s'accorde avec les models classiques de ségrégation, et atteint un maximum $\Delta x \cong 0.15$ pour $x \cong 0.55$ pour une température de 700°C.

Nous avons étudié par AFM en surface la structure tridimensionnelle des profils auto-limités des échantillons non-planaires. La morphologie de surface des facettes qui forment les sillons reproduit les structures à marches monoatomiques observées sur les substrats planaires de même orientation. Toutefois, sur les facettes qui se forment sur les substrats non planaires, la structure des marches est plus ordonnée, par rapport à l'épitaxie planaire. Ce fait est dû à la modification de la diffusion en surface, observée lorsque la largeur des facettes est du même ordre ou plus petite que la longueur de diffusion.

Dans la dernière partie du projet, nous avons développé un modèle permettant de relier les phénomènes d'auto-organisation observés aux variations locales du potentiel chimique de surface μ. Comme μ décroît lorsque la concavité de la surface augmente, il provoque un flux de capillarité vers le fond, dépendant de la courbure locale de la surface. Si la vitesse de croissance, dans l'absence de capillarité, est plus élevée sur les parois du sillon que sur les facettes du fond, l'augmentation par capillarité de la vitesse de croissance au fond du sillon peut équilibrer exactement la vitesse de croissance sur les parois (croissance auto-limitée). Les comportements différents de l'OMCVD (ou l'auto-organisation est observée au fond) et de la croissance par jets moléculaires (ou l'auto-organisation arrive plutôt au sommet) peuvent alors être expliqués par les différents anisotropies de vitesse de croissance entre le deux techniques. Dans une alliage ternaire, la composition au fond est localement affectée, à cause des différentes longueurs de diffusion de Ga et Al. Toutefois, l'entropie de mélange qui en résulte tend à s'opposer à cette ségrégation, et influence les profils auto-limités des alliages.

Les prédictions du modèle ont été vérifiées sur nos profils crûs par OMCVD, et peuvent être utilisées pour projeter et optimiser de nombreuses nanostructures, comme VQWs, fils quantiques et super-réseaux de fils quantiques dans le système GaAs/AlGaAs, et mis a profit pour le système InGaAs/GaAs.

Table of Contents

CHAPTER 1 INTRODUCTION.....5

1.1 LOW-DIMENSIONAL QUANTUM CONFINED STRUCTURES.....7
1.1.1 DENSITY OF STATES IN LOW-D SEMICONDUCTOR STRUCTURES.....7
1.1.2 REQUIREMENTS FOR THE OBSERVATION OF QUANTUM CONFINEMENT EFFECTS.....9
1.1.3 NANOSTRUCTURES FABRICATION TECHNIQUES.....9
1.1.4 QUANTUM CONFINEMENT IN V-SHAPED QUANTUM WIRES.....12
1.2 OVERVIEW OF THE OMCVD GROWTH PROCESS.....14
1.2.1 THERMODYNAMICS.....15
1.2.2 GROWTH KINETICS.....16
1.2.2.1 Mass transport.....17
1.2.2.2 Reaction kinetics.....17
1.2.3 OMCVD GROWTH OF GAAS FROM TMGA AND AsH_3.....18
1.2.3.1 Growth of $Al_xGa_{1-x}As$ ternary alloys.....20
1.3 MODELS OF NONPLANAR EPITAXY.....20
1.3.1 EQUILIBRIUM SHAPE OF CRYSTALS.....20
1.3.2 ORIENTATION DEPENDENCE OF THE GROWTH RATES.....22
1.3.3 DIFFUSION MODELS OF NONPLANAR GROWTH.....23
1.3.4 MONTE CARLO SIMULATIONS OF NONPLANAR GROWTH.....25
1.3.5 SUMMARY.....26

CHAPTER 2 SELF-ORDERED NONPLANAR GROWTH AND FORMATION OF NANOSTRUCTURES.....29

2.1 EXPERIMENTAL.....29
2.1.1 NONPLANAR SUBSTRATE PREPARATION.....29
2.1.2 OMCVD GROWTH.....31
2.2 CROSS-SECTIONAL ANALYSIS OF PATTERNED GROWTH.....32
2.2.1 FACET FORMATION DURING GROWTH.....32
2.2.2 STUDY OF THE GROWTH RATE DISTRIBUTIONS.....38
2.3 CROSS-SECTIONAL ANALYSIS OF SELF-LIMITING GROWTH.....43
2.3.1 FACETING OF THE BOTTOM PROFILE.....43
2.3.2 TRANSIENT EVOLUTION TOWARDS SELF-LIMITING PROFILES.....44
2.3.3 DEPENDENCE OF SELF-LIMITING PROFILES ON THE GROWTH CONDITIONS.....48
2.3.3.1 Influence of temperature and composition.....49
2.3.3.2 Influence of the growth rate.....50

2.3.3.3 Influence of growth interruptions 51
2.3.3.4 Influence of the reactor pressure 52
2.3.3.5 Discussion 54
2.3.4 SELF-ORDERING OF QUANTUM WIRES 54
2.3.4.1 $GaAs/Al_xGa_{1-x}As$ quantum wires 54
2.3.4.2 $In_xGa_{1-x}As/GaAs$ quantum wires 57
2.3.5 SELF-ORDERING OF QUANTUM WIRE SUPERLATTICES 58
2.3.5.1 Fabrication of quantum wire superlattices 58
2.3.5.2 Model of self-limiting QWR superlattice growth 62
2.3.5.3 Predictions of the model and design of new structures 65
2.4 SUMMARY 67

CHAPTER 3 THREE-DIMENSIONAL STRUCTURE OF SELF-LIMITING PROFILES 69

3.1 INTRODUCTION TO THE AFM MEASUREMENTS 69
3.2 SURFACE MORPHOLOGY OF PLANAR (AL)GAAS EPITAXY 72
3.2.1 (100) SURFACES 72
3.2.2 (311)A SURFACES 76
3.2.3 (111)A SURFACES 77
3.3 SURFACE MORPHOLOGY OF NONPLANAR (AL)GAAS EPITAXY 78
3.3.1 GROOVE MORPHOLOGY BEFORE AND AFTER GROWTH 80
3.3.2 STEP ORDERING AT THE TOP OF THE MESAS 82
3.3.3 SIDEWALLS MORPHOLOGY 85
3.3.4 MORPHOLOGY AT THE BOTTOM OF THE GROOVES: {311}A FACETS 86
3.3.5 MORPHOLOGY AT THE BOTTOM OF THE GROOVES: (100) FACETS 89
3.4 SUMMARY 93

CHAPTER 4 SELF-ORDERING OF ALLOYS 95

4.1 CROSS SECTIONAL ATOMIC FORCE MICROSCOPY OF SEMICONDUCTOR HETEROSTRUCTURES 96
4.1.1 EXPERIMENTAL TECHNIQUE 96
4.1.2 EXPERIMENTAL RESULTS 97
4.1.3 OXIDATION MECHANISMS 99
4.1.4 APPLICATION TO THE IMAGING OF NANOSTRUCTURES 101
4.2 SELF-ORDERING OF $AL_xGA_{1-x}AS$ VERTICAL QUANTUM WELLS 103
4.2.1 OVERVIEW OF THE VQW STRUCTURES 103
4.2.2 ALLOY COMPOSITION IN V-GROOVED STRUCTURES 104
4.2.2.1 AFM measurements 104
4.2.2.2 EELS measurements 106
4.2.2.3 Luminescence measurements 107

4.2.3 STRUCTURE OF THE VQWS....108
4.2.3.1 General features....108
4.2.3.2 Dependence on the growth conditions....110
4.2.4 STUDY OF THE GA SEGREGATION IN THE VQWS....113
4.3 SUMMARY....116

CHAPTER 5 MODELING OF SELF-ORDERING ON NONPLANAR SURFACES....119

5.1 SURFACE RELAXATION AND ORDERING DRIVEN BY DIFFUSION....119
5.1.1 THE SURFACE CHEMICAL POTENTIAL....119
5.1.1.1 Chemical potential of a smoothly curved surface....120
5.1.1.2 Chemical potential of a faceted surface....122
5.1.1.3 Chemical potential of a stressed surface....122
5.1.2 THERMAL SMOOTHENING OF A NONPLANAR PROFILE....123
5.1.3 VERTICAL SELF-ORGANIZATION OF STRAINED 3D ISLANDS....126
5.2 MODELING OF SELF-LIMITING GROWTH ON V GROOVES....127
5.2.1 GENERAL EQUATIONS....127
5.2.1.1 Growth rate anisotropy....127
5.2.1.2 Faceting of the profile....129
5.2.2 FLATTENING OF THE PROFILE IN THE ABSENCE OF GROWTH....133
5.2.3 SELF-LIMITING PROFILES DURING EPITAXIAL GROWTH....134
5.2.4 SELF-ORDERING OF ALLOYS: ENTROPIC CONTRIBUTIONS....136
5.2.5 EVOLUTION TOWARDS SELF-LIMITING PROFILES....138
5.3 APPLICATION OF THE DIFFUSION MODEL TO NONPLANAR OMCVD....140
5.3.1 FLATTENING OF THE PROFILE IN THE ABSENCE OF GROWTH....140
5.3.2 SELF-LIMITING GAAS AND $AL_xGA_{1-x}AS$ PROFILES....142
5.3.2.1 Dependence on the composition....142
5.3.2.2 Dependence on the growth temperature....145
5.3.2.3 Effects of the growth rate....146
5.3.2.4 Effects of the reactor pressure....147
5.3.3 SELF-LIMITING EVOLUTION OF GAAS AND $AL_xGA_{1-x}AS$....148
5.3.4 FORMATION OF QUANTUM-CONFINED NANOSTRUCTURES....150
5.4 MONTE CARLO SIMULATIONS OF NONPLANAR EPITAXY....152
5.5 SUMMARY....155

CHAPTER 6 CONCLUSIONS AND FUTURE DIRECTIONS....157

APPENDIX....161

A SELF-ORDERING MODEL IN THE HYPERBOLIC APPROXIMATION....161

B SELF-ORDERING MODEL FOR A THREE-FACETS BOTTOM PROFILE 163
C ENTROPY OF MIXING FOR A TWO-PHASES, TWO-COMPONENTS SYSTEM 165

BIBLIOGRAPHY 167

CURRICULUM VITAE 173

ACKNOWLEDGMENTS 179

Chapter 1

Introduction

"Self-organization is *creation without a creator attending to details.* More precisely: the formation of patterns and structures that form from the initial state, without intervention, in a dynamical system" [1]. The notion of self-organized systems, defined in this suggestive sentence in quite general terms, has found applications in a very wide range of different disciplines. One outstanding example is the theory of evolution, through a self-organization of DNA in an effort to adapt organisms to the environment, as opposed to creationism, in which the creator shaped the living beings in a deterministic way. Another application of the concept of self-organization is the learning process at the base of neural networks, inspired by the functions of the human brain (see, for example, [2]). In these systems, an interconnected assembly of simple processing elements can undergo a process of adaptation to, or learning from, a set of training patterns (note the difference with respect to a conventional computer, which must be told in advance the exact series of steps required to perform the algorithm). Even in the field of economy, the dualism between self-organization and external control is a central concept. In free market economies prices result from equilibria between supply and demand, while centrally-planned economies prices and productions are imposed externally [3]. In the field of biology, many cellular components and polymeric structures are generated by self-assembly of their constituent molecules. In these processes, the information required for molecules to bind together in the proper orientation is contained in the molecules themselves, without the need of any outside information or intervention [4].

In this thesis, we will analyze self-organization phenomena in the field of epitaxial growth of semiconducting materials. In a general sense, epitaxy itself is a self-organized process. Atoms or molecular species, arriving *at random positions* on a crystalline substrate, rearrange themselves, through surface reactions and diffusion, until they are incorporated on *well-defined lattice sites*, to extend the ordered, crystalline phase. An important issue however, when depositing two or more growth species, is the ability of separating them into different phases, to create ordered structures containing a defined number of lattice sites, occupied by given atomic species, in one or more directions. In particular, the ability to embed in a controlled way a low bandgap semiconductor in a higher bandgap one will provide a way to quantum confine charge

carriers. One can establish a direct relationship between the material and the electronic properties. In the envelope function approximation, the electronic wavefunctions are factorized into Bloch wavefunctions, following the lattice periodicity, and slowly varying envelope functions, determined by the confining potential [5]. There is therefore a parallelism between lattice ordering and "ordering" of the electron wavefunction on the lattice periodicity, and between ordered superstructures and confinement of charge carriers. Depending on the number of confined dimensions, these structures are termed quantum wells (QWs), quantum wires (QWRs) and quantum dots (QDs), for 1D, 2D and 3D quantum confinement, respectively.

Confinement in only one dimension does not require any self-ordering process, in the sense defined above. In fact, epitaxial techniques such molecular beam epitaxy (MBE) and organometallic chemical vapor deposition (OMCVD) provide *direct* control at the atomic level of the material composition along the growth direction. This direct control is however not a suitable method for QWR and QD fabrication, which involves lateral patterning on the growing surface. Post-growth etching and regrowth suffers from limitations in terms of size reduction, homogeneity and interface quality [6]. On the other side, atom-by-atom direct positioning by means of scanning tunneling microscopy techniques [7] is not practically applicable in our context. A way to overcome these limitations is to employ self-ordering during growth, in the sense described above. The idea is to make atoms migrate onto preferential sites, provided that a suitable driving force for *lateral* epitaxy can be established. The shape, size and uniformity of the resulting structures depend on this lateral driving force, and in particular on how it can contrast the intrinsic randomness of the nucleation process, which favors a statistical distribution of atoms on the lattice sites. An example in this direction is the formation of Stranski-Krastanow islands in lattice-mismatched epitaxy, where the lateral driving force is provided by surface strain fields [8-11].

In this project, we have analyzed self-organization processes during OMCVD growth, in which the lateral driving force is due to the nonplanarity of the surface. The nonplanar profile is defined before growth, as an array of V grooves (for QWRs) or a matrix of pyramidal recesses (for QDs), which form templates for tailoring surface diffusion. In this way, only the location of the resulting nanostructures is controlled directly by the operator, through the template design. On the contrary, the nm-scale details of the growth profile are determined by the self-ordering properties of the growth mechanism, and depend only on the material and growth conditions. In this way, reproducibility better than 5% can be obtained, from site to site of the array and from growth to growth. We will treat here in particular the properties of GaAs/$Al_xGa_{1-x}As$ QWRs grown on V-grooved substrates. This technique has been developed more than ten years ago and has been widely used since then [12-16]. However, the physics of the self-ordering process leading to QWR formation has not been clarified yet. The clarification of these mechanisms is the objective of this thesis.

The rest of **Chapter 1** contains an introduction to low-dimensional quantum structures, and to the physics of OMCVD growth, applied in particular to nonplanar epitaxy. In **Chapter 2**

we will present an experimental analysis of low-pressure OMCVD growth of (Al)GaAs alloys on V-grooved substrates. Particular attention will be devoted to the establishment of self-limiting profiles at the bottom of the grooves, and to the formation of low-dimensional quantum structures in this region. **Chapter 3** presents an atomic force microscopy analysis of the three-dimensional structure of the self-limiting profiles discussed here. The compositional self-ordering of nonplanar growth of $Al_xGa_{1-x}As$ alloys will be discussed in **Chapter 4**. Finally, **Chapter 5** presents a physical model that can account quantitatively for the self-ordering phenomena described here. The key element is the definition of the surface chemical potential on a corrugated surface, and of the related diffusion fluxes, which can self-adjust in order to yield self-limiting growth. Quantitative comparisons with experimental results and kinetic Monte Carlo simulations will conclude the chapter.

1.1 Low-dimensional quantum confined structures

1.1.1 Density of states in low-D semiconductor structures

Introduction of quantum confinement in one, two or three dimensions affects dramatically the energy band structure and the density of states (DOS) of the charge carriers in semiconductors. This is at the origin of peculiar transport and optical properties of low-dimensionality quantum confined structures [17]. In principle, the carrier energy levels can be determined by solving the Schrödinger equation in the effective mass approximation [18]:

$$\left[-\frac{\hbar^2}{2m^*}\nabla^2 + V(x,y,z)\right]\psi(x,y,z) = E\psi(x,y,z)\,,$$

where $\psi(x,y,z)$ is the carrier envelope wave function, m^* is the carrier effective mass, $V(x,y,z)$ is the potential distribution and E is the energy spectrum. This equation is in general impossible to solve analytically. In the simple case of infinitely deep, rectangular potential wells with dimensions t_x, t_y and t_z, , the Schrödinger equation can be solved by separation of variables, giving confinement energies

$$\begin{aligned} E_l &= \frac{\hbar^2\pi^2 l^2}{2m^* t_x^2} + \frac{\hbar^2\left(k_y^2 + k_z^2\right)}{2m^*} && 1D \text{ confinement} \\ E_{l,m} &= \frac{\hbar^2\pi^2}{2m^*}\left(\frac{l^2}{t_x^2} + \frac{m^2}{t_y^2}\right) + \frac{\hbar^2 k_z^2}{2m^*} && 2D \text{ confinement} \\ E_{l,m,n} &= \frac{\hbar^2\pi^2}{2m^*}\left(\frac{l^2}{t_x^2} + \frac{m^2}{t_y^2}\frac{n^2}{t_z^2}\right) && 3D \text{ confinement} \end{aligned} \qquad (1.1)$$

where $l, m, n = 1, 2, ...$are the level quantum numbers and k_y and k_z are the wave vector components along the non-confined directions [1]. Confinement of carriers in 1D, 2D and 3D

[1] Note that for valence band states a multiband model should be used, taking into account band mixing effects (see, e.g., [19]).

results in the formation of quantum wells (QWs), quantum wires (QWRs) and quantum dots (QDs), respectively. The corresponding DOS per unit volume, including spin degeneracy, are given by

$$\rho_{bulk} = \frac{\left(2m^*/\hbar^2\right)^{3/2}}{2\pi^2}\sqrt{E}$$

$$\rho_{QW} = \frac{m^*}{\pi\hbar^2 t_x}\sum_l \theta\left(E - E_l\right)$$

$$\rho_{QWR} = \frac{\left(2m^*\right)^{1/2}}{\pi\hbar t_x t_y}\sum_{l,m}\left(E - E_{l,m}\right)^{-1/2}$$

$$\rho_{QD} = \frac{2}{t_x t_y t_z}\sum_{l,m,n}\delta\left(E - E_{l,m,n}\right)$$

(with $\theta(x) = 0$ for $x < 0$ and $\theta(x) = 1$ for $x > 0$). As can be seen in Figure 1.1, the DOS distribution becomes sharper as the dimensionality decreases. In particular, the QWR and QD DOS present singularities corresponding to the energy levels. As a result of the reduced carrier energy distribution, higher optical and differential gains should be achievable in quantum confined laser structures. This higher optical gain, and the reduced volume of the active regions should in turn reduce the threshold currents of QWR and QD lasers [20].

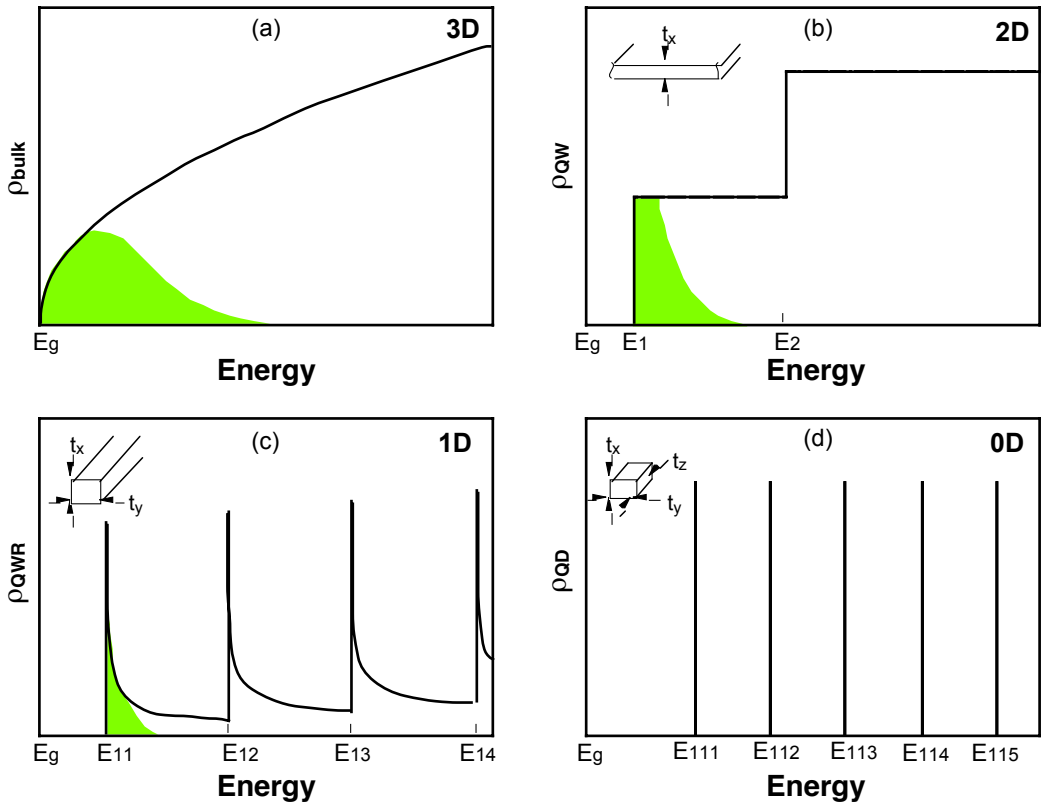

Figure 1.1: Schematic representation of the DOS for (a) bulk, (b) QW, (c) QWR and (d) QD structures. Insets show schematically the potential wells configuration corresponding to each structure. Shaded areas indicate occupied states for similar carrier densities [18].

1.1.2 Requirements for the observation of quantum confinement effects

- **Size.** If, at a temperature T, more subbands are populated, an effective motion *along* the confinement direction results. Therefore, to preserve the dimensionality, only the ground state must be populated. This means that the subband separation ΔE_{12} must be greater that $k_B T$. For infinite square QWs, for example, the first of eq. (1.1) implies that

$$t_x < \sqrt{\frac{3\hbar^2\pi^2}{2m^* k_B T}} \ .$$

  This means, for GaAs at 300K, $t_x < 20$nm. Equivalent sizes can be deduced for the other confinement dimensions in QWRs and QDs.

- **Uniformity.** Size nonuniformities in the confined structures can result in inhomogeneous broadening of the DOS. The effects of inhomogeneous broadening on a crescent-shape GaAs/AlGaAs QWR DOS are shown in Figure 1.2 [21]. In the case of an infinite square QW (first of eq. (1.1)), fluctuations δt_x in the well width cause variations δE_l that are related by $|\delta E_l|/E_l = 2\delta t_x/t_x$. Therefore the requirement $\delta E_l \ll E_l$ implies $\delta t_x \ll t_x$. In practice, values of $\delta t_x/t_x$ lower than 10% must be achieved in order to retain the quantum confinement characteristics.

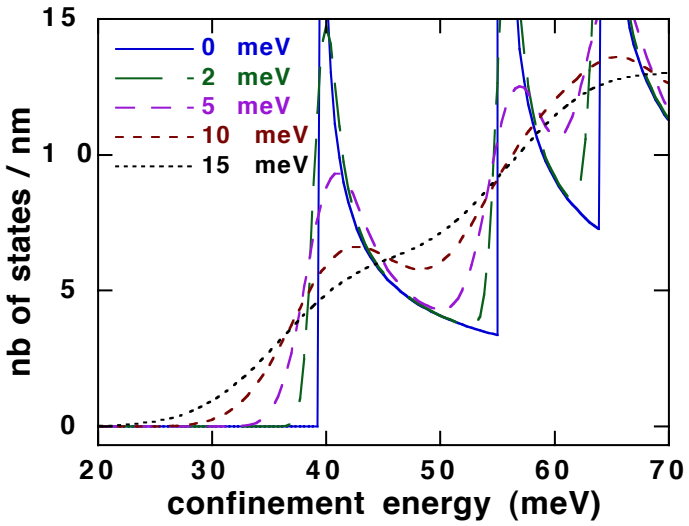

Figure 1.2: Electron DOS in a crescent-shaped GaAs/AlGaAs QWR with different gaussian-shaped inhomogeneous broadenings [21].

1.1.3 Nanostructures fabrication techniques

The requirements above, in terms of size and uniformity, are currently met for QWs by modern epitaxial techniques, such as molecular beam epitaxy (MBE) and organometallic chemical vapor deposition (OMCVD) [22, 23]. These requirements, however, still represent a challenging technological task in the case of lower-dimensionality structures, where confinement must be achieved also in the direction(s) *perpendicular* to the growth axis.

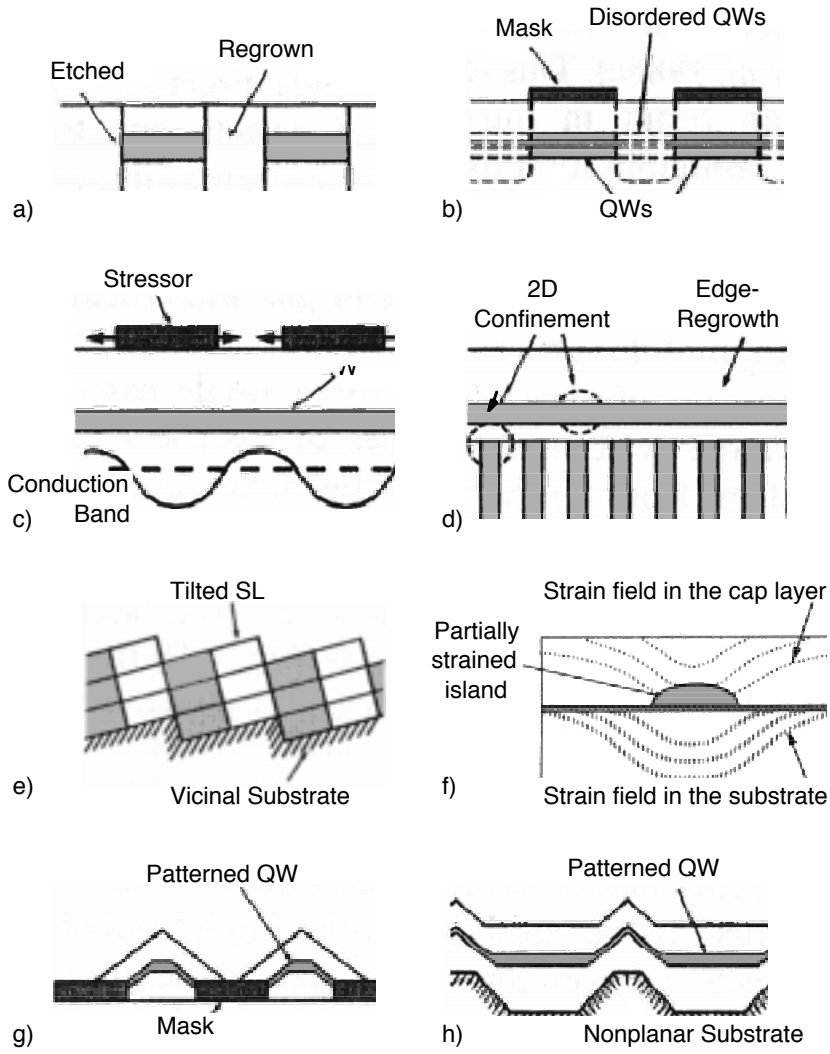

Figure 1.3: Techniques for lateral patterning of semiconductor heterostructures. (a): Etching and regrowth. (b): Selective QW disordering. (c): Strain-induced bandgap modulation. (d) Regrowth on cleaved edge of a QW heterostructure. (e) Growth on vicinal substrates. (f) Strain-induced self-assembled QD. (g) Growth on masked substrates. (h) Growth on nonplanar substrates. ▭: High bandgap; ▬: Low bandgap. (a)-e), g)-h): [6]; f): [24])

An approach to form low-D confined nanostructures consists in growing conventional, planar QWs and defining the lateral pattern with a *post-growth* process. Representative examples of this approach are shown in Figure 1.3(a-c). The most direct method consists in removing selectively parts of the QW by lithography and etching, and in subsequent epitaxial regrowth of the barrier material for surface passivation (a) [25, 26]. Alternatively, the bandgap and refractive index of the QW have been patterned by selective disordering, induced by implantation or diffusion of impurities through a mask or with focused ion beams (b) [27-29]. Another method consists in depositing patterned "stressors" adjacent to the QW, to produce lateral band-gap modulation via strain effects (c) [30]. These approaches provide flexibility in designing the patterned heterostructure; however, they are limited, in terms of lateral nanostructures size, by the resolution of the lithographic techniques. Besides, this limitation is also detrimental for size and shape uniformity, which can lead to inhomogeneous broadening

effects. Finally, while stressor deposition (c) can yield smooth and defect-free lateral interfaces, etching and regrowth (a) produces incorporation of defects into these interfaces, and impurities implantation (b) can result in material contamination.

Due to these limitations of the post-growth techniques, efforts have been made to avoid lithographic processes in the nanostructure fabrication. 2D confinement can be achieved by regrowing a QW or a modulation-doped heterostructure on the cleaved (011) edge of a (multiple) QW structure, inducing a lateral variation in the potential energy (d) [31]. Similarly, a twofold cleaved edge overgrowth yields the formation of QDs [32]. This technique allows control of the QWR and QD sizes to the monolayer (ML) scale, but suffers from weak lateral confinement (generally less that 30meV) and reduced flexibility for structure design.

A widely exploited idea is to rely on the epitaxial process itself to generate nanostructures by *spontaneous self-ordering* (Figure 1.3(d-e)). Growth of fractional-layer QWR SLs using vicinal substrates has been proposed and studied (d) [33, 34]. In this case, the lateral and vertical definition, as well as the alignment of the wires, rely on surface diffusion and preferential attachment of adatoms to the ledges of monolayer steps. The nonuniformities in such SL structures, resulting from imperfect step configuration, incomplete adatom segregation and growth rate variations, were partly rectified by resorting to growth of serpentine SL structures, in which the growth rate is intentionally varied during the deposition of the fractional layer SL on the vicinal substrate [35]. Similarly, a certain degree of lateral and vertical ordering has been observed in strained wire SLs formed on macrosteps during growth on misoriented substrates [36]. A widely studied approach for the formation of QDs is the self-organized island growth of lattice-mismatched layers on planar substrates (f) [8-11] (dislocation-free Stranski-Krastanow growth). Such techniques have the advantage that lateral patterning of the nanostructures is a one-step process, without the need for any surface patterning before or after growth. However, they suffer from a limited control on uniformity of size and lateral position[2] due to the intrinsic random nature of the nucleation process.

These drawbacks can be avoided by using a combination of lithography and self-ordering effects, namely, the growth of low-D nanostructures on substrates patterned with a dielectric mask (g) [42-45] or with a nonplanar surface profile (h) [12-16]. With these *seeded self-ordering* techniques, the idea is to form *nm-size templates* due to faceting on such substrates, and then to use tapered QW structures to form the lateral potential wells. All the interfaces of the resulting lateral wells are formed *in situ*, and thus they are potentially defect- and contamination-free. The position of each nanostructure is exactly defined by the mask template, thus yielding nucleation sites predictable within ~10nm. Besides, with a suitable choice of the growth technique and substrate geometry, it is possible to exactly reproduce the templates after growth of each QWR. This provides the possibility of obtaining dense vertical arrays of wires, with uniformity in the nm scale. Since the growth habit on the different facets is determined by

[2] Strain-induced *vertical* self-ordering of QDs has been reported [37-41] (see Section 5.1.3).

nature, it is important to understand the epitaxial mechanisms on such nonplanar surfaces, in order to optimize the QWR quality in terms of size reduction and uniformity. The rest of this thesis is devoted to such studies, applied in particular to the lattice-matched GaAs/AlGaAs system on nonplanar (100) substrates.

1.1.4 Quantum confinement in V-shaped quantum wires

The thickening of QW structures at the bottom of a V-grooved substrate results in a lateral, local decrease of the effective bandgap in this region, as shown in Figure 1.4 [14]. This decrease is due to transverse quantum size effects, i.e., the strong variation of the carrier confinement energy with the QW thickness.

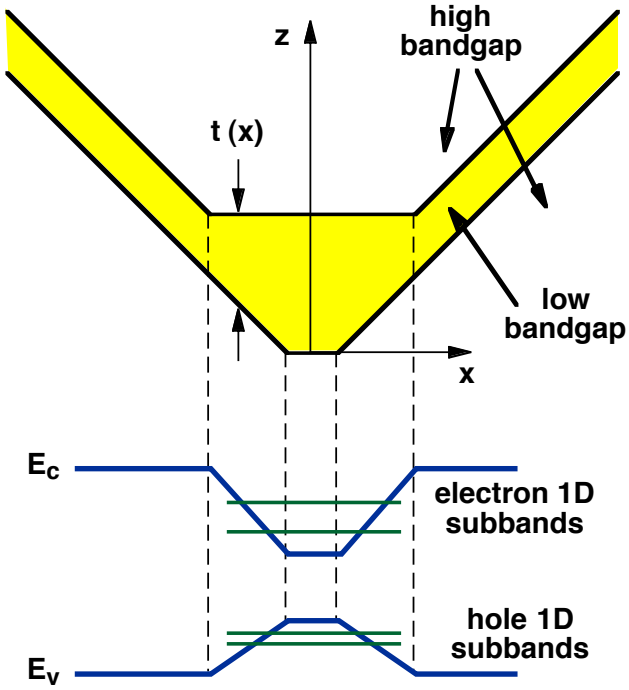

Figure 1.4: Lateral quantum confinement in a tapered QW heterostructure grown on a nonplanar substrate. The lateral QW thickness variations translate into lateral effective bandgap variations. Charge carriers can be laterally trapped in the thicker parts of the tapered QW. 1D conduction and valence subbands are formed for sufficiently narrow channels.

If the lateral (x) potential variations are much slower than the transverse (z) ones, then the 2D Schrödinger equation for the QWR envelope wave function $\psi(x,y)$ can be approximated by two coupled, 1D equations (*adiabatic approximation)* [46]:

$$\left[-\frac{\hbar^2\nabla_y^2}{2m^*}+V_x(z)\right]\chi_x^n(z)=E_{conf}^n(x)\chi_x^n(z)$$

$$\left[-\frac{\hbar^2\nabla_y^2}{2m^*}+E_{conf}^n(x)\right]\varphi^{nm}(x)=E^{nm}\varphi^{nm}(x)$$

where $V_x(z)$ is the 1D confining potential. Solving the first equation for different values of x yields the lateral confining potential $E_{conf}^n(x)$, which is then used in the second equation to

determine the lateral subband energies E^{nm}. In the case of a high Al mole fraction barrier, $V_x(z)$ can be approximated using an infinitely deep square well model, which yields a lateral confining potential

$$E^{n}_{conf}(x) \cong \frac{\hbar^2 \pi^2 n^2}{2m^* t^2(x)} .$$

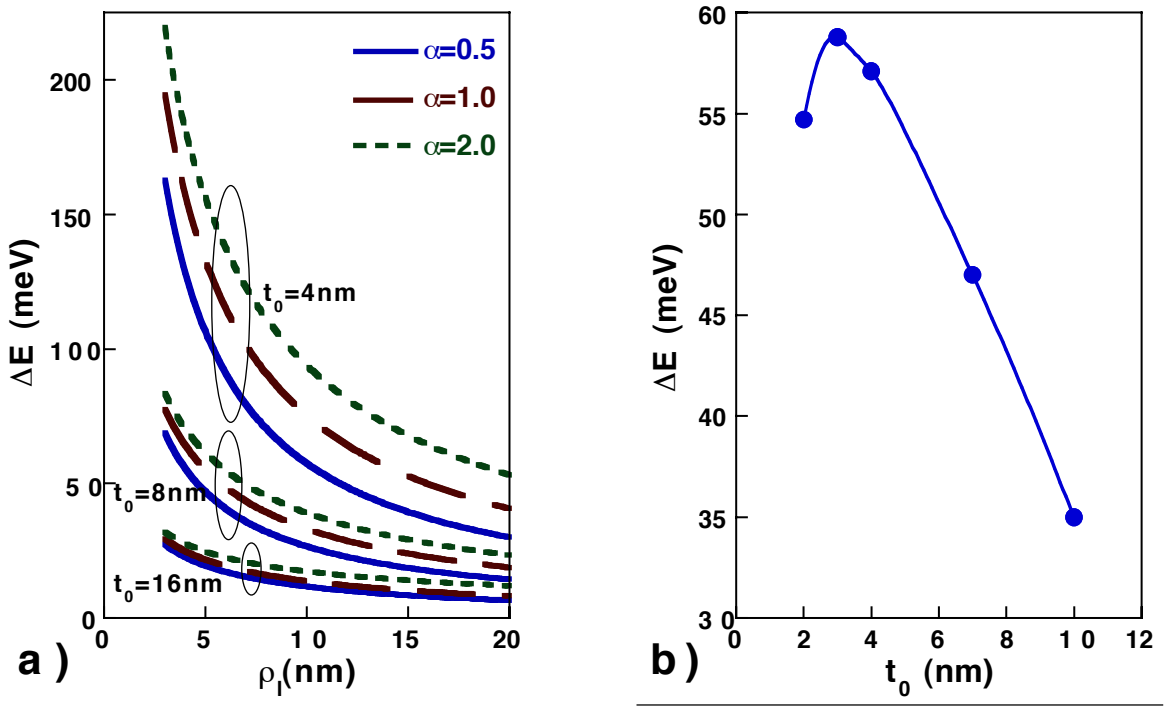

Figure 1.5: a) Dependence of the electron subband separation ΔE on ρ_l, for different values of t_0 and α, in the adiabatic approximation (see text for explanation of symbols). b) Dependence of ΔE on t_0 in the full 2D model of Ref. [47].

By approximating the QWR profile with two hyperbolic boundaries[3], as appropriate for OMCVD-grown profiles [48], which are characterized by bottom and top radii of curvature ρ_l and ρ_u, respectively, the lateral subband energies are then given by [48]

$$E^{nm} \cong \frac{\hbar^2 \pi^2 n^2}{2m^* t_0^2} + \frac{\hbar^2 \pi^2 \alpha^{1/2} n}{m^* t_0 \bar{\rho}} (m - 1/2) ,$$

where t_0 is the thickness at the QWR center, $\bar{\rho} = (\rho_l \rho_u)^{1/2}$, and $\alpha = (\rho_u - \rho_l)/t_0$. This equation shows that, for a given thickness, the quantum confinement in the QWR increases as the lower curvature increases and the upper one decreases, i.e., when the wire assumes a more "compact" shape. Besides, E^{nm} increases as the wire becomes thinner. The dependence of the electron subband separation ΔE on ρ_l is shown in Figure 1.5a, for different values of α and t_0. A full 2D numerical model of the electronic confinement energies in crescent-shaped QWRs has shown, however, that the subband separation *decreases* below a certain critical thickness, due to wave function spreading into the barriers [47]. Figure 1.5b shows the results of this model for

[3] See Appendix A.

ρ_l = 5nm and ρ_u = 11nm (as we will see in the next chapters, these are sizes currently obtainable with OMCVD growth of QWRs on nonplanar substrates). Note that the maximum electron subband separation, occurring for t_0 = 3nm, is nearly 60meV, that is more than $2k_BT$ at room temperature, thus reducing thermal populations of the excited electronic states even at 300K.

1.2 Overview of the OMCVD growth process

OMCVD is today one of the leading epitaxial techniques for semiconductor thin-film growth. In OMCVD, the growth species are transported to the heated substrate by a carrier gas (generally purified H_2 or N_2), under the form of volatile precursor molecules. For the growth of III-V compound semiconductors, the cation precursors are generally organometallic molecules (commonly trimethyl- or triethyl- species), while the group V elements are generally introduced through hydrides (AsH_3, PH_3)[4]. Generally, OMCVD reactors are made either in a horizontal geometry, where gases are inserted laterally with respect to the sample, which is mounted on a slowly-rotating (~60 RPM) susceptor plate, or in a vertical geometry, where gases enter from the top, and the sample is mounted on a fast-rotating (~500-1000 RPM) susceptor plate. A schematic diagram of a horizontal reactor system with a dual-line injection manifold (organometallics + hydrides) is shown in Figure 1.6 [49].

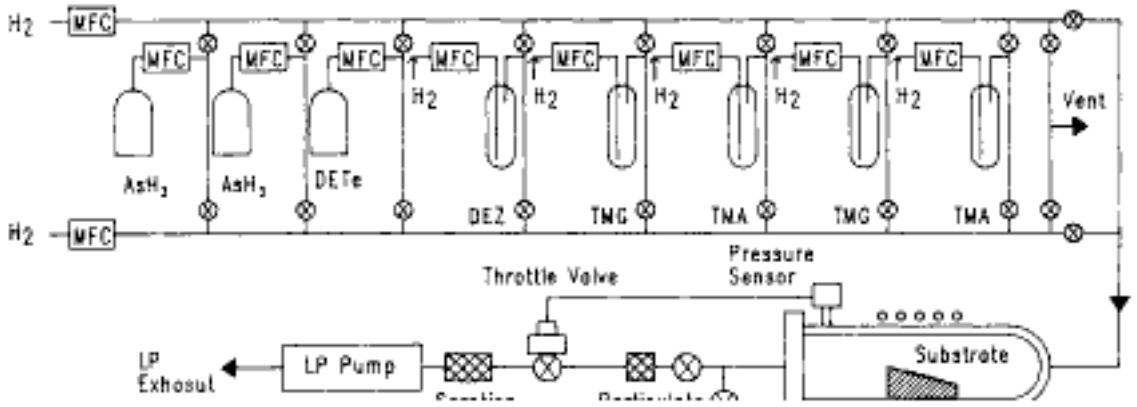

Figure 1.6: Schematic diagram of a low pressure, horizontal reactor system with a dual-line injection manifold [49].

For the standard process of GaAs growth from TMGa and AsH_3, the overall chemical reaction can be represented as

$$[Ga(CH_3)_3]_{gas} + [AsH_3]_{gas} \rightarrow [GaAs]_{solid} + [3CH_4]_{gas} .$$

Despite the relative simplicity of this relation, the detailed mechanisms bringing to epitaxy, even in this well-established GaAs growth, are far from being fully understood. One reason is the

[4] Due to safety reasons, group V alkyl compounds are also becoming common.

relative lack, with respect to MBE, of *in-situ* probes to monitor the gas-phase reactions and the surface morphology (in recent years, optical and X-ray scattering have provided some insight on the surface processes [50]). Another reason derives from the inherent complexity of the epitaxial process itself. Here we will only outline shortly the main growth steps; exhaustive treatments of the OMCVD growth process can be found in the references [23]. In Figure 1.7 we represent schematically a possible subdivision of the different steps involved in the process, and of the factors determining the growth rate. These aspects will be addressed below.

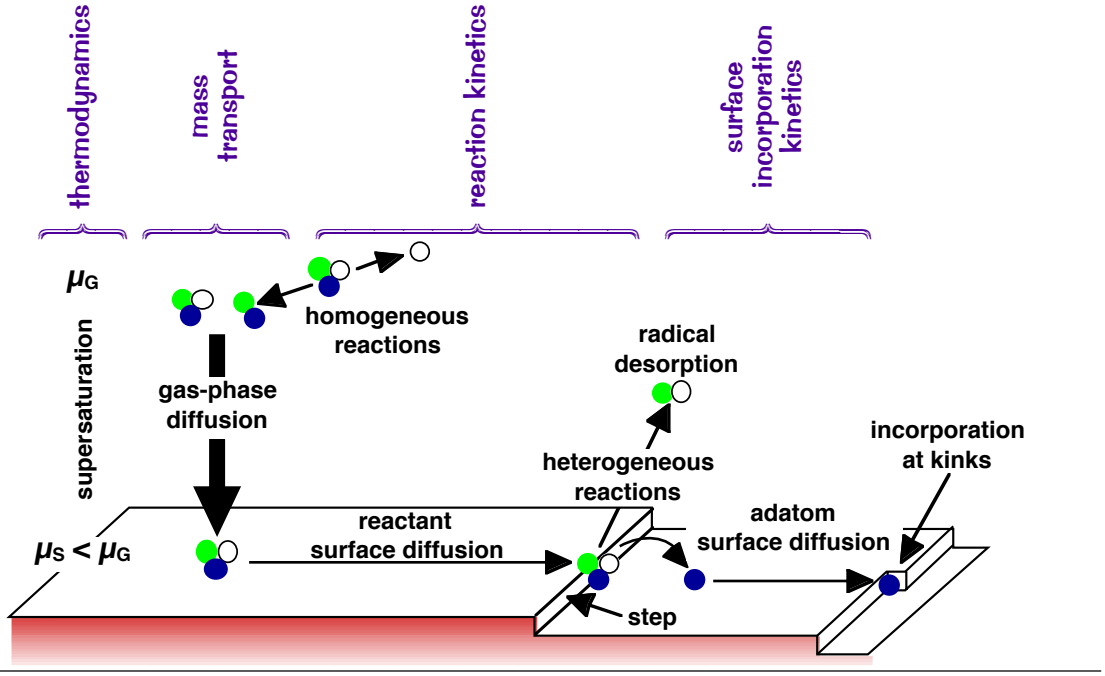

Figure 1.7: Schematic representation of the different steps involved in the OMCVD growth process.

1.1.1 Thermodynamics

Thermodynamical considerations provide the driving force for epitaxy, i.e., the maximum growth rate that can be obtained. This is related to the chemical potential difference $\Delta\mu$ between the gas phase and the surface. In each phase, μ for each component depends on the component concentration x. For non-ideal solutions, it is customary to express μ in terms of the activities $a = x \cdot \gamma$, where γ is a non-ideality factor. Under non-equilibrium conditions, the difference $\Delta\mu$ between two phases A and B can be expressed as [23] $\Delta\mu = RT \ln(a_A^e a_B / a_A a_B^e)$, where $a^e_{A,\,B}$ are the equilibrium activities, R is the gas constant and T is the growth temperature. The maximum quantity of solid that can be produced is therefore simply the amount that would establish equilibrium (the supersaturation). The growth rate is however normally much lower than this thermodynamic limit indicates, for various reasons. Precursor reaction kinetics may not be fast enough to ensure equilibrium at all times. Often, mass transport in the gas phase can limit the reaction and growth rates. Finally, growth rates can be limited by surface reaction rates. These factors will be discussed next.

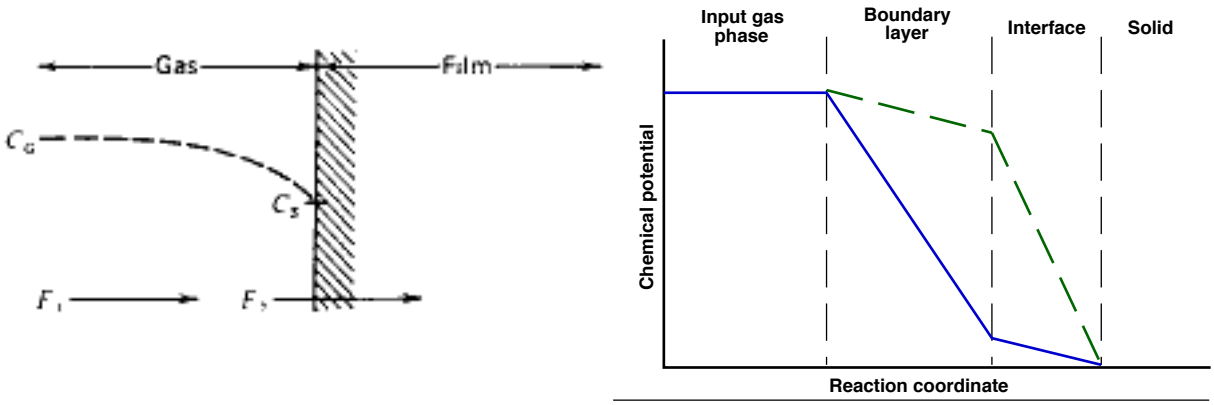

Figure 1.8: Left: Gas-phase concentration profile of a reactant molecule. Direction of gas flow is normal to the plane of paper [51]. Right: Schematic diagram of the chemical potential versus reaction coordinate. Dashed line: kinetically limited growth; solid line: mass transport limited growth.

1.1.2 Growth kinetics

To illustrate the growth kinetics, we begin with the simplified deposition process of a film, starting from a molecule AB in the gas phase [51]:

$$\mathrm{AB(g)} \rightarrow \mathrm{A(s)} + \mathrm{B(g)}.$$

The molecular flux J_1 from the gas phase to the substrate surface, and the consumption flux of AB corresponding to the surface reaction J_2 can be approximated, respectively, by

$$\begin{aligned} J_1 &= h_G\,(C_G - C_S) \\ J_2 &= k_S C_S\,, \end{aligned} \tag{1.2}$$

where h_G is a gas diffusion rate constant, C_G is the concentration of AB in the gas; C_S is the concentration of AB at the surface, and k_S is a heterogeneous rate constant (see Figure 1.8, left). In steady-state conditions we have

$$J_1 = J_2 = J = \frac{C_G}{k_S^{-1} + h_G^{-1}}\,.$$

The growth rate $R = J{\cdot}\Omega_0$ (with Ω_0 the unit volume of the crystal) is therefore proportional to the mole fraction of the species AB in the gas phase, and determined by the smaller of the rate constants h_G, k_S. In the two limiting cases we have

$$\begin{aligned} R \approx k_S C_G \Omega_0 \quad &\Leftrightarrow \quad \text{surface kinetics control} \quad (h_G \gg 1) \\ R \approx k_S C_G \Omega_0 \quad &\Leftrightarrow \quad \text{mass transport control} \quad (k_S \gg 1). \end{aligned} \tag{1.3}$$

Note that the relative importance of surface kinetics and mass transport can be interpreted as a function of the chemical potential dependence on the reaction coordinate (Figure 1.8, right). If most of the chemical potential drop occurs in the boundary layer (solid line), the growth is controlled by mass transport; if it occurs at the interface (dashed line), the growth is kinetically limited [49].

1.1.1.1 Mass transport

Mass transport in OMCVD systems is a fundamental aspect in reactor design. The gas flow in the reactor is affected by several factors, and its determination is usually extremely complex. One has to take in account temperature, concentration and momentum gradients, gravity (that produce convection), and homogeneous or heterogeneous chemical reactions (that can produce parasitic nucleation). In a simplified picture, gas flow in horizontal systems (like the one used in the present experiments), can be broken into two regions [52] (see Figure 1.9). In the upper region, turbulence or vorticity are observed, giving good mixing and heat transfer. Close to the susceptor, a region of laminar flow (*boundary* or *stagnant layer*) provides molecular diffusional transport to the hot substrate, where the transverse velocity is zero. By assuming a gas velocity $U = U_\infty$ in the bulk gas phase, and $U = 0$ at the growth surface, the resulting boundary layer width has been calculated to be of the form $\delta \sim (PU_\infty)^{-1/2}$, where P is the total reactor pressure [53]. If the molecular transport in the boundary layer proceeds by diffusion alone, the rate constant h_G appearing in the first of eq. (1.2) can be written as

$$h_G = \frac{D}{\delta}, \tag{1.4}$$

where $D \sim P^{-1}$ is the diffusion coefficient. The mass transport-limited growth rate can be expressed, therefore, as [23]

$$R \sim p_{AB}\sqrt{\frac{U_\infty}{P}}, \tag{1.5}$$

where we have put $C_G \sim p_{AB}$, p_{AB} being the partial pressure of the species AB. The growth rate is therefore practically independent of the growth temperature, and depends linearly on the species partial pressure.

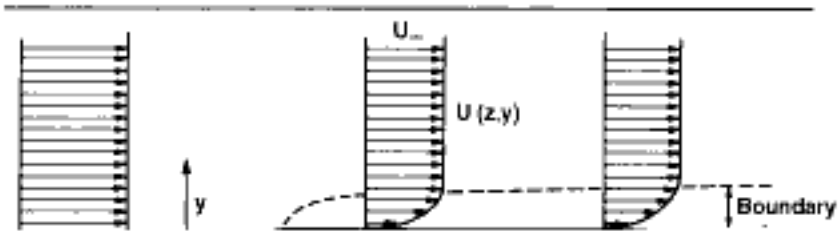

Figure 1.9: Boundary layer development over a susceptor plate in a horizontal OMCVD reactor [23].

1.1.1.2 Reaction kinetics

In the OMCVD growth process, one must take into account both reactions in the gas phase (*homogeneous* reactions) and at the surface (*heterogeneous* reactions). Both kinds of reactions are thermally activated, i.e., their forward and reverse rates are characterized by rate constants that can be expressed in an Arrhenius form: $k = A \exp(-E/k_B T)$, where E is the activation energy for the process. For homogeneous reactions, the reaction rates are also

proportional to the product of the partial pressures of each species involved in the reaction.

Surface kinetics are poorly known processes, in which a number of sub-processes can be identified. Among them: adsorption of reactant species, heterogeneous decomposition reactions, surface migration, and incorporation and desorption of products. In the most simplified picture, the chemistry of heterogeneous reactions can be modeled by taking into account only adsorption and desorption:

$$AB(g) + * \underset{k_{des}}{\overset{k_{ads}}{\leftrightarrow}} A^* + B(g) \tag{1.6}$$

where $*$ is a vacant surface site, A^* is an adsorbed state, and k_{ads} and k_{des} are the adsorption and desorption rate constants. In this approach, the fraction of occupied lattice sites Θ is expressed in terms of p_{AB}, by assuming no interaction between absorbed species and an equivalence among all the adsorption sites. In the steady state (adsorption rate = desorption rate), it can be easily seen that Θ assumes the form of a *Langmuir isotherm*:

$$\Theta = \frac{Kp_{AB}}{1 + Kp_{AB}}\ , \tag{1.7}$$

where $K = k_{ads}/k_{des}$ is the adsorption coefficient. For OMCVD of binary compound semiconductors, two molecules AB and CD are transported to the surface, and are adsorbed on cation and anion sites, respectively. For this noncompetitive process, the growth rate of the bimolecular reaction is proportional to the anion and cation surface coverages:

$$R = k_{\text{AB-CD}}\, \Theta_{\text{AB}}\, \Theta_{\text{CD}}\ .$$

With Θ_{AB} and Θ_{CD} following Langmuir isotherms (1.7), the growth rate is written under the form of a *Langmuir-Hinshelwood isotherm*:

$$R = \frac{k_{AB-CD} K_{AB} p_{AB} K_{CD} p_{CD}}{\left(1 + K_{AB} p_{AB}\right)\left(1 + K_{CD} p_{CD}\right)}\ .$$

The reaction (1.6), which forms the basis of the Langmuir model, is an oversimplifying assumption, since in reality adsorption is a complex sequence of physisorption, where no chemical bond is made to the surface, and chemisorption, that involves surface bonds. Additionally, the adsorption enthalpy changes with surface coverage, and not all adsorption sites are equivalent. This second effect is particularly important for epitaxial layers grown on nonplanar profiles, exposing facets with different orientations [23]. In this case, the adsorbed species diffuse to the lowest energy positions prior to atomic incorporation at half-crystal sites. This happens also in the mass transport limited regime, where the *macroscopic* growth rate is independent of the surface orientation. This effect of surface kinetics in mass transport limited growth is one of the basic elements of self-limiting growth on nonplanar substrates, that will be the subject of the next chapters. A discussion of growth rate distributions on nonplanar substrates will be given later, in Section 1.3.

1.1.3 OMCVD growth of GaAs from TMGa and AsH_3

For a binary compound like GaAs, the Langmuir-Hinshelwood isotherm can be simplified

for typical growth conditions with very high V/III ratios (~100). In this case one can approximate $\Theta_{Ga} \ll 1$ (step-flow growth is commonly observed, indicative of significant surface diffusion, which is possible only for low coverages) and $\Theta_{As} \cong 1$ [54, 55]. The Langmuir-Hinshelwood isotherm can therefore be approximated as

$$R \cong K' \, p_{TMGa} ,$$

with K' a typical rate constant for the process. The growth rate depends in this limit only on the Ga partial pressure, and not on the As one.

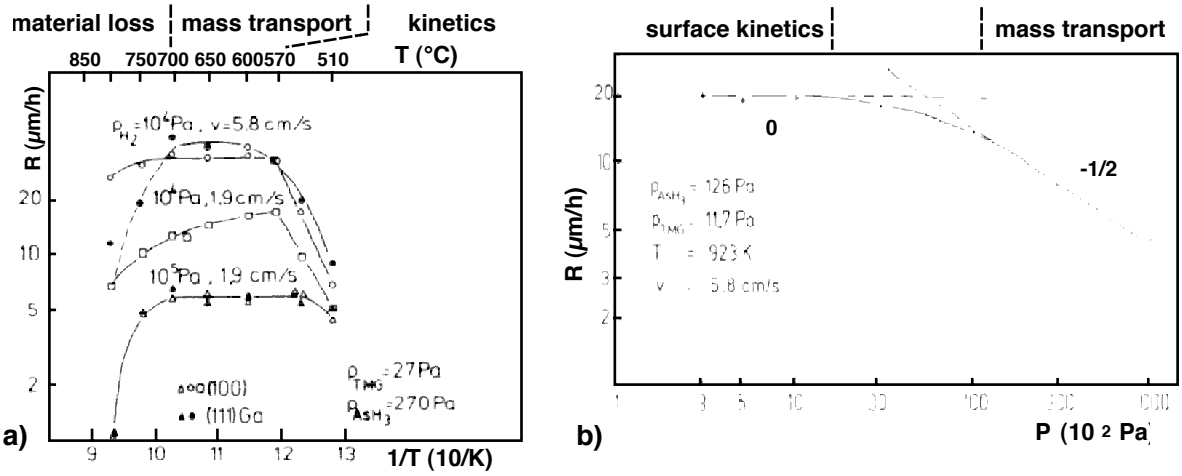

Figure 1.10: a): Dependence of the GaAs growth rate, using TMGa and ASH_3, on the substrate temperature for different reactor pressures and gas velocities [23]. Different growth regimes are indicated. b): Dependence of the GaAs growth rate, using TMGa and AsH_3, on the total reactor pressure [23].

Substrate temperature and reactor pressure are the two determinant parameters affecting the growth mechanisms; their effects have been extensively studied [23]. The effects of the growth temperature are shown in Figure 1.10a, for atmospheric pressure (AP - 10^5Pa = 1000mbar) and for 10^4Pa = 100mbar. At both pressures, one can recognize three regimes. At low T, growth is kinetically limited, and therefore strongly dependent on T, but practically pressure-independent. In this regime, the growth rate dependence of the TMGa partial pressure was found to follow a Langmuir-Hinshelwood isotherm [53]. At mid temperatures, the growth rate does not depend appreciably on T, but increases with decreasing pressure, as expected for mass transport-limited growth. In this case, $R \sim p_{TMGa}$, as implied by eq. (1.5). At even higher T, increasingly low growth rates are observed, probably due to homogeneous reactions in the gas phase, causing a depletion of reactants. The dependence of the growth rate on the reactor pressure is plotted in Figure 1.10b, for $T = 650$°C and V/III ratio ≈ 100 [23]. In this case, two regimes can be recognized. At $P > 100$mbar, growth is limited by mass transport, and $R \sim P^{-1/2}$, as expected from (1.5) [5]. After a transition region, at $P < 20$mbar, the growth rate becomes independent on P, and growth becomes kinetically limited.

[5] There are some controversies, however, on the interpretation of the mass-transport limited growth rate dependence on the reactor pressure in terms of eq. (1.5) [53].

1.1.1.1 Growth of $Al_xGa_{1-x}As$ ternary alloys

For ternary (or, rather, pseudobinary) alloys of the type $A_xB_{1-x}C$, where mixing occurs on the cation sublattice, the relation between the solid and the vapor composition becomes very simple for standard (mass transport limited) growth conditions. We have seen above that in this case the concentration of group-III species at the surface is negligible, since they are essentially all incorporated. Therefore, the solid composition is determined by the rate of mass transport of each group III element to the surface. From the second of eq. (1.3), the solid composition x is

$$x = \frac{R_A}{R_A + R_B} = \frac{h_{G,A} C_{G,A}}{h_{G,A} C_{G,A} + h_{G,B} C_{G,B}} ,$$

where $C_{G,i} \sim p_i$, partial pressure of each group III species. By assuming diffusive flow in the boundary layer, we have, from (1.4), $h_{G,i} \sim D_i$ and, if the two diffusion coefficients are approximately equal, we obtain

$$x = \frac{p_A}{p_A + p_B} .$$

The solid composition is therefore in this case equal to the composition in the gas phase, given by the input partial pressure of the two group III components. This assumption has been verified experimentally for the AlGaAs system from TMGa and TMAl precursors (and for InGaAs and AlGaSb as well) [23]. Note, however, that measurements of the distribution coefficient

$$k = \frac{x}{p_A/(p_A + p_B)} \tag{1.8}$$

in the case of $Al_xGa_{1-x}As$ from TMAl and TMGa yielded $k = 2$, since TMAl is a dimer in the vapor phase [23].

1.3 Models of nonplanar epitaxy

In this section, we will address the issue of the shape that a nonplanar surface assumes during epitaxial growth. With a semi-empirical approach, this shape can be constructed with a formalism analogous to the Wulff construction of the equilibrium crystal shapes, starting from the growth rates on a particular set of facets. We will see, however, that gas-phase and lateral surface diffusion can alter this simple picture, in a way that is strongly dependent on the growth technique. A brief review of Monte Carlo simulations of nonplanar epitaxy will conclude the section.

1.3.1 Equilibrium shape of crystals

In 1901, Wulff [56] developed a model that predicts the equilibrium shape of a small crystal. According to the Wulff theorem, the equilibrium crystal shape is the one that minimizes the total surface free energy, defined as the integral

$$\int \gamma(\mathbf{n}) dS , \tag{1.9}$$

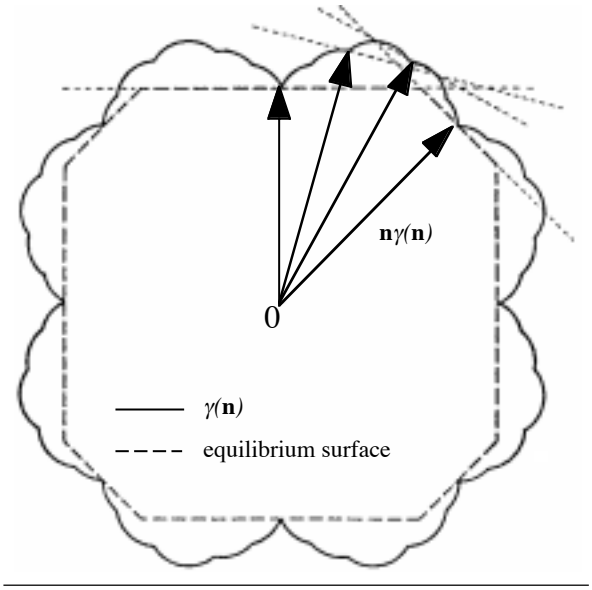

Figure 1.11: Two-dimensional polar plot of the surface energy γ(θ), and relative Wulff construction [57].

extended over the surface of the body. γ is the specific surface free energy, that depend on the local surface orientation $\mathbf{n} = (\theta,\phi)$ (note that for an isotropic γ, the equilibrium shape is a sphere). Once the orientation dependence of γ is known, the equilibrium shape can be determined geometrically as follows (see Figure 1.11). Using a polar plot of $\gamma(\theta,\phi)$, one constructs the set of planes perpendicular to the vectors $\mathbf{n}\gamma(\mathbf{n})$ pointing from the origin, and passing through to the points of extremal values of $\gamma(\mathbf{n})$. The Wulff theorem states that the equilibrium crystal shape is given by the inner envelope of these planes. After the original formulation by Wulff, this construction has been subsequently reformulated by Herring [57] and Andreev [58]. It can be proven *a posteriori* that the Wulff construction satisfies the uniformity of the chemical potential on the crystal surface ([59], Chap. 3). Note that:

i. This construction favors correctly the formation of planes with low surface energy, which lie closer to the origin.
ii. The γ-plot presents cusps for the lowest-energy orientations (that are in general high-symmetry, low-Miller indexes orientations), determining the appearance of flat facets.
iii. As the temperature T increases, the γ-plot becomes less and less cusped, causing the disappearance of facets as T exceeds the individual facet roughening temperature T_r, and until the γ-plot becomes isotropic (spherical equilibrium shape) (see, e. g., [60], Chap. 6).

For GaAs crystals, Moll et al. estimated the equilibrium shape by calculating the absolute surface energies for different orientations, as a function of the chemical potentials and of the related surface reconstructions, under the assumptions that only {100}, {011}, {111}A and {111}B facets exist [61]. In As-rich environments, which are usually present in OMCVD, all four orientations were found to coexist in equilibrium, with little variation of the surface energy with orientation [61].

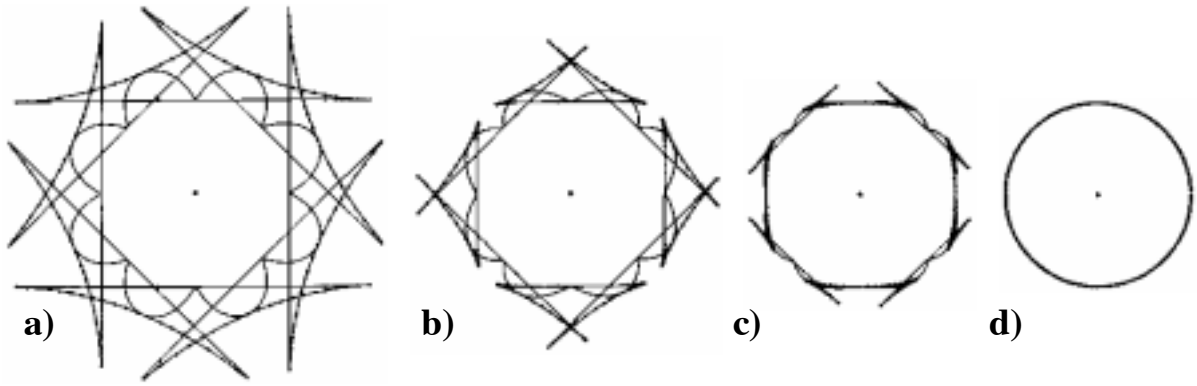

Figure 1.12: γ-plots and equilibrium shapes for a hypothetical 2D crystal with (11) and (10) facets, at different T: a) T=0; b): 0<T< $T_r^{(10)}$; c): $T_r^{(10)}$<T< $T_r^{(11)}$; d): T> $T_r^{(11)}$ [60].

1.1.2 Orientation dependence of the growth rates

In this section, we will address the issue of what shape a crystal assumes during growth. In particular, we will treat the case of the evolution of the growth profile during epitaxial growth on a patterned, nonplanar surface. Based only on geometric considerations, it easy to see [62] that at a convex corner between two facets, the slow growing facet will consume the fast growing one. The rate of this facet consumption is given by the angle ϕ between the growth direction and the propagation direction of the intersection between the facets (see Figure 1.13a):

$$\tan\phi = \cot\alpha\left(\frac{r_2}{r_1} - 1\right), \tag{1.10}$$

where α is the angle between the facets, and r_1 and r_2 are the growth rates of the facets 1 and 2, respectively, projected in the growth direction. At a concave corner, the slow growing facet is consumed by the fast growing one, at the same rate (see Figure 1.13b).

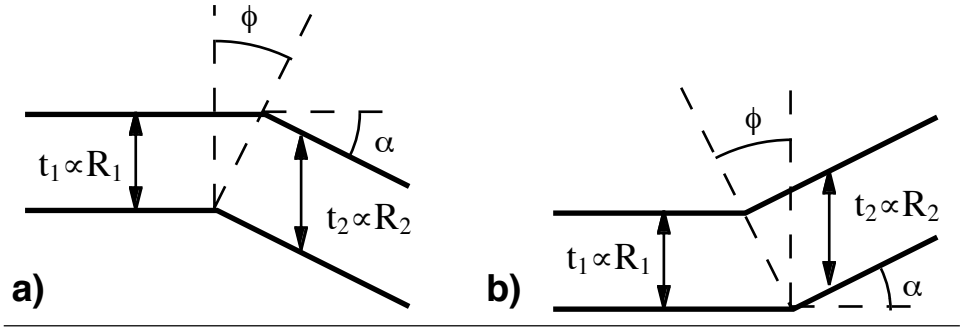

Figure 1.13: a) Evolution of a convex surface profile. The thickness of facet i, t_i, is proportional to the growth rate R_i. b) The same for a concave profile.

This simple model has been successfully applied to describe the facet evolution during MBE growth of GaAs on patterned substrates [62]. However, it can not take in account the formation of new facets at the corners between two existing ones, which is often observed. The reason is that in this model the growth rates in the orientations between two facets are supposed to be linearly interpolated. On the other hand, if the growth rate presents minima (maxima) for some intermediate orientations, new facets with these orientations will appear at this convex

(concave) corner. An interesting attempt to take this experimental fact into account is based on the Wulff construction mentioned above [63, 64]. In this model, the evolving surface shape is given by:

$$\min \int R(\mathbf{n}) dS \quad \text{convex profile}$$

$$\max \int R(\mathbf{n}) dS \quad \text{concave profile}$$

These equations are formally identical to the Wulff equation (1.9); a mathematical justification of this "dynamic" Wulff construction can be found, e. g., in Ref. [59], page 48. According to this model, the growth shape at a convex (concave) contour will therefore be given by the inner (outer) envelope of planes constructed with this "*R*-plot". In particular, new facets will develop, corresponding to the possible extrema in the growth rate (see Figure 1.14).

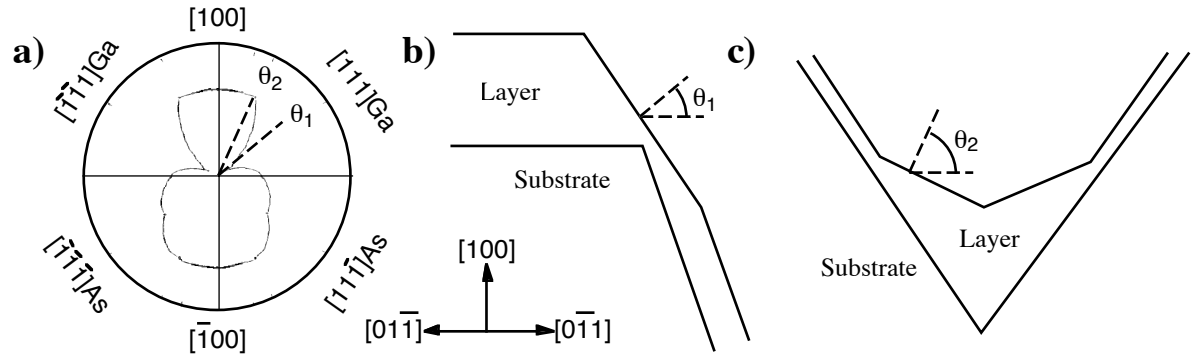

Figure 1.14: a) Example of polar plot of the growth rates. b, c): Resulting growth profile at a convex (b) and concave (c) corners. Note the formation of a new facet, at an orientation corresponding to a cusped minimum (b) or maximum (c) of the growth rate, for angles θ_1 and θ_2, respectively [63].

The polar plots of the growth rates were determined for OMCVD growth by Jones *et al*, using the fact that the surface reaction flux for an arbitrary facet (*hkl*) $J_s^{(hkl)}$ can be expressed in terms of the reaction fluxes of 13 basic site types J_i:

$$J_s^{(hkl)} = \sum C_i^{(hkl)} J_i \tag{1.11}$$

where $C_i^{(hkl)}$ is the density of sites of type (*i*) on the (*hkl*) surface [64], i.e., its surface concentration, normalized such that $\sum C_i^{(hkl)} = 1$. Since $C_i^{(hkl)}$ are known universal values depending only on the crystallographic structure, the complete crystallographic dependence of the growth rate can be determined once the J_i's are measured. Jones *et al*. measured these quantities on a set of planar and multifaceted substrates, giving a good agreement with the experimental observations on the evolution of nonplanar surfaces.

1.1.3 Diffusion models of nonplanar growth.

A drawback of the model presented above is that the growth rate on a facet is affected by interactions with other facets, giving rise to surface diffusion fluxes, as well as by effects of the

nonplanar profile on the transport of precursor species to the surface in OMCVD. Both these effects can alter relation (1.11), which therefore loses its generality. For example, Dzurko *et al.* [65] found that the ratio of the OMCVD growth rates between the sidewall of a V-groove and the adjacent (100) ridges depends strongly on the groove width, for grooves wider than 2μm, as a result of lateral surface diffusion.

Similarly, on a flat-bottom groove, the growth rates on the bottom (100) facets are generally lower than those on the ridge with the same orientation, and increase with the groove width [67, 68]. This is due to the fact that the growth rate is proportional to the concentration gradient of group III species diffusing from the gas phase to the surface through the boundary layer. As can be seen in Figure 1.15, this gradient is lower above the bottom of the groove, and decreases with increasing groove depth and decreasing width [69]. These effects are stronger at higher reactor pressures (where the mean free path of the species in the boundary layer is lower) and when the lateral surface diffusion is lower (e.g., in AlGaAs compared to GaAs) [67]. The relative importance of surface reaction and gas phase diffusion effects has been studied in Ref. [70]. Consistently with experimental observations, it was found that increasing either the surface or the gas phase diffusion rates yields a more uniform concentration profile above the surface.

A striking effect of the lateral diffusion appears in OMCVD growth of AlGaAs on V-grooves, if the more unstable triethylgallium (TEGa) and dimethylethylaminealane (DMEAAl) are used, instead of the traditional precursors TMGa and TMAl. In this case, the shorter diffusion length of the growing species causes the growth rates on the sidewalls to be nonuniform, and decreasing towards the bottom of the groove [71]. This effect can be interpreted quantitatively by using a geometric model that considers the "shadowing" effects of the groove on the arrival flow [71]. For low pressure OMCVD growth with TM species, this effect is washed out because of the very large lateral diffusion length of the growth species (several μm). The two different growth modes are schematized in Figure 1.16, and are compared to the "cos θ rule" of MBE growth. According to this rule, the MBE growth rate on each facet (in the absence of interfacet diffusion) is proportional to the cosine of the angle that the normal to the facet forms with the nearly vertical atomic flux J_0.

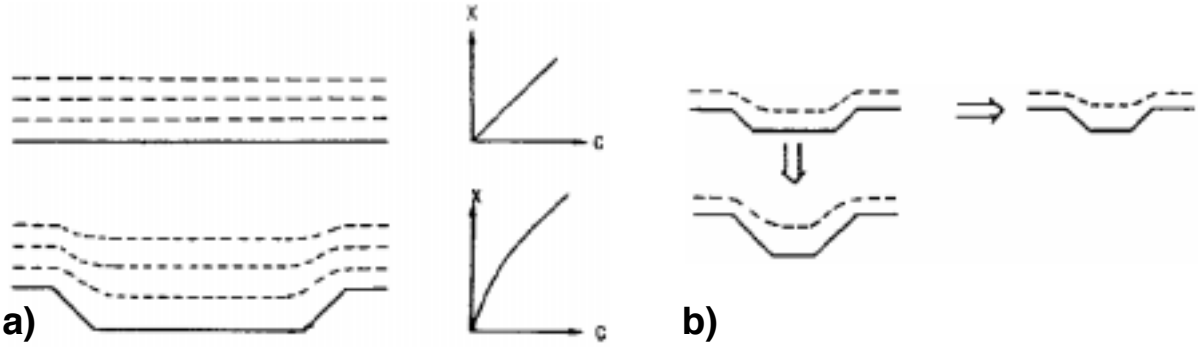

Figure 1.15 a): Concentration gradients above a planar and nonplanar substrates. Dashed lines are surfaces of constant concentrations (X = height above the substrate, C= concentration of group III species). b): Influence of groove depth and width [66].

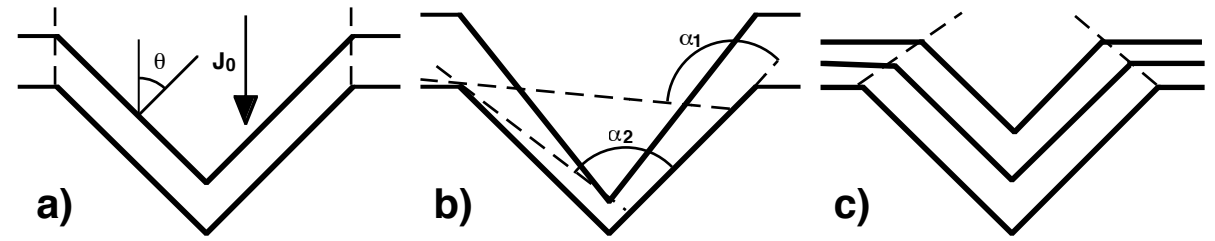

Figure 1.16 a): Dependence of the impinging flux on the cosine of the facet angle θ in MBE ("cos θ rule"). b) Shadowing effects in OMCVD growth: the reactant flow in the groove is shadowed and proportional to the solid angle α, which decreases going towards the bottom of the groove [71]. c) In OMCVD with TM precursors, if the groove width is much smaller that the precursor surface diffusion length (several μm), shadowing effects disappear (providing a uniform flow occurs on the surface), and all the facets evolve parallel to themselves.

The facet-dependent growth rate in nonplanar epitaxy appears therefore to be the result of a combination of the different surface morphology of the exposed facets (giving rise to different incorporation rates and lateral diffusion fluxes) and of the influence of the surface geometry on the concentration gradients at the surface. The former effect is dominant when the surface reaction rates are the limiting step in OMCVD growth, e.g., at low reactor pressures (where gas phase diffusion through the stagnant layer is more efficient) and for higher surface diffusion.

1.3.4 Monte Carlo simulations of nonplanar growth

Kinetic Monte Carlo (MC) simulations are a useful tool to test the epitaxial growth mechanisms on the atomic level [72]. The advent of atomic resolution imaging techniques such STM and AFM allows a direct benchmark for the simulated growth mechanisms. MC simulations are performed in general on the so-called solid-on-solid (SOS) model, in which the substrate is assumed to consist of a simple cubic lattice with neither vacancies nor overhangs, so that every atom has another atom beneath it [73]. "Growth" then takes place via a random deposition of atoms and surface diffusion, in the form of nearest-neighbor hopping, with a hopping rate given by:

$$k(T) = k_0 \exp(-E_D / k_B T),$$

where k_0 is an adatom vibrational frequency (taken as a constant $\approx 10^{13}$ s^{-1}, or equal to $2k_BT/h$, with k_B the Boltzmann constant and h the Plank constant), and E_D is a hopping barrier, with a contribution E_S from the substrate and a lateral one nE_N, proportional to the number n of nearest-neighbors (see, for example, [74]). These latter parameters can be adjusted to reproduce the experimental results.

These models could reproduce successfully different growth modes in MBE on singular and vicinal surfaces; they are not adequate however to describe the growth kinetics in cases where atoms are supplied by precursor molecules via chemical reactions [75]. Some efforts in this direction have been made to simulate planar organometallic MBE growth of GaAs with TEGa and TMGa precursors (by adding to the model a precursor with higher surface mobility than that of atomic Ga) [76]. For OMCVD, however, flows, reactions, heat and mass transfer in

the gas phase can not be ignored [75]. In an attempt to simulate selective OMCVD growth on a masked substrate, a simulation of flow, heat transfer and mass transport in the reactor was combined with a MC simulation of kinetic transport of the species inside the exposed parts of the substrate [77].

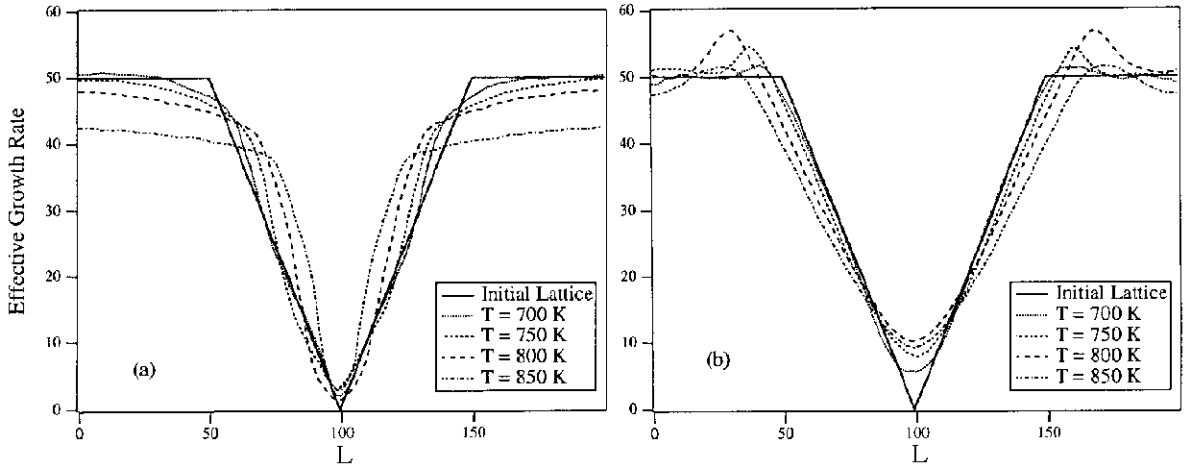

Figure 1.17 Effective growth rates on a V groove, after simulated growth of 500 ML GaAs at different temperatures. This nominal thickness has been subtracted from the grown profiles, to compare them with the initial ones. Horizontal and vertical scales are in units of MLs. a) Adatom mobility lower on the sidewalls than on the ridges. b) The opposite situation [78].

The few reported simulations on nonplanar substrates are at present restricted to an MBE-like growth environment. An additional difficulty arises when a square lattice is used in the presence of facets other than (100). To circumvent this problem, Haider *et al.* have chosen to take in account also second-nearest-neighbor interactions E_{2N} in the evaluation of E_D [78]. Depending on the chosen relative magnitude of E_N andE_{2N}, the sidewalls of the groove have a higher ($E_{2N} < E_N$, Figure 1.17(a)) or lower ($E_{2N} > E_N$, Figure 1.17(b)) growth rate than the surrounding (100) ridges, due to the lower (higher) adatom mobility on the sidewalls, with respect to the ridges. These effects are enhanced at higher T, and bring in either case to a planarization of the groove. These two situations correspond qualitatively to what has been observed by microprobe RHEED on MBE grown V-groove samples exposing {111}B or {111}A sidewalls, respectively [78].

1.3.5 Summary

In the first part of this chapter, we have seen that, in order to exploit the potential advantage of low-dimensional semiconductor nanostructures, some stringent criteria must be met, in term of size, uniformity and interface quality. A suitable method for QWR and QD formation relies on the creation, before growth, of templates for these nanostructures on particular sites of a nonplanar substrate. Subsequent epitaxial growth of semiconductor heterostructures leads to nanostructure formation on these sites. Since the shape of the growth profiles depends on the self-ordering properties of the epitaxial process, it is of fundamental importance to understand and possibly control the physics of nonplanar epitaxy. After an overview of the OMCVD

process, the current status of the knowledge of epitaxy on corrugated substrates was given in the last part of the chapter. These notions will be applied in the next chapter to OMCVD growth of GaAs/$Al_xGa_{1-x}As$ heterostructures on V-grooved substrates. We will see how these models can interpret the growth features we observed at the μm-scale, and what are the necessary conditions for establishing sharp profiles at the bottom of the V grooves, where QWRs are grown. However, models based on fixed growth rate differences between two adjacent facets can not explain the self-limiting growth behavior at the bottom regions on the 10nm scale, which is fundamental for QWR formation. We will develop an analytic model to understand these phenomena in Chapter 5.

Chapter 2

Self-ordered nonplanar growth and formation of nanostructures

In this chapter, we will present a detailed cross-sectional analysis of OMCVD growth on V-grooved substrates. We will treat in particular the case of low-pressure (LP, 20mbar) OMCVD of GaAs/$Al_xGa_{1-x}As$ heterostructures, except otherwise indicated. The chapter will begin with a description of the experimental setup and parameters for the preparation of the nonplanar substrates, and for the subsequent OMCVD growth. In Section 2.2 we will analyze the general morphology of our growth profiles, on the scale of the V-groove corrugations. In particular, we will analyze the formation and evolution of the facets composing the grooves, and will study their relative growth rates. The main part of the chapter (Section 2.3) will present a study of the self-limiting growth profiles, forming at the bottom of the grooves at the 10nm-scale. We will see that these profiles are composed of a set of nm-sized facets, whose growth rates can self-adjust in order to yield a steady-state, self-limiting evolution of the growth front. The dependence of these self-limiting profiles on the material and growth conditions evidence that their width and shape are controlled by surface diffusion. At the end of the chapter, we will see how the self-limiting behavior of the growth front at the bottom of the groove can be exploited to form arrays of quantum wires and quantum wire superlattices. In particular, a semi-empirical model will be proposed to explain the formation of these latter structures in terms of the self-limiting properties of the constituent materials.

2.1 Experimental

2.1.1 Nonplanar substrate preparation

The first step in the process of nonplanar epitaxy is the preparation of the corrugated substrates, patterned with an array of V grooves. Substrate preparation consists of a lithographic process, which serves to create periodic arrays on a resist layer deposited on a planar (100) GaAs substrate, and subsequent wet chemical etching to transfer the pattern onto the substrate. Depending on the size and characteristics of the required V-grooved pattern, we employ three

different fabrication methods.

Optical lithography is used for V-groove array pitches larger than 3μm. This is the method used for most of the growth studies presented here, since it is the fastest and easiest fabrication technique for large-area arrays (up to a quarter of a 2-inch wafer), and is the method of choice if the V groove density is not an issue. The wafers are first coated with a ~1.3μm-thick photoresist film (positive S1813 resist), deposited on a spinner (5000RPM), for better uniformity (Figure 2.1a). The coated wafers are then introduced into a mask aligner (Karl Suss MA56), where they are pressed against a Cr-written mask (contact printing). The lines written on the mask are then aligned in the $[01\bar{1}]$ orientation of the GaAs wafer, with accuracy better than 0.01°. The sample is illuminated with a Hg lamp through the mask, thus creating an array of exposed lines on the resist film (Figure 2.1b). Illumination changes the chemistry of the exposed parts of the resist: in the case of positive resist the illuminated parts are removed through subsequent developing (Figure 2.1c). After a bake (about 30' at 120°C), to better fix the resist, the sample is etched in a H_2SO_4:H_2O_2:H_2O (1:8:40 by volume) solution, to transfer the pattern onto the substrate (Figure 2.1d). The anisotropy of the etching exposes groove sidewalls in the {111}A orientations that, for optimal etching conditions, meet with sharp corners at the top and at the bottom of the structure, thus forming an array of V-shaped grooves. A final degreasing in solvent solution removes residual particles of resist from the surface.

When a higher QWR density is desirable, or if faster planarization of the corrugated surface during growth is required, V groove pitches of 0.5μm to 0.25μm are needed. In this case, the necessary resolution can be achieved with holographic photolithography. In this technique, the substrate is coated with a Si_3N_4 antireflective coating and a negative AZ5200 resist. The grating is defined on the resist layer by a two-beam interferometer, using a 364nm Ar laser light, and then transferred into the Si_3N_4 layer by CF_4 reactive ion etching. The anisotropic wet chemical etching is done again in a H_2SO_4:H_2O_2:H_2O (1:8:40 by volume) solution. Finally, the residual mask is cleaned in a buffered HF solution.

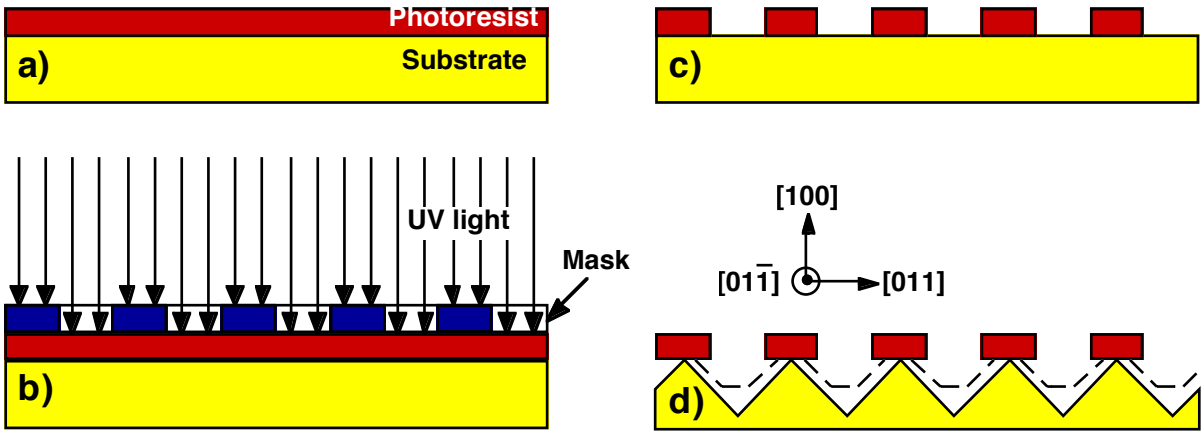

Figure 2.1: Schematics of the optical lithography and etching process. a) Deposition of the resist film. b) Exposure through a contact mask. c) Development of the resist. d) Anisotropic wet chemical etching.

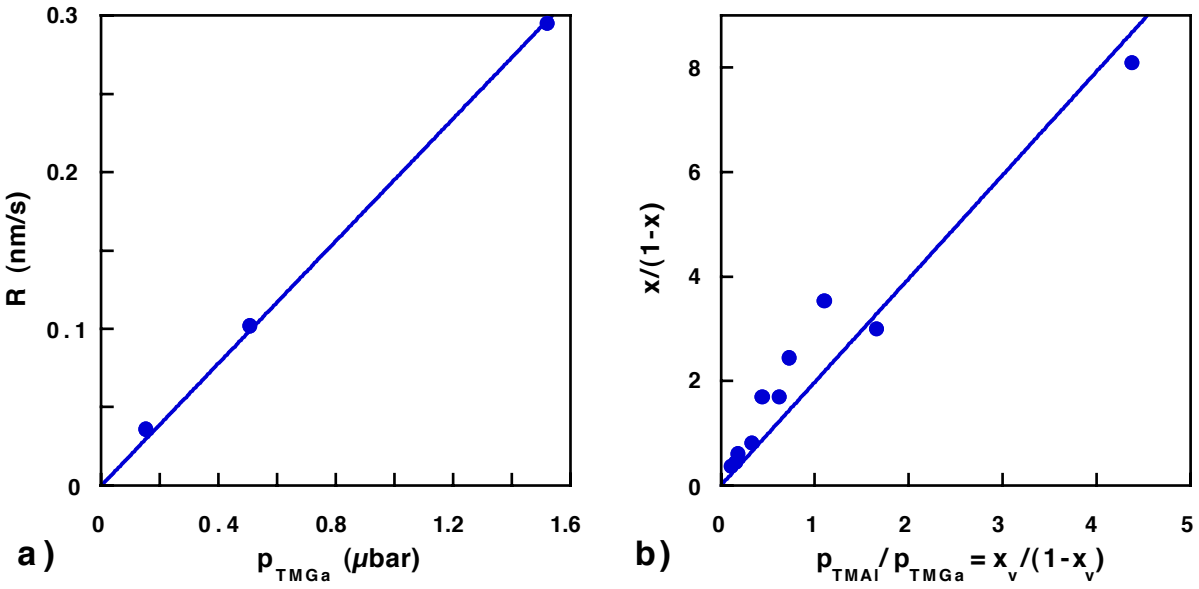

Figure 2.2: a) Measured GaAs growth rate, as a function of the TMGa partial pressure. b) Ratio of the solid Al mole fraction to solid Ga mole fraction, as a function of the ratio of the TMAl and TMGa partial pressures during $Al_xGa_{1-x}As$ growth.

For special purposes, such as variable-size, high-resolution arrays, electron-beam lithography (EBL) is used. Electron beam writing is done in a JEOL 6400 SEM with a 35keV beam, on a PMMA resist film, followed by a suitable resist development [79]. Pattern transfer into the substrate is similar to that used after the photolithographic techniques. Due to the serial character of EBL writing, the throughput is much lower than for the optical methods, and pattern arrays are therefore much smaller (areas $\lesssim$1mm^2).

2.1.2 OMCVD growth

OMCVD growth was performed in a commercial Aixtron 200 horizontal reactor with a rotating susceptor plate. The reactor consists of an outer quartz tube and an inner quartz liner tube, where all reaction gases are injected. The sample is inserted through a glove box onto a rotating graphite susceptor plate, placed in the liner tube and capable of supporting a single 2-inch wafer. Heating is provided by an IR heater with five tubular quartz lamps. The gas handling system consists of two separate gas lines, for metalorganics and hydrides. The temperature- and pressure-controlled metalorganic sources are TMGa (2X), TMAl, TMIn (2X), and DMZn for p-type doping. The hydrides are AsH_3, PH_3 and SiH_4 for n-type doping. The carrier gas is Pd-purified H_2, also used for substrate rotation. The flow rates of all gases are adjusted using electronic mass flow controllers (MFCs).

The total reactor pressure was kept at 20mbar, and the total carrier gas flow was 6l/min. Typical growth temperatures varied between 550°C and 700°C for GaAs, and 600°C and 750°C for $Al_xGa_{1-x}As$. For GaAs growth, the partial pressures of the growth species were typically 0.33mbar for AsH_3 and 1.52μbar for TMGa. The resulting GaAs growth rate R on (100) planar

substrates was about 0.3nm/sec[1]. Under these conditions, GaAs growth on a planar (100) substrate is limited by mass transport, and the growth rate R depends essentially only on the TMGa partial pressure, and is independent of the growth temperature (eq. (1.5)). The linearity of the GaAs growth rate with the TMGa partial pressure is shown in Figure 2.2a. The values were measured by cross sectional TEM on three ~100nm-thick GaAs layers; growth at either 650 or 700°C yielded exactly the same rates. $Al_xGa_{1-x}As$ growth is limited by mass transport as well. As a consequence, the ratio $x/(1-x)$, as a function of the ratio of the TMAl and TMGa partial pressures is nearly a straight line (Figure 2.2b). The slope of this line is the ratio of the Al to Ga distribution coefficients (eq. (1.8)), and yields a value of 1.98±0.14, consistent with the fact that TMAl is a dimer in the gas phase [23]. $Al_xGa_{1-x}As$ growth was generally performed by keeping fixed the AsH_3 and TMGa partial pressures and varying the TMAl one. A TMAl partial pressure of 0.47μbar yielded $x = 0.45$ and $R = 0.5$m/sec. For very high Al contents, however, the resulting growth rates would be too high to yield good epitaxy on the nonplanar substrates. Such high growth rates would hinder diffusion towards the bottom of the grooves, thus originating extended growth defects. Therefore, in the case of high x (>~60%), we reduced the TMGa partial pressure, to keep the growth rates low enough.

2.2 Cross-sectional analysis of patterned growth

2.2.1 Facet formation during growth

Figure 2.3 is a TEM cross section of a typical growth study structure, deposited on a 3μm-pitch V groove. The structure was grown at 700°C, and is composed of a nominally 900nm-thick $Al_{0.45}Ga_{0.55}As$ layer, in which ten 7nm-thick GaAs markers were inserted. A 6-period, (25nm/20nm) $Al_{0.45}Ga_{0.55}As$/GaAs superlattice (SL) layer was grown as a buffer. Figure 2.3 exhibits a number of features, typical for our growth structures:

1. After an initial transient, the growth front evolves parallel to itself, and is composed of a stable set of facets with constant orientation, i.e., with a uniform growth rate across each facet. The top of the mesa is formed by a central (100) facet, surrounded by two {311}A ones and by high crystallographic index sidewalls.
2. The growth rate is anisotropic; this orientation dependence favors the growth inside the groove, with respect to the top mesas, leading to a gradual planarization of the surface.
3. The bottom of the groove narrows down, from the initial profile defined by lithography, until it reaches a stable self-limited cross-sectional width, with extension on the 10nm-scale.

[1] All the "nominal" thicknesses and compositions given here and in the rest of the text have been measured by transmission electron microscopy (TEM) and X-ray diffraction (XRD) on a planar (100) reference sample, grown in parallel with the patterned substrate in the same growth run.

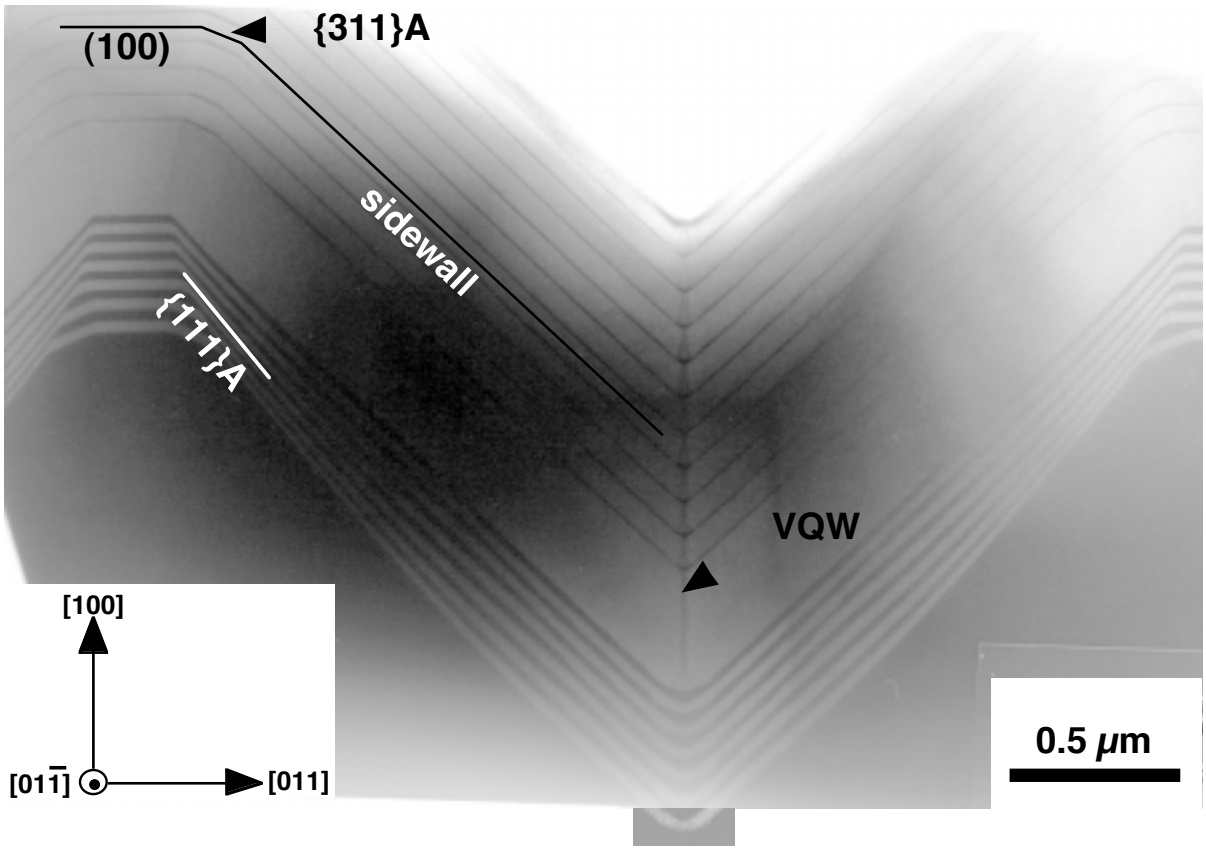

Figure 2.3: TEM cross section of a GaAs/$Al_{0.45}Ga_{0.55}As$ multilayer structure, grown at 700°C on a 3μm-pitch V-grooved substrate. The different facets are indicated.

4. The GaAs layers are thicker at the bottom of the groove, thus forming a quantum wire crescent, whose size and shape are reproducible from layer to layer.

5. A darker stripe is visible at the bottom of the groove, in the AlGaAs layers, due to a higher Ga concentration. This region forms a so-called *vertical* quantum well (VQW).

The nm-scale behavior of the growth front at the bottom of the groove will be the subject of detailed studies in the rest of the thesis. In particular, points 3 and 4 will be examined in Section 2.3, and the structure and properties of the VQW (point 5) will be the subject of Chapter 4. In this section, we will concentrate on the general properties of the growth front, at the scale of the groove size.

Figure 2.3 shows that the sidewalls of the groove are slightly concave before growth, with an orientation, with respect to the (100) planes, that is steeper in the vicinity of the top ridges than at the bottom of the groove. Close to the top, the orientation is exactly {111}A, while at the bottom it does not correspond to any low-index crystallographic direction, and forms an angle θ of about 45° with the (100). These high-index regions develop during growth, at the expense of the {111}A planes. After about 200nm, the high index facets have occupied the whole sidewall area. During further growth, their orientation remains stable if the material and growth conditions do not change, implying a uniform growth rate across their width.

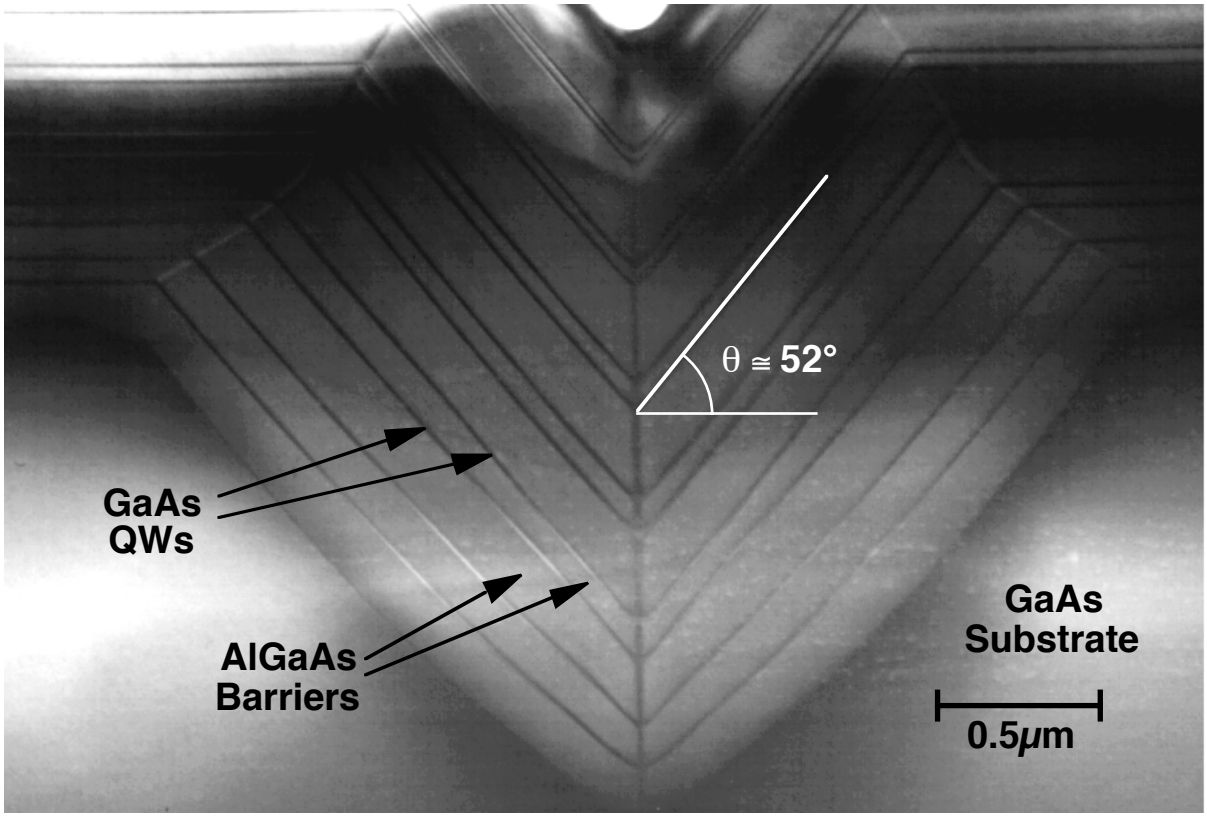

Figure 2.4: Dark-field TEM cross section of a multiple-QW GaAs/$Al_{0.48}Ga_{0.52}As$ structures, grown at 650°C by AP OMCVD on a 3.5μm-pitch V-grooved substrate.

The formation and stability of these sidewall facets should be analyzed in some detail. Ratsch and Zangwill [80] have shown that, if growth is limited by gas phase diffusion, *low-index* sidewall facets can not propagate parallel to themselves for standard growth conditions, due to variations of the supersaturation in different positions of the groove. On the other hand, if the growth rates are not too high, *vicinal* facets with a particular orientation can develop and grow with a uniform rate across their section. However, experiments showed that the OMCVD growth habit on patterned substrate changes drastically by changing the group-III precursor set, by keeping otherwise the same growth conditions [81] (see the discussion in Section 1.3.3). This confirms therefore that precursor surface kinetics play an important role in determining the nonplanar growth rates. As anticipated in Section 1.3.3, the stability of the sidewalls implies that the surface diffusion length of precursors or intermediate reaction products is much longer than the size of the grooves. In the semi-empirical model of Jones *et al.* [64], the highest growth rate on the orientation corresponding to the sidewalls is interpreted in terms of the large density of highly reactive (001)/{111}A stepped sites, for surfaces vicinal to the {111}A.

Figure 2.4 is a TEM cross section of a multiple GaAs/$Al_{0.48}Ga_{0.52}As$ structure, grown by atmospheric pressure (AP) OMCVD at 650°C on a 3.5μm-pitch V-grooved substrate, using the same set of precursors and similar growth conditions as in our growths. As for the LP case, the profile after annealing appears curved: it is nearly-{111}A oriented near the ridge, and has an orientation $\theta \cong 45°$ close to the bottom. However, this latter orientation is not maintained during

growth, differing from what was observed in Figure 2.3, and the steady-state orientation of the sidewall planes is closer to the {111}A, as compared to LP ($\theta \cong 52°$ in this case). This difference can be accounted for by the less efficient gas-phase diffusion towards the bottom of the groove through the boundary layer, as the reactor pressure is increased [67]. The reduced gas-phase diffusion at AP could hinder the growth rate enhancement at the bottom of the groove, which is at the origin of the formation of the high-index facets that develop at this region (see Figure 2.3).

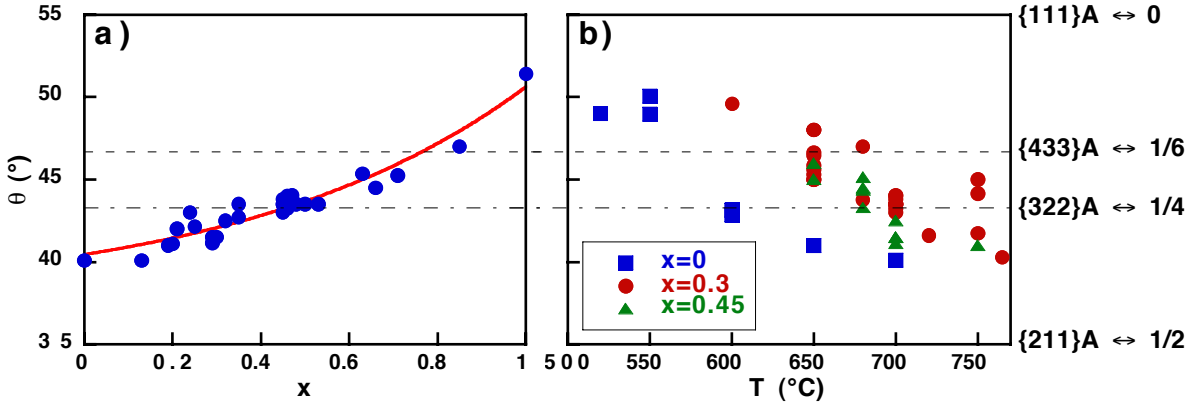

Figure 2.5: a) Variations of the angle θ that the sidewalls form with the (100) planes, as a function of the Al mole fraction in $Al_xGa_{1-x}As$ layers, for T = 700°C. Data include samples grown at 20mbar on 3μm- and 0.5μm-pitch V-groove arrays. b): Variation of θ as a function of T, for x = 0 (squares), x = 0.3 (triangles) and x = 0.45 (circles). The dashed line in both figures indicates θ corresponding to a {433}A plane (46.7°), and the dashed dotted line to a {322}A plane (43.3°). The limits of the y-axis correspond approximately to {111}A (54.7°) and {211}A planes (35.3°). Plane names are indicated on the right, together with the density of (001)/{111}A steps (see text).

The orientation θ of the sidewalls, observed in our LP structures, depends on the material composition and growth conditions, and varies over a range of about 10°. Figure 2.5a shows the dependence of θ on the nominal Al composition x in $Al_xGa_{1-x}As$ layers grown at 700°C, on 3μm- and 0.5μm-pitch grooves. Figure 2.5b shows the dependence of θ on the growth temperature T, for $x = 0$ (squares), $x = 0.3$ (triangles) and $x = 0.45$ (circles). Angles corresponding to low-index planes are indicated by the upper limit of the y-axis ({111}A ↔ 54.7°), by the dashed line ({433}A ↔ 46.7°), by the dashed-dotted line ({322}A ↔ 43.3°), and by the lower limit of the y-axis ({211}A ↔ 35.3°). The sidewalls have in all cases an orientation intermediate between {111}A and {211}A, and in most cases are oriented between {433}A and {322}A. Their orientation deviates from ideal, unstepped {111}A planes as the Al mole fraction decreases, and as the growth temperature is increased. The density of (001)/{111}A steps on a vicinal {111}A surface can be easily calculated: if the surface orientation is {hkk}, with h > k, the ratio m/n = (number of steps)/(number of {111}A surface sites) is $m/n = (h/k - 1) / 2$. This ratio is indicated, for the planes mentioned above, on the right side of the plots in Figure 2.5, together with the designation of the plane. In Figure 2.6 we show the atomic structure of the zincblende lattice, in the $(01\bar{1})$ cross section. The lattice is cut along

some low-index {hkk} directions[2]. The {211}A and {311}A facets have a (001)/{111}A step every two or one {111}A sites, respectively. The groove sidewalls, all with orientations between the {111}A and {211}A, have a (001)/{111}A step every n {111}A sites, with $n > 2$. Orientations between the {111}A and the (011) are composed by steps and terraces of these two orientations, and therefore do not form, since growth on (011) surfaces is very small in our conditions [64].

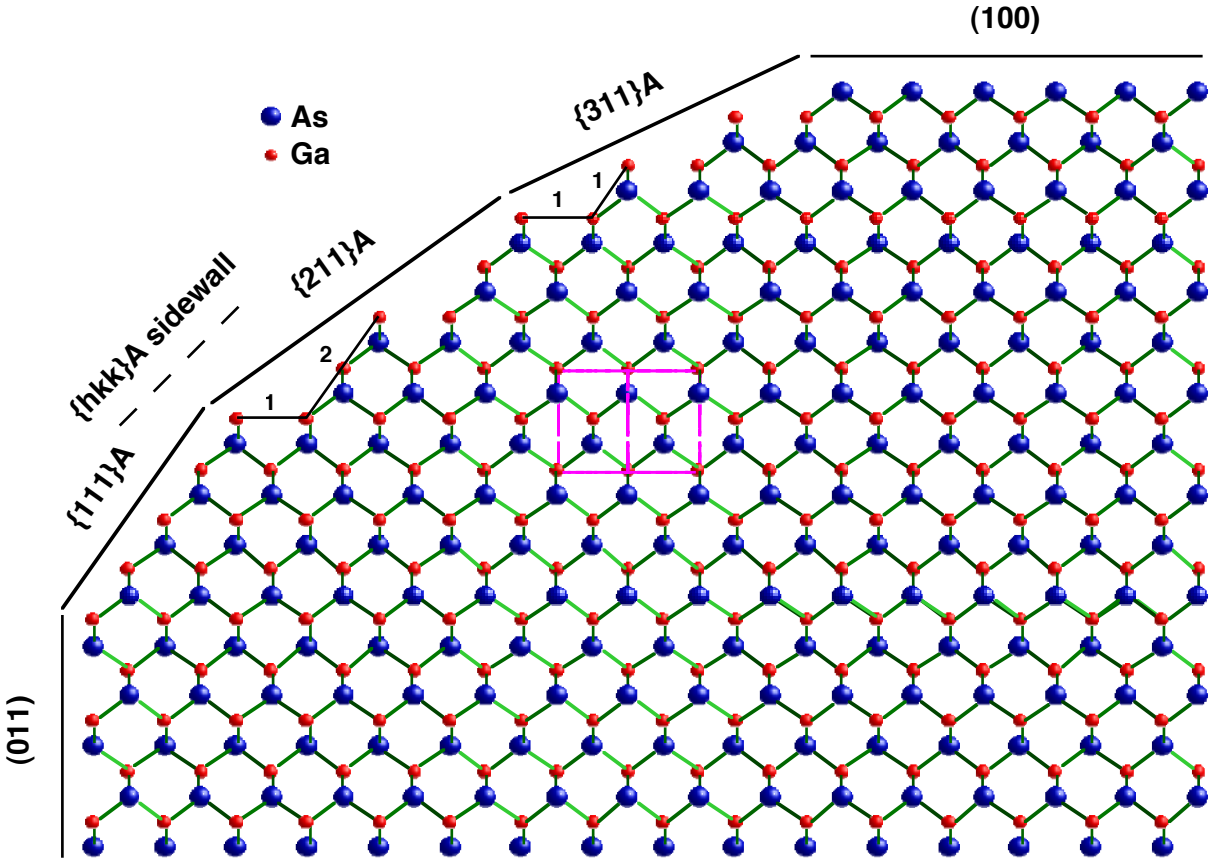

Figure 2.6: $(01\bar{1})$ *cross-sectional atomic structure of a zincblende lattice. The ideal, unreconstructed atomic terminations in some low-index {hkk} orientations are indicated.*

Since no growth rate gradients are observed across the sidewalls, and no orientation difference exists between 0.5μm- and 3μm-pitch grooves, the relevant surface diffusion lengths should be much higher than the typical size of the grooves. As we have seen in Section 1.3.3, the formation of these high-index sidewalls with stable orientation is peculiar to (Al)GaAs OMCVD with trimethyl-group III precursors, and depends on the reactor pressure (see above). This suggests that the establishment of steady-state sidewall orientations is related to gas-phase

[2] These hypothetical surfaces do not correspond to real surface structures, since atomic relaxation and reconstruction, and possible faceting are neglected. Atomic rearrangement at surfaces is particularly important on the polar {h11}A facets, which otherwise would not satisfy the electron counting criterion (all the electrons originating from surface dangling bonds must be on states below the Fermi energy) [61]. For example, we will see in Section 3.3.4 that the {311}A planes are faceting along the groove, due to step bunching.

mass transport, and to lateral diffusion and decomposition of precursors and/or intermediate reaction products (rather than diffusion of atomic species). We can obtain some insight into the mechanisms determining the sidewall steady-states by analyzing the trends in Figure 2.5, and by comparing our LP profiles with those obtained at AP. Since TMGa is less stable than TMAl, and the precursor decomposition efficiency increases with T [23], both plots of Figure 2.5 show that the tendency to deviate from exactly-oriented {111}A sidewalls, by forming a more stepped surface, should be related to faster decomposition processes. We can infer therefore that the steady-state sidewall orientation is the result of an equilibrium between effects of surface kinetics, which tend to broaden the sidewall aperture, favoring the formation of high-index facets (see x and T dependence), and of the inhibition of gas-phase diffusion, which tends to sharpen the groove (see pressure dependence).

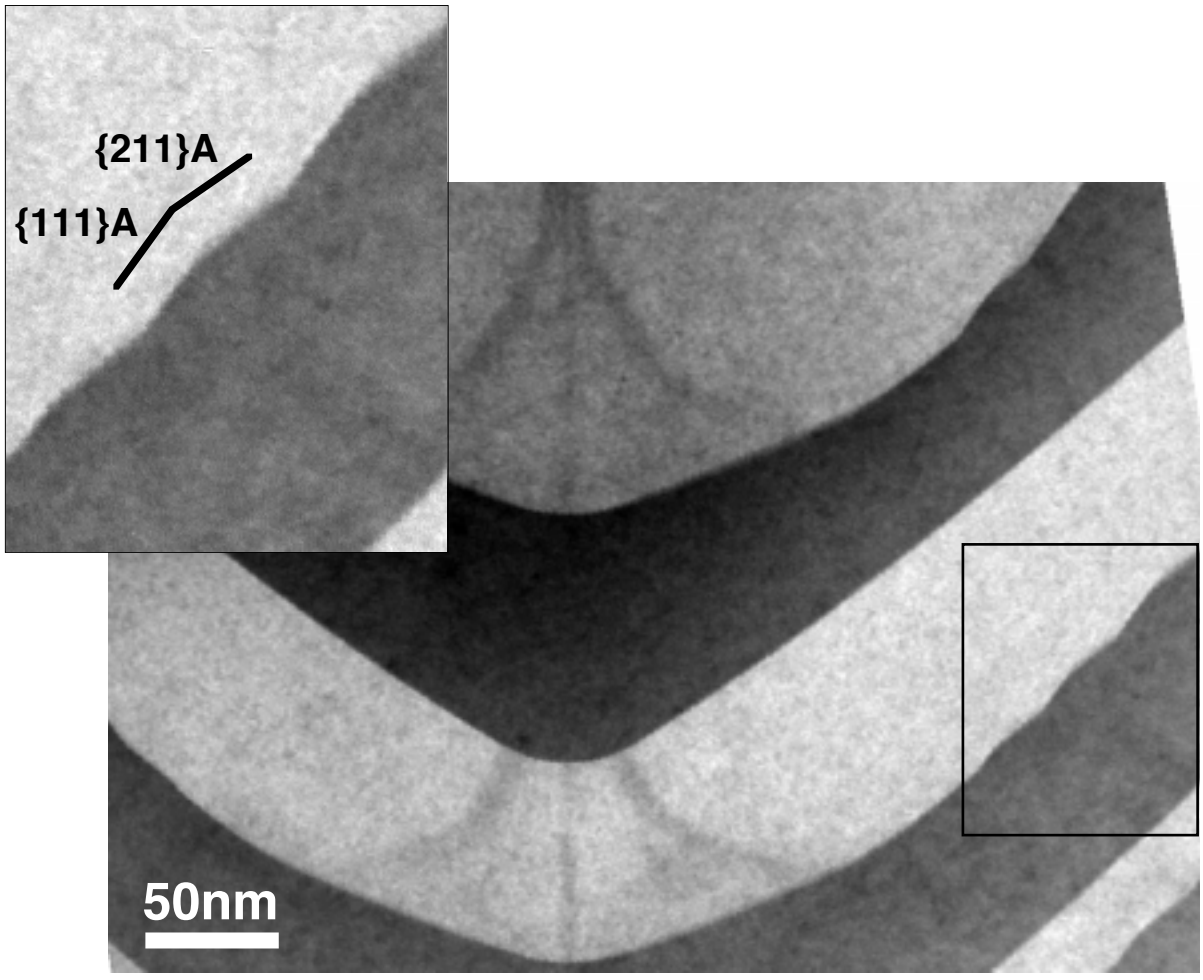

Figure 2.7: Dark field TEM image of a GaAs/$Al_{0.45}Ga_{0.55}As$ heterostructure at the bottom of a V groove, grown at 750°C. The inset shows a high magnification view of the region where step bunching is formed.

Figure 2.7 is a dark field TEM image of a GaAs/$Al_{0.45}Ga_{0.55}As$ multiple layer structure, grown at 750°C on a 3μm-pitch V groove. The region at the bottom of the groove is shown. The sidewall GaAs layers show an atomically-smooth lower interface, whereas the orientation of the upper interface varies quasi-periodically between two low-index planes, {111}A and

{211}A, due to step bunching. These planes correspond exactly to the range of variation of the sidewall orientation, as x and T are changed (Figure 2.5). The high-index sidewalls, therefore, break up into {111}A terraces, where no step are present, and step bunches with {211}A orientation, corresponding to the maximum density of steps achievable on the sidewalls in our growth conditions (Figure 2.6).

Step bunching results in periodic thickness variations, with a height of about 3-4nm and a period of about 30-40nm. Similar periodic faceting was observed in strained InGaAs layers grown on V grooves at AP-OMCVD with TMGa, TMIn and AsH_3 precursors [82]. In nonplanar OMCVD with TEGa, DMEAAl and AsH_3, step bunching is observed also in AlGaAs layers at $T = 650$°C, giving rise to tilted SL structures [83]. Besides, step bunching has been found to be the normal growth mode for vicinal, planar (111)A surfaces in GaAs atomic layer epitaxy with TEGa and AsH_3, for temperatures as low as 520°C [84]. However, this kind of step bunching is observed in our samples only for GaAs, at temperatures higher than about 750°C. Note that no evidence for tilted SL is found in the AlGaAs layers (whose upper interfaces appear to be atomically smooth), probably because the step bunches are annihilated in the first stages of AlGaAs growth. In the higher magnification image shown in the inset, it seems that a very weak composition modulation is present in the first monolayer of AlGaAs, barely visible as slightly diffused interfaces corresponding to the {211}A facets. These facets, corresponding to the bunches, should incorporate atoms better than the {111}A terraces; the higher diffusion length of Ga, relative to the Al one, should therefore favor Ga-rich regions at the edge of the step bunches [83]. However, it seems that the precursor set used in our experiments hinders formation of step bunching and tilted SLs, except for situations of very strong surface diffusion (GaAs at high temperatures).

2.1.2 Study of the growth rate distributions

We have studied the growth rate distributions on the different facets composing the profiles of the grooves, for GaAs and AlGaAs at different growth temperatures. Figure 2.8 shows polar plots of the GaAs (squares, right side of the plots) and $Al_{0.45}Ga_{0.55}As$ (circles, left side) growth rates r_G and r_{AG}, for $T = 650$°C (a) and $T = 700$°C (b), relative to the nominal ones[3]. Growth rates have been measured in the growth direction; to obtain the rates perpendicular to the facets, one needs to multiply them by the cosine of the angle that the normal to the facet forms with the [100] direction. The (100) and {311}A growth rates have been measured on the facets forming at the top of the mesas, for mesa widths larger than ~50-100nm. As we will see in Section 2.3.2, growth rates on facets with smaller cross sections are strongly altered by additional, width-dependent surface fluxes due to capillarity effects. We must therefore measure r on large enough facets, to ascribe it only to morphological differences among the different

[3] We will indicate all quantities relative to GaAs, $Al_xGa_{1-x}As$ and AlAs with indexes "G", "AG" and "A", respectively.

surface orientations, which determine different surface kinetics (i.e., decomposition and attachment/detachment rates and surface diffusion).

Figure 2.8 indicates a marked growth rate anisotropy among the facets composing the groove. This implies that, even if the *overall* growth rate on a planar sample is mass-transport limited under these growth conditions (see Section 2.1.2), the growth rate *distribution* for neighboring facets is strongly affected by surface kinetics. Besides, we observed no evident difference in the growth rate distributions between GaAs and $Al_{0.45}Ga_{0.55}As$, and between the two different growth temperatures. In qualitative agreement with what has been already observed in LP-OMCVD with TMG and TMA [64, 71], r_G and r_{AG} are maximal on the high-index orientation, between the [111]A and the [311]A, defining the sidewalls of the grooves. On these sidewalls, the growth rates are approximately equal to the nominal ones. The growth rates on the exactly oriented {111}A facets are generally less than half of the ones on the high index planes. Therefore, as can be seen in Figure 2.3, these planes are consumed during growth, since growth in a concave region favors the expansion of the faster-growing orientations (see Figure 1.13).

Since in our samples the vertical r is maximal on the sidewalls, according to Figure 2.8, no other facets can be formed at the concave bottom of the groove. This region will therefore be composed of a sharp corner at the intersection between the two high-index sidewalls. We will see in Section 5.2 that this picture is valid only down to the ~50nm-scale, below which capillarity effects, giving rise to self-ordering and QWR formation, become important. On the convex top of the mesas, the growth rate anisotropy shown in Figure 2.8 causes an expansion of the slower-growing facets, with respect to the faster-growing ones, leading eventually to the disappearance of these latter facets. Since, according to Figure 2.8, the growth rate distribution is in the order $r_{100} < r_{311} < r_{sw}$ (where 100, 311 and sw design the (100), {311}A and sidewall planes, respectively), both the {311}A facets and the sidewalls eventually disappear as growth proceeds, and the surface will planarize in the (100) orientation.

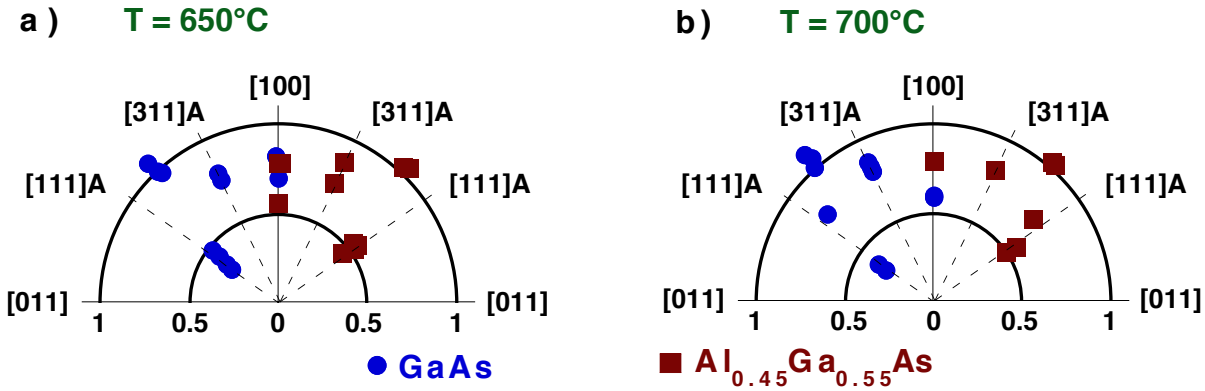

Figure 2.8: Polar plots of the relative growth rates on the facets composing a 3µm-pitch V groove array, for T = 650°C (a) and T = 700°C (b). GaAs rates (circles) are represented on the left part of the plots, and $Al_{0.45}Ga_{0.55}As$ rates (squares) on the right parts. The growth rates are measured along the growth direction, and normalized to the nominal ones, measured on a planar (100) reference substrate.

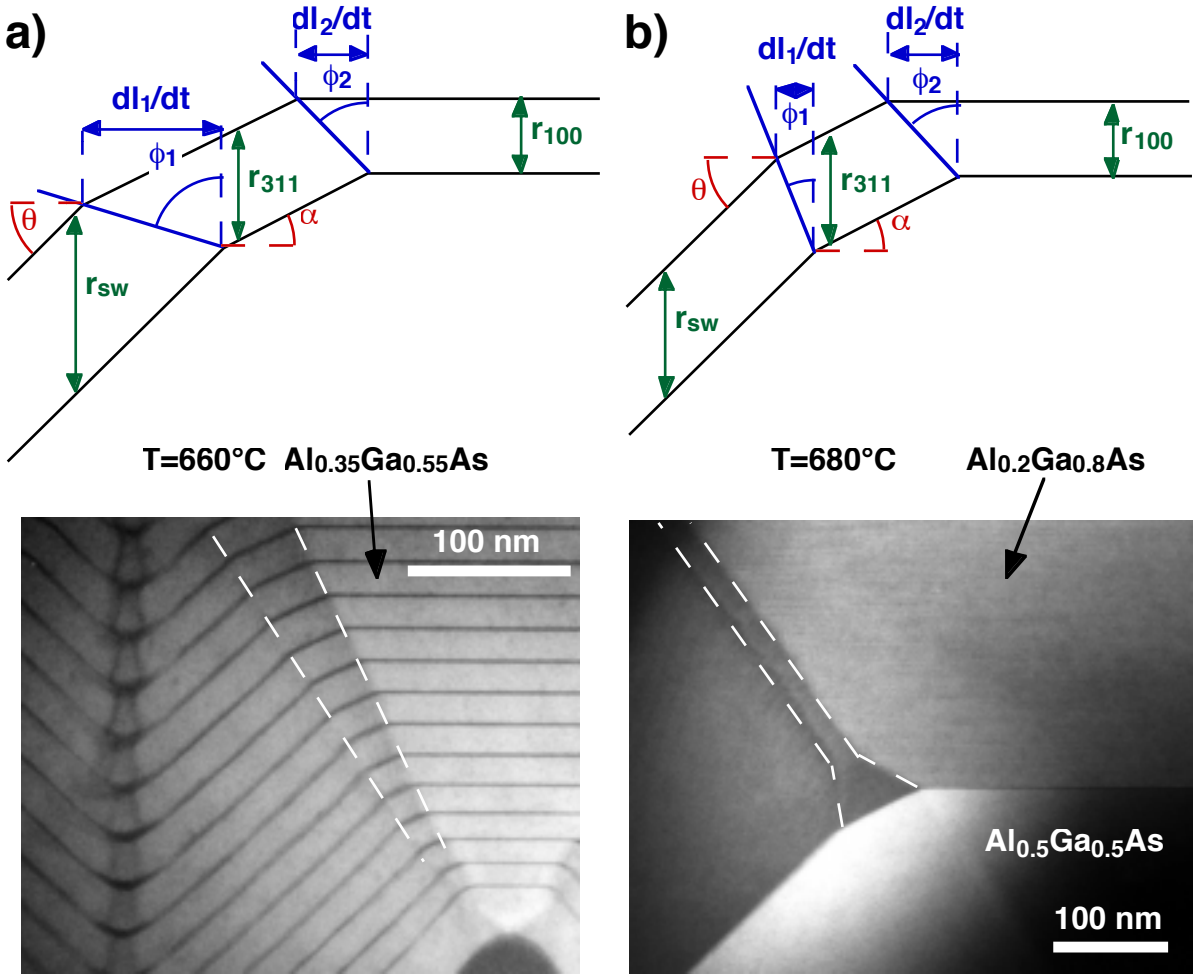

Figure 2.9: Schematic drawings (top) and dark-field TEM cross sections (bottom) of two different evolutions of the ridge {311}A facets. In a), the {311}A/sidewall consumption rate is higher than the (100)/{311}A one; as a consequence, the {311}A facets undergo an overall expansion as growth proceeds. In b) the opposite situation takes place; the {311}A shrinks until (see the TEM image) it reaches a minimum (non-zero) extension, and the inter-facet angle is determined by the relative growth rates of the (100) and sidewall planes.

Note that the top {311}A facets consume the sidewalls, and are in turn consumed by the top (100) facets. Depending on the relative rates of consumption, therefore, the {311}A facets will be annihilated or will expand before the complete planarization. The exact type of evolution is important because, in the case of annihilation of these facets, parasitic QWR-like structure can form in these regions, whose PL emission can interfere energetically with that of the bottom QWRs. The evolution of the {311}A/sidewall and of the (100)/{311}A boundaries can be measured, respectively, by the angles ϕ_1 and ϕ_2, or by the equivalent horizontal expansion rates dl_1/dt and dl_2/dt, as shown in the schematics at the top of Figure 2.9. These angles and expansion rates are related to the facet growth rates by the equations

$$\tan\phi_1 = \frac{r_{sw} - r_{311}}{r_{311}\tan\theta - r_{sw}\tan\alpha}, \quad \tan\phi_2 = \frac{r_{311} - r_{100}}{r_{100}\tan\alpha}, \text{ or}$$

$$\frac{dl_1}{dt} = \frac{r_{sw} - r_{311}}{\tan\theta - \tan\alpha}, \quad \frac{dl_2}{dt} == \frac{r_{311} - r_{100}}{\tan\alpha},$$

where θ and α are the angles that the sidewalls and the {311}A planes form with the (100), respectively (see Figure 2.9). The relative importance of the boundary evolution is given by the ratio

$$\frac{dl_2}{dl_1} = \frac{r_{311} - r_{100}}{r_{sw} - r_{311}} \left(\frac{\tan\theta}{\tan\alpha} - 1 \right), \tag{2.1}$$

where $dl_2/dl_1 > 1$ (< 1) corresponds to an overall contraction (expansion) of the {311}A facet. Since, with $\theta \approx 45°$ and $\alpha \cong 25°$, $(\tan\theta/\tan\alpha - 1) \approx 1$, the trend is directly given by the relative importance of the growth rate differences $r_{311} - r_{100}$ and $r_{sw} - r_{311}$.

Examples of the two different situations are shown in the dark-field TEM cross sections in Figure 2.9. The image in part a) is part of a GaAs/$Al_{0.35}Ga_{0.65}As$ multiple QWR structure grown at 660°C on a 0.5μm-pitch grating (part of the bottom region is also visible, showing the QWR formation). The boundaries between the different ridge facets, marked by white dashed lines, are evident due to the GaAs layers, and show an overall expansion of the {311}A facets. The image in b) is part of a heterostructure composed of a 300nm-thick $Al_{0.2}Ga_{0.8}As$ layer (darker in the image), deposited over a 250nm-thick $Al_{0.5}Ga_{0.5}As$ buffer (brighter). The structure was grown at 680°C on a 3μm-pitch grating. Only part of the ridge is visible in this image. Here the boundaries between the facets are marked by a slightly different grayscale contrast, due to small variations of the Al content in the different facets (we will analyze the local Al composition in Chapter 4). The {311}A facet in this case tends initially to shrink in the low-Al content layer. After about 50nm, however, the two boundaries with the sidewalls and the top (100) start to evolve parallel to each other, before the {311}A facet disappears completely. This sort of "self-limiting" evolution of the {311}A facet, with a cross-sectional size around 20nm, can not be explained in this framework; its existence can be accounted for with the same model that explains the self-limiting VQW formation at the bottom of the grooves (see Chapter 5). Note that these short and uniform {311}A facets can form the seed for the parasitic QWRs mentioned above.

Figure 2.10 shows experimental values of the vertical growth rates on the top (100) (circles) and {311}A facets (squares) and on the sidewalls (triangles) for GaAs (a), $Al_{0.29}Ga_{0.81}As$ (b) and $Al_{0.45}Ga_{0.55}As$ (c), measured as a function of the growth temperature. $Al_{0.29}Ga_{0.81}As$ and $Al_{0.45}Ga_{0.55}As$ growth rates was measured on two different samples, consisting of thick (~100nm) $Al_xGa_{1-x}As$ layers, separated by GaAs markers, grown at various temperatures T (625°C ≤ T ≤ 750°C), on 3μm-pitch gratings. GaAs growth rates were measured on a different sample for each T; the structures consisted of 50nm-thick GaAs layers separated by $Al_{0.45}Ga_{0.55}As$ markers. We should mention that non-systematic measurements on other samples, grown on 0.5μm and 3μm-pitch gratings, yielded (100) and {311}A growth rates that could differ from the ones shown here by as much as ±10%, while the sidewall growth rates appeared to be more reproducible from sample to sample. The error bars reported in Figure 2.10 reflect this dispersion of the measured values. This effect could be due to the finite size of

the ridge, or to differences in the facet roughness due to the etching procedure. Both effects could affect drastically the growth rates at the top of the mesa, for given growth conditions; we will see, however, that self-limiting growth at the bottom of the groove yields much more reproducible profiles in this region.

Figure 2.10 does not show a strong dependence of the growth rate anisotropy on the temperature in the interval considered, except for r_{100} for GaAs, which decreases by about 45% at 550°C, with respect to higher temperatures. Similarly to the two examples of Figure 2.8, the growth rates decrease generally in the order $r_{sw} > r_{311} > r_{100}$, with r_{sw} about 20% larger than r_{311} and $r_{311} \sim r_{100}$. Note also that the sidewall growth rate is in all cases approximately equal to the nominal growth rate (0.25nm/s for GaAs; 0.35nm/s for $Al_{0.29}Ga_{0.81}As$ and 0.45nm/s for $Al_{0.45}Ga_{0.55}As$). Since in general $r_{311} - r_{100} < r_{sw} - r_{311}$, according to (2.1) the {311}A facets should normally tend to expand. However, due to the dispersion of the data, in some samples the opposite can take place. It appears therefore that, in order to reproduce more reliably the evolution of the top of the mesa, a more accurate control of the lithographic process is needed, in terms of cross-sectional profile and surface roughness.

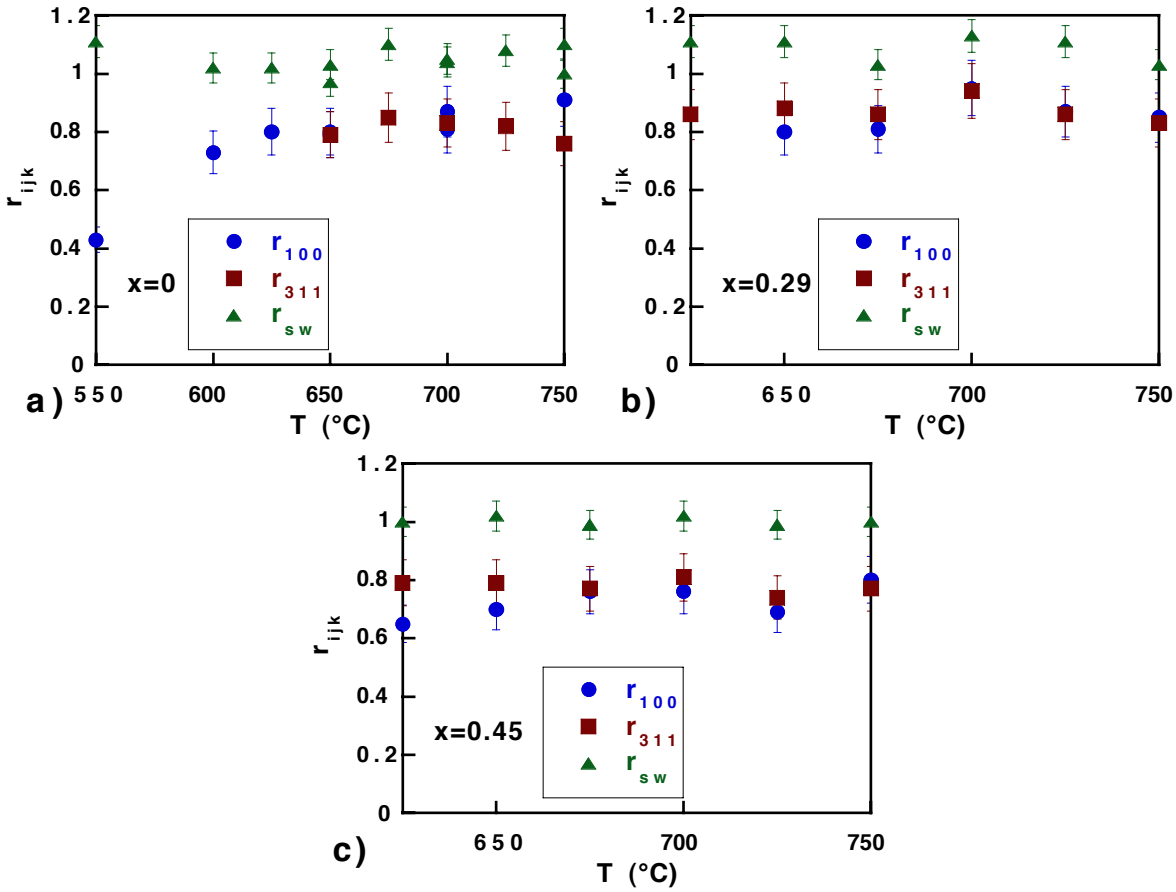

Figure 2.10: Measured vertical growth rates at the top (100) (circles) and {311}A facets (squares) and on the sidewall planes (triangles), as a function of the growth temperature, in GaAs (a), $Al_{0.29}Ga_{0.81}As$ (b) and $Al_{0.45}Ga_{0.55}As$ (c) layers grown on 3μm substrates. Growth rates are normalized to the nominal ones (0.25nm/s for GaAs; 0.35nm/s for $Al_{0.29}Ga_{0.81}As$ and 0.45nm/s for $Al_{0.45}Ga_{0.55}As$).

2.3 Cross-sectional analysis of self-limiting growth

2.3.1 Faceting of the bottom profile

Figure 2.11a is a dark-field TEM cross section of the 4th and 5th GaAs layers from Figure 2.3, showing the details at the bottom of the groove. The image reveals several growth features at the 10nm scale:

1. The AlGaAs VQW exhibits a fine structure composed of three different branches with enhanced Ga content: a narrow branch surrounded by two wider lateral ones. A more detailed discussion of the VQW properties will be given in Chapter 4.
2. The two interfaces defining the GaAs layer are very different from each other. In particular, the upper AlGaAs/GaAs boundary is much less curved than the lower one. This widening of the profile is accompanied by a thickening of the GaAs layer at the bottom of the groove (about 13nm, as compared with the 7nm on the sidewalls), that gives rise to the formation of a crescent-shaped QWR.
3. The upper QWR interface consists of a set of facets: a central (100) surrounded by two wider {311}A facets. A short, exactly-oriented {111}A "necking" connects the {311}A facets to the sidewalls.

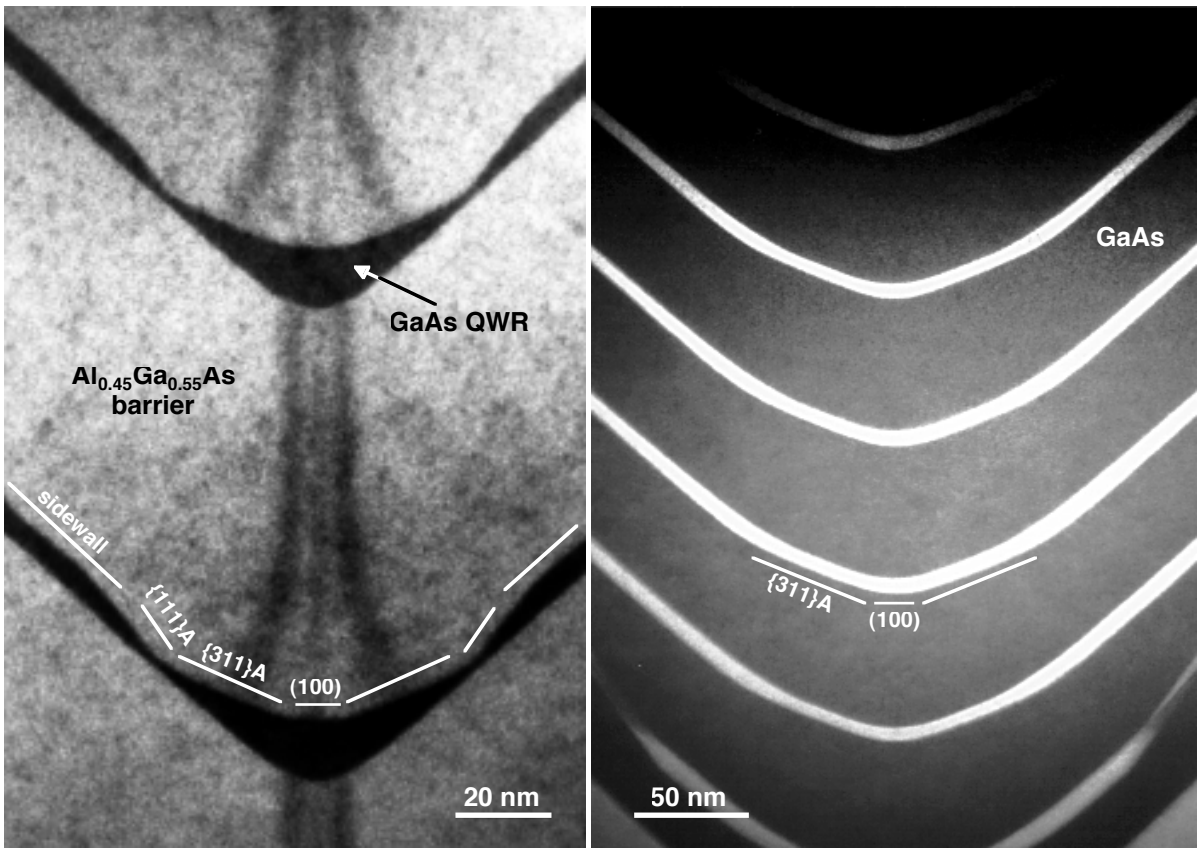

Figure 2.11: a) Dark-field TEM cross section of the bottom region of the groove, from the sample of Figure 2.3 (4th and 5th GaAs layers). b) Dark-field TEM cross section, at the bottom region of a 3µm-pitch groove, of part of a 1µm-thick GaAs layer, in which 5nm-thick AlGaAs markers were inserted every 50nm. The growth temperature was 700°C for both samples.

4. The VQW branches just above the QWR crescent are wider than the ones below it, and originate from the (100) and {311}A facets. Their width and separation decrease rapidly as AlGaAs growth continues until, after ~30nm, they recover the sizes they had before the QWR deposition.
5. If a second GaAs QWR is grown, it has the same shape and width as the one below, provided that the AlGaAs barrier is thick enough to fully recover the surface profile. This sequence can be repeated as long as the groove has not planarized.

Since the VQW branches, that originate clearly from the (100) and {311}A facets at the top boundary of the QWR, are visible and distinct also at the lower interface, we can infer that also this latter boundary is composed of the same facets. The fact that the faceting of the profile is not clearly visible in AlGaAs is due likely to the smallness of the facets in this material, which become comparable with the vertical interface width and the TEM resolution. The faceting becomes visible also at the lower boundary if the profile is larger, i.e., for lower x and higher T (see below).

Figure 2.11b is a dark-field TEM cross section of part of a 1μm-thick GaAs layer, grown at the bottom of a V groove, where 5nm-thick AlGaAs markers were inserted every 50nm. The growth temperature was 700°C, like for the structure in Figure 2.11a. The GaAs profile exhibits the same set of {311}A and (100) facets as the AlGaAs one. A comparison of the two images shows however that the lateral extension of these facets is much larger in GaAs than in $Al_{0.45}Ga_{0.55}As$, for the same growth conditions. The profile evolution during growth is complementary to that of Figure 2.11a: the AlGaAs markers, thinner at the center than on the sidewalls, induce a partial narrowing of the profile, which is fully recovered during deposition of the thick GaAs layers.

We conclude therefore that both the AlGaAs and the GaAs profiles evolve in a steady-state way at the bottom of the V grooves. The profiles are characterized by a set of low index facets, which are wider in GaAs than in AlGaAs.

2.3.2 Transient evolution towards self-limiting profiles

We have studied the evolution of the bottom facets during GaAs/AlGaAs and AlGaAs/GaAs deposition, before steady-state growth is achieved. The growth sequence used for the GaAs/AlGaAs study is sketched at the left of Figure 2.12. The core of the structure consists of 10 GaAs layers, with nominal thicknesses t_G increasing from 1 to 50nm, separated by 100nm-thick $Al_{0.3}Ga_{0.7}As$ barriers. Growth studies were performed on 3μm-pitch V grooves. As can be monitored by the VQW width, the AlGaAs barriers are thick enough to ensure steady-state AlGaAs growth before the GaAs is deposited. The right part of Figure 2.12 shows dark-field TEM cross sections of three layers of such a structure, with t_G = 1, 5 and 20nm, grown at 700°C. The white contours mark the central (100) and the lateral {311}A facets forming at the

bottom of the groove, before and just after QWR deposition [4]. Their extension $l_{\{ijk\}}$, constant at the lower GaAs/AlGaAs interface (l_{100}=5.5±0.4nm, l_{311}=13.8±1.0nm), is increasing progressively during GaAs growth, to 7.2 and 16.6nm after 1nm GaAs, 9.5 and 29.2nm after 5nm GaAs, and 19.5 and 48.0nm after 20nm GaAs.

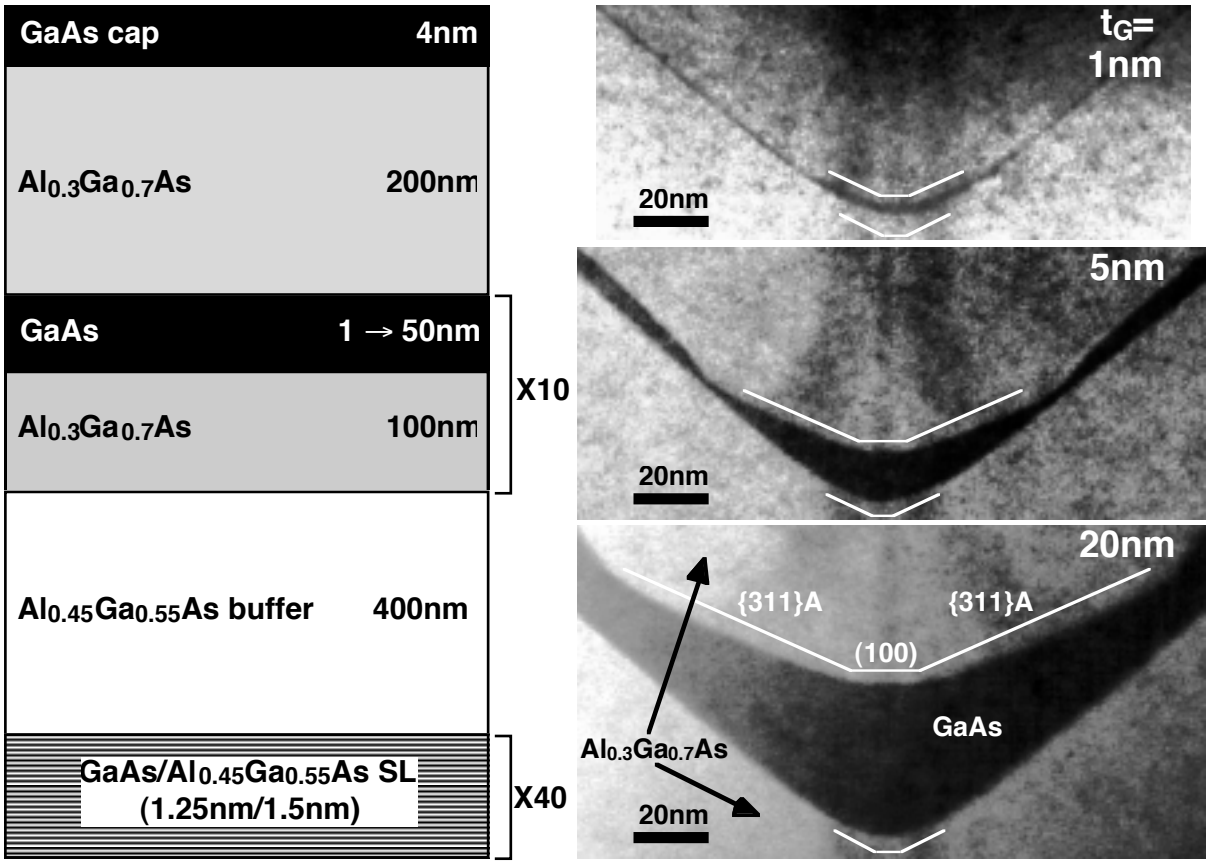

Figure 2.12: Left: schematics of a typical growth sequence, used to monitor the transient growth behavior of GaAs/AlGaAs epitaxy. The central part of the sequence consists of 10 GaAs layers, with nominal thicknesses t_G *increasing from 1 to 50nm, separated by 100nm-thick* $Al_{0.3}Ga_{0.7}As$ *barriers. Right: dark-field TEM cross sections of three GaAs layers, with* t_G *= 1, 5 and 20nm, from the growth sequence on the left. The sample was grown at 700°C on a 3µm-pitch V-grooved substrate. White contours indicate the extension of the (100) and {311}A facets.*

In Figure 2.13a we plot the lengths l_{100} and l_{311} of the (100) and {311}A facets (circles and squares, respectively) at the top of the GaAs layers, as a function of the nominal GaAs thickness t_G. Values at $t_G = 0$ are averages of the lengths measured at the bottom boundary of the GaAs layers. To check the stability of the profile, we have plotted in the figure the GaAs facet widths from the thick GaAs layers in the sample Figure 2.11b (data at t_G= 50nm). After the initial transient in the first ~30nm, the length of the facets reaches a steady-state value, that

[4] The angle of the {311}A facets delimiting the upper QWR interface appears to change at high GaAs thicknesses. This could be due to the development of facets vicinal to {311}A, but could also be an artifact due to the increase of height modulation on these surfaces along the QWR axis (see Section 3.3.4), resulting in an apparent change of slope in the TEM images, due to the tilt of the images with respect to the axis.

remains constant within ~5% fluctuations (l_{100} = 22.7±0.7nm, l_{311} = 58.3±0.9nm). In Figure 2.13b, we show the evolution of the (100) and {311}A lengths for the reverse growth sequence. The sample structure is similar to that of Figure 2.12, and identical growth conditions were employed. In this case, the core structure consisted of 10 $Al_{0.3}Ga_{0.7}As$ layers, with thickness increasing from 1 to 120nm, separated by 60nm-thick GaAs layers. The evolution of the AlGaAs profile is analogous to the GaAs one: after a transient narrowing, the facets reach a steady-state extension that stays constant during further growth. We have marked, for both figures, the steady-state values of l_{100} and l_{311} in $Al_{0.3}Ga_{0.7}As$ and GaAs with short-dashed and long-dashed lines, respectively. These values are identical, meaning that the steady-state profile shapes are reproducible from sample to sample, and do not depend on the structure below the layer in question, provided the growth conditions are the same.

We can therefore conclude that both AlGaAs and GaAs growths on V-grooved substrates proceed in a *self-limiting* way. Starting from an arbitrary bottom profile, the width of the facets composing it evolve towards values that are typical of the material being grown; once this profile is reached, it keeps it shape unchanged during growth of the same material. The self-limiting profile width is much wider for GaAs than for AlGaAs, for the same growth conditions (both facets are about 4 times larger in GaAs than in $Al_{0.3}Ga_{0.7}As$ in the samples described here). The material dependence of the profiles will be studied in more detail in the next section. Note that the recovery lengths are smaller for AlGaAs/GaAs than for the reverse growth sequence, i.e., when the profile is narrowing down. By fitting the data of Figure 2.13 with exponential functions of the form

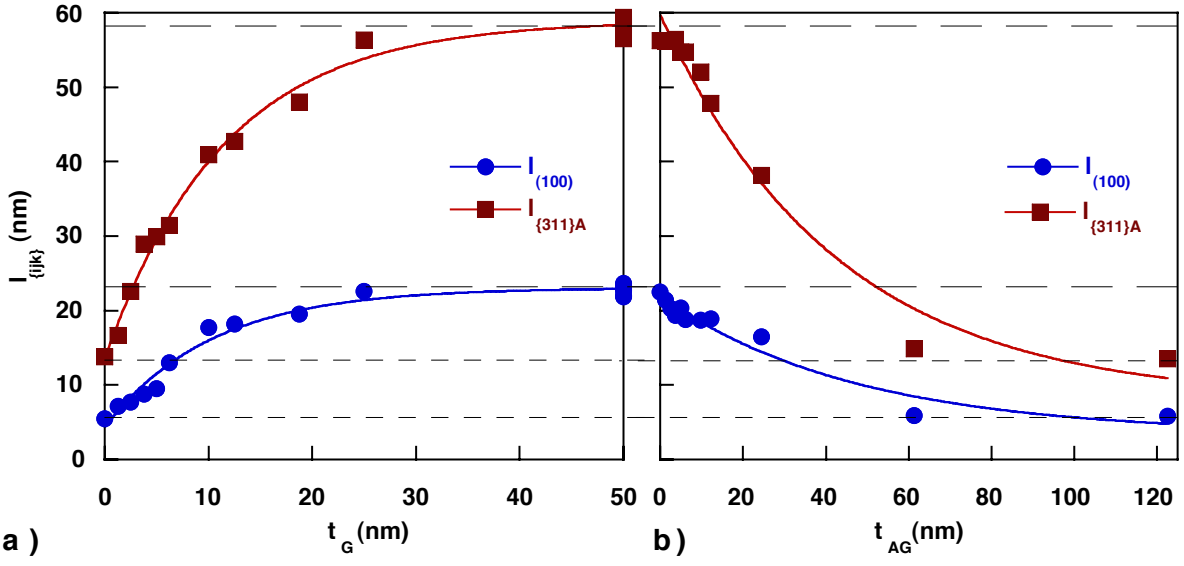

Figure 2.13: a) Lateral extension of the (100) (circles) and {311}A (squares) facets, as a function of t_G *during GaAs/*$Al_{0.3}Ga_{0.7}As$ *heteroepitaxy for the sample of Figure 2.11. b) The same for a sample in which the reverse sequence was grown, at the same growth conditions. Short-dashed and long-dashed lines mark the self-limiting (100) and {311}A facet extensions in* $Al_{0.3}Ga_{0.7}As$ *and GaAs, respectively. Solid lines are exponential fits of the data.*

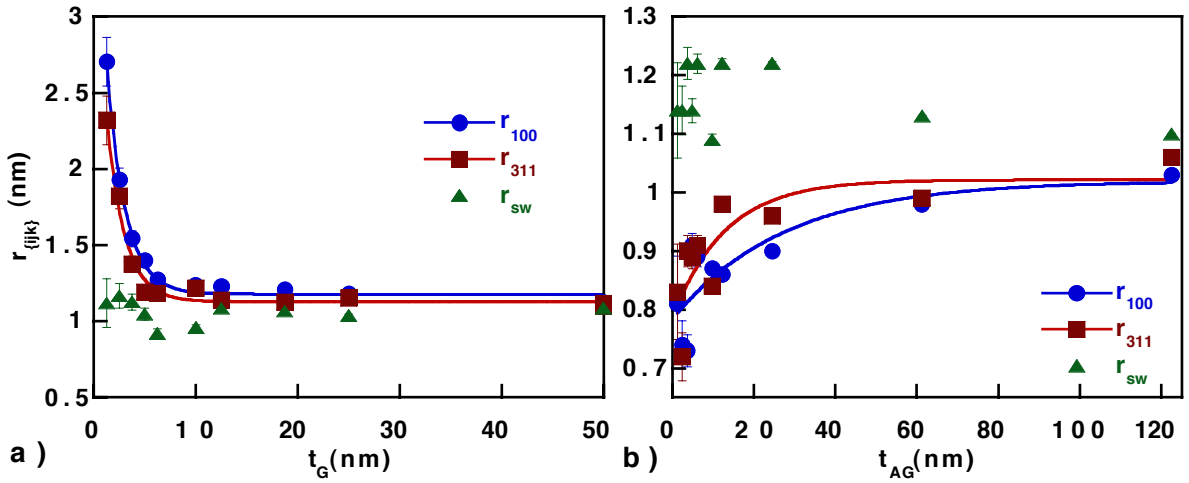

Figure 2.14: Evolution of the (100) (circles), {311}A (squares) and sidewall (triangles) growth rates, as a function of the GaAs (a) and AlGaAs (b) nominal thicknesses, for the samples of Figure 2.13. Growth rates are normalized to the nominal ones.

$$l_{\{ijk\}}(t_G) = l_{\{ijk\}}^{sl,G} + \left(l_{\{ijk\}}^{sl,AG} - l_{\{ijk\}}^{sl,G}\right)\exp\left(-t_G / \tau_{\{ijk\}}^{G}\right), \qquad (2.2)$$

$$l_{\{ijk\}}(t_{AG}) = l_{\{ijk\}}^{sl,AG} + \left(l_{\{ijk\}}^{sl,G} - l_{\{ijk\}}^{sl,AG}\right)\exp\left(-t_{AG} / \tau_{\{ijk\}}^{AG}\right),$$

(solid lines), we obtain characteristic recovery thicknesses τ_{100}^{G} = 10.3±1.2nm, τ_{311}^{G} = 11.4±0.7, for GaAs, and τ_{100}^{AG} = 51±15nm, τ_{311}^{AG} = 45±8nm for $Al_{0.3}Ga_{0.7}As$ (see Figure 2.13).

As discussed in Section 1.3.2, the expansion (contraction) of the facets at the concave bottom profile is related to an increase (decrease) of their growth rates, with respect to the rates of the neighboring ones. We expect, therefore, $r_{100}, r_{311} > r_{sw}$ during the transient growth of GaAs on AlGaAs discussed above, and $r_{100}, r_{311} < r_{sw}$ for the reverse transient growth sequence. In Figure 2.14 we plot these growth rates, normalized to the nominal ones, as a function of the nominal thicknesses, for the layers of Figure 2.13. Part a), corresponding to the GaAs/AlGaAs case, shows that in the first stages of GaAs growth $r_{100} > r_{311} \gg r_{sw}$. While initially r_{100} and r_{311} reach values up to 2.5 times the nominal growth rates, the sidewalls growth rate remains practically constant throughout the thickness range considered. This growth rate is equal to the one measured on thick layers and shown in Figure 2.10a (r_{sw} = 1.06±0.07). As growth further proceeds, the profile relaxes to the new self-limiting shape, and the bottom growth rates rapidly approach the values measured on the sidewalls. When the new self-limiting profile is achieved, all the growth rates become identical, and growth proceeds in a steady-state way.

Note that r_{100} and r_{311} are considerably higher than those measured on the same facets at the top of the mesas, at the same growth conditions (Figure 2.10a). This difference is more apparent when the profile is narrower, and tends to decrease as the profile broadens. Even for the broader profiles, however, these growth rates differ from the ones measured at the top of the mesas. For the AlGaAs/GaAs case the opposite is observed: while r_{sw} is again practically constant, r_{100} and r_{311} are initially lower than 1, and close to the values measured in thick layers. As growth proceeds, the profile narrows down to the AlGaAs self-limiting shape, and the bottom growth rates increase towards r_{sw}.

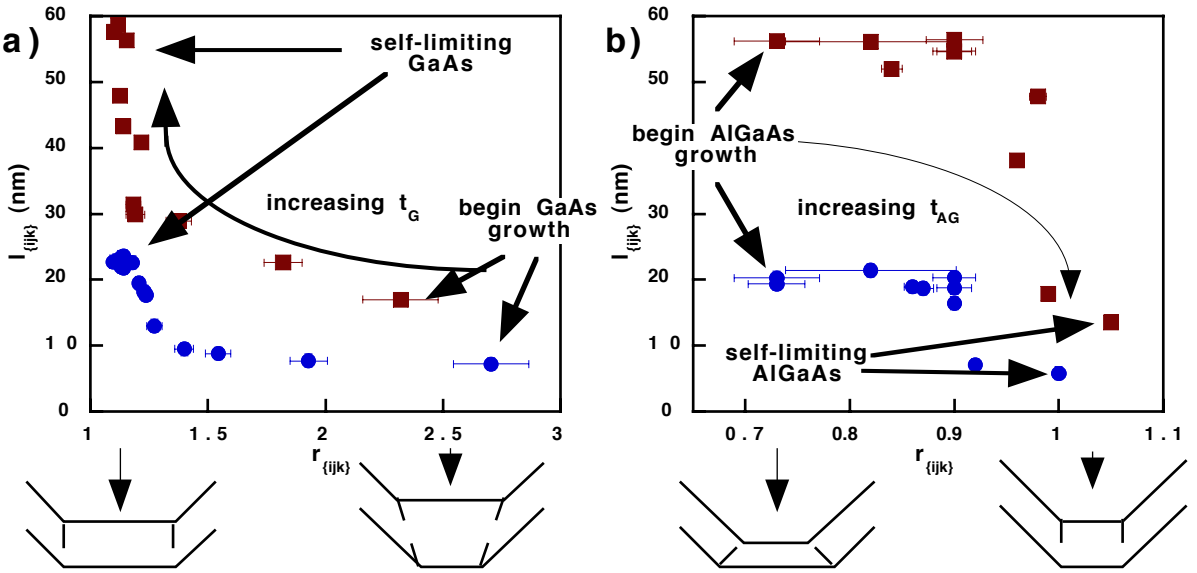

Figure 2.15: Lateral extension of the (100) (circles) and {311}A facets (squares), as a function of their normalized growth rates. Part a) and b) correspond to the data of Figure 2.13 a) and b), respectively. The schematics below the plots show the facets evolution at a concave corner (only one bottom facet is shown for simplicity), as a function of the relative growth rates.

The correlation between the length of the bottom facets and their relative growth rate is better visualized in Figure 2.15. The plot in part a) shows data from GaAs/$Al_{0.3}Ga_{0.7}As$ heteroepitaxy from the figures above. When growth is switched from AlGaAs to GaAs, this material is initially deposited on a profile that is much narrower than its self-limiting one. Therefore, r_{100} and r_{311} must *increase* to cause an expansion of these facets in a concave profile (schematic drawing at the bottom right). Then, as growth proceeds, the profile widens and the growth rates relax towards the sidewall values, as the new self-limiting profile is reached. This profile results in a vertical propagation of the corners between adjacent facets. This condition is realized when the growth rate (projected in the [100] direction) becomes the same for all the facets (see the schematic drawings at the left). The plot in part b) shows the corresponding data for $Al_{0.3}Ga_{0.7}As$/GaAs, again from the figures above. In this case, AlGaAs is deposited on an initial profile that is much wider than its self-limiting one; therefore, r_{100} and r_{311} must *decrease* to cause a contraction of these facets (schematic drawing at the bottom left). Also in this case, as the profile approaches its self-limiting shape, growth rates tend towards the sidewalls ones, and steady state growth is achieved, with vertical propagation of the corners between the facets (schematics at the right).

2.3.3 Dependence of self-limiting profiles on the growth conditions

In the previous section, we have shown that growth of GaAs or $Al_xGa_{1-x}As$ by OMCVD on a V-grooved substrate results in the formation of stable, self-limiting profiles at the bottom of the groove. We will see now that the resulting profiles can be reproduced from sample to sample, and can be controlled by adjusting the growth conditions.

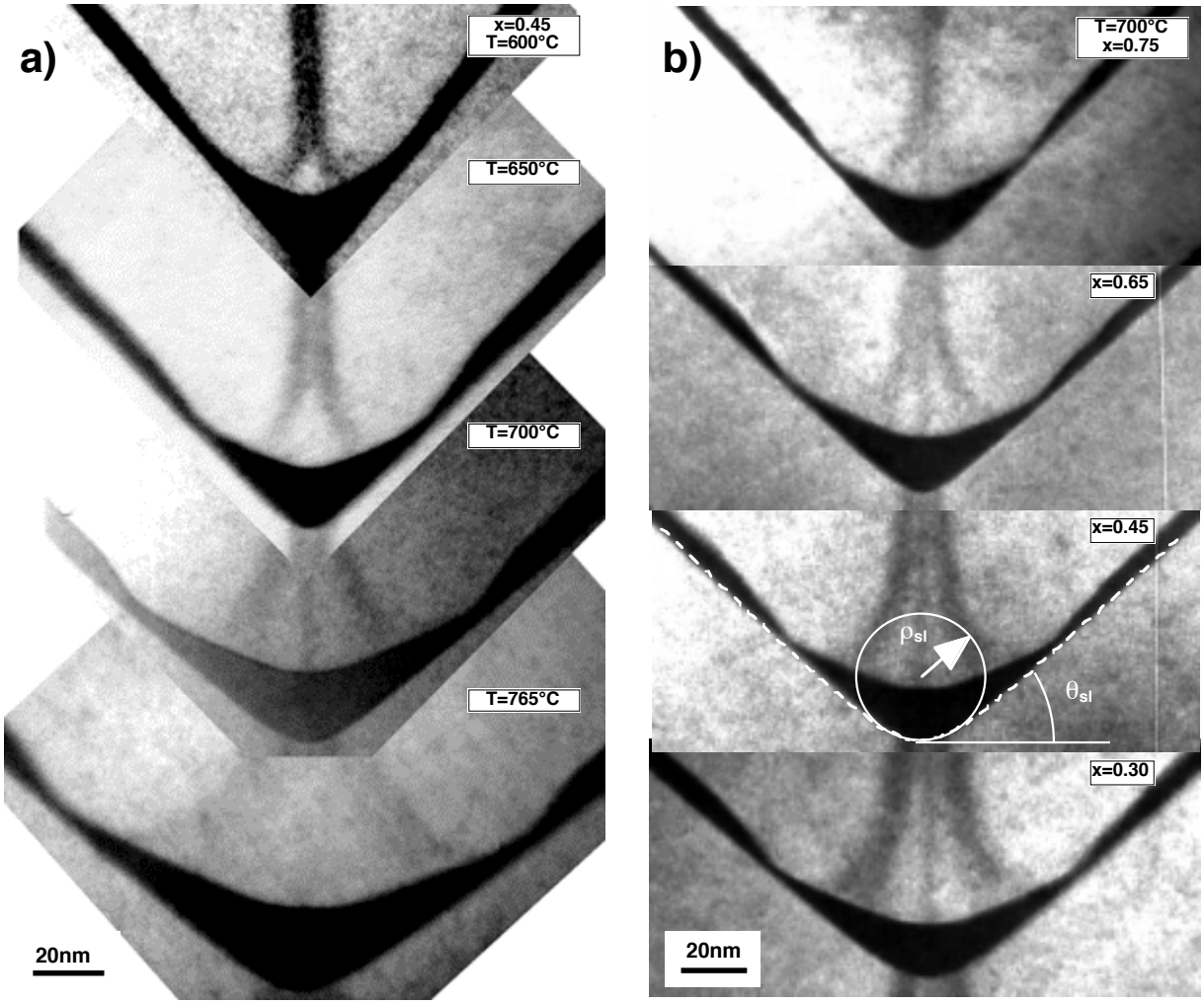

Figure 2.16: a) A series of four GaAs QWRs, with nominal thickness 8.7nm, embedded in $Al_{0.45}Ga_{0.55}As$ barriers, grown at different temperatures, ranging between 600°C and 765°C. b) A series of four GaAs QWRs, with nominal thickness 5nm, embedded in $Al_xGa_{1-x}As$ barriers, with x *ranging between 0.30 and 0.75, grown at 700°C. A hyperbolic fit of the self-limiting AlGaAs profile is indicated for* x = 0.45.

2.3.3.1 Influence of temperature and composition

Figure 2.16a shows a series of dark-field TEM cross sections of nominally 8.7-thick GaAs/$Al_{0.45}Ga_{0.55}As$ QWRs, grown at different temperatures (600°C to 765°C). In addition, Figure 2.16b shows a series of dark-field TEM cross sections of nominally 5nm-thick GaAs/$Al_xGa_{1-x}As$ QWRs, grown at 700°C, with x increasing between 0.30 and 0.75. The images show that the bottom profile and the sidewall angle become sharper as the growth temperature is decreased and as the Al mole fraction is increased.

The width of the profile is characterized by the length of the (100) and {311}A facets. However, as discussed in Section 2.3.1, when the profile becomes too narrow, these facets are not easily distinguishable. In this case, it is useful to approximate the profile with a hyperbola tangent to the bottom and sidewall facets. The growth front is therefore fully identified by the radius of curvature ρ at the bottom of the hyperbola (that is proportional to the (100)+{311}A

facet length) and by the asymptotic angle θ of the sidewalls (see Appendix A). Such a fit is shown for the self-limiting $Al_{0.45}Ga_{0.55}As$ profile in Figure 2.16b. We have studied systematically the dependence of the $Al_xGa_{1-x}As$ self-limiting radius of curvature ρ_{sl} on the growth temperature and the Al mole fraction. Figure 2.17 shows the measured values of ρ_{sl} for $Al_xGa_{1-x}As$ alloys, as a function of the nominal composition x, for different growth temperatures. The values were measured on a number of different samples, grown on 3μm- and 0.5μm-pitch gratings, and are reproducible for samples grown under the same conditions. Consistently with the trends shown in Figure 2.16, ρ_{sl} decreases with increasing Al mole fraction and increases with increasing growth temperature.

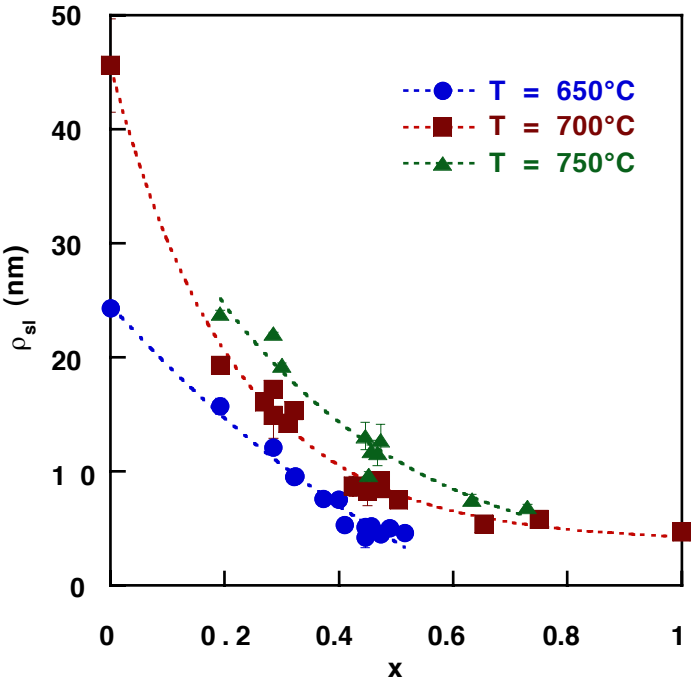

Figure 2.17: Measured self-limiting radius of curvature ρ_{sl} in $Al_xGa_{1-x}As$, as a function of the nominal composition x, *for* T = *650°C (circles), 700°C (squares) and 750°C (triangles). Dotted lines are guides to the eye.*

2.1.1.2 Influence of the growth rate

We have studied the influence of the growth rate on the GaAs self-limiting profile on a series of thick GaAs layers, grown with different growth rates R, ranging between 0.036 and 0.370nm/s (nominal values). Two series of layers were grown at 650°C and 700°C, respectively. The GaAs layers were separated by 10nm-thick AlGaAs markers. Figure 2.18a is a TEM cross section of the series grown at 650°C. The growth rates increase progressively from layer 1 to 4. It can be seen from the upper interface of the GaAs layers to the AlGaAs markers that the profile narrows down as R increases. Figure 2.18b shows ρ_{sl} as a function of R, for T = 650°C (circles) and T = 700°C (squares). In both cases, ρ_{sl} decreases by a factor of ~2.5 upon increasing the growth rate from 0.036 to 0.370nm/s.

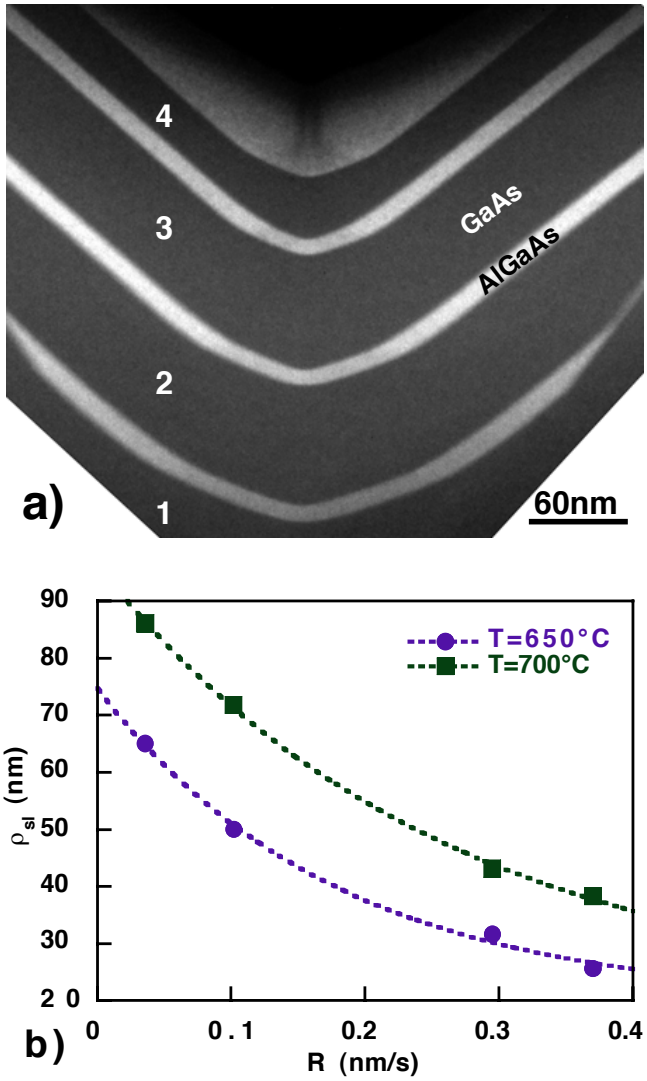

Figure 2.18 a) Dark-field TEM cross section of 4 GaAs layers, separated by AlGaAs markers, and grown at 650°C. The nominal growth rates were 0.036nm/s (layer 1), 0.102nm/sec (2), 0.295nm/sec (3), and 0.370nm/sec (4). b) Evolution of the self-limiting GaAs radius of curvature as a function of the nominal growth rate, for T = 650°C (circles) and T = 700°C (squares). Dashed lines are guides to the eye.

2.1.1.3 Influence of growth interruptions

We have studied the effects of growth interruptions on the bottom profile by growing a series of 100nm-thick AlGaAs layers, after which growth was stopped for increasing time intervals. This thickness ensures the achievement of a self-limiting profile in AlGaAs, just before the interruption. 5nm-thick GaAs marker layers were grown just after the growth interruptions, to quench and identify the relaxed AlGaAs profiles. Figure 2.19a shows the schematics of this layer sequence, and two examples of such studies, relative to $Al_{0.45}Ga_{0.55}As$ layers grown at 700°C, without (top) and with a 3600s (bottom) growth interruption before the marker layers. The widening of the profile as an effect of the growth interruption is evident from these cross sections. In Figure 2.19b, we plot the $Al_{0.45}Ga_{0.55}As$ radius of curvature ρ for growth temperatures of 700°C (circles) and 750°C (squares), as a function of the growth

interruption time *t*. For both temperatures, ρ increases by about a factor of three, when *t* increases from 0 to 1800s.

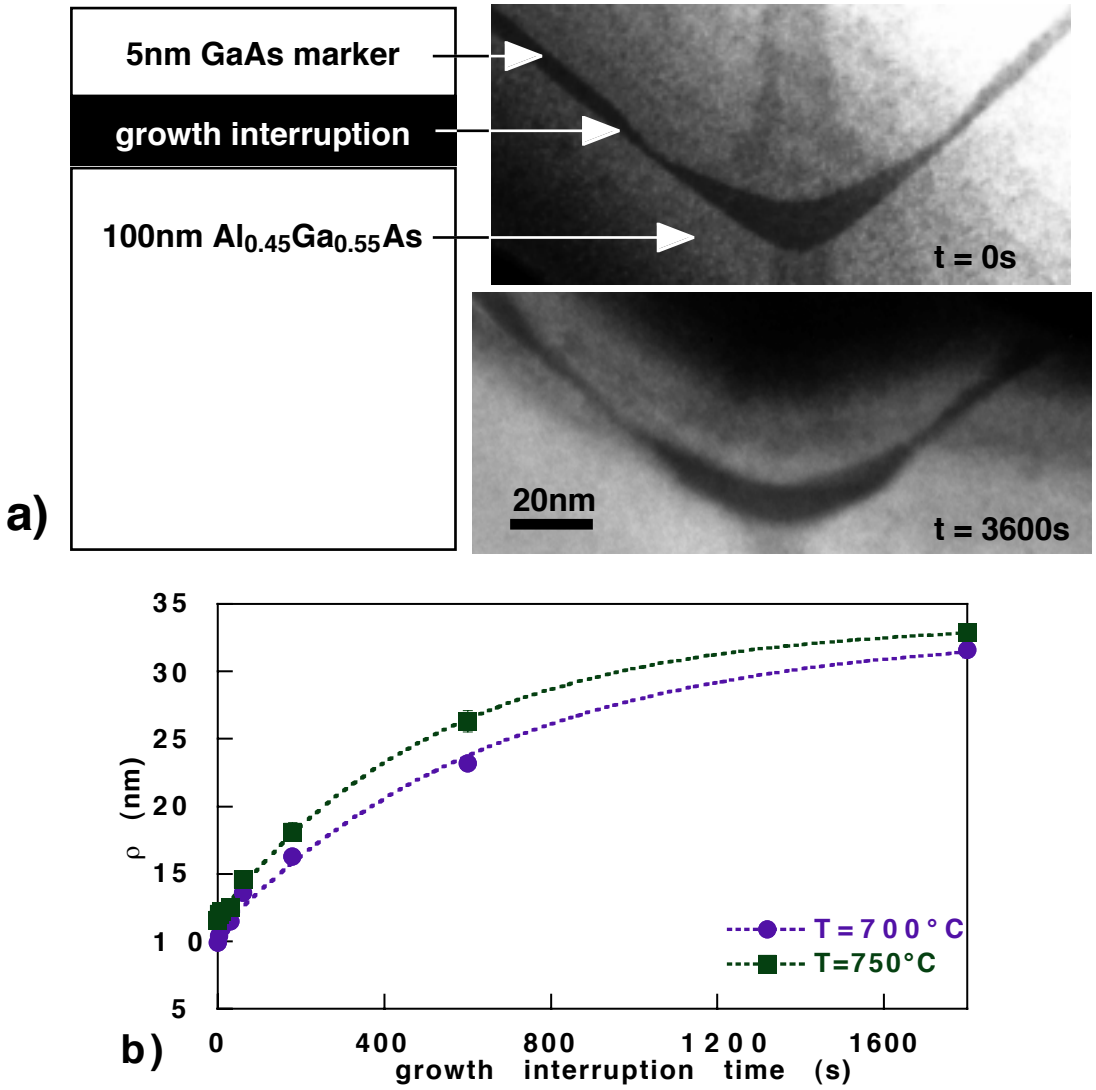

Figure 2.19 a): Left: schematics of the layer sequence used for growth interruption studies. Right: TEM cross sections of the profiles at the bottom of the groove for a growth interruption of 0s (top) and 3600s (bottom), after growth of a 100nm-thick $Al_{0.45}Ga_{0.55}As$ layer at 700°C. b) Dependence of the $Al_{0.45}Ga_{0.55}As$ radius of curvature on the growth interruption time for T = *700°C (circles) and* T = *750°C (squares). Dotted lines are guides to the eye.*

2.1.1.4 Influence of the reactor pressure

Figure 2.20 is a dark-field TEM cross section of a nominally 5nm-thick $GaAs/Al_{0.5}Ga_{0.5}As$ QWR grown at AP, at a temperature of 650°C, and otherwise similar conditions as for the sample grown at 20mbar. One can notice that the faceting at the upper boundary of the QWR is less pronounced than at LP; this roundness of the QWR interfaces is also reflected in the absence of a distinct branching in the AlGaAs VQW. In Table 2.1, we compare representative values of the self-limiting $Al_xGa_{1-x}As$ radius of curvature, at AP and LP, for selected growth temperatures and Al mole fractions.

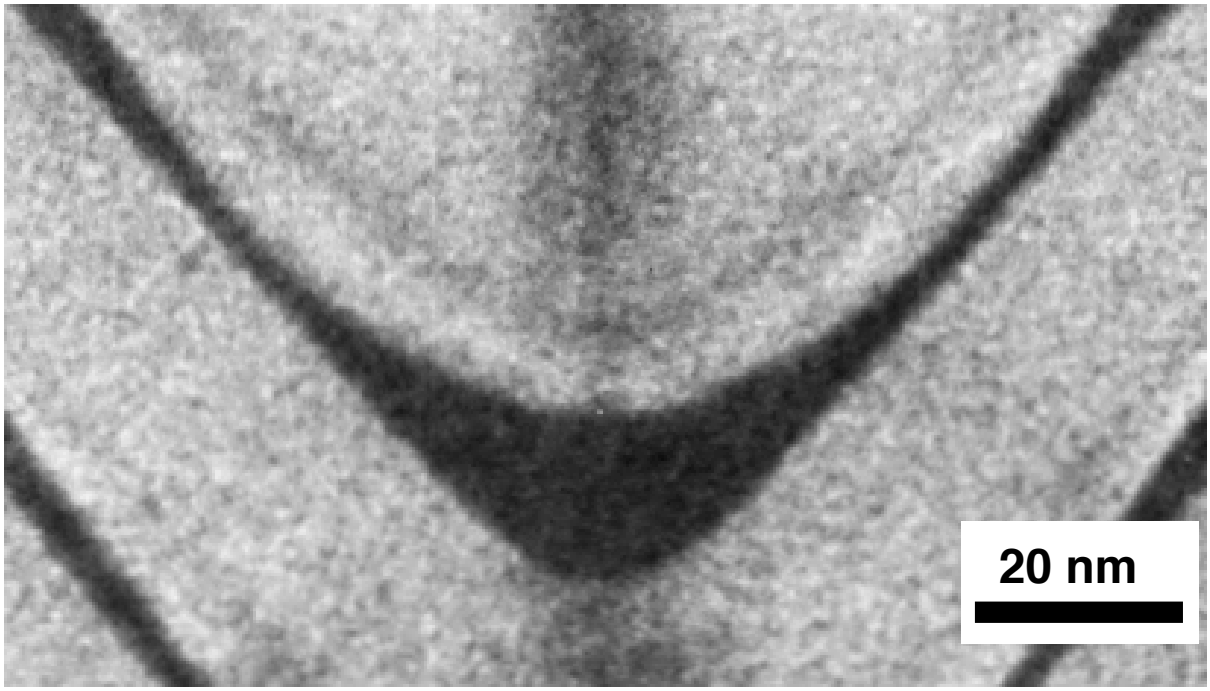

Figure 2.20: Dark-field TEM cross section of a nominally 5nm-thick GaAs/$Al_{0.5}Ga_{0.5}As$ QWR, grown at AP at 650°C.

T (°C)	x	ρ_{sl} (nm) - AP	ρ_{sl} (nm) - 20mbar
650	0.5	7.7±0.7	4.8±0.4
670	0.45	10.2±1.3	6.9±0.2*
680	0.3	17.2±1.0	12.6±0.9
750	0.7	16.4±0.8	6.9±0.2

*: T = 680°C.

Table 2.1: Comparison between the self-limiting radii of curvature of $Al_xGa_{1-x}As$ layers grown at AP (3rd column) and at LP (4th column), for different values of T *and* x.

The table shows that the self-limiting AlGaAs profiles grown at LP are systematically sharper than those grown at AP. A quantitative comparison of the two series of samples is not completely justified, since they are grown in two different machines. Therefore, other parameters, such as growth temperature, gas velocities and V/III ratios, though nominally similar, can have some slight uncontrolled variations. The systematic differences between the two series, however, range between 30 and 80%. This remarkable difference can be ascribed therefore mainly to pressure variations, since this is the only parameter that is systematically different in the two cases. It seems therefore that the increased rate of mass transport, as the reactor pressure is reduced, increases the degree of faceting and the sharpness of the facets at the bottom of the groove.

2.1.1.5 Discussion

In this section, we have shown how different growth parameters affect the shape of the profiles at the bottom of the V grooves. It is possible to draw some general conclusion from the phenomenology observed above. The profiles become wider at high temperatures, low Al compositions, low growth rates and when growth interruptions are introduced. In other words, in these limits growth is more favorable at the bottom of the groove, with respect to the sidewalls, since facets expansion in a concave profile is related to growth rate enhancement. All these trends suggest that the profile width be governed by surface diffusion of adatoms towards the bottom: as surface diffusion becomes more efficient, more atoms can be incorporated in the bottom region. In particular:

- Surface diffusion increases as the growth temperature becomes higher ↔ ρ_{sl} increases with T.
- The surface mobility of Ga atoms is higher than that of Al ones [85-87] ↔ ρ_{sl} increases with decreasing x.
- At lower growth rates, atoms have more time to diffuse on the surface, before being incorporated into the crystal by the arrival of new atoms ↔ ρ_{sl} increases with decreasing R.
- During growth interruptions, atoms are free to diffuse on the surface, since no growth flux is present ↔ ρ_{sl} increases with increasing growth interruption time.

The effects of the reactor pressure will be better explained in Chapter 5. Note, finally, that the self-ordering process described in Section 2.3.2 implies that the surface diffusion fluxes identified above are able to "self-adjust", depending on the width of the profile. We will develop in Chapter 5 a theoretical model that can explain the origin these fluxes, and can account for all the phenomenological observations described above.

2.1.4 Self-ordering of quantum wires

2.1.4.1 GaAs/$Al_xGa_{1-x}As$ quantum wires

From the discussion and the images above, it appears clear how self-ordered QWRs form. If a layer of a lower-bandgap, higher diffusivity material (GaAs) is grown on a higher-bandgap, lower diffusivity one ($Al_xGa_{1-x}As$), the facets at the bottom of the groove will expand and the layer thickens, thus creating a crescent-shape wire. Deposition of the upper barrier will relax the profile back to the self-limiting $Al_xGa_{1-x}As$ size, recovering from the surface perturbation introduced by GaAs growth. If the barrier is thick enough, the recovery is complete, and the $Al_xGa_{1-x}As$ profile can serve as the seed of a second QWR, identical in size and shape to the first. Thanks to the stability of the profile, this procedure can be repeated indefinitely, until the groove planarizes through the expansion of the top facets. This planarization distance depends on the size and sharpness of the groove and on the growth conditions, and is typically of the order of the groove width. An example of vertical stacking of identical, self-ordered GaAs/$Al_xGa_{1-x}As$ QWRs can be seen in Figure 2.11.

T (°C)	ρ_{sl}^{AG} (nm)	θ_{sl}^{AG} (nm)	ρ^G (nm)	r_{100}	α
600	3.0±0.7	50.5±1.5	12±1	1.62±0.09	1.0±0.1
650	5.3±0.5	44.5±0.5	17±3	1.72±0.17	1.3±0.3
700	8.7±0.9	40.5±1.0	27±2	1.89±0.05	2.1±0.2
765	11.9±1.1	38.5±1.0	37±4	2.13±0.05	2.8±0.4

Table 2.2: Temperature dependence of the self-limiting $Al_{0.45}Ga_{0.55}As$ radius of curvature ρ_{sl}^{AG} and sidewalls angle θ_{sl}^{AG}, of the radius of curvature at the upper QWR interface ρ^G, of the relative QWR growth rate, with respect to the sidewalls r_{100}, and of the radius of curvature increase rate α, for the QWRs shown in Figure 2.16a.

Since the quantum confinement properties of the QWRs depend drastically on their shape, it is important to optimize the growth conditions to maximize the QWR confinement. The dependence of ρ and θ on the growth conditions and the Al mole fraction, determined so far, allow us to make predictions on the wire characteristics for a given set of growth parameters. In particular, it should allow us to optimize them to obtain wires of the desired size and shape. We have seen in Section 1.1.4 that, to enhance the 1D confinement properties, it is preferable to have wires as compact as possible. This can be done by creating wires of nearly triangular shape, with a lower, self-limiting boundary as sharp as possible, and a flat upper boundary. At the lower interface, in terms of the QWR geometrical parameters, this means minimizing ρ_{sl} and maximizing θ_{sl} of the AlGaAs barriers. At the upper interface, for given ρ_{sl} and θ_{sl}, one should maximize the relative growth rate at the bottom r_{100} (to enhance the wire thickness, with respect to the planar QW) and hence the radius of curvature ρ^G. For typical QWR thicknesses, $t^G \ll \tau^G$, therefore the first relation of (2.2), written as a function of ρ^G, can be linearly approximated as $\rho^G(t^G) = \rho_{sl}^{AG} + \alpha \cdot t^G$. The expansion rate of ρ can therefore be characterized by the parameter α, defined in Section 1.1.4.

In Table 2.2, we summarize the geometrical parameters of the QWRs shown in Figure 2.16a, as a function of the growth temperature. The 2nd and 3rd columns show the self-limiting radius of curvature and sidewall angles of the $Al_{0.45}Ga_{0.55}As$ barriers (ρ_{sl}^{AG} and θ_{sl}^{AG}, respectively); the 4th, 5th and 6th columns shows ρ^G, r_{100} and α, respectively. It can be seen that ρ_{sl}^{AG} becomes smaller and θ_{sl}^{AG} becomes larger as T decreases; therefore, decreasing the growth temperature produces a sharper profile at the bottom of the wire. On the other hand, both r_{100} and α increase with T; the temperature should therefore be increased to produce a thicker wire, with a flatter upper profile. A compromise between the two requirements must therefore be found, for example by choosing an intermediate temperature and increasing the Al mole fraction in the barriers, to keep the bottom profile sharp enough. However, an Al content higher than $x = 0.5$-0.6 can result in the formation of dense structural defects, due to the decreased surface diffusion of atoms/reactants to the bottom of the groove. To avoid these problems, very low AlGaAs growth rates should be used, that in turn tend to widen again the profile (see 2.3.3.2).

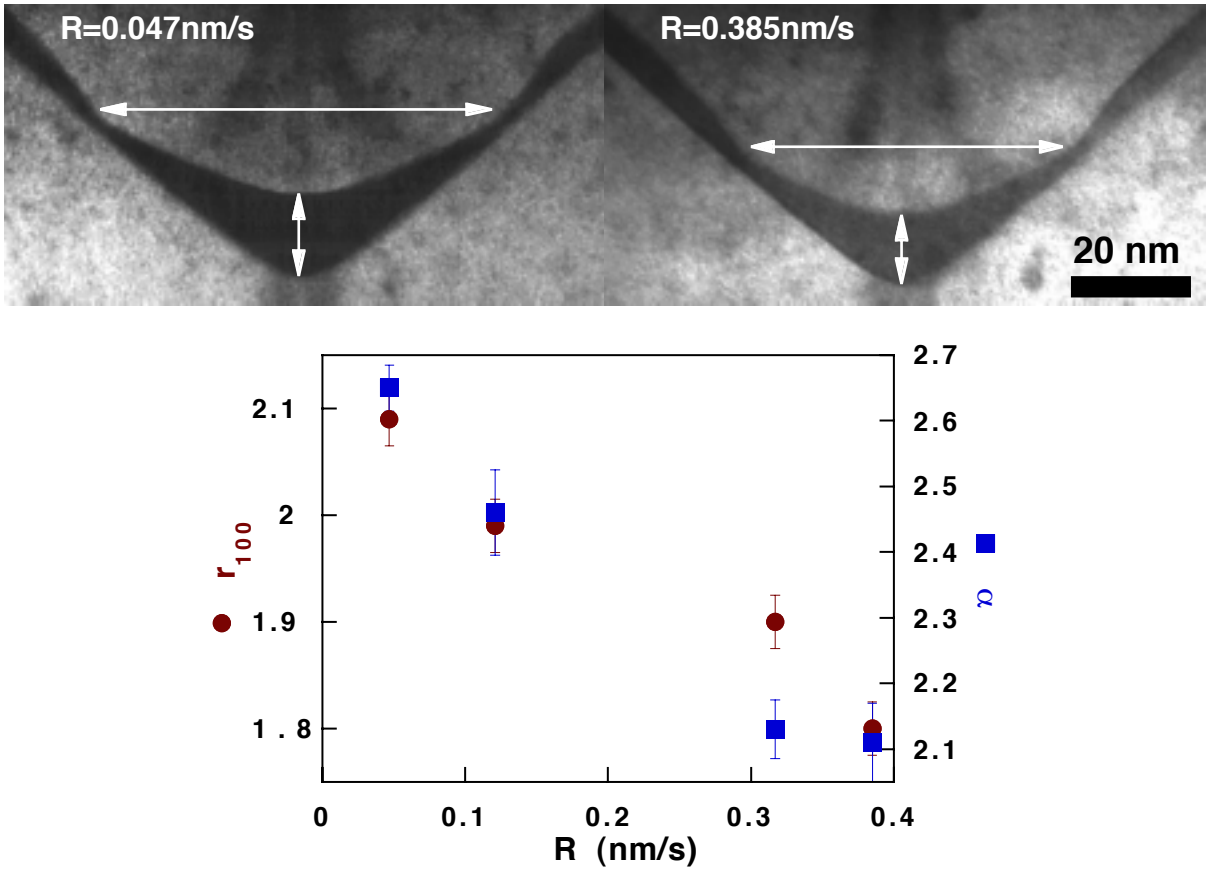

Figure 2.21: Top: dark field TEM cross sections of two GaAs/$Al_{0.45}Ga_{0.55}As$ QWRs grown at 700°C, at a growth rate R of 0.047nm/s (left) and 0.385nm/s (right). The nominal thickness is 7.5nm for both wires. Vertical arrows indicate the maximum QWR thickness, while horizontal arrows indicate approximately the (100) + {311}A facet width. Bottom: Dependence of r_{100} (circles) and α (squares) on the nominal QWR growth rate, for GaAs/$Al_{0.45}Ga_{0.55}As$ wires grown at 700°C.

To widen the upper QWR interface, by keeping the lower one fixed, it is possible to increase the GaAs diffusion by decreasing the GaAs growth rate, or by inserting a growth interruption after the QWR. By adopting the second solution, however, growth interruptions should be at least of the order of 3' to have a ρ increase of the order of 50% (see Figure 2.19). Such long times could bring to the accumulation of impurities at the interface, and therefore should be avoided in order to preserve the intrinsic QWR luminescence efficiency.

We have studied the effect of the GaAs growth rate on the QWR profile on a set of three QWRs with nominal thicknesses of 2.5nm, 5nm, and 7.5nm, respectively. The wires were grown at 700°C on self-limiting $Al_{0.45}Ga_{0.55}As$; we have grown four sets of QWRs, with nominal GaAs growth rates R ranging between 0.047 and 0.385nm/s. The self-limiting $Al_{0.45}Ga_{0.55}As$ radius of curvature was 8.3±0.5nm. The top part of Figure 2.21 shows TEM cross sections of the nominally 7.5nm-thick QWR profiles for $R = 0.047$nm/s (left) and $R = 0.385$nm/s (right). Vertical arrows indicate the QWR thicknesses at the center of the groove, while horizontal arrows indicate approximately the (100) + {311}A facet widths. The images show clearly that, by decreasing the growth rate, the QWRs thicken and expand, for a

given nominal GaAs thickness. At the bottom of Figure 2.21 we show how r_{100} (circles) and α (squares) depend on R. Values of r_{100} are shown for t^G = 7.5nm, to better compare these results with those of Table 2.2, which correspond to t^G = 8.7nm. Values with the same nominal growth rate (0.317nm/s) agree in both series of samples. By decreasing the growth rate, both r_{100} and α increase, thanks to the more efficient surface diffusion. For R = 0.047nm/s they reach the values 2.09±0.03 and 2.65±0.04, approaching the values measured at 765°C for higher growth rates. Decreasing the GaAs growth rate should therefore modify the QWR shape in order to improve quantum confinement in the wire.

2.1.1.2 $In_xGa_{1-x}As$/GaAs quantum wires

Since GaAs growth on V grooves exhibits the same self-limiting properties as for AlGaAs, GaAs can also be used as a barrier material for growth of InGaAs/GaAs QWRs. Such structures are important for device applications involving regrowth. Due to the much lower oxidation rate, a GaAs (rather than AlGaAs) barrier layer would facilitate the regrowth on the patterned substrate. However, due to the longer diffusion length of Ga, with respect to Al, the GaAs profile is much wider than that of AlGaAs, for a given growth temperature (see Figure 2.17). To form profiles with lateral dimensions in the sub-10nm range, we have lowered the growth temperature to 550°C, obtaining GaAs profiles with a curvature similar to those of $Al_{0.5}Ga_{0.5}As$ surfaces grown at 650°C. In terms of facet length, we measured in GaAs l_{100}=4.2±0.4nm and l_{311}=8.2±0.8nm at 550°C. These values are quite comparable to those of the narrowest AlGaAs profile we have obtained at 650°C (l_{100}=3.7±0.8nm and l_{311}=7.3±1.3nm on average for different samples with x=0.45-0.50).

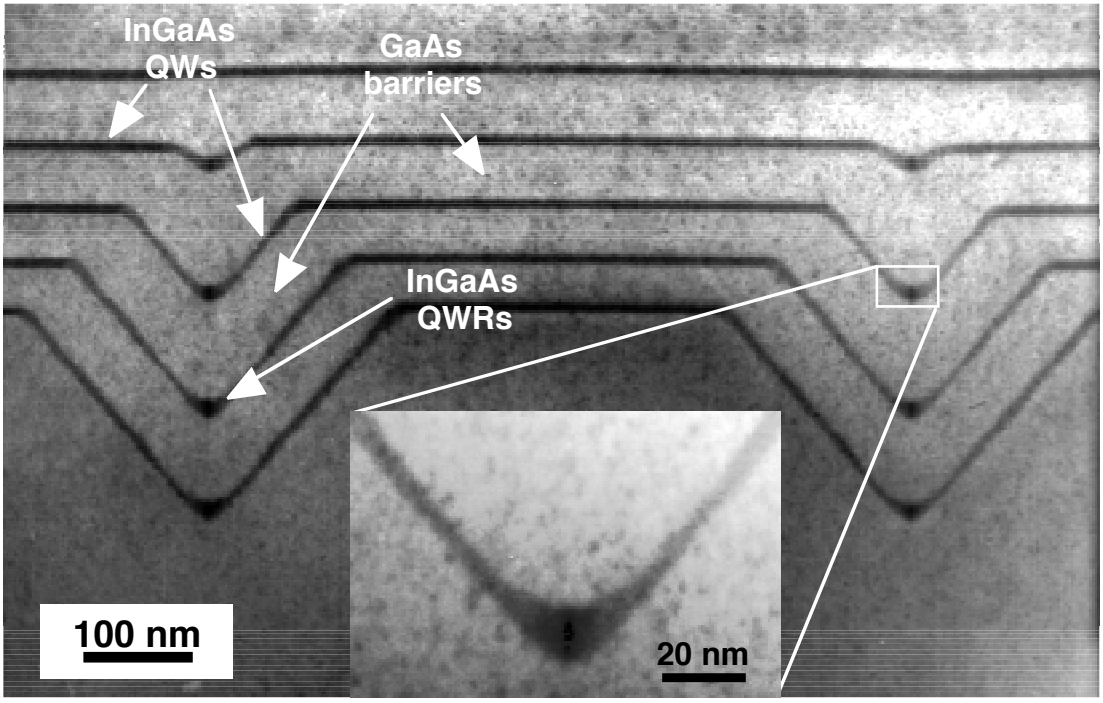

Figure 2.22: Bright field cross sectional TEM of a vertical array of InGaAs QWRs grown on self-limiting GaAs on a 0.5μm-pitch grating. The inset shows a magnified view of one of the wires.

Figure 2.22 is a cross sectional TEM image of a vertically-stacked, multiple $In_{0.15}Ga_{0.85}As$ QWR array grown on GaAs barriers at 550°C, on a 0.5μm pitch grating. The nominal InGaAs and GaAs thicknesses were 6 and 45 nm, respectively. Planarization of the grating is reached between the fourth and the fifth InGaAs layers. The inset shows a magnified view of an InGaAs layer at the bottom of the groove. The higher growth rate of the InGaAs at the V-corner gives rise to the formation of a QWR, via a thickening and an expansion of the facets at the bottom of the groove. At their center, the QWRs are about twice as thick as the corresponding planar (100) quantum wells. Indium segregation at the center of the InGaAs wire gives rise to a narrow In-rich region, recognizable from the TEM contrast in the inset. This region is about 5nm wide and extends vertically across the entire crescent. This phenomenon is analogous to the formation of Ga-rich VQWs in AlGaAs; in both cases the species with a higher diffusion length (Ga in AlGaAs, In in InGaAs) are able to segregate preferentially at the bottom of the groove. Since lateral quantum confinement effects have been measured in such AlGaAs VQWs [88], also the In-rich InGaAs region could provide additional lateral carrier confinement at the center of the wire, enhancing the confinement due to the layer tapering at the InGaAs crescent.

Since the sharp curvature at the bottom of the GaAs regrown grooves recovers to its self-limiting value, following the growth of the InGaAs layer and the upper GaAs barrier, stacking of several InGaAs wires with identical size and shape is possible. In the sample of Figure 2.22, the first 3 InGaAs wires are uniform within 5% in thickness and width. Wires grown closer to the planarization level show variations in size due to the disappearance of the near-{111}A sidewalls near that point.

2.1.5 Self-ordering of quantum wire superlattices

2.1.5.1 Fabrication of quantum wire superlattices

The self-ordering properties mentioned above make possible the formation of uniform vertical arrays of GaAs/AlGaAs QWRs, provided the thickness of the AlGaAs barriers is larger than the one necessary to recover the self-limiting AlGaAs profile (~20-30nm). We have extended the self-ordering properties of OMCVD on nonplanar substrates, by investigating the possibility of growing GaAs/AlGaAs QWR superlattices (QWR-SLs). These nanostructures cannot be formed with self-limiting AlGaAs barrier profiles, since coupling effects in SLs usually appear at barrier thicknesses that are much lower (a few nm) than the critical ones required for full recovery of the self-limiting profile[5]. We have however shown that QWR SLs growth is characterized by a peculiar self-limiting state, even in the case of sub-critical barrier thickness.

[5] In principle, for a GaAs thickness that approaches zero, a very thin AlGaAs barrier will be sufficient for a full recovery.

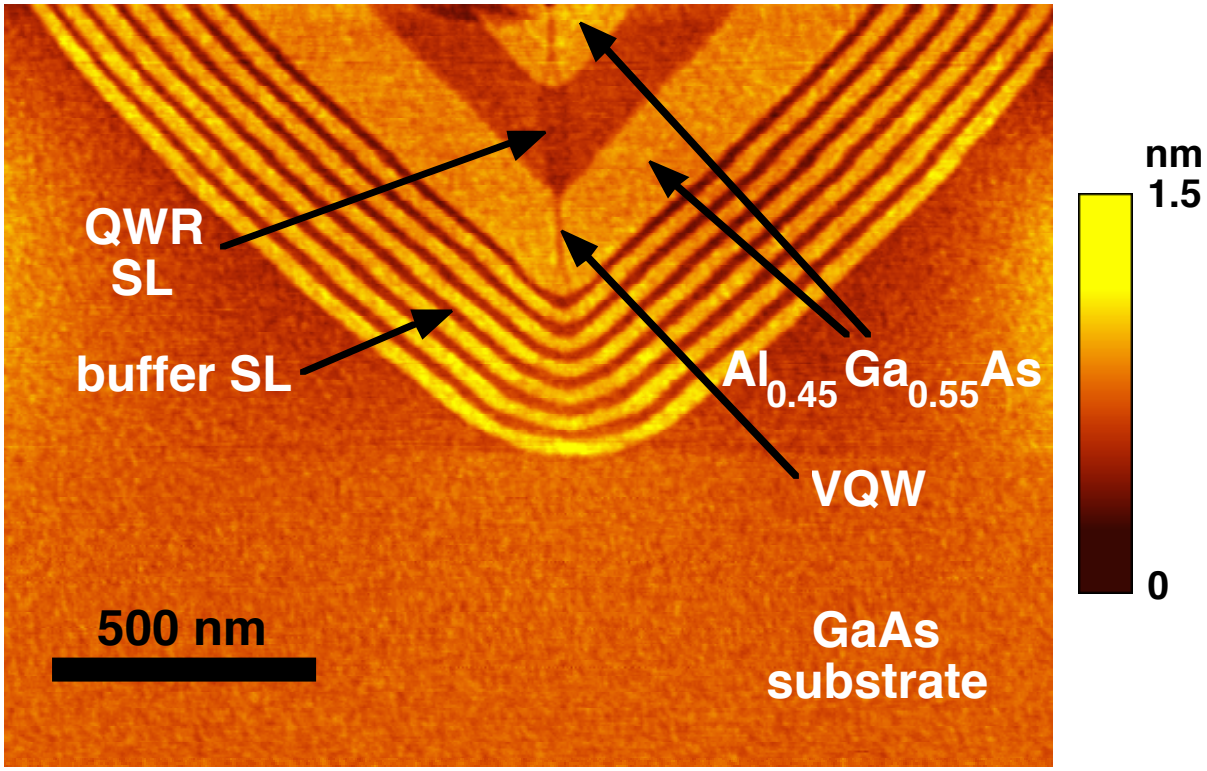

Figure 2.23: AFM cross section of a GaAs/ $Al_{0.45}Ga_{0.55}As$ (1.8nm/2.2nm) QWR SL structure grown in a V groove at 650°C.

We have grown a series of several samples, at $T = 650$°C. All structures consisted of a ~350nm thick large period (20nm/25nm) GaAs/$Al_{0.45}Ga_{0.55}As$ buffer SL, a 150nm thick $Al_{0.45}Ga_{0.55}As$ barrier, a 140nm thick GaAs/$Al_{0.45}Ga_{0.55}As$ SL, and a 100nm thick $Al_{0.45}Ga_{0.55}As$ upper barrier. The nominal thicknesses of the SL layers were $t^G = 1.8$nm for GaAs and $t^{AG} = 60$, 11.6, 7.8, 3.9 and 2.2 nm for AlGaAs for the different samples. The number of SL periods was adjusted from sample to sample (10 to 30 periods), to keep the total SL thickness constant. Figure 2.23 shows an example of such structures.

Figure 2.24 shows dark field transmission electron microscopy (TEM) cross sections of four of the samples, with $t^{AG} = 60$, 11.6, 3.9 and 2.2nm. In all cases, the first GaAs QWR was grown on a self limiting $Al_{0.45}Ga_{0.55}As$V-groove profile with ρ_{sl}^{AG}=5.9±0.4nm. This value increases to 10.5±0.9nm after the growth of the first GaAs QWR. When t^{AG} is well above the minimal thickness (~20-30nm in this case) needed for a full recovery of the AlGaAs self-limiting profile, as for the sample of Figure 2.24a, all the vertically stacked QWRs are identical to the bottom one (within ~5% size fluctuations due to pattern and growth rate nonuniformities). In the QWR SLs of Figure 2.24(b-d), on the other hand, t^{AG} is smaller than the recovery thickness, and therefore ρ just below the second GaAs crescent is larger than ρ_{sl}^{AG}. However, after a transient expansion in the first 20nm of the SL structure, it is seen that the groove profile reaches a stable shape, with the groove width increasing as t^{AG} is reduced.

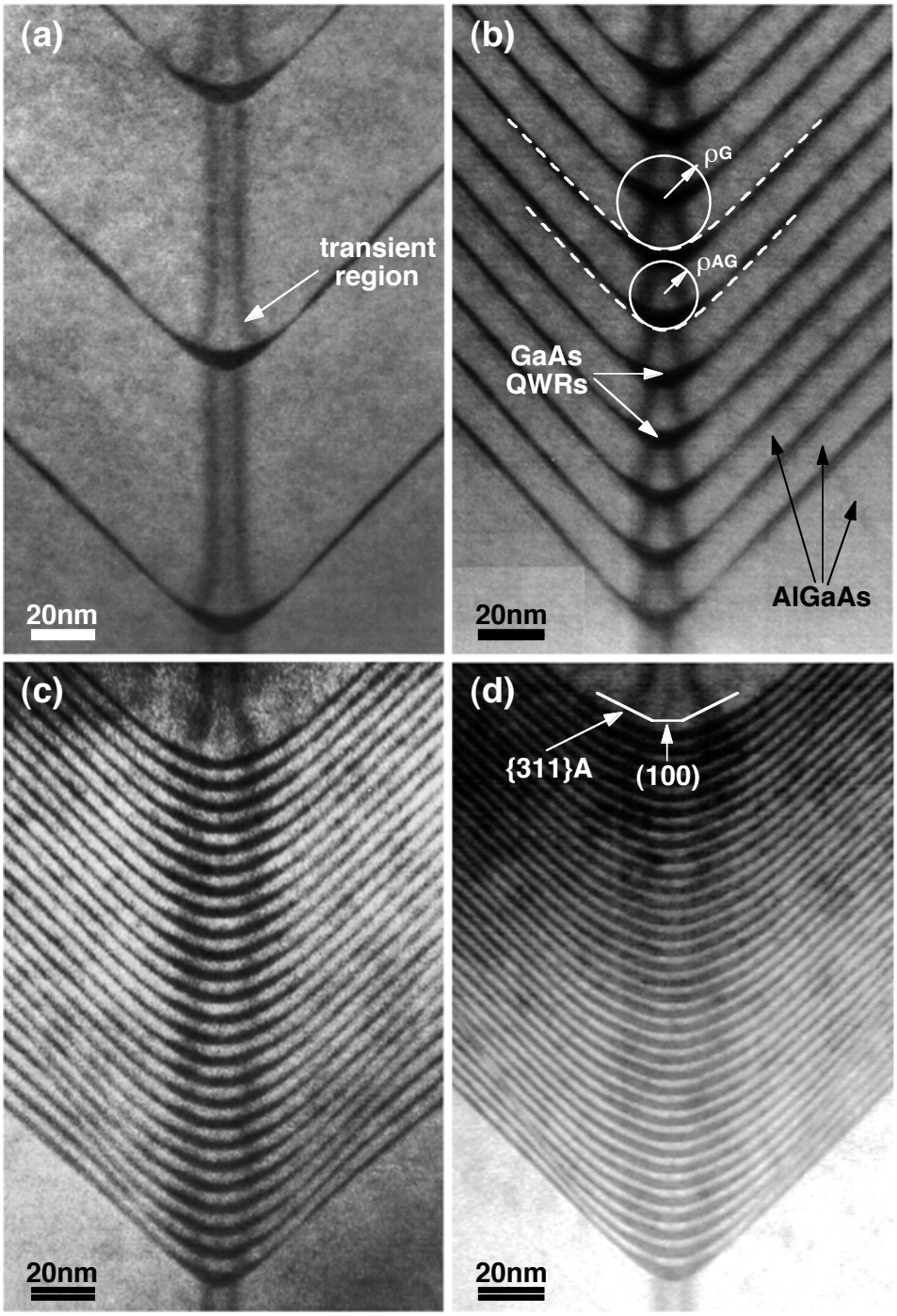

Figure 2.24: TEM cross sections of: (a), part of a multiple GaAs/$Al_{0.45}Ga_{0.55}As$ QWR structure (1.8nm/60nm); (b-d), 140nm-thick GaAs/$Al_{0.45}Ga_{0.55}As$ QWR SLs with t_g*=1.8nm and* t_a*=11.6, 3.9, and 2.2nm, respectively.* T_s*=650°C for all samples.*

The evolution of the surface profile during the SL growth is summarized quantitatively in Figure 2.25(a), which shows the measured values of ρ at the lower (ρ^{AG}, circles) and the upper (ρ^{G}, squares) interfaces of each GaAs QWR for the sample of Figure 2.24(c), as a function of the nominal growth thickness and QWR number. After the initial widening of the groove, due to the deposition of the first QWR, the profile narrows down again upon deposition of AlGaAs. However, deposition of a second wire after only 3.9nm of AlGaAs widens further the profile.

This overall increase of ρ during a SL period saturates after about four periods, resulting in a new self-limiting profile. The mechanism underlying its formation consists of a widening during the wire deposition (ρ^{G}), balanced by an (incomplete) recovery of the AlGaAs profile during the subsequent deposition of the barrier layer (ρ^{AG}). This sequence can be repeated indefinitely, yielding a stable average profile. The self-limiting average radius $\bar{\rho}^{SL} = (\bar{\rho}^{AG} + \bar{\rho}^{G}) / 2$ is constant within ±2% ($\bar{\rho}^{SL}$ =15.6±0.3nm, solid line), as can be seen in the plot. The remaining fluctuations in $\bar{\rho}^{SL}$ are probably due to small variations in the nominal growth rate, and lithography-related nonuniformities at the bottom of the groove.

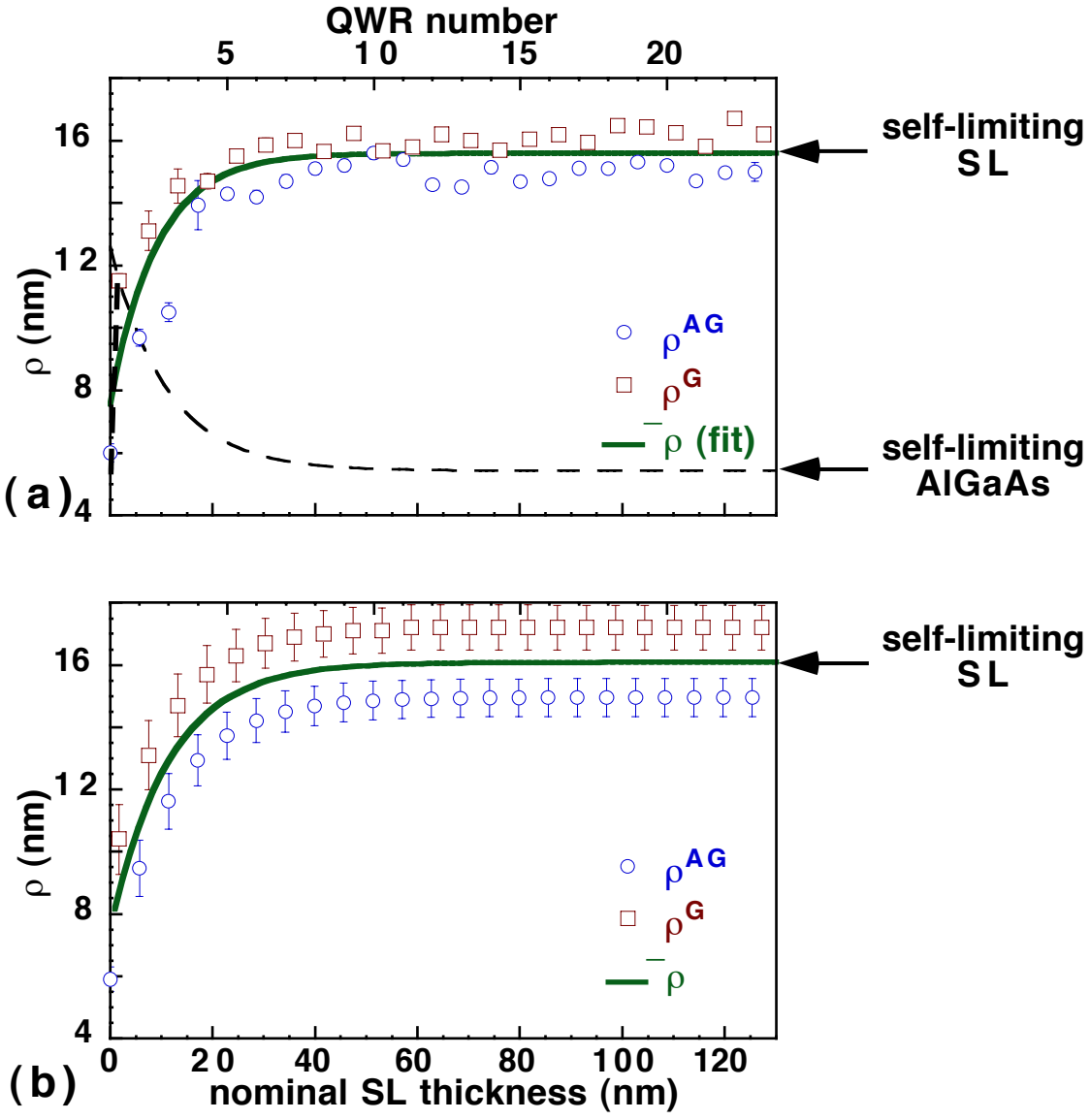

Figure 2.25: (a) Measured evolution of the radius of curvature at the GaAs/AlGaAs and AlGaAs/GaAs interfaces for the structure in Figure 2.24(c). The solid line is a fit of the average radius for each SL period, the dashed line corresponds to a full recovery of ρ that would be obtained with a growth of a thick AlGaAs layer after the first GaAs layer. (b) Simulated evolution of the radius of curvature for the QWR-SL of part a).

2.1.1.2 *Model of self-limiting QWR superlattice growth*

The formation of the stable QWR-SL phase can be understood in terms of the self limiting growth features of "thick" GaAs and AlGaAs layers at the bottom of the V-groove. Starting from an initial radius of curvature ρ_i at the bottom of the groove, ρ is found to recover exponentially to its self-limiting value ρ^{sl}. According to (2.2), we can write

$$\rho(t) = \rho^{sl} + \left(\rho_i - \rho^{sl}\right)\exp(-t/\tau), \tag{2.3}$$

where t is the nominal grown thickness (proportional to the growth time) and τ is a characteristic recovery thickness. Similar expressions hold for GaAs and AlGaAs growth, with parameters τ and ρ^{sl} depending on the Al mole fraction, growth temperature, and other growth parameters, as mentioned in the previous sections. The evolution for the case of GaAs (AlGaAs) growth starting from a self limiting AlGaAs (GaAs) profile is shown by the gray curves in Figure 2.26. To obtain the evolution of ρ for a GaAs/AlGaAs QWR-SL structure, we apply (2.3) repeatedly, obtaining the radius of curvature at the upper GaAs and AlGaAs surfaces of the nth SL period, respectively, as

$$\begin{aligned}
\rho_n^G &= \rho_{sl}^{AG} + \left(\rho_{sl}^G - \rho_{sl}^{AG}\right)\exp\left(t^{AG}/2\tau^{AG}\right)\left(1-\exp\left(-n\left(t^G/\tau^G + t_a/\tau_a\right)\right)\right)\sinh\left(t^G/2\tau^G\right)/\sinh\left(t^G/2\tau^G + t^{AG}/2\tau^{AG}\right) \\
\rho_n^{AG} &= \rho_{sl}^{AG} + \left(\rho_{sl}^G - \rho_{sl}^{AG}\right)\exp\left(-t^{AG}/2\tau^{AG}\right)\left(1-\exp\left(-n\left(t^G/\tau^G + t_a/\tau_a\right)\right)\right)\sinh\left(t^G/2\tau^G\right)/\sinh\left(t^G/2\tau^G + t^{AG}/2\tau^{AG}\right).
\end{aligned} \tag{2.4}$$

The self-limiting superlattice surface curvatures are obtained by setting $n \to \infty$ in (2.4), which yields

$$\begin{aligned}
\rho^{SL,G} &= \rho_{sl}^G + \left(\rho_{sl}^{AG} - \rho_{sl}^G\right)\exp\left(-t^G/2\tau^G\right)\sinh\left(t^{AG}/2\tau^{AG}\right)/\sinh\left(t^G/2\tau^G + t^{AG}/2\tau^{AG}\right) \\
\rho^{SL,AG} &= \rho_{sl}^{AG} + \left(\rho_{sl}^G - \rho_{sl}^{AG}\right)\exp\left(-t^{AG}/2\tau^{AG}\right)\sinh\left(t^G/2\tau^G\right)/\sinh\left(t^G/2\tau^G + t^{AG}/2\tau^{AG}\right).
\end{aligned}$$

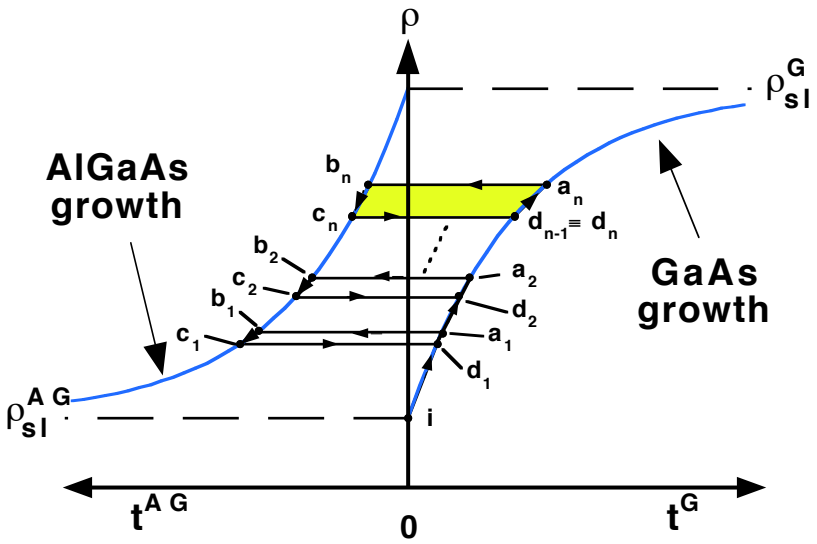

Figure 2.26: Schematic representation of the curvature evolution during SL growth in the first, second and nth period. Changes of curvature during GaAs and AlGaAs growth take place by following the curvature recovery curves of the material (gray lines), towards self-limiting GaAs and AlGaAs values (long-dashed lines).

The average self-limiting radius and the difference between the GaAs and AlGaAs radii are given by:

$$\begin{aligned}\bar{\rho}^{SL} &= \frac{\rho^{SL,AG}+\rho^{SL,G}}{2} = \frac{\rho_{sl}^{AG}+\rho_{sl}^{G}}{2} + \frac{\rho_{sl}^{G}-\rho_{sl}^{AG}}{2}\sinh\left(t^{G}/2\tau^{G} - t^{AG}/2\tau^{AG}\right)\Big/\sinh\left(t^{G}/2\tau^{G} + t^{AG}/2\tau^{AG}\right) \\ \Delta\rho^{SL} &= \rho^{SL,G} - \rho^{SL,AG} = 2\left(\rho_{sl}^{G}-\rho_{sl}^{AG}\right)\sinh\left(t^{G}/2\tau^{G}\right)\sinh\left(t^{AG}/2\tau^{AG}\right)\Big/\sinh\left(t^{G}/2\tau^{G} + t^{AG}/2\tau^{AG}\right).\end{aligned} \tag{2.5}$$

The evolution of ρ^{G} and ρ^{AG} after each SL period is illustrated in Figure 2.26. The SL profile starts evolving from the value ρ_{sl}^{AG} (point *i*) along the GaAs recovery curve, and after the first GaAs layer it reaches the value ρ_1^{G} (point a_1) determined by (2.3). This value, shifted horizontally onto the AlGaAs recovery curve (point b_1), represents the starting point of the evolution during AlGaAs deposition. After completing the AlGaAs layer, ρ decreases to the value ρ_1^{AG} (point c_1), that is traced back to the GaAs curve for convenience (point d_1). Since $\rho_1^{AG} > \rho_{sl}^{AG}$,the deposition of the first full SL period (contour *i* - a_1 - b_1 - c_1 - d_1) yields an overall widening of the profile. This construction is repeated for the second period (contour d_1 - a_2 - b_2 - c_2 - d_2), after which the profile is characterized by $\rho_2^{AG} > \rho_1^{AG}$. The difference between the initial and final profile in each period tends however to decrease at each period, until $\rho_n^{AG} = \rho_{n-1}^{AG}$, (contour d_{n-1} - a_n - b_n - c_n - d_n, filled area in Figure 2.26). At this point, growth of a full SL period forms a closed loop in the (ρ, *t*) plan, that can be repeated *ad infinitum* [6].

Figure 2.25b shows ρ_n^{G} and ρ_n^{AG} obtained with eq. (2.4), as a function of the total (nominal) thickness and QWR number, for the SL of Figure 2.25a. The recovery curves were obtained from TEM cross sectional data of growth studies for thick GaAs and AlGaAs layers. As for the measured profiles of Figure 2.25a, both ρ_n^{G} and ρ_n^{AG} stabilize to values intermediate to ρ_{sl}^{AG} and ρ_{sl}^{G} after an initial transient. The average radius $\bar{\rho}^{SL}$ thus obtained is 16.1±0.5nm (fitted line), in very good agreement with the experimental value.

In the 2nd and 3rd column of Table 2.3 we compare the measured and calculated values of $\bar{\rho}^{SL}$, for all the four SLs, showing excellent agreement for each of them. By considering the geometry of the nanofacets at the bottom of the groove, we can also relate the actual growth rate r_b at the center of the QWRs to $\Delta\rho^{SL}$. This growth rate is related to the one on the sidewall $r_{sw} \cong 1$ by

$$r_b = r_{sw} + \Delta\rho\left(\tan\theta - \tan\alpha\right) \tag{2.6}$$

[6] Of course, after growth of a sufficiently thick structure (of a thickness comparable to the depth of the initial groove), the structure planarizes, due to the expansion of the top of the mesas. A periodic recovery of the surface profile as in Figure 2.26 occurs only at the bottom of the groove before planarization is achieved.

t^{AG} (nm)	$\bar{\rho}^{SL}$ (nm)		r_b^G		r_b^{AG}	
	meas.	simul.	meas.	simul.	meas.	simul.
2.2	19.1.±1.1	18.5±0.4	1.5±0.1	1.6±0.3	0.57±0.09	0.54±0.23
3.9	15.6±0.3	16.1±0.5	1.6±0.1	1.8±0.3	0.71±0.05	0.63±0.15
7.8	12.9±0.5	13.0±0.5	2.0±0.1	2.1±0.4	0.77±0.03	0.75±0.09
11.6	11.0±0.7	11.4±0.5	2.5±0.2	2.2±0.4	0.80±0.06	0.81±0.06

Table 2.3: Measured and simulated values of the self limiting average radius of curvature $\bar{\rho}^{SL}$*, and of the relative growth rates of the GaAs (*r_b^G*) and AlGaAs layers (*r_b^{AG}*), in GaAs/*$Al_{0.45}Ga_{0.55}As$ *QWR SLs with different nominal thicknesses of the AlGaAs barrier* t^{AG}*, and* T_s*=650°C.*

where $\alpha = 25°$ is the angle between the (100) and the {311}A facets, $\theta \cong 45°$ is the angle between the (100) and the sidewalls (see page 133). The measured and calculated values of r_b (using (2.5) and (2.6)) for the four QWR SL samples are given in Table 2.3. As expected, $r_b^G > 1$ and $r_b^{AG} < 1$. Good agreement was obtained between the experiment and the model. In our SLs, r_b^G varied from about 1.5 to about 2.5, and r_b^{AG} from about 0.6 to about 0.8, for t^{AG} ranging between 2.2 and 11.6nm, respectively. The overall growth rate over a SL period, however, is always equal to the nominal and sidewall ones, within the experimental errors, as expected for a self-limiting growth.

In the limit of a short-period QWR SL, i.e., $t^{AG} \ll \tau^{AG}$, $t^G \ll \tau^G$, (2.5) can be written as

$$\bar{\rho}^{SL} = \frac{\rho_{sl}^{AG} + \rho_{sl}^{G}}{2} + \frac{\rho_{sl}^{G} - \rho_{sl}^{AG}}{2} \frac{x\tau^{AG} - \bar{x}\left(\tau^{AG} + \tau^{G}\right)}{x\tau^{AG} - \bar{x}\left(\tau^{AG} - \tau^{G}\right)}, \qquad (2.7)$$

where $\bar{x} = x\, t^{AG} / (t^{AG} + t^G)$ is the average SL Al mole fraction (Note that $\bar{\rho}^{SL} \to \rho_{sl}^G$ for $\bar{x} \to 0$, and $\bar{\rho}^{SL} \to \rho_{sl}^{AG}$ for $\bar{x} \to x$, as expected). In Figure 2.27 we plot the values of $\bar{\rho}^{SL}$ obtained experimentally (squares) and from (2.7) (solid line) as a function of the average Al composition in the SL at the bottom of the groove. The measured data are well reproduced by expression (2.7). However, the observed radius of curvature of the SL is systematically larger than the measured self limiting radius ρ_{sl}^{AG} for AlGaAs *alloys* with the same equivalent composition x grown under the same conditions (circles in Figure 2.27; the corresponding dashed line is a guide to the eye). In other words, the surface curvature depends not only on the local relative abundance of the group III species but also *on the order* in which they are deposited (pure GaAs + $Al_xGa_{1-x}As$, or $Al_yGa_{1-y}As$ alloy). In particular, since eq. (2.7) is independent of the absolute thicknesses of the SL layers, the discrepancy above holds also in the limit of t^{AG}, t^G -> 0, that would correspond to the epitaxial growth of an alloy by alternate deposition of its constituents ("digital" alloy). In Chapter 5 we will interpret this discrepancy in terms of the entropy of mixing associated with a nonuniform composition at the growth surface.

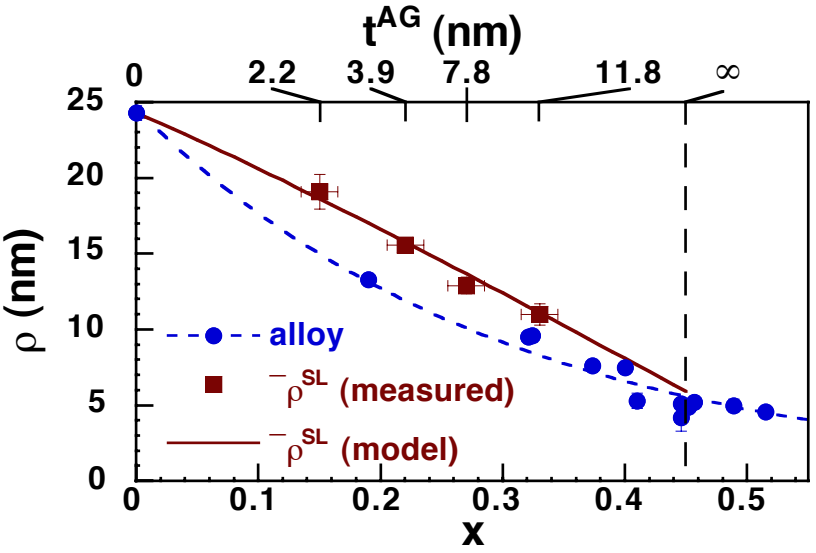

Figure 2.27: Measured (squares) and calculated (solid line) mean QWR-SL radius of curvature, as a function of the average Al mole fraction in the SL, for T_s=650°C. Self-limiting radii of curvature of AlGaAs alloys are shown by circles, with a dashed line as a guide to the eye.

2.1.1.3 Predictions of the model and design of new structures

With the construction of Figure 2.26, it is possible to predict and design the profile of a QWR SL structure once the recovery curves of the materials composing the individual SL layers are established. For example, one can select a desired set of values of $\bar{\rho}^{SL}$ and $\Delta\rho^{SL}$ (provided that $\bar{\rho}^{SL} - \Delta\rho^{SL}/2 > \rho_{sl}^{AG}$ and $\bar{\rho}^{SL} + \Delta\rho^{SL}/2 < \rho_{sl}^{G}$) and construct on Figure 2.26 a closed loop with $\rho_{G,AG}^{SL} = \bar{\rho}^{SL} \pm \Delta\rho^{SL}/2$. This loop will define univocally a pair of values of t^{AG} and t^{G}, yielding such a closed loop. This graphic procedure is, of course, equivalent to solving the system of equations (2.5) for t^{AG} and t^{G}. Furthermore, it is possible to reduce or eliminate the initial transient by growing the SL on an AlGaAs buffer with a lower Al mole fraction than in the SL barriers, selected in such a way that its self-limiting radius of curvature is equal to ρ^{SL}. In this case, the SL growth profile would start from the beginning to evolve on the closed loop of Figure 2.26. Note, however, that this procedure would not remove the differences of the first QWR with respect to the others, since this wire would have in this case an asymmetric barrier, with a lower barrier smaller than the upper one.

By applying eq. (2.3) repeatedly at each SL period, it is possible to predict the profile evolution of SL structures that are not strictly periodic, and therefore not expressible analytically in terms of eq. (2.4). We have applied this procedure to two cases: a SL in which a random noise was added to each layer thickness, and a SL consisting of two alternating periods.

In Figure 2.28 we show the simulated ρ^{G} and ρ^{AG} (circles), as well as the GaAs and AlGaAs bottom thicknesses (squares), for a sample similar to that of Figure 2.25b. In this simulation, a 20% (a) or 50% (b) random noise was added to each layer thickness. This noise is reflected in a 20% or 50% random variation of the bottom thicknesses. However, the SL radius of curvature after each layer is fluctuating much less: the difference between the highest and

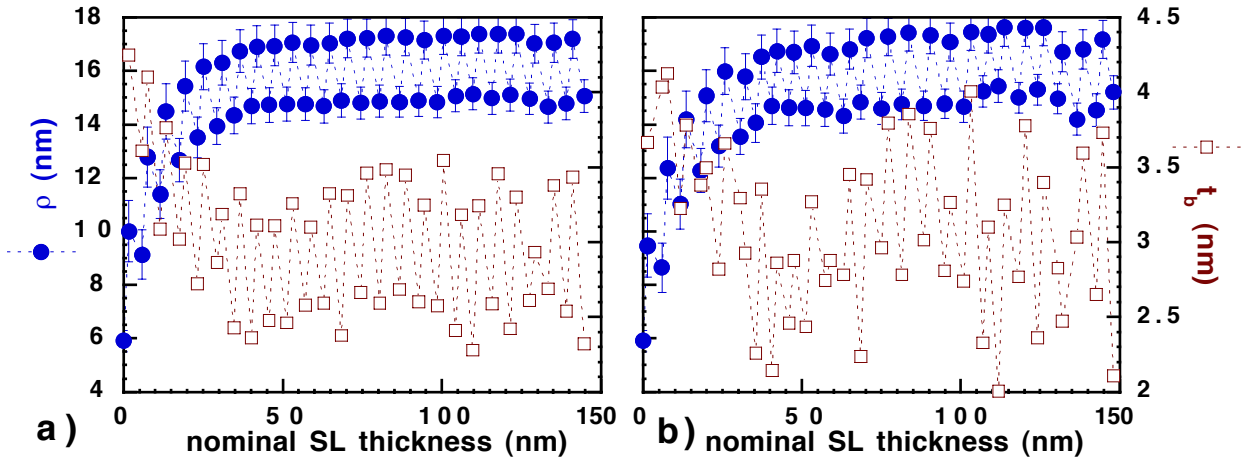

Figure 2.28: Simulated radius of curvature after each layer (circles) and individual layer thicknesses at the bottom of the groove (squares) for the SL of Figure 2.25b. A random noise of 20% (a) and 50% (b) was added to the nominal GaAs and AlGaAs thicknesses.

lowest point is only about 3% of the average value in the case (a), and about 7% in the case (b). Thus, the SL profile is able to self-adjust, and smooth out random growth fluctuations. This is related to the fact that both the GaAs and AlGaAs recovery curves become steeper as the profile deviates more from the average, and flatter as it approaches the average. For example, if a GaAs layer were thicker (thinner) than the average, the profile after it would be larger (smaller) than the average. The recovery during AlGaAs would be therefore stronger (weaker) than the average, and would in either case compensate partially for the perturbation. An equivalent compensation happens in GaAs, after a perturbation in the AlGaAs layer.

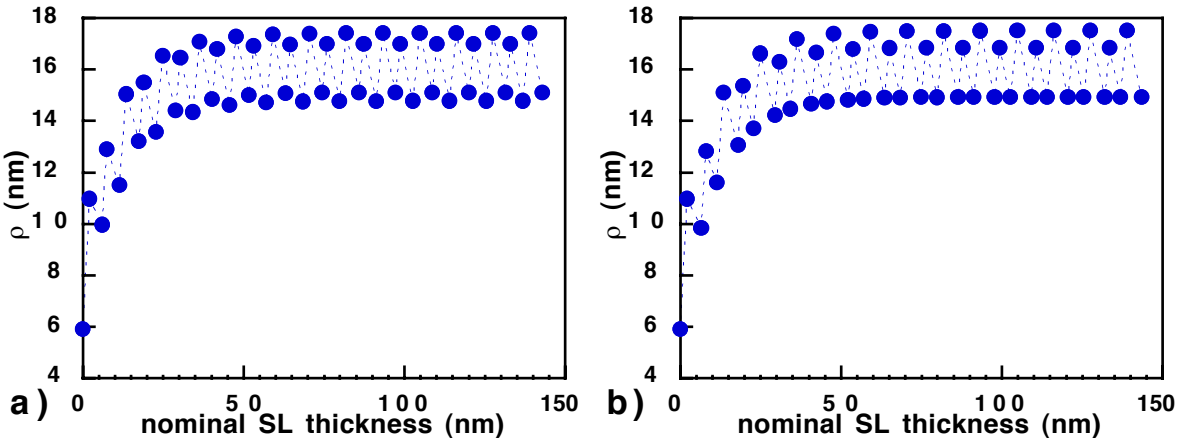

Figure 2.29: a) Simulated radius of curvature after each layer of a GaAs/$Al_{0.45}Ga_{0.55}As$ SL, consisting of two alternating periods with thicknesses (2.1nm/3.9nm) and (1.5nm/3.9nm). b) The same for (2.1nm/4.4nm) and (1.5nm/3.4nm).

In Figure 2.29, we show the simulated radius of curvature of a GaAs/$Al_{0.45}Ga_{0.55}As$ SL consisting of two alternating periods. The average thickness of the individual layers over two periods was fixed to the same values as the simulation of Figure 2.25b. In part a) we kept fixed $t^{AG} = 3.9$nm, and we alternated between $t^{G} = 2.1$ and 1.5nm. When the stable profile is reached, also the radius of curvature becomes bi-periodic like the thicknesses. Besides, $\bar{\rho}^{SL} = 16.1$nm as

in the simple-periodic situation of Figure 2.25. By alternating also t^{AG} (t^{AG} = 4.4 and 3.4nm, and t^{G} = 2.1 and 1.5nm, respectively), we could reach a SL profile in which only $\rho^{SL,\ G}$ oscillates, while $\rho^{SL,\ AG}$ keeps stable (Figure 2.29), and again $\bar{\rho}^{SL}$ = 16.1nm.

2.2 Summary

Low pressure OMCVD growth of GaAs/$Al_xGa_{1-x}As$ heterostructures on corrugated substrates results in the formation of a faceted growth profile. In particular, both the top of the mesas and the bottom of the grooves are composed of (100) facets, surrounded by {311}A ones. The sidewalls of the groove, connecting the top and bottom regions, are vicinal {111}A planes, misoriented towards the (100) by an amount that depends on the material and on the growth temperature. This orientation is the one for which the growth rate is the highest, between the [100] and [011] directions. However, when the size of the bottom (100) and {311}A planes is reduced to some tens of nanometers, the growth rates of these facets is increased by surface diffusion towards the bottom. These growth rates can self-adjust, in order to yield a vertical propagation of the corner between the different facets. The resulting self-limiting profiles depend on the material and growth conditions, and widen as the surface diffusion length increases. Self-limiting growth has been observed both for GaAs and for $Al_xGa_{1-x}As$. By growing a QW structure, in which the barrier material has a shorter diffusion length than the QW material, a QWR can be formed at the bottom of the groove, thanks to a thickening and widening of the bottom facets. QWR formation is followed by a self-limiting recovery during deposition of the upper barrier. Uniform vertical arrays of GaAs/$Al_xGa_{1-x}As$ and $In_xGa_{1-x}As$/GaAs QWRs have been successfully grown with this technique, using a barrier thickness larger than the critical thickness required for recovering of the surface profile. On the other hand, if the barrier thickness is reduced to a few nm, carrier coupling effects become important, and SL minibands can be formed. To have significant SL effects, the barrier must be much thinner than the one needed to completely recover the self-limiting profiles, after deposition of each QWR. However, we have shown that growth of GaAs/$Al_xGa_{1-x}As$ QWR SLs is also self-limiting, with an average profile (over a SL period) that stabilizes to a width intermediate between the self-limiting GaAs and $Al_xGa_{1-x}As$ ones. The resulting SL structures exhibit better uniformity than other low dimensional (QWR or QD) SL structures produced via different self ordering mechanisms, such as strain induced SK or tilted SL structures, indicating a stronger driving force of the grown species to their nucleation sites in the case of the nonplanar growth. These structures should thus be useful for studying the coupling and tunneling phenomena in SLs of 1D systems [89]. SL growth can be accurately explained in terms of the self-limiting properties of the constituent materials. The SL profiles are larger than the ones measured in self-limiting AlGaAs alloys with the same equivalent composition over a SL period. We will see in Chapter 5 that these differences can be ascribed to the different role played by the entropy of mixing in the two cases.

Chapter 3

Three-dimensional structure of self-limiting profiles

This chapter is devoted to AFM studies of the GaAs and AlGaAs surface morphology in nonplanar epitaxy. A brief introduction to the AFM technique will be given at the beginning. This will be followed by an overview of surface studies of *planar* GaAs and AlGaAs growth, realized on unpatterned (100), (311)A and (111)A substrates grown side-by side with the V-grooved ones. Planar GaAs and AlGaAs OMCVD growth has been already extensively studied by SPM techniques [90-93]. However, a morphological analysis of these specific surfaces is important for nonplanar surface studies, since these are the facets forming in our etching and growth process. The rest of the chapter is devoted to AFM studies of the surface morphology of our nonplanar samples. We analyze features due to lithography-related roughness and, more importantly, step ordering phenomena taking place at the top of the mesas and at the bottom of the grooves. The modifications of the step structure, relative to planar surfaces of the same orientations, can be ascribed to modifications of surface diffusion due to the creation of mesa structures, with sizes comparable to the surface diffusion length.

3.1 Introduction to the AFM measurements

AFM is a scanning probe microscopy (SPM) technique, introduced in 1986, where the topographical information of the surface being scanned is provided by measuring forces on the atomic scale [94]. This method was proposed to overcome the limitations of STM, which can be applied only to conducting samples. Today, AFM-related techniques can measure a variety of interactions, such as magnetic, dipping, frictional and electrostatic forces [95]. In AFM, the probing tip is attached to a cantilever-type spring, which is deflected in response to the forces between the tip and the sample (Figure 3.1). Typical forces range between 10^{-11} and 10^{-6}N, therefore non-destructive imaging is possible with a wide variety of materials. The sample is generally mounted on a piezoelectric scanner that provides the x-y movement. As the sample is scanned, changes in the surface topography induce variations of the forces, and therefore of the tip deflection. This deflection is measured, e.g., by reflecting a laser beam from the head of the tip and measuring the beam deflection with a position-sensitive photodiode (Figure 3.1).

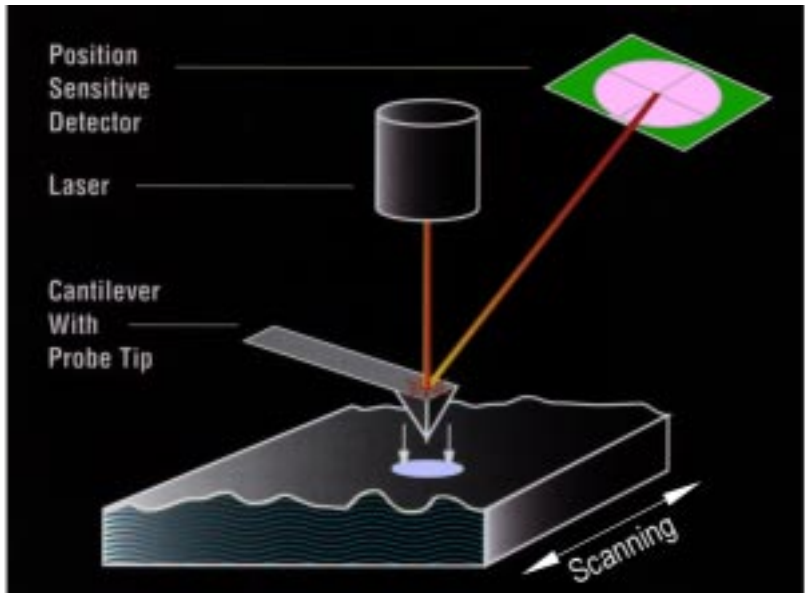

Figure 3.1: Schematic drawing of the working principle of an atomic force microscope (AFM).

Different modes of AFM operation have been developed. In *contact mode,* the tip is dragged across the surface, with separations of the order of 0.1nm. In this range, dominant forces are ionic repulsions, which allow, under the best conditions, imaging with atomic resolution. However, under ambient air conditions, most surfaces are covered by a layer of adsorbed water or of other contaminants, which can be several nm thick. Surface tension of these layers gives rise to additional capillary forces that can pull the cantilever down to the layer, and therefore distort the image (Figure 3.2a).

In *non-contact mode,* the tip stands 10 to 100nm above the sample, where attractive Van der Waals forces dominate. At these distances, problems of capillarity are eliminated; besides, forces are much weaker than in contact mode, giving the possibility of imaging soft surfaces, which could be damaged in contact mode. Additionally, magnetic and electrostatic forces can be imaged on specific samples [95]. However, the spatial resolution is generally smaller than in contact mode.

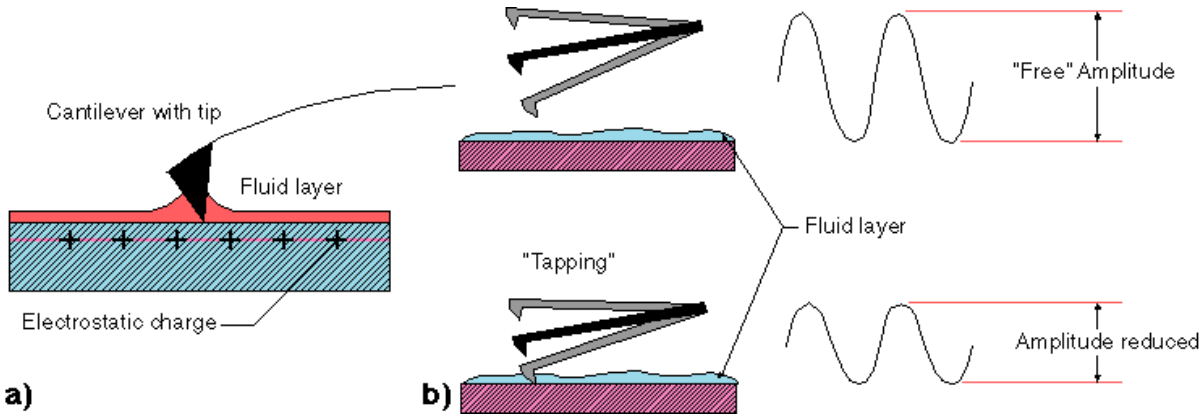

Figure 3.2: Different AFM modes of operation. a): Contact mode. b): TappingMode. Schematic illustration courtesy Digital Instruments, Santa Barbara, California.

In both AFM modes, the topography information is given by the deflection z of the cantilever in response to the force F between the tip and the surface. The deflection is given by Hooke's law $F = kz$, where k is the spring constant. For Si cantilevers, typical spring constants are of the order of 0.5N/m. Usually, better resolution is obtained in constant force mode, where the cantilever deflection is kept constant by regulating the sample-tip distance through a feedback loop.

An alternative to the static modes described above is to oscillate the cantilever close to its resonant frequency (typically 100-300kHz) [96]. In this *dynamic* or *TappingMode*™ [97] variant, the "free air" amplitude of the oscillations (≈100nm), obtained when the tip is far away from the sample, is damped as the tip approaches the surface, due to the interaction forces (Figure 3.2b). Operation in air is done by maintaining this reduced amplitude constant, as the tip scans the surface, through a feedback loop that adjusts the tip-sample separation. Since the tip enters in contact with the surface at each oscillation, resolution comparable with the contact mode can be achieved. Besides, withdrawing the tip from the surface can overcome capillarity, and reduces the contact forces significantly (≈10^{-10}N [96]), thus minimizing both tip and sample degradation.

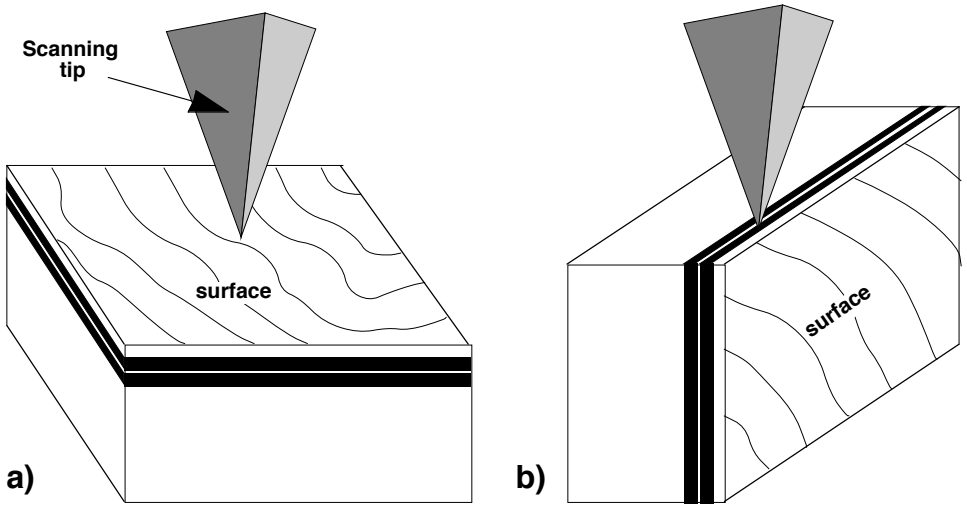

Figure 3.3: a) Schematic top-view AFM setup. b): Schematic cross sectional AFM setup.

In our experiments, we used a MultiMode™ SPM with a NanoScope® III control system by Digital Instruments [97], operated in TappingMode AFM. TappingMode was found to lead qualitatively to the same results as obtained with contact mode, but with a lower noise level. In TappingMode, we used silicon tips with a radius of curvature below 10nm (as imaged by SEM), mounted on a 125μm long cantilever, with tip vibration frequencies of 250 - 300kHz and forces around 10^{-10}N. At scanning speeds below 1Hz/line, we obtained noise levels of about 0.03nm (RMS) and a high lateral resolution (≈1nm). Accurate z-calibration of the piezo scanner was achieved by measuring the height of steps on a (100) graphite surface, which were found to be multiples of the thickness of a monoatomic layer (ML). From this, we deduced that the systematic error in our height measurements is smaller than 0.05 nm. On the graphite

crystallographic planes, atomic resolution was obtained and the average noise was 0.03nm. We have imaged planar and nonplanar samples, both in top view (Figure 3.3a) and in cross section (Figure 3.3b). Top-view analysis is discussed in this chapter, while cross sectional studies will be discussed in Chapter 4.

Ex situ AFM imaging in air, after the growth process is completed, can be applied to visualize surface morphology, if the modification of the morphology due to oxidation and contamination is small enough. As we will show in Chapter 4, the oxide growth on the (011) surfaces nearly saturates at a thickness of ~0.6nm for GaAs and <2nm for $Al_{0.58}Ga_{0.42}As$ after several days of exposure. We will also see that the surface of this oxide stays atomically smooth (0.05nm RMS roughness) up to Al concentrations of $x = 0.5$. Oxide growth rate on the (100) surface was found to be lower than on the (011) surface in the case of high temperatures [98]. Therefore, it can be assumed that, at least on (100) surfaces, the oxidation rate at room temperature is as well lower than on (011) faces. In addition, the surface is covered with at least two layers of arsenic after growth, during the sample cooling under AsH_3 overpressure (forming a c(4×4) reconstruction on the (100) surface [54, 99, 100]), which probably delays the oxidation process.

3.2 Surface morphology of planar (Al)GaAs epitaxy

3.2.1 (100) surfaces

Two-dimensional growth is assumed to be the major process in OMCVD on (100) surfaces. Adsorption of atoms or molecules on the surface, followed by 2D diffusion and preferential attachment to steps or kinks, leads to the formation of growth islands or large terraces, separated by steps of one or a few monolayer height. The migration of these steps over the growing surface can be determined by in situ spectroscopy during OMCVD [99, 101, 102]. Several features of surface morphology, such as step density and height, island size or terrace width, are characteristic of the material, of the growth parameters, including temperature and partial pressures of organometallics and hydrides, and of the substrate misorientation.

Figure 3.4 shows a series of $5\times5\mu m^2$ surface AFM images of GaAs layers, with thicknesses of at least 50nm, grown on planar (100) GaAs substrates. In all images, the axes lie in the $\langle 011 \rangle$ directions. The growth temperature increases from 520°C (sample (a)) to 750°C (sample (f)). On each sample, one can recognize the presence of terraces, whose width depends on the substrate misorientation. The terraces are separated by *monolayer-high steps* (1ML ≅ 0.28nm). Figure 3.5a shows a line scan of the AFM image shown in Figure 3.4f. The ML steps can be well resolved in the scan, since the scanning noise is about 0.03nm. Note that the oxidation of the samples in air, though preventing atomic resolution imaging, preserves the underlying ML structure of the (100) surfaces. Since the oxide thickness can be assumed to be smaller than 0.6nm, as found in the (011) cross-sectional studies (Chapter 4), we can conclude that AFM imaging after oxidation well represents the original surface morphology.

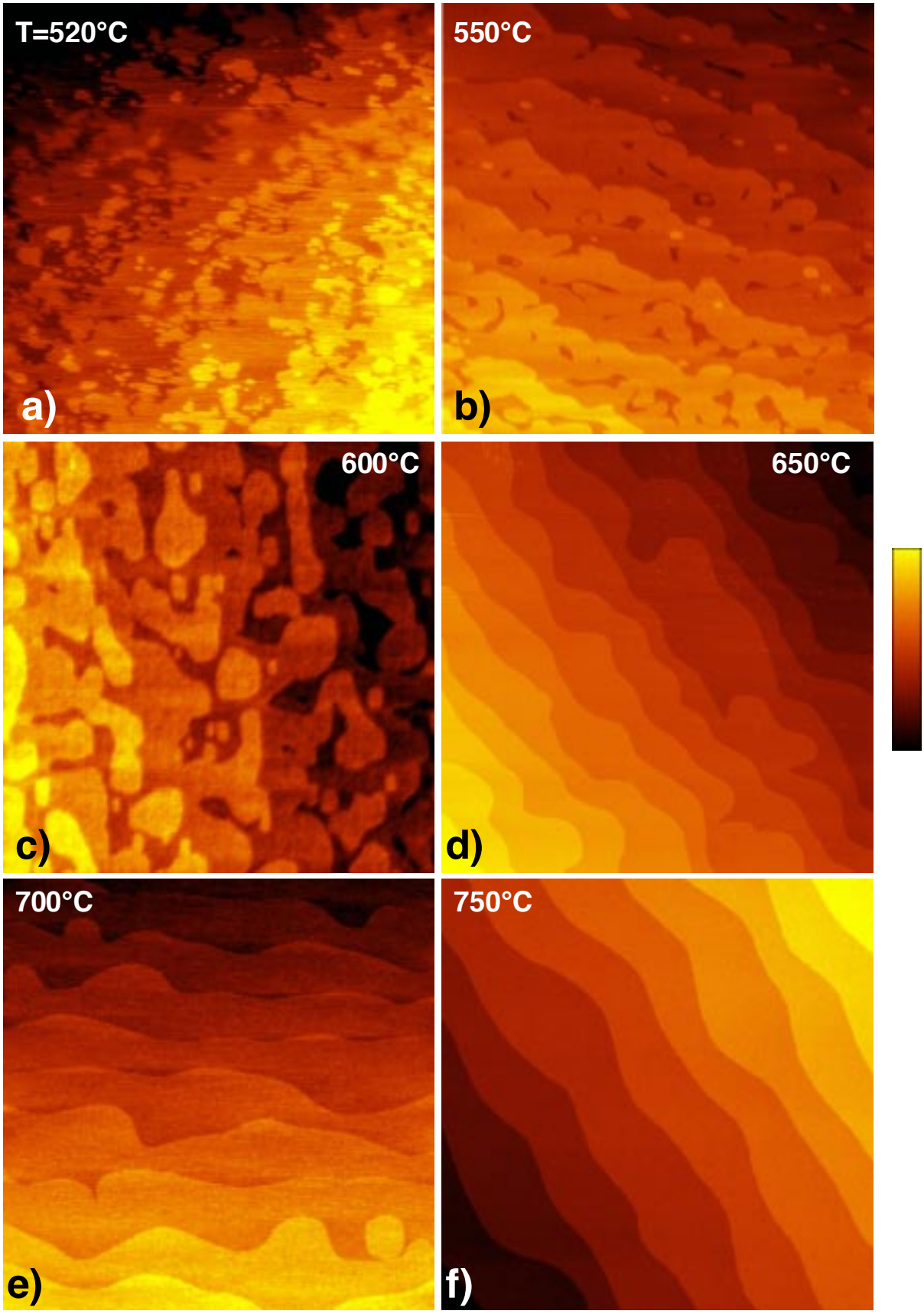

Figure 3.4: 5×5μm² AFM images of the surface of thick (≥50nm) GaAs layers grown on planar (100) GaAs substrates, at increasing temperatures. The height scale on the right depends on the number of ML terraces present in the image, and varies between 2 and 5nm.

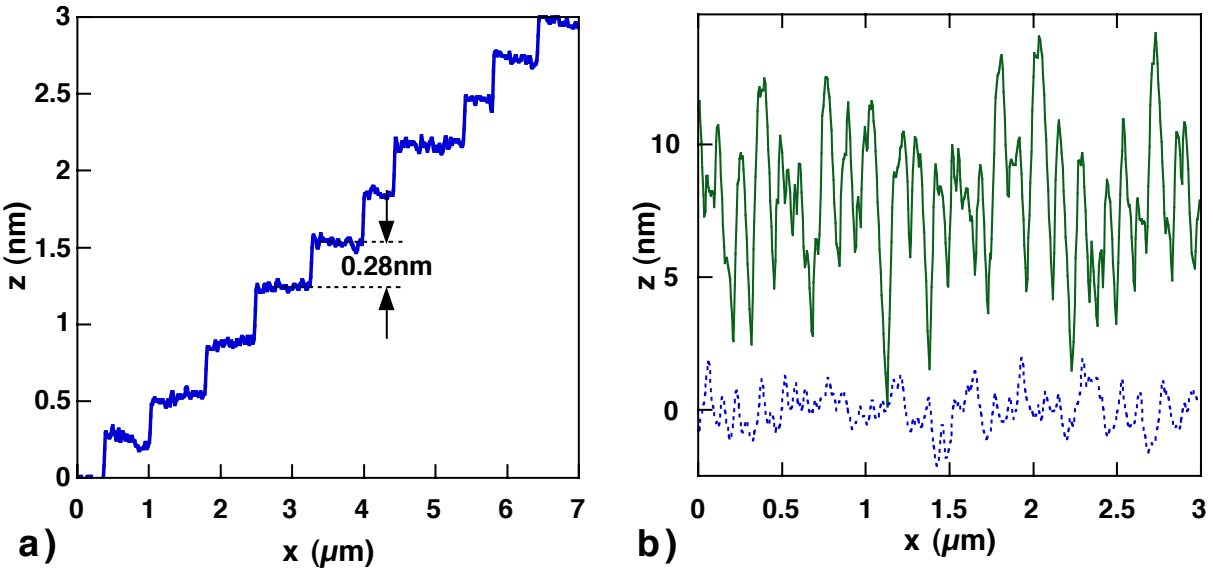

Figure 3.5: a): AFM line scan along the diagonal of Figure 3.4f, showing monolayer steps on (100) GaAs surfaces. b): AFM scans along the [01$\bar{1}$] direction of Figure 3.8, showing the morphology of (311)A surfaces. Solid line: GaAs; dotted line: $Al_{0.2}Ga_{0.8}As$.

The terrace width ranged between about 0.45μm for sample (d) (corresponding to an average misorientation $\theta = 0.035°$) and about 1.2μm for sample (c) (corresponding to $\theta = 0.015°$). Note that all the misorientations are below the specifications of the epi-ready wafers (±0.1°), and run in random directions.

As the growth temperature increases, one can notice a marked evolution of the surface morphology. At 520°C (a) the steps separating the different terraces are very irregular, and a large density of 2D islands can be seen on the terraces between the steps. The islands are elongated along the [011] direction (this orientation is horizontal in image (a)), with a size about 2-3 times the size in the orthogonal direction. This anisotropy was already observed by ultra-high vacuum STM on GaAs layers grown by OMCVD at a similar temperature [92], and was attributed to an anisotropy either of the Ga surface diffusion or of the sticking coefficient at the step. The islands are smaller near step-down edges, and tend to grow and coalesce in regions near step-up edges. This could be explained by a growth mode in which some islands can nucleate on a terrace, and expand until they merge among themselves and with a propagating step edge. The low surface diffusion at this temperature, therefore, favors a certain degree of island nucleation, in addition to step flow. Note also the roughness of the step edges, and the presence of voids between coalesced islands and steps. At 550°C (b), fewer isolated islands are observed, with a more symmetrical shape, and the step edges appear smoother, but still with a considerable density of void regions. The lower anisotropy of the 2D islands, as the temperature increases, can be due to the decrease of the anisotropy between the lateral growth rates at [011] and [01$\bar{1}$] step edges [23, 103]. At 600°C (c), the density of voids appears lower than at 550°C, but a large island density is still observed. This is possibly due to the smaller misorientation of this substrate (terrace size is about 1.2μm, as compared with 0.8μm of sample (b)), that favors

island nucleation. For higher temperatures, growth can be unequivocally attributed to pure step flow. One can still notice, however, an improved step smoothness, due to an increase of surface diffusion along the steps, upon increasing the growth temperature from 650°C (d) to 700°C (e) and 750°C (f).

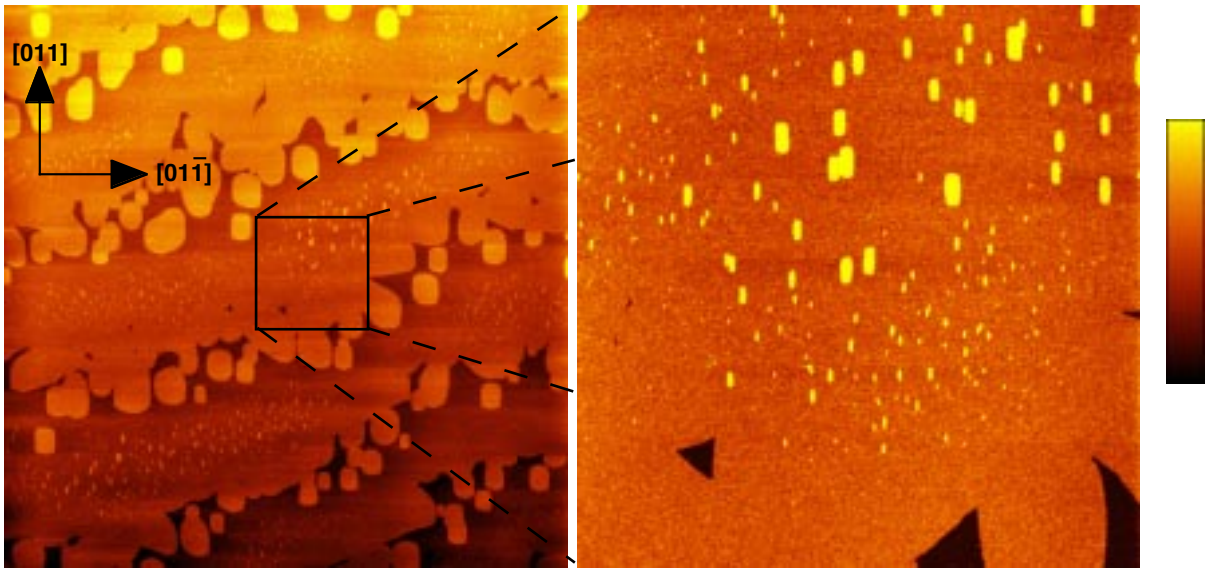

Figure 3.6: Left: 15×15μm² surface AFM image of a GaAs layer grown at 700°C on a planar GaAs substrate misoriented by 0.004° from the (100). Right: 3×3μm² detail of the left image. The full height scale is 1.2nm for the left image and 1.0nm for the right one.

Step-flow growth for $T \geq 650$°C indicates that the surface diffusion length of Ga adatoms, or of the relevant Ga species, is larger than about half of the terrace width (0.45μm, 0.50μm and 0.65μm for images (d), (e) and (f), respectively). Some information on the effective diffusion length can be inferred from a sample in which the unintentional misorientation was exceptionally low (0.004°, corresponding an average terrace width of about 4μm). Figure 3.6 shows surface AFM images of a GaAs layer grown at 700°C on such a substrate. Some interesting features can be observed in the 15×15μm^2 image on the left, and the 3×3μm^2 detail shown on the right. In the central area of each terrace, one can notice a region with a high density of small asymmetric islands, elongated in the [011] direction. The size of the islands decreases and their density increases towards the step-down edges. At the center of the terraces, islands have an approximate area of 5×10^{3}nm, with a density of about 10/μm^2, while towards the step-down edges the area decreases to about 5×10^{2}nm and the density increases to about 50/μm^2. The regions extending about 400nm on both sides of the steps are free from small islands, but just below the steps much bigger (~0.5μm^2 area), nearly square-shaped islands are present, that eventually merge into the step edges. These features suggest a mechanism of 2D nucleation on the terraces. After a new step edge has formed, 2D nucleation can take place on the terrace above in regions distant from it by more than the surface diffusion length. As growth proceeds, some 2D islands become bigger, and attract material from the smaller ones, which tend to disappear. As a new step edge approaches, two scenarios are possible, depending on the size of

the remaining islands. Islands that are larger than the critical nucleus for stable nucleation[1] continue to expand, and eventually coalesce with the step. Islands smaller than this critical nucleus disappear when their distance from the step-up edge (or from a stable island) is shorter than the diffusion length, leaving this region free from small islands. From the extension of the island-free regions, we estimate a Ga surface diffusion length of about 400nm at 700°C. Finally, note that the presence of these island-free regions symmetrically on both sides of the steps indicates that the Schwoebel barrier for diffusion at a step edge is negligible under these conditions [59, 105].

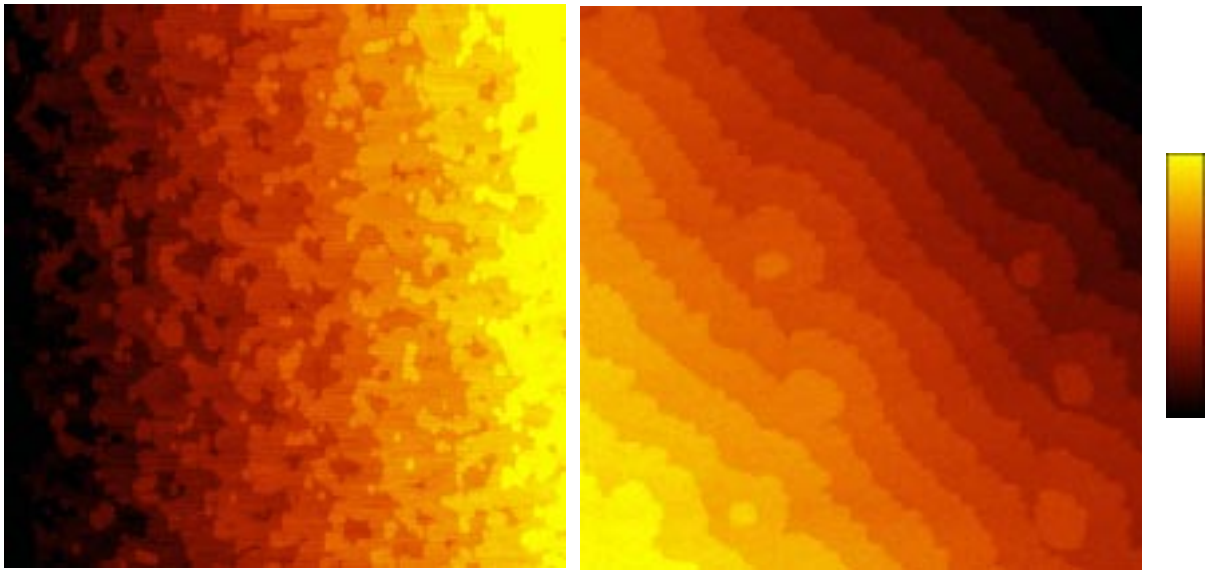

Figure 3.7: 5×5μm² surface AFM images of thick (≥50nm) $Al_{0.3}Ga_{0.7}As$ layers grown on planar (100) GaAs substrates, at 660°C (left) and 750°C (right). The full height scale is 3.5nm for the left image and 5nm for the right image.

Figure 3.7 shows the surface morphology of $Al_{0.3}Ga_{0.7}As$, for $T = 660°C$ (left) and 750°C (right). The mean misorientation angles and terrace widths were 0.03° and 0.55μm (left) and 0.05° and 0.3μm (right), respectively. $Al_{0.3}Ga_{0.7}As$ growth at 660°C is qualitatively similar to GaAs growth at lower temperature (Figure 3.4a), with meandering steps coalescing with 2D islands. At 750°C, $Al_{0.3}Ga_{0.7}As$ growth proceeds essentially in step-flow mode, with isolated island formation for terrace width exceeding about 0.3μm. An average diffusion length of about 150nm can be estimated from the island-step mean separation. Note that the steps, whose average orientation is close to the ⟨001⟩ direction, break up into small [011] and $[01\bar{1}]$ facets, possibly due to anisotropic surface diffusion.

3.2.2 (311)A surfaces

The growth behavior of the (311)A surfaces is significantly different from that of the (100), even if the growth window is similar. In MBE, GaAs growth on (311)A substrates is

[1] The size of the critical nucleus in GaAs OMCVD growth has been estimated to be much larger than one atom [104].

known to yield periodic corrugations along the [$\bar{2}$33] direction, with a periodicity of 3.2nm and a height modulation of 0.34nm (2ML) [106]. This (8×1) surface reconstruction, via As dimerization in the first and second layer, is required to minimize the dangling bond density and eliminate the excess electron density [106]. OMCVD growth results in corrugations on a much larger scale [93]. These corrugations have the same orientation as in MBE, but periods of the order of tens of nm, and similar height to period ratio (about 1:10). In GaAs/AlGaAs heteroepitaxy, the corrugations become larger as the temperature increases and as the GaAs thickness increases, until a saturation value is reached for about 100nm GaAs [93]. These behaviors were attributed to step bunching, limited by the surface diffusion length, as a mechanism for minimizing the (311)A surface energy via the formation of an array of nanofacets [93].

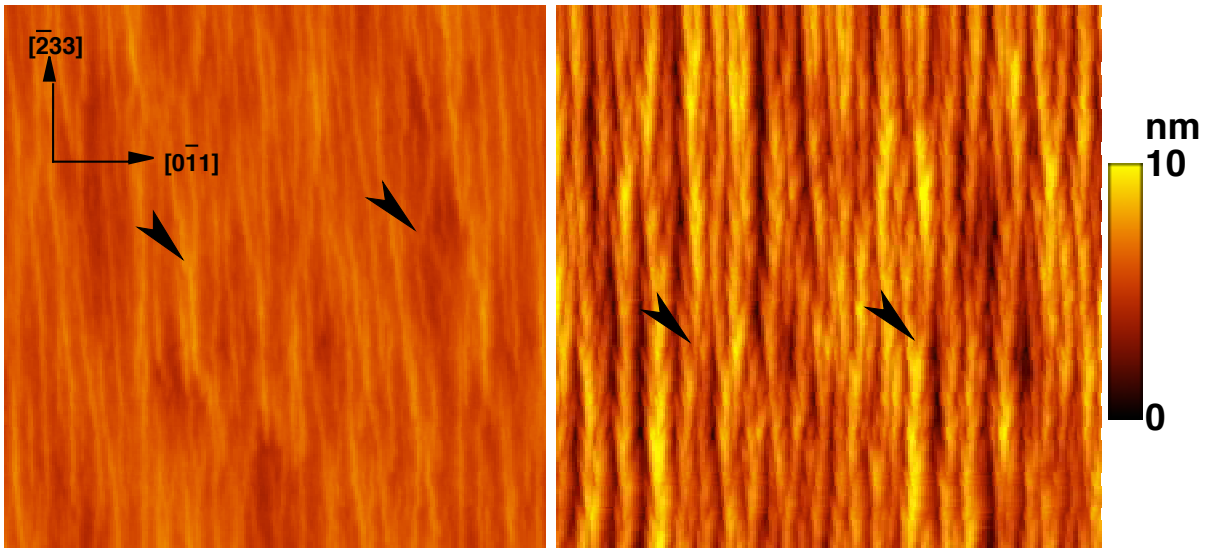

Figure 3.8: 3×3μm² surface AFM images of the $Al_{0.2}Ga_{0.8}As$ (left) and GaAs (right) (311)A surface structures, for a growth temperature of 750°C. Arrows mark some of the numerous step bifurcations, forming in both materials.

This pronounced faceting was observed also in our structures, as shown in the AFM images of Figure 3.8. The left image shows the (311)A surface after growth of 250nm $Al_{0.2}Ga_{0.8}As$ at 750°C. Corrugations are visible along the [$\bar{2}$33] directions. A line scan of this image, taken in the [01$\bar{1}$] direction, is shown in Figure 3.5b (dotted line). The height h and period d of step bunching are about 2.5nm and 40nm, respectively. Step bunching increases considerably after deposition of 100nm of GaAs in the same growth conditions (right image), resulting in $h \approx 8$nm and $d \approx 90$nm (see the solid line scan in Figure 3.5b). Note that the periodicity is very irregular, and step bifurcations (like the ones marked by arrows) are very common, both for $Al_{0.2}Ga_{0.8}As$ and for GaAs.

3.2.3 (111)A surfaces

The growth window for obtaining a good surface morphology in GaAs growth on (111)A-oriented substrates differs considerably from the one used here for nonplanar epitaxy.

Mirror-like surfaces are obtained typically in a limited interval of temperatures and AsH_3 pressures $p(AsH_3)$. With TMGa and AsH_3 precursors, temperatures for good surface morphology range between 550°C for $p(AsH_3) < 1$mbar and 650°C for $p(AsH_3) \approx 8$mbar [107]. At T ≈ 700°C, a high density of pyramidal hillocks with {111}B-oriented sidewalls is observed [107, 108]. The poor surface morphology at high T and low $p(AsH_3)$ was attributed to the resulting low AsH surface coverage in these conditions. This in turn lowers desorption of methyl radicals from the surface, that are supposed to be the species hindering 2D growth [107]. However, growth on (111)A substrates misoriented towards the $[\bar{2}11]$ and [100] direction, showed good surface morphology, with evidence for quasi-periodic step bunching, even at temperatures as high as 720°C [84].

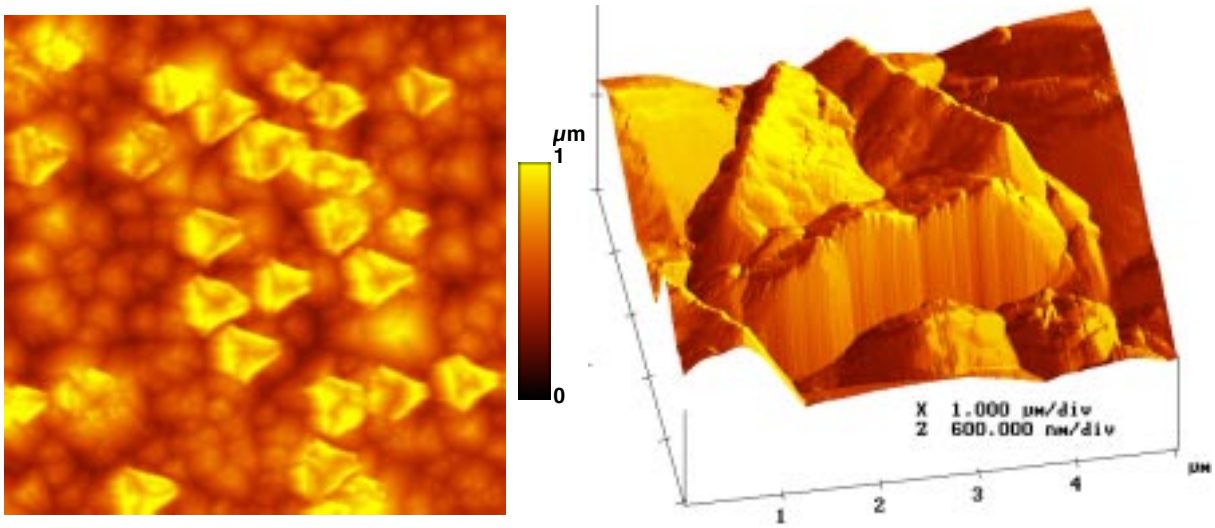

Figure 3.9: 30×30µm² top surface AFM image (left) and 3D, 5×5µm² detail of a hillock (right) of a GaAs layer grown on a (111)A substrate at 750°C.

An example of (111)A GaAs epitaxy from our OMCVD system is shown in Figure 3.9, for $T = 750$°C. The hillocks appear as pyramids about 400nm high, with a side about 4μm long. The sidewalls are {111}B planes, misoriented about 10° towards ⟨011⟩. The pyramids present a crater in the center, under the form of an inverted pyramid, whose faces are misoriented about 10° from the (111)A planes. The natural formation of these vicinal planes could be related to the development of vicinal facets on the sidewalls of our V groove structures.

3.3 Surface morphology of nonplanar (Al)GaAs epitaxy

Figure 3.10 shows a three-dimensional AFM image of the surface of a 15nm-thick GaAs layer, grown at 750°C on a 200nm-thick $Al_{0.45}Ga_{0.55}As$ buffer in an EBL-written, 0.5μm-pitch V groove array. Despite the lower spatial resolution of AFM, as compared with TEM, the faceted structure of the profile, evident in TEM cross sections of buried layers, can be recognized in the image. The different facets composing the groove are indicated: (100) and {311}A at the top of the mesas, a high index sidewall and again (100) and {311}A at the bottom of the groove.

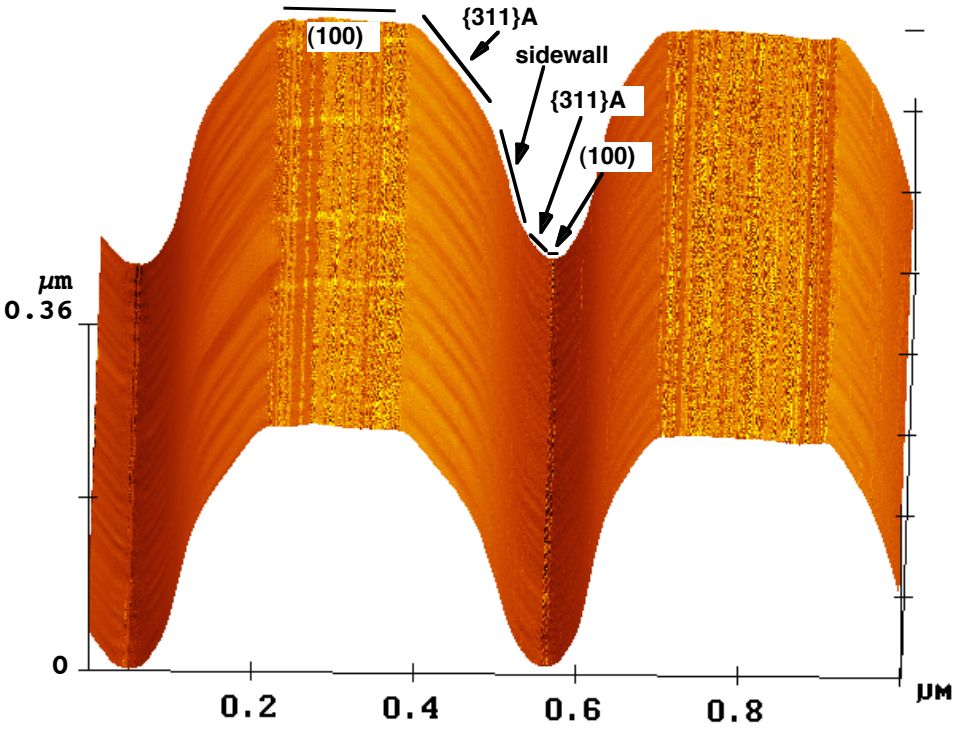

Figure 3.10: AFM image of a 15nm-thick GaAs layer grown on a 200nm-thick $Al_{0.45}Ga_{0.55}As$ buffer at T = 750°C, on an EBL-written 0.5μm pitch grating. All the facets observed in buried GaAs V groove profiles can be seen. The different facets are indicated.

To better visualize the morphology on inclined planes, we used *flattened* images, starting from AFM scans in which scan lines are acquired parallel to the grooves. For each scan line, we calculate the best-fit average line, and subtract its absolute position from the original line. In this way, all the line scans, and therefore all the facets composing the groove, lie on the same average plane, and the resulting image is the "projection", on the (100) plane, of the original structure. In Figure 3.11 we show the same AFM image of Figure 3.10, after a linear flattening in the direction of the grooves. The details of the profile along the groove are now much clearer, and reveal peculiar features of each of the facets at the nm height scale [2]. At the bottom of the figure, we show representative line scans of each facet along the groove, from the same sample, on a 2μm range. The (100) facets on the ridges present atomically-smooth terraces separated by ML steps. The {311}A at the top show corrugations similar to those discussed in Section 3.2.2 for planar substrates. The sidewalls (whose (100) projection is very narrow, due to their inclination) are characterized by long-range (hundreds of nm) height fluctuations, due to lithographic imperfections. The {311}A facets at the bottom are characterized by step bunching as the top {311}A ones, but with a smaller amplitude, superimposed on the long-range fluctuations found on the sidewalls. Finally, the (100) facet at the bottom appears smoother than the surrounding planes. The study of these features will be the main subject of the rest of the chapter.

[2] Note that the flattening procedure also removed the noise on the (100) ridges, visible in the original image of Figure 3.10, and due to the lack of complete height coherence between adjacent scan lines.

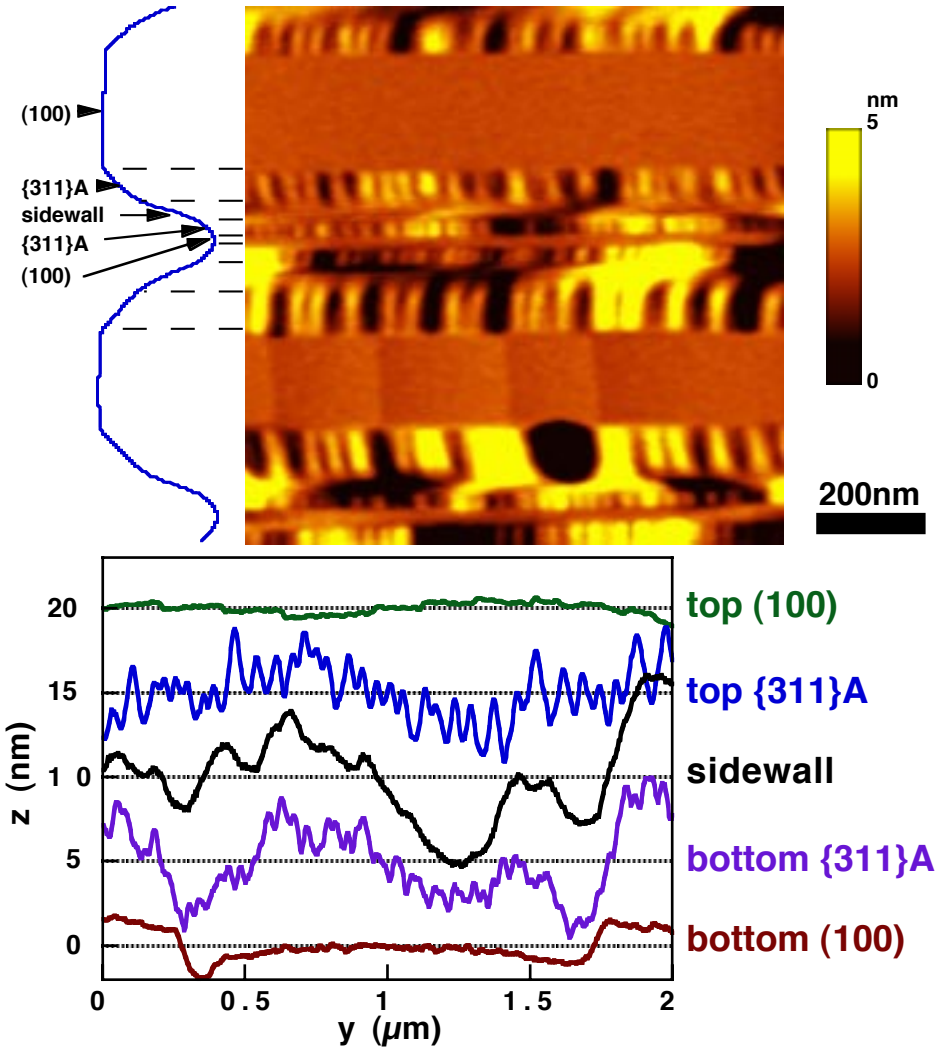

Figure 3.11: Top: AFM image from Figure 3.10, flattened in the direction parallel to the grooves. The measured section of the original profile is indicated on the left. Bottom: 2μm-long line scans along the groove of the same sample, corresponding to each facet.

3.3.1 Groove morphology before and after growth

In Figure 3.12 we compare the V groove surface profiles of an as-etched substrate and of a grown sample. On the left of the images, we plot cross-sectional scans of the two samples, showing the groove profiles. The left image is a flattened AFM view of part of a 3μm-pitch V groove array, measured after standard wet chemical etching and degreasing. The top region is very rough, and does not show the formation of any low-index facets. The bottom region separating the sidewalls is some 100nm wide and is characterized by a smoothly varying angle. The discontinuity visible at the bottom of the groove is due to the lack of correlation between the height profiles of the sidewalls on the two sides of the bottom region. No evident sign of (100) or {311}A faceting can be seen in the region. Note also the presence of numerous (~10/μm^2) etch hillocks, with lateral size in the range 30-100nm, and heights of about 5-30nm. These hillocks are possibly oxidized GaAs chunks, since they are removed after the heat-up process in the OMCVD reactor. If isolated pieces of resist remained on the surface, they would not be removed before growth, and they would give rise to extended growth defects.

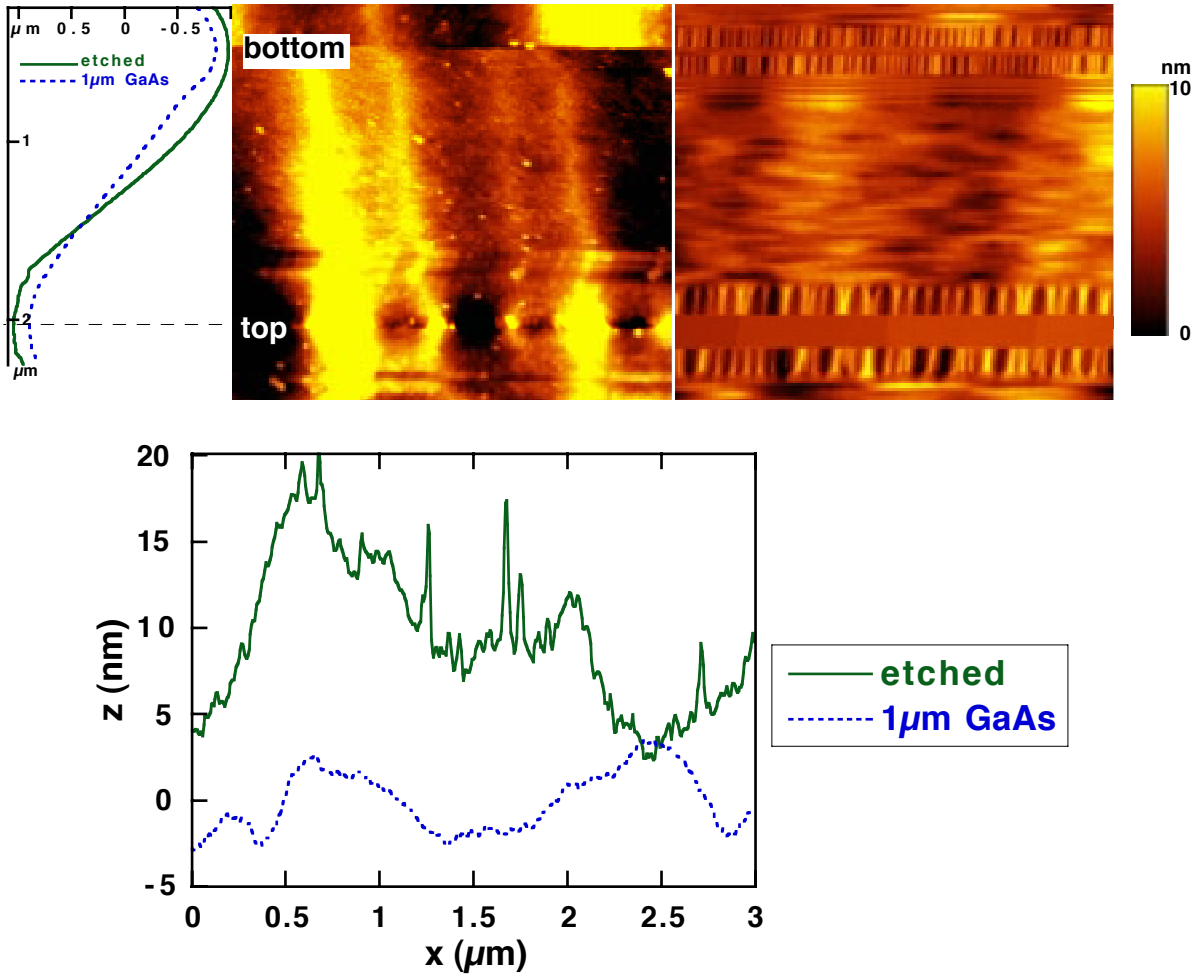

Figure 3.12: Top: 3×2.25μm flattened AFM images of part of a 3μm-pitch V groove after etching (left) and after growth of 1μm GaAs at 750°C (right). The measured profiles of both grooves are shown on the left. Bottom: line scans corresponding to the sidewall planes for the etched (solid line) and for the grown (dotted line) profiles.

The right image of Figure 3.12 shows part of a V groove from the same substrate, after deposition of a 1μm-thick GaAs layer at 750°C. One can notice that the etch defects have disappeared from the surface, and that the (100)+{311}A structure of the groove extrema is fully developed[3]. Besides, the sidewalls are smoother than on the as-etched substrate. Note also that some undulations have formed on the sidewalls, in the direction perpendicular to the groove axis. Two representative line scans of the sidewall profile along the groove are shown at the bottom of the figure, for the as-etched substrate (solid line) and for the grown sample (dashed line). On the etched profile, one can notice at least six defects, while the height variations are of the order of 15nm over 3μm length. This roughness is reduced to about 5nm after growth.

[3] AFM images of substrates after the heat-up process in the reactor show that the same facet structure is already forming at the top and at the bottom of the corrugations during the heat-up, probably due to mass transport effects.

3.3.2 Step ordering at the top of the mesas

In this section, we will focus on the ML step structure of the (100) facets forming at the top of the mesas. To analyze the orientation and surface distribution of these steps, we have grown a structure at 750°C, consisting of 15nm GaAs on a 200nm-thick $Al_{0.45}Ga_{0.55}As$ buffer, on an EBL-written nonplanar substrate. The substrate included four $100\times100\mu m^2$ areas with different patterns, separated by unpatterned areas. Before growth, the grooves in each area were about 0.3μm deep and 0.5-0.6μm wide, and were separated by (100) ridges of width $w = 0$, 0.3, 0.9 and 1.4μm, corresponding to a V-groove pitch $\Lambda = 0.5$, 1.0, 1.5 and 2.0μm, respectively (the 0.5μm-pitch area was shown in Figure 3.10 and Figure 3.11).

Figure 3.13 depicts the edge of the 2μm-pitch corrugated region, while Figure 3.14 shows the images in the central regions of all four pitches we have investigated. We will discuss in the following three different properties of the morphology of the steps and the ridges, as demonstrated by the two figures:

- The orientation of the steps on the ridge with respect to the groove edges.
- The spacing between steps and their direction (going up or down along the ridge).
- The relation between the step density and the ridge width.

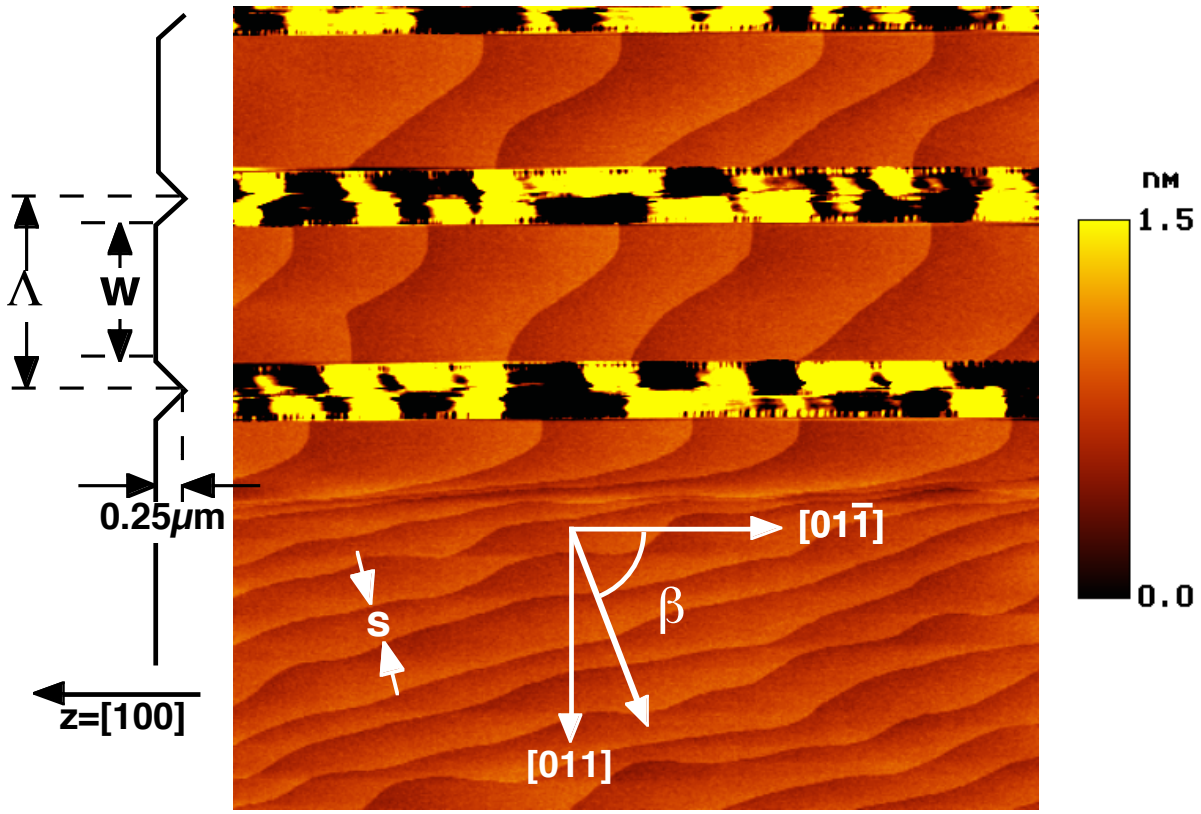

Figure 3.13: Flattened $8\times8\mu m^2$ AFM image of the GaAs-surface of an $Al_{0.45}Ga_{0.55}As$/GaAs heterostructure, deposited by OMCVD on a GaAs substrate with 2μm-spaced V grooves. The image is taken on the edge of a $100\times100\mu m^2$ pattern. On the left we depict the cross-sectional profile of the sample, showing the ridge width $w = 1.4\mu m$ and groove depth 250nm. The step orientation angle β, as well as the step distance s *are indicated.*

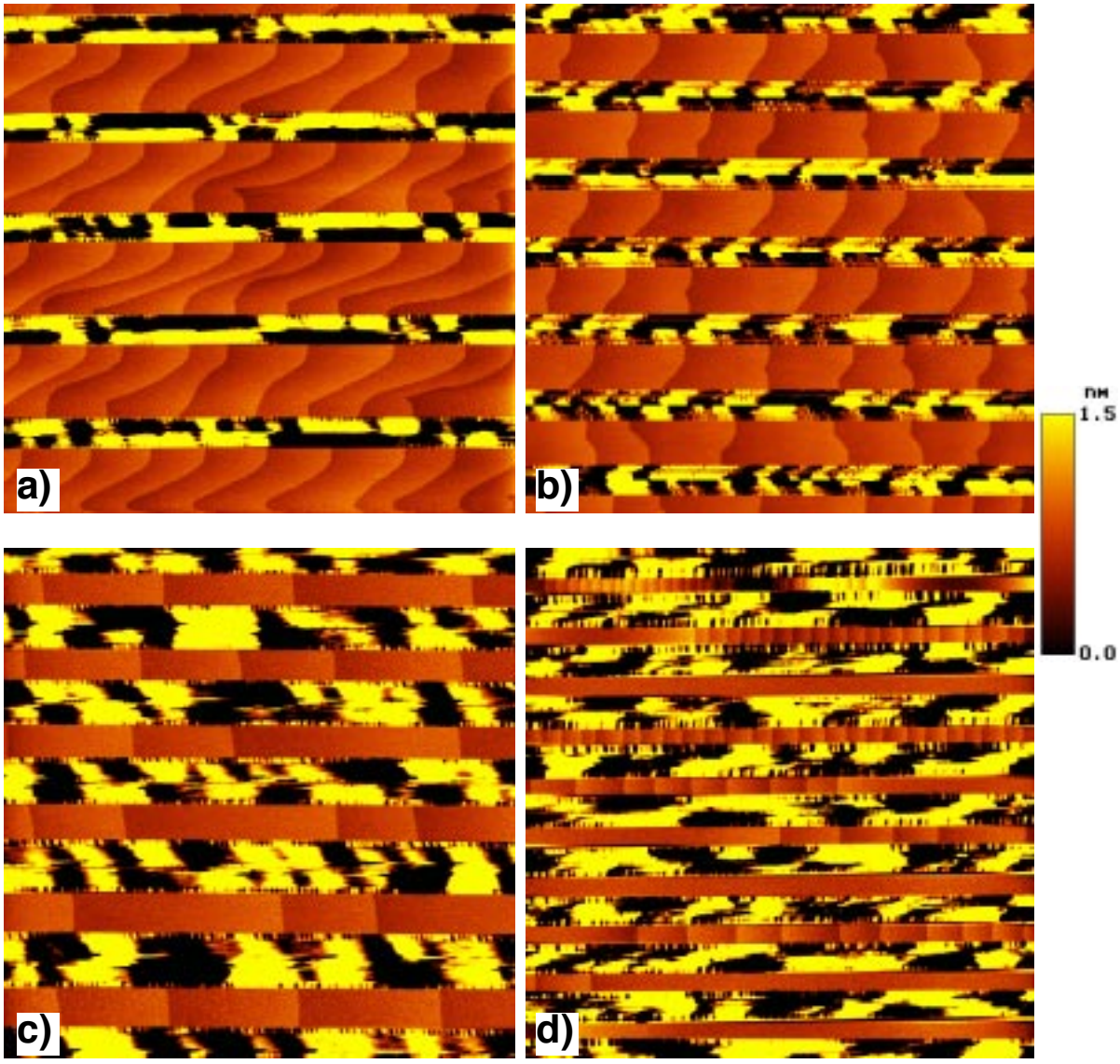

Figure 3.14: Flattened AFM images of the GaAs surface of the same structure as in Figure 3.13, deposited on a GaAs substrate with V-grooves of different pitches : Λ = 2μm (a), Λ = 1.5μm (b), Λ = 1.0μm (c)=, Λ = 0.5μm (d). The first two images are of 10×10μm^2 area and the last two are of 5×5 μm^2 area, all taken in the central region of the 100×100 μm^2 pattern.

In Figure 3.13 the border region between the 2.0μm-pitch corrugated region and the neighboring unpatterned part is shown. Terraces separated by monolayer steps are observable both on the (100) ridges and on the unpatterned region, far away from the groove, where the topography is the same as the one on an unperturbed, infinite surface. The steps exhibit a mean orientation angle ß $\approx 70^\circ$ with respect to the $[01\bar{1}]$ direction and a mean spacing $s = 430$nm, reflecting the average misorientation of the specific substrate (0.04˚). Due to the undulation of the steps, the terrace width can vary between 100 nm and 1500 nm, conforming to the random movement and attachment of the atoms at the surface. At a distance between 750nm and 400nm from the first groove, the surface topography at "infinite" distances does not hold any more and step bunching occurs, with the steps orienting parallel to the groove (ß $\sim 90^\circ$; $s \approx 50$nm). At a

distance smaller than 400nm from the first groove, the steps are more widely spaced and are *perpendicular* to the groove (ß = 0°). Similar step ordering is observed on the (100) ridges between the grooves, as is shown in detail for different values of Λ and *w* in Figure 3.14. In the case of the patterns with Λ = 0.5μm and Λ = 1μm, where every point on the ridge is within a distance of less than 400 nm from the edge of the groove, the steps are almost perfectly straight and perpendicular to the groove. For Λ = 1.5μm, the mean width *w* of the ridge is about 950 nm, and the slope of the steps deviates from perpendicular alignment only in the center of the groove. For Λ = 2.0μm, with *w* ~ 1.4μm, the topography in the center of the ridge is similar to that in the unpatterned region, and the steps are aligned only at the boundaries to the groove. In summary, the steps are *straight* and *perpendicular* to the grooves for ridges narrower than about 800 nm.

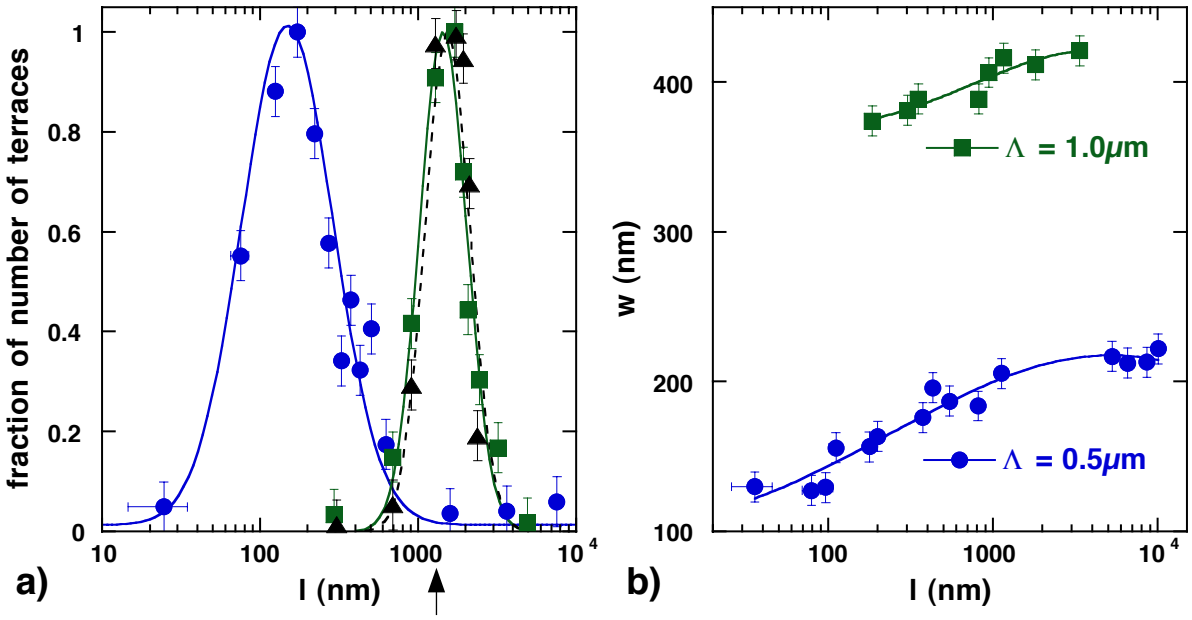

Figure 3.15: a) Normalized terrace length distribution on the (100) ridges, from the patterns of Figure 3.14, for Λ = 0.5μm (circles), Λ = 1.0μm (squares), and Λ = 1.5μm (triangles), measured within a 30×30 μm² surface. The lines are guides to the eye. b) The width w *of the (100) ridge as a function of the terrace length* l *for Λ = 0.5μm (circles) and Λ = 1μm (squares), for the terraces in (a). The lines are guides to the eye.*

In analyzing the step direction, we note that it is *bi-directional* (going up *and* down in the left-to right direction) for Λ = 0.5μm, whereas it is *unidirectional* (going *always* down in the left-to right direction in Figure 3.14) for Λ ≥ 1μm. The distributions of terrace lengths *l*, extracted out of a total surface area of 30×30μm², are shown in Figure 3.15a, for the different pitches (0.5 - 1.5μm). For Λ = 0.5μm we see a high density of short terraces (*l* ~ 150nm), as well as a few terraces of several μm length (*l* ≥ 5μm). For Λ = 1μm and Λ = 1.5μm, the distribution of terrace lengths is much narrower, with average length of 1.4±0.3μm and 1.4±0.3μm, respectively. These values are close to the projection of the mean step spacing *s* of the unpatterned surface along the $[01\bar{1}]$ direction: $s_{[01\bar{1}]} = s/\cos\beta = 1.3 \pm 0.5\mu m$, indicated by an

arrow in the plot. The misorientation towards $[01\bar{1}]$ is only 0.010°±0.002°, which is only a quarter of the misorientation of the initial surface. For $\Lambda = 2\mu$m, we can study the crossover to an infinite ridge, where the topography inside the ridge is similar to that of the unpatterned surface, and step alignment and wide spacing is achieved only near the boundary to the groove. The broader and bi-directional step distribution in the case $\Lambda = 0.5\mu$m is due to the fact that for this pitch the original epi-ready surface on the ridges is completely etched away.

Finally, we analyzed the ridge width, which is defined (within < 10nm) by the boundaries to the {311}A surfaces on both sides. We found that there is a fluctuation in width of up to 10% between different stripes, which is presumably due to fluctuations in the substrate patterning. Within one stripe almost no width fluctuations along the ridges were found for $\Lambda = 1.5\mu$m and $\Lambda = 2\mu$m; the average widths being 0.95μm and 1.4μm, respectively. For $\Lambda = 0.5\mu$m and $\Lambda = 1\mu$m, the ridge width increases with the terrace length (Figure 3.15 b). For $\Lambda = 0.5$μm, the width changes from about 120nm for short terraces ($l \leq 100$nm) and high step density, to about 220nm for long terraces ($l \geq 5\mu$m) and low step density. For $\Lambda = 1$μm, the narrower length distribution results in a smaller range of terraces widths variations (380 to 420nm). The width of the {311}A facets neighboring the (100) ridge changes in a complementary way, decreasing for increasing (100) ridge width.

We explain these observations by assuming that crystal growth proceeds by adsorption of atoms or molecules on the (100) terraces, followed by random surface diffusion until an attachment to a step is accomplished (step-flow growth mode). Incorporation into the crystal can occur either at the boundary step separating the (100) and the {311}A facets or at the monolayer steps between (100) terraces. Hence, about a diffusion length away from this boundary, only adatoms moving parallel to the groove edge contribute to the growth of the flowing steps, which results in the step alignment normal to the boundary.

3.3.3 Sidewalls morphology

We have seen in Figure 3.11 and Figure 3.12 that the sidewalls of the groove present long range (μm-scale) height fluctuations along the groove of about 5-10nm, due likely to the etching process before growth. However, Figure 3.12 shows also a corrugation structure on these planes in the direction perpendicular to the groove axis. Since small height variations exactly perpendicular to the scanning direction are lost in the AFM image processing, to fully account for this sidewall structure, with steps elongated along the groove, we have to consider images scanned perpendicular to the groove, i.e., in the [011] direction.

Figure 3.16 displays such an image, for the sample shown on the right side of Figure 3.12 (GaAs at 750°C on a 3μm-pitch V groove). The scan is taken only on the sidewall area, with a constant average inclination to the horizontal. This inclination can be easily subtracted from the image, thus obtaining a projection of the sidewall on the (100) plane (see schematics on the left), and preserving fully the nm-size structure perpendicularly to the groove. An irregular array of

corrugations can be seen, all running parallel to the groove axis, and with height variations in the range ~2 to ~10nm. This structure is consistent with the step bunching observed in cross-sectional TEM in Section 2.2.1, even if with somewhat more marked corrugations, due possibly to the growth termination and cool down. Note that this step bunching is the normal growth mode of planar GaAs OMCVD with TEGa and AsH_3 on planar (111)A substrates, misoriented both in the [$\bar{2}$11] and in the [100] direction [84]. However, in the planar [100]-misoriented case, corrugations similar to those reported here are observed at temperatures as low as 520°C, while at 720°C a zigzag step pattern emerges [84]. In our case, a marked step bunching is visible only on GaAs layer grown at high temperature, due possibly to the different precursor set used here.

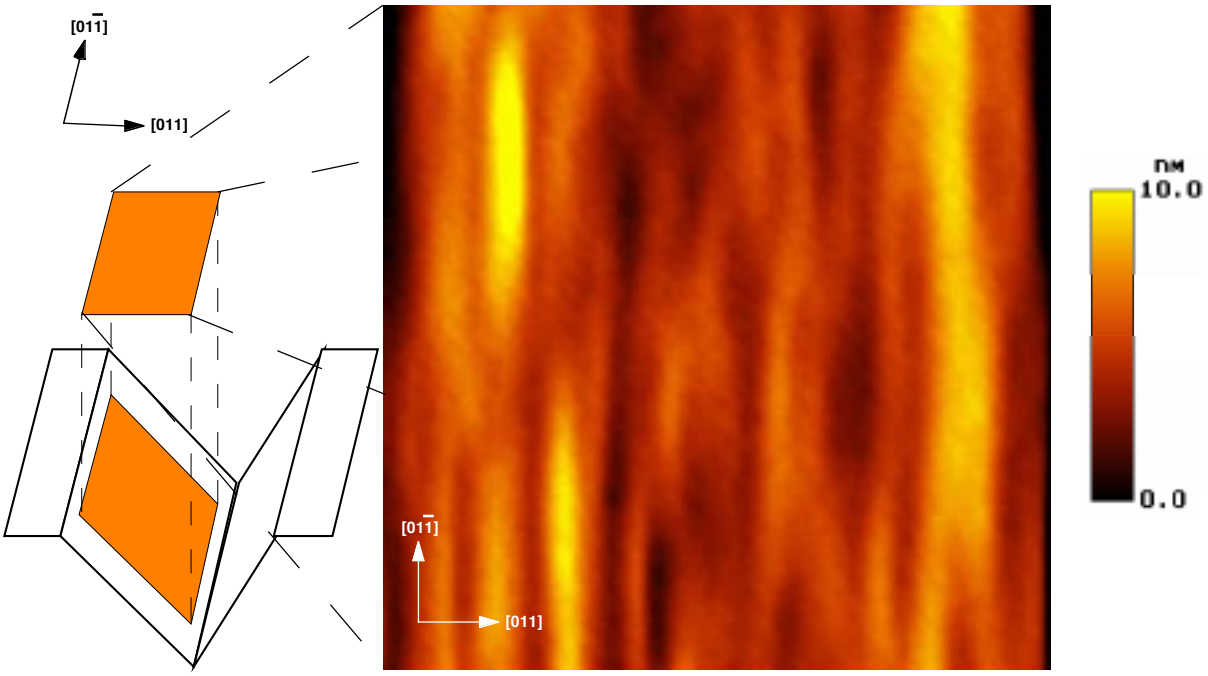

Figure 3.16: 1×1μm² AFM image (scanned normal to the groove axis) of part of the sidewall plane, from the sample of Figure 3.12 (right). The schematics on the left show the region corresponding to the scanned area, in the V groove structure.

3.3.4 Morphology at the bottom of the grooves: {311}A facets

We have seen above that the bottom of the groove presents a faceted profile, composed of two {311}A planes surrounding a central (100) facet. We investigated further the three-dimensional structure of these facets by AFM observations of the top surface of samples consisting of self-limiting AlGaAs layers, grown on 3μm-pitch substrates, on which GaAs films of increasing nominal thickness t (0 to 100nm) were deposited. We selected a growth temperature of 750°C and a nominal Al mole fraction of 0.2, since under these conditions (high T and low x) the AlGaAs profiles become wider than the lateral resolution of the AFM (see Section 2.3.3.1). This allows observations of even the narrow profile of the AlGaAs surface, at least for the {311}A facets.

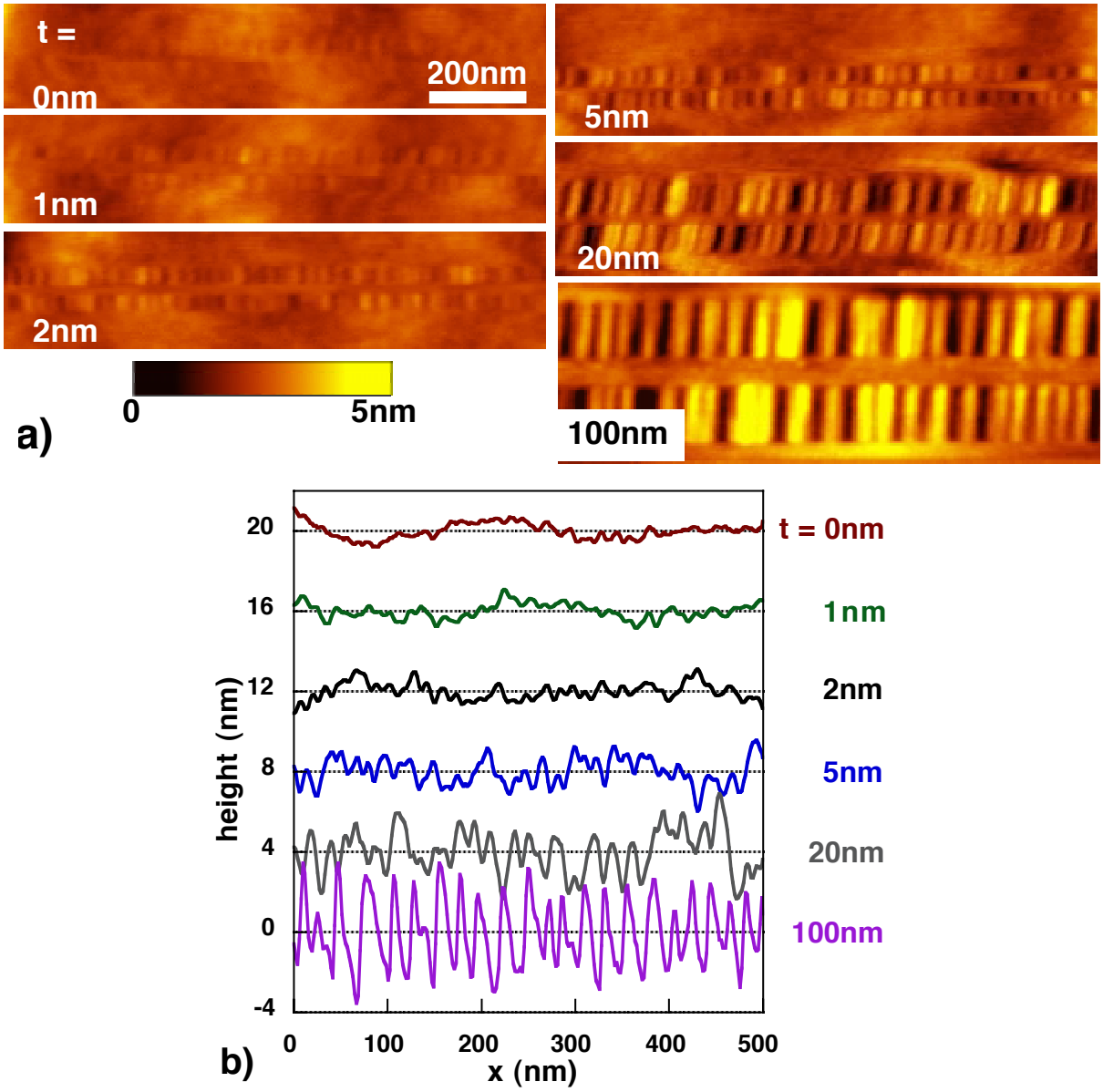

Figure 3.17: a): Flattened AFM scans along the bottom of a V groove of surface GaAs/$Al_{0.2}Ga_{0.8}As$ heterostructures, grown at 750°C, with GaAs thicknesses ranging between 0 and 100nm. b): Line scans along the {311}A facets, from the images in part (a).

In Figure 3.17a, we show a series of flattened AFM scans of the bottom of a V-groove of six different samples with surface GaAs layers of t increasing from 0 to 100nm. The long range fluctuations (typical period ~0.5-1μm), due to lithographic imperfections, are visible both on the sidewalls and on the {311}A planes. Representative AFM line scans along the {311}A facets for all six samples are shown in part (b). In the first two samples ($t \leq$ 1nm) the (100) and {311}A planes are barely distinguishable from the surrounding sidewall, and the {311}A height profile is dominated by the long range fluctuations. However, as t increases, the {311}A facets develop quasi-periodic height modulations due to step bunching (that are hardly visible for $t \leq$ 1nm), whose height and period increase with increasing t. Note that the central (100) facet is flatter, showing evidence for ML steps (at least for sufficiently large t, when it becomes clearly visible), as will be discussed below.

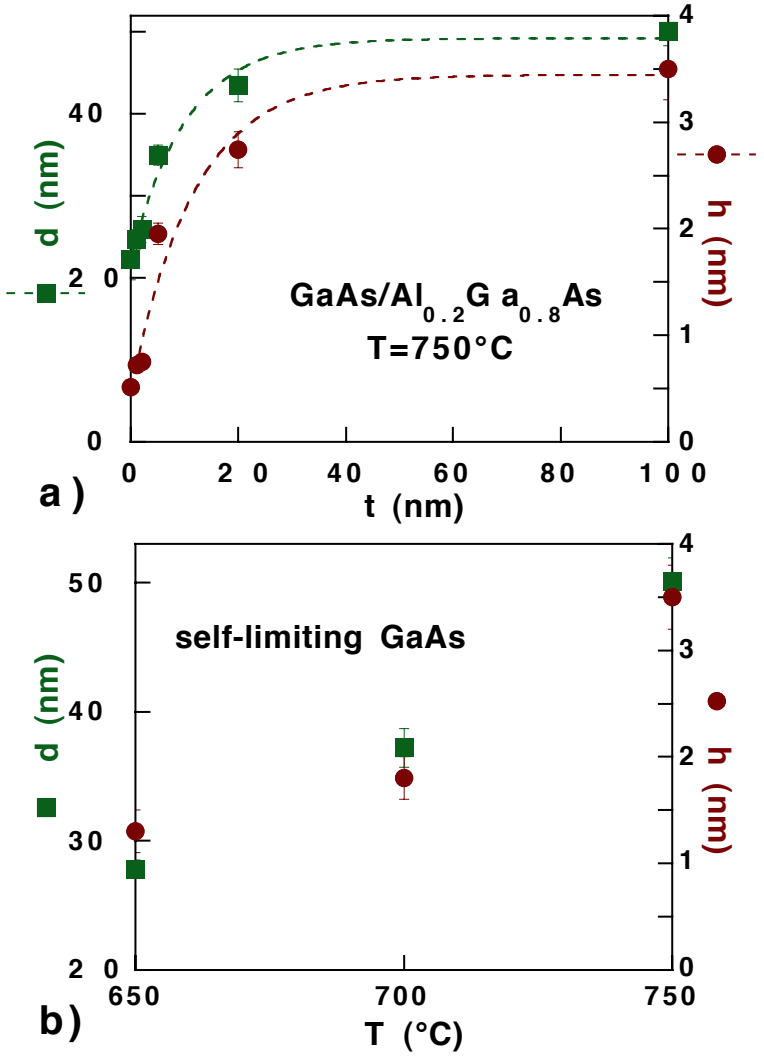

Figure 3.18: a) Average period d *(squares) and height* h *(circles) of the {311}A step bunching, as a function of the GaAs thickness* t*, for the samples of Figure 3.17. b) Average* d *and* h *for self-limiting GaAs profiles, as a function of the growth temperature* T.

The evolution of the period d and the height h of the {311}A step bunching for the samples of Figure 3.17 is shown in Figure 3.18a, as a function of t. The saturation of d at a value d_{sat} with increasing thickness follows the same trend as the cross-sectional width of the {311}A facets l_{311} (see Section 2.3.2). By fitting the saturation curves with exponential functions (eq. (2.2)), we find characteristic recovery thicknesses τ of 10.4±0.1nm for d and 11.8±1.7nm for h. Therefore, this recovery takes place on the same thickness scale as for l_{311}, indicating a strong correlation of the facet width with its step morphology along the groove. Similarly, both l_{311} and d_{sat} of self-limiting GaAs increase as a function of T. In particular, as shown in Figure 3.18b, d_{sat} ranges between 27.8±0.7nm at T_s=650°C and 50.1±1.8nm at T_s=750°C.

As seen in Section 3.2.2, step bunching has been already observed in OMCVD of *planar* GaAs (311)A [93] (and confirmed on our (311)A control samples), and has been attributed to the minimization of the (311)A surface energy via the formation of an array of $(\bar{2}33)$ microfacets. The similarity of the corrugations, and of the evolution of their period as a function

of the GaAs thickness and of the temperature in the planar [93] and nonplanar case, suggest that the same phenomenon is taking place in both situations. In both cases, the diffusion length of the growth species (higher for Ga than for Al) is limiting the periodicity and height of the steps. In the nonplanar case, the development of {311}A step bunching with a characteristic period and amplitude is achieved together with the stabilization in the width of the (100) and {311}A facets. The self-limiting lateral size of these facets also depends on the diffusion length of the group III species, increasing with decreasing Al mole fraction and increasing T (see Section 2.3.3.1). The group III diffusion length appears to determine the surface curvature at the bottom of the V groove, via the lengths of the (100) and {311}A facets, with wider facets obtained for a longer diffusion length. Thus, the three-dimensional self limiting surface profile of AlGaAs (and GaAs), including the step bunching on the {311}A facets, may be explained by a diffusion-limited minimization of the surface energy.

Note however that the period of step bunching in our V-groove samples is generally smaller than the one observed in Ref. [93] (and on our (311)A reference samples), and that the V-groove step alignment and periodicity are much more regular. For example, step bifurcations, that are typical in planar (311)A samples like in Figure 3.8, were never observed in the nonplanar case. This alignment of the step bunches is similar to the monolayer step alignment observed on the (100) ridges between two adjacent grooves, described above. The better alignment is possibly related to the presence of regular boundaries near the facets along the $[01\bar{1}]$ direction, which limits their lateral extension to sizes lower than, or comparable to, the diffusion length of the growth species.

3.3.5 Morphology at the bottom of the grooves: (100) facets

The morphology of the (100) facet at the bottom of the groove is difficult to study, due to its narrow width, as compared with the AFM tip. As can be seen in Figure 3.17a, this facet can be identified unequivocally only on thick enough GaAs layers grown at high temperature (≥700°C). The discussion of the (100) surface morphology will be therefore limited only to these restricted situations, though some conclusions can be extrapolated to narrower profiles, where surface diffusion is smaller. In the plot of Figure 3.11, the bottom (100) facet appears to be much smoother than the surrounding facets, with some influence of the sidewall roughness on the profile. We will address this issue in more detail below.

Figure 3.19 shows a flattened AFM image of the bottom region of the last sample shown in Figure 3.17a (self-limiting GaAs grown at 750°C), but on a longer range ($3\times1.3\mu m^2$). The apparent slant of the {311}A facets is an artifact of the AFM image, due to the difficulty of finding a reference plane at the bottom of a ~2μm-deep groove. The bottom of the figure shows line scans of the bottom (100) and of the two surrounding sidewalls. The sidewall line scans have been displaced vertically from the (100) one for clarity.

As seen above, both sidewall planes present random height fluctuations, due to lithographic imperfections, which are of the order of 10-15nm on the 3μm range of the plot.

The height profiles of the two planes are in general not correlated, due to the randomness of the lithography-induced roughness. Only in one region, at $x \cong 0.7\mu$m in the plot, both sidewalls present a valley of about 5-10nm. The central (100) facet is much smoother than the surrounding planes, and the sidewall roughness is mostly washed out. In particular, one can notice the formation of *ML-high steps* at the positions indicated by the arrows. When both sidewalls present a valley, the sidewall profile is only weakly reflected at the central plane, where a dip is formed, corresponding to a bunching of about 5ML steps. On the right side of the dip, a domain at least 2μm long is formed, which is flat on the ML scale.

Figure 3.20 shows a flattened AFM image of the bottom region of a self-limiting GaAs layer grown on an $Al_{0.45}Ga_{0.55}As$ buffer at 700°C. As can be seen in the plot below, the roughness of the two sidewall planes is in this particular case much more correlated than in the previous example. A hill-and-valley structure, with a height difference of about 10nm and a period of about 1.5μm is visible on both sidewall planes. These height fluctuations propagate much more effectively than before onto the bottom (100) facet, where they are about 5nm high. Some evidence for ML-high steps can be inferred from the (100) line scan in the central region.

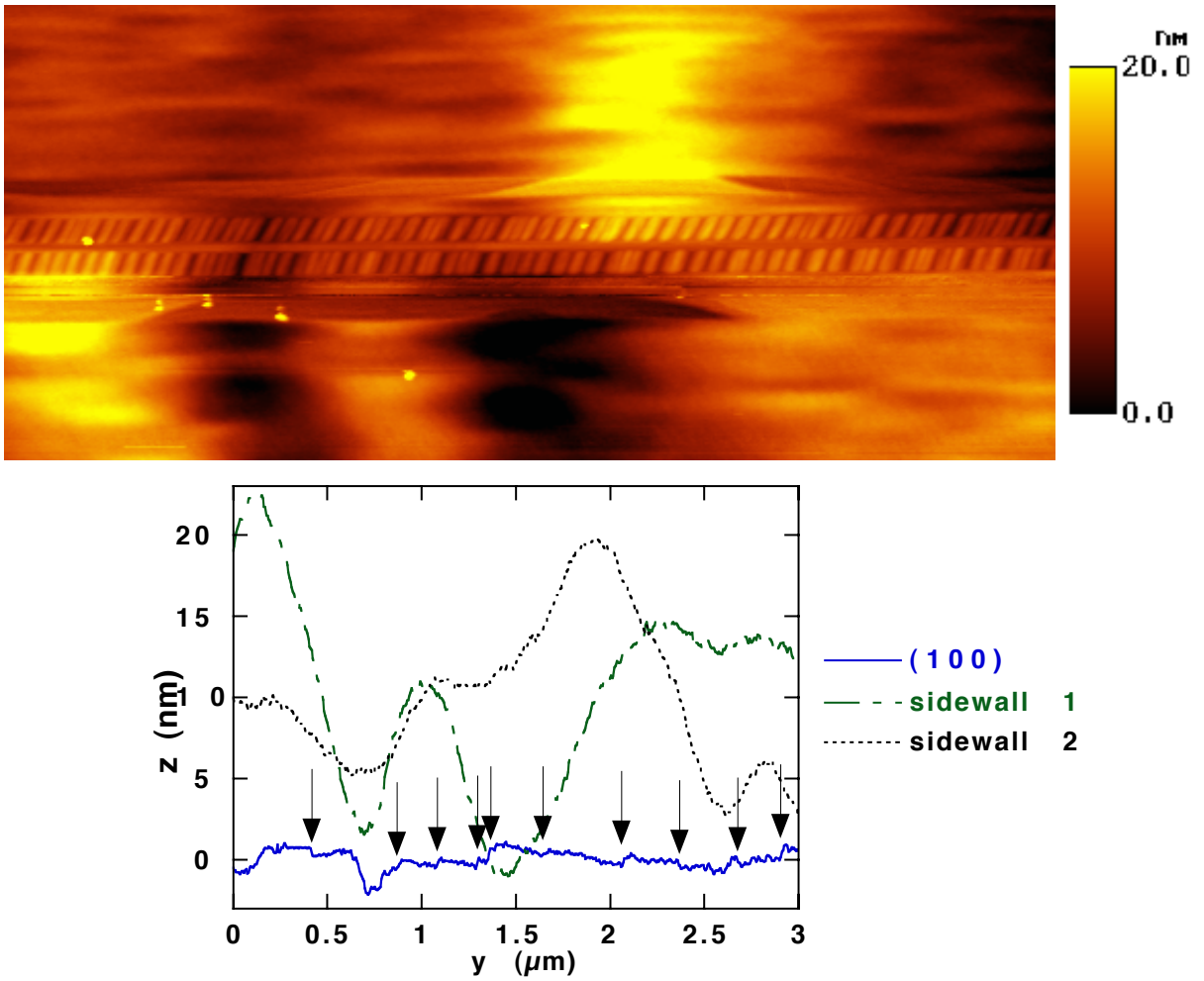

Figure 3.19: Top: Flattened 3×1.3μm² AFM image at the bottom of a 3μm groove of the last sample of Figure 3.17a. Bottom: line scans along the groove of the bottom (100) facet and of the two sidewall planes. Arrows indicate steps of ML height.

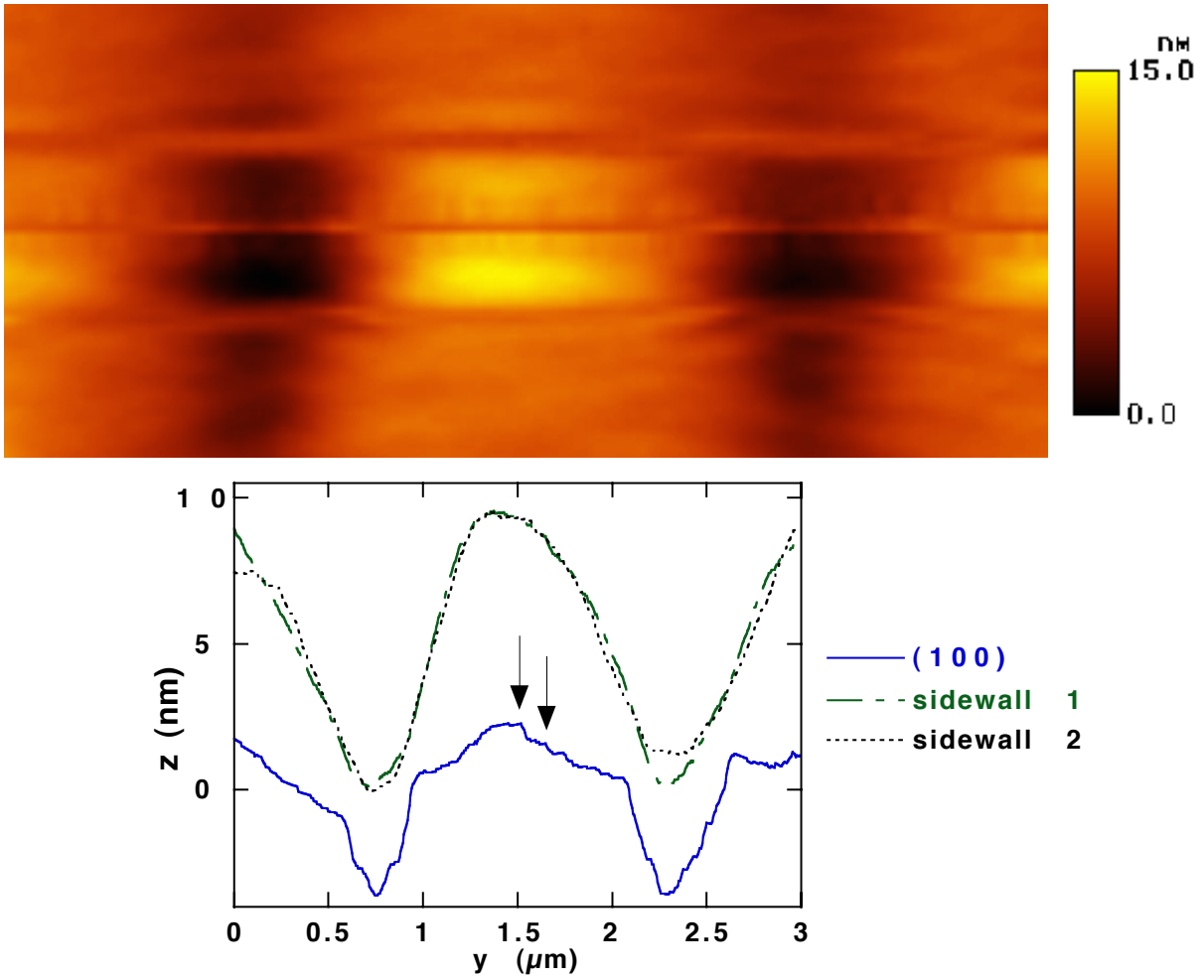

Figure 3.20: Top: Flattened 3×1.3μm² AFM image at the bottom of a 3μm groove of a self-limiting GaAs surface grown at 700°C. Bottom: line scans along the groove of the bottom (100) facet and of the two sidewall planes. Arrows indicate steps of ML height.

The marked difference between the (100) profiles of the two samples above can be ascribed to the difference of surface diffusion in the two cases. As we will see in Chapter 5, capillarity effects tend to smoothen out the corrugations of a nonplanar profile [109]. This smoothening process is limited by the surface diffusion length. We will see in the same chapter how capillarity *across* the grooves is at the base of self-limiting growth on nonplanar substrates. However, since the profile presents corrugations also *along* the groove (though much smaller than in the perpendicular orientation), capillarity can smoothen the profiles also in this direction. Since in all the images shown above the sidewall height fluctuations are damped in the bottom (100) facets, the diffusion length on these planes should be higher than on the sidewalls. This observation will be confirmed independently in Chapter 5.

The effects of surface diffusion on the (100) profile are sketched schematically in Figure 3.21. The schematics on the left represent top views of a V groove (with the groove axis y running horizontally) composed, for simplicity, only of two sidewalls surrounding a central bottom facet. Solid lines are contour lines. Areas enclosed by the contour lines are marked by different grayscale levels, with lighter levels corresponding to higher areas. On the right of each

schematics, we show the cross sectional height profiles along the grooves, corresponding to each facet. In each case, height variations along the groove have been introduced on each facet: both sidewalls have a valley at the center of the diagram. In figure (a), this valley propagates without any damping onto the bottom facet, that therefore has the same height profile as the sidewalls. This is the situation corresponding to a negligible surface diffusion on the bottom facet, where the corrugated profile can not be smoothened out. In figure (b), the same height profile is present on the sidewalls, but in this case it is completely smoothened out in the bottom facet by surface diffusion. Note that the intersection between the sidewalls and the bottom is completely straight for case (a), while it follows the sidewall contour lines in case (b). These are two ideal, extremal cases in which the sidewall corrugations are completely correlated, and surface diffusion is either negligible or capable of completely smoothening out the bottom profile. The cases in which both sidewalls present a hill at the same position can be easily deduced from the discussion and the schematics discussed here.

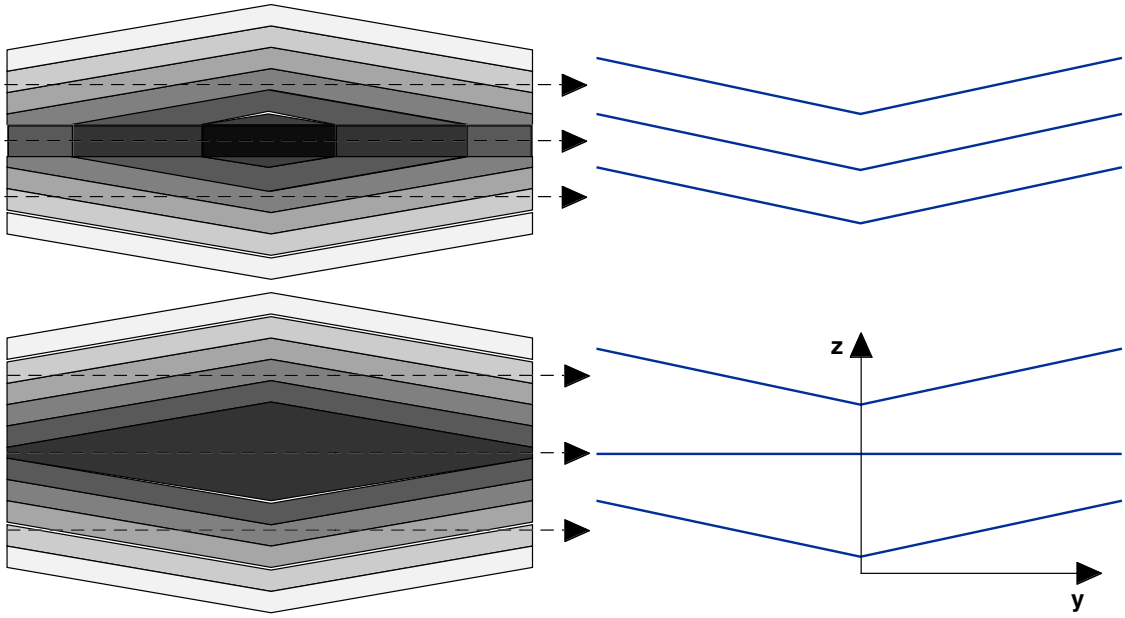

*Figure 3.21: Left: top projections of a V groove, formed by two sidewalls and a central bottom facet. The axis of the groove (*y*) runs horizontally on the plane of the page. Height fluctuations (not to scale) are present along the groove axis. Different grayscale levels represent zones with the same vertical coordinate* z *(in the growth direction). Cross sections of the profiles, along the groove axis, are shown on the right for the sidewalls and the bottom facet. a): Both sidewalls present a valley, that propagates without attenuation onto the bottom facet. b): The same situation, but the sidewall height fluctuations are completely damped in the bottom facet.*

The AFM images above show that real profiles have in all cases a less marked character than in the extremal cases presented schematically. GaAs growth at 700°C (Figure 3.20) shows that, even if the sidewall profiles are completely correlated, the bottom profile is somewhat smoother, due to surface diffusion. The degree of smoothening increases for $T = 750$°C, where the surface diffusion length is higher, as in Figure 3.19. In this case, at the point where both sidewalls have a valley, the height of this valley is reduced to about 1.5nm at the bottom, compared with the ~10nm on the sidewalls. A careful look at the AFM image shows that, in

agreement with the schematics of Figure 3.21b, the bottom (100) facet is about 20% wider on the hill than on the surrounding areas. This difference in width is negligible for the sample in Figure 3.20, where the sidewalls height profile is more conserved at the bottom. When the corrugations on the sidewalls are uncorrelated, as for most of the profile in Figure 3.19, the bottom profile is smooth at the ML level. This smoothness is only partially due to a washing out of the sidewall corrugations, since the bottom profile is much smoother than the average profile of the two sidewalls. Therefore, the formation of ML steps is essentially due to the smoothening effects of surface diffusion along the groove. Note that the long-range roughness of the {311}A facets is intermediate between the ones on the sidewalls and on the (100) (Figure 3.11). Therefore, partial smoothening due to diffusion is present also on these facets.

The observations above, valid for thick GaAs at $T \geq 700$°C, can provide some indirect informations on the morphology of GaAs/$Al_xGa_{1-x}As$ QWRs, where AFM observations along the groove are not possible, due to the narrowness of the profiles. Since the bottom facets become smoother as the surface diffusion increases, we expect AlGaAs bottom profiles to be more influenced by the sidewall height fluctuations. Evidence in this sense is provided by measuring the RMS roughness along the groove in the bottom facets of the last three samples shown in Figure 3.17 (GaAs/$Al_{0.2}Ga_{0.8}As$ layers grown at 750°C). This roughness, measured on 2μm- and 3μm-long scans, increases from 0.9±0.1nm to 1.2±0.2nm to 2.1±0.3nm for GaAs thicknesses of 100nm, 20nm and 5nm, respectively. The (100) facet is too small to be measured reliably for lower GaAs thicknesses, while the sidewall roughness is about the same for the whole series of samples shown in Figure 3.17 (~3nm). Self-limiting $Al_{0.2}Ga_{0.8}As$ profiles grown at 750°C should have therefore a RMS roughness between 2 and 3nm. This roughness should increase with decreasing T and increasing x, but further quantification is not possible at present.

3.4 Summary

In this chapter, we have analyzed the surface structure of planar and nonplanar GaAs/AlGaAs epitaxy, using atomic force microscopy. Planar (100) and (311)A layers are found to exhibit the same morphology as commonly observed in OMCVD growth, with surface diffusion playing a fundamental role in determining the step structure of these surfaces. (100) epitaxy takes place via ML-step flow growth, while step bunching is observed on (311)A surfaces. Facets with the same orientations, present at the extremal regions of corrugated samples, exhibit a modified step structure, with respect to planar samples. This ML step ordering is due to a modification of surface diffusion, when the facet width becomes comparable to, or lower than, the surface diffusion length. In particular, ML steps present on the (100) ridges tend to align perpendicularly to the grooves near the groove edge. Step bunching on the bottom {311}A facets is directly correlated to the evolution of the facet cross–sectional width, thus suggesting a fully three-dimensional self-ordering process in this region. Long-range (on the μm scale) height fluctuations are present on all the facets composing the groove, due to

lithographic imperfections. However, surface diffusion along the groove is effective in smoothening out these fluctuations in the bottom region. As a result, ML-smooth domains are formed on the bottom (100) facets, which can be up to several μm long in the most favorable conditions.

The roughness at the bottom of the groove has a potential impact on the confinement properties of the QWRs, since it results in longitudinal variations of the potential well of the wires and of the energies of the confined 1D states. These variations are responsible for inhomogeneous broadening of the PL and PLE linewidths, and give rise to a Stokes shift between the luminescence and the absorption spectra [110]. In GaAs/$Al_{0.3}Ga_{0.7}As$ QWRs grown at 680°C, the low-temperature (8K) PLE linewidth was measured to vary between 3.7 and 12.0meV, for nominal wire thicknesses ranging between 1.5 and 5nm [111]. Similarly, the Stokes shift varied between 3.6 and 8.5meV. The small PLE linewidths and Stokes shifts attest the high quality of these wires. In particular, the PLE linewidths were always smaller than the separations between the lowest-energy transitions (15 to 26meV for thicknesses from 5nm to 1.5nm, respectively) [111], allowing therefore the observation of 1D-confinement features. The potential variations along the wire axis is also able to quantum confine excitons into QD-like structures, corresponding to the monolayer-smooth domains described earlier. This additional confinement gives rise to a splitting of the QWR PL line into very narrow (<200μeV) lines, observable at low laser power densities ($\lesssim$2000W/cm^2) through small apertures ($\lesssim 2\mu$m) realized on a metal layer coating on the sample surface [112].

From the discussion above, it appears clear that a further improvement of the QWR uniformity would be beneficial for the observation of the 1D confinement properties. Since the primary source of roughness along the grooves is the substrate preparation, an optimization of this process would be the most important step towards a better uniformity of the profile. An alternative to conventional etching in a H_2SO_4:H_2O_2:H_2O solution is to use a Br_2-methanol etching through a SiO_2 mask. Preliminary AFM measurements on planarized surfaces of samples grown on a 0.5μm-pitch substrate etched with this method showed a reduced surface roughness, which is comparable to that of epi-ready (100) wafers). The nonplanar profiles can be further smoothened out during the heat-up process in the OMCVD reactor prior to growth. The mass transport during this phase tends to flatten the profile in the directions parallel and perpendicular to the grooves. This process depends drastically on the heat-up parameters, such as temperature, AsH_3 partial pressure and heat-up time. Therefore optimum conditions should be found, for which a significant smoothing of the ~10nm roughness along the groove is achieved, without affecting significantly the ~100nm-μm high V-shaped profile.

Chapter 4

Self-ordering of alloys

In addition to the *geometrical* self-ordering, illustrated in Chapter 2, OMCVD growth of AlGaAs alloys yields also a *compositional* self-ordering, since each self-limited facet composing the bottom of the groove is characterized by a peculiar composition [113]. Since these facets are more Ga-rich than the surrounding sidewalls, the resulting vertical planes, with an overall width in the 10-20nm range, have been termed *vertical quantum wells* (VQWs) [114, 115]. The Ga segregation in the VQWs, visible in TEM and SEM cross sections [114-118]. has been quantified by PL and CL techniques [88, 114-118].

Several groups found evidence for lateral quantum confinement in the VQWs. Polarization anisotropy was found in PL spectra [115], and its dependence on the nominal Al mole fraction and growth conditions was studied. More recently, optical anisotropy was observed in polarized PL excitation spectra, with evidence for interband transitions, revealing several electron and hole subbands [88]. Intersubband absorption at normal incidence (with respect to the wafer plane) was also found in n-doped VQWs [118]. Lasing was observed in VQW laser diodes, with output laser beams polarized in the VQW planes; this gain anisotropy was as well attributed to lateral confinement [119]. Finally, recent time-resolved PL measurements pointed out that the temperature dependence of the VQW radiative lifetime could be attributed to the two-dimensionality of excitons in the wells [120]. The role of the VQW confinement properties has been recognized in promoting carrier capture into GaAs quantum wires forming at the bottom of the V grooves [114, 116, 121].

In this chapter, we present a systematic study of the structural properties and of the formation mechanisms of self-ordered AlGaAs VQWs grown by LP-OMCVD on V-grooved substrates. Section 4.1, describes the principles of cross-sectional AFM measurements in air of GaAs/$Al_xGa_{1-x}As$ heterostructures, based on the composition-dependent oxide growth rates on the cleaved edges of the sample. This technique, together with energy loss spectroscopy (EELS), PL and chatodoluminescence (CL), is applied in Section 4.2.2 to measure the Ga segregation in the VQWs. TEM cross sections evidence the formation of a fine structure in the VQW; in Section 4.2.3 we study its geometrical features, as a function of the nominal Al mole fraction x and of the growth temperature T. Finally, in Section 4.2.4, we show that the Ga

segregation in the VQWs follows the same segregation model, originally proposed by McLean [122], that applies to phenomena such as segregation to surfaces [123] and grain boundaries [122].

4.1 Cross sectional atomic force microscopy of semiconductor heterostructures

Scanning probe microscopy (SPM) techniques have been extensively used to investigate the chemical composition of surfaces with lateral resolution down to the atomic level. Chemical composition imaging of cleaved semiconductor surfaces with atomic resolution has been achieved with scanning tunneling microscopy (STM) performed under ultrahigh vacuum (UHV) conditions [124]. In that case, the chemical identification is directly provided by the tunneling process between the scanning probe tip and the different atomic species. These techniques necessitate expensive UHV equipment and require more careful SPM techniques, as compared with SPM in air.

In the case of SPM in air, the exposure of the surface to air leads to chemical reactions, especially with molecular oxygen, which complicates the interpretation of tunneling spectroscopy [125]. Although the reaction of oxygen with clean III-V semiconductor surfaces has been extensively studied using surface sensitive techniques [126], there is only little knowledge about the structure of these surfaces under ambient conditions and the nature of the oxide growth in reactive AlGaAs compounds. The generalization of SPM to these non-ideal surfaces is important for applications in device fabrication processes. AFM under ambient conditions is the ideal tool for such studies, because of its insensitivity to the detailed electronic structure of the scanned surface and its rapid application, without a need for complicated sample preparation steps.

We have studied the growth of native oxides on the cleaved $(01\bar{1})$ surface of GaAs and $Al_xGa_{1-x}As$ layers with well-known Al mole fractions x, using the AFM to measure the height profiles at constant force. We will show in the rest of this section that the oxide growth follows the mechanism introduced by Cabrera and Mott for metal surfaces, and that the layer composition can be quantified by measuring the oxide height, after a proper calibration.

4.1.1 Experimental technique

Two calibration samples were grown on planar (100) GaAs substrates for the purpose of studying the oxide growth on the cleaved edge. The first was grown by Chemical Beam Epitaxy and consisted of a stack of 20 pairs of 65 nm-thick GaAs layers and 69 nm-thick $Ga_{0.5}In_{0.5}P$ layer. The second was grown by OMCVD and was composed of nine layers of $Al_xGa_{1-x}As$, with composition x ranging from 0.12 to 0.72 and thickness of 85-260 nm, separated by 75 nm thick GaAs spacers. The Al mole fractions were inferred from growth rate calibrations of the MFCs and verified by X-ray diffraction measurements.

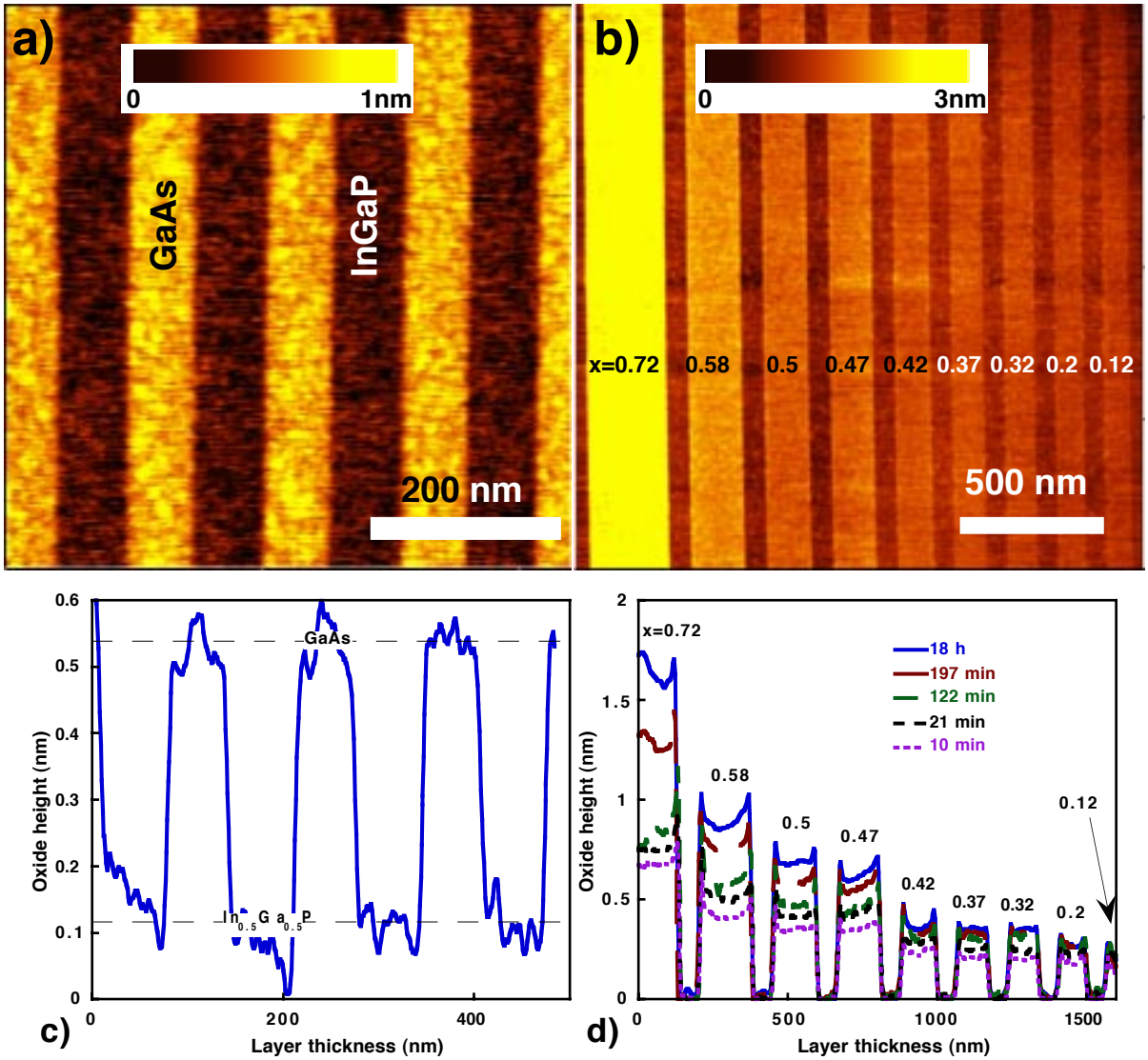

Figure 4.1: a): AFM topographical image of the cleaved $(01\bar{1})$ surface of a GaAs/$Ga_{0.5}In_{0.5}P$ (65nm/69nm) heterostructure after 18 h of oxidation, taken at constant force in contact mode. b): AFM height image of the cleaved $(01\bar{1})$ surface of a $Al_xGa_{1-x}As$/GaAs heterostructure after 18 h of oxidation, taken at constant force in contact mode. Nine layers of $Al_xGa_{1-x}As$ with increasing Al mole fraction x and thickness are embedded between GaAs layers of a nominal thickness of 75nm. c) Line scan from Figure 4.1a, showing the oxide height difference between GaAs and $In_{0.5}Ga_{0.5}P$. d) Line scans from the sample of Figure 4.1c, taken at different oxidation times. The oxide height increases as the oxidation time and the Al mole fraction increase.

The samples were cleaved in air and at room temperature, then mounted vertically in a specially designed AFM holder. The edge region of the cleaved surface was scanned with a silicon tip in tapping mode at a constant force in the range of 10^{-10}N (see Section 3.1). The surface was exposed to air for a period varying between several minutes and several weeks prior to investigation by AFM.

4.1.2 Experimental results

AFM images of both samples after 18 h of oxidation are shown in Figure 4.1a and b. In the image of the $Ga_{0.5}In_{0.5}P$/GaAs heterostructures (Figure 4.1a), the oxidized GaAs layers appear

as lighter (higher) than the intermediate $Ga_{0.5}In_{0.5}P$ layers. Figure 4.1b shows that the oxidized $Al_xGa_{1-x}As$ layers stick higher than the neighboring GaAs layers, by an amount that increases with the Al mole fraction *x*. Figure 4.1c shows a line scan of the $In_{0.5}In_{0.5}P$/GaAs heterostructure from Figure 4.1a. The difference in the oxide height between the GaAs and the $Ga_{0.5}In_{0.5}P$ layers is about 0.5nm after an oxidation time of 18h. Figure 4.1d shows a series of line scans of the $Al_xGa_{1-x}As$/GaAs heterostructure from Figure 4.1b, for oxidation times ranging between 10min and 18h. The difference between the $Al_xGa_{1-x}As$ and GaAs oxide heights increases with increasing exposure. For the highest Al mole fraction, this difference increases by about a factor 2.5 between the shortest and the longest oxidation times.

For high Al mole fractions and large exposure times, the height profiles show fluctuations that could be due to inhomogeneities in the oxidation process for the corresponding Al concentrations, or to Al clustering [124]. The roughness of the $Al_xGa_{1-x}As$ oxide surface is similar to the roughness of the GaAs oxide surface for *x* up to 0.5, and then slowly increases with increasing *x*. In the extreme case of an 80nm-thick pure AlAs layer embedded in GaAs, we observed extremely fast oxide formation, resulting in a rough (RMS~ 3nm after 5min), high (30nm height after 5 min, 200nm after a day) and broad (150nm) oxide region, which is presumably the result of three dimensional growth of porous oxide. Due to lateral oxide growth above the neighboring GaAs region, the dimensions of the original AlAs layer could not be precisely deduced from the resulting height profile of the AlAs oxide.

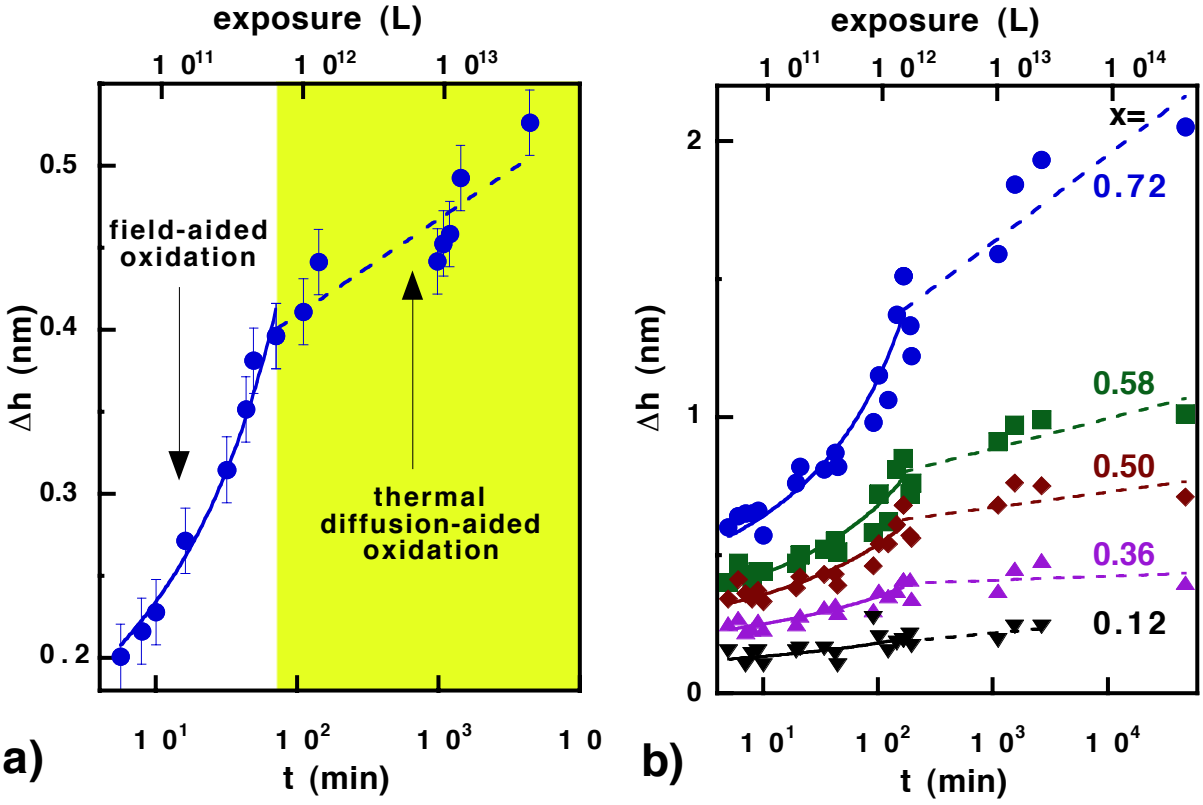

Figure 4.2: a): Mean height difference between oxidized GaAs and $Ga_{0.5}In_{0.5}P$ as a function of exposure time in air, for the sample in Figure 4.1a. b) the same between $Al_xGa_{1-x}As$ and GaAs, for selected values of x, for the sample of Figure 4.2b.

We studied the evolution of the height profile for both samples, as a function of exposure time in air. In Figure 4.2a we plot the mean height difference between GaAs and $Ga_{0.5}In_{0.5}P$ as a function of time after cleavage, for the sample in Figure 4.1a. The height difference increases quickly from an initial value of 0.2nm four minutes after the cleave, up to a nearly saturated difference of about 0.5 nm, after periods of the order of 10 hours. The same results were obtained for dark as well as for normal light conditions. The upper abscissa indicates the oxygen exposure, which was calibrated to be about 10^{10} L per minute of exposure to air, at atmospheric pressure (≅ 1bar). In Figure 4.2b we plot the mean height difference between $Al_xGa_{1-x}As$ and GaAs as a function of time after cleavage, for the sample in Figure 4.1b, in $Al_xGa_{1-x}As$ layers with selected values of *x*. As for the GaAs/$Ga_{0.5}In_{0.5}P$ oxidation, this difference increases with time, at a rate that is faster for exposures until about 10^{12} L, and then appears to slow down for higher exposures.

4.1.3 Oxidation mechanisms

The mechanism of oxidation of a (011) GaAs surface was extensively investigated [126-128] and was explained by the formation of a protective layer on top of the cleaved surface, consisting of elemental arsenic and Ga_2O_3 [129], which acts as a diffusion barrier. Three main oxidation phases were identified on cleaved III-V semiconductor surfaces, as shown for GaAs in Figure 4.3a [127]. The initial oxidation stages were attributed to adsorption at cleavage-induced defects (*S* in the figure). This phase is followed by activated oxygen adsorption directly on the semiconductor surface (T_2). This is the dominant mechanism up to about 0.6ML coverage, and exposures up to 10^7L. This value would correspond to about 0.1s exposure time in air, much shorter than our observation time scale; therefore we will not treat the first two oxidation stages here. After this virtually instantaneous formation of an initial oxide layer, the oxide growth proceeds more slowly (phase T_2 in the figure). This so-called *field-aided oxidation* mechanism was explained first by Cabrera and Mott for metal oxidation [130]. They proposed that a strong electric field, induced by adsorbates bonded to surface states, is set up across the oxide layer, which pulls substrate or oxygen ions through the layer. Since the electrostatic potential is assumed to be due to O^- ions on the surface, it will be independent of the film thickness. The mechanisms works at low enough temperatures, for which thermal diffusion is negligible. This model yields an inverse logarithmic growth law for the oxide thickness *h* as a function of time *t*:

$$h^{-1}(t) = h_0^{-1} - h_1^{-1} \ln\left\{\tau\left[pt - (pt)_0\right] + 1\right\} . \qquad (4.1)$$

In this equation, h_0 is the film thickness after the exposure $(pt)_0$, above which the oxide grows by the Cabrera-Mott mechanism, and τ is an oxidation time parameter, which was found to be about $300L^{-1}$ for GaAs [127]. The parameter h_1 contains the Mott potential *V* across the oxide film: $h_1 = d_a \cdot eV / k_B T$, where d_a is the thickness of a ML of oxide, that was found to be 1.7Å on GaAs(011) [131].

In our experiments, we are considering oxygen exposures much larger than the onset for

the field-aided oxidation ($(pt)_0 \sim 10^7$L). Therefore we can approximate $pt \gg (pt)_0$, and $\tau pt \gg 1$, and (4.1) simplifies to

$$h^{-1}(t) = h_2^{-1} - h_1^{-1} \ln(pt) \,, \tag{4.2}$$

where $h_2^{-1} = h_0^{-1} - h_1^{-1} \ln \tau$. Besides, our AFM data provide only *relative* oxide heights between two materials. To estimate the *absolute* oxide heights, we consider the GaAs/$Ga_{0.5}In_{0.5}P$ case, and we note that GaAs oxidizes about twice as fast as InP (see Figure 4.3b) [127]; therefore, similar proportions should hold also for GaAs/$Ga_{0.5}In_{0.5}P$. In general, the height difference $\Delta h = h^{GaAs} - h^{GaInP}$ follows a more complicated time evolution than eq. (4.2). However, if the oxidation rates of two materials are different enough, Δh^{-1} can be approximated as $\Delta h^{-1} \approx \Delta h_2^{-1} - \Delta h_1^{-1} \ln(pt)$, where $\Delta h_1 \cong h_1^{GaAs} - h_1^{GaInP} = d_a \cdot e\Delta V / k_B T$ (ΔV being the difference between the Mott potentials of the two materials), and $\Delta h_2 \cong h_2^{GaAs} - h_2^{GaInP}$.

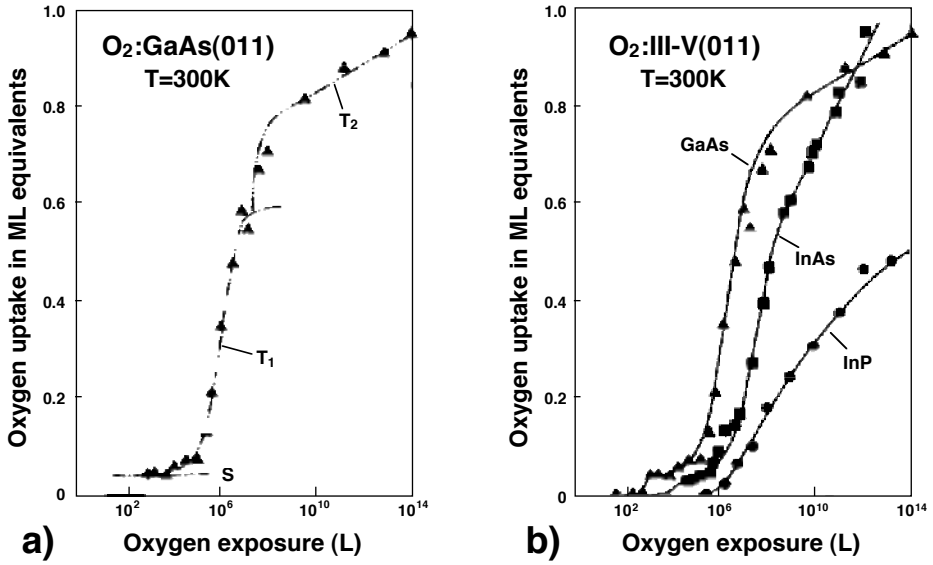

Figure 4.3: a): Oxygen uptake at a cleaved GaAs(011) surface as a function of exposure to molecular oxygen at room temperature. Three oxidation mechanisms can be identified: Saturation of cleavage-induced defects (S), activated adsorption (T_1) and field-aided film growth (T_2) [127]. b): Oxygen uptake of cleaved GaAs, InAs and InP(011) surfaces, as a function of exposure to molecular oxygen at room temperature [127].

We fitted Eq. (4.2) to the GaAs/$Ga_{0.5}In_{0.5}P$ height data obtained by AFM and found a good agreement up to 70 min of exposure (solid line in Figure 4.2a). The fit yields $\Delta V = 0.16 \pm 0.01$eV. For longer exposure times and sufficiently thick films, the field assisted oxidation is not effective any more and thermal diffusion becomes the dominant mode, leading to a logarithmic growth law (dashed line in Figure 4.2a). This agrees well with the model of field-aided oxidation, followed by diffusion-related oxide growth, similar to the behavior in metals [132].

In $Al_xGa_{1-x}As$, the time dependence of the height can be modeled in a way similar to that for GaAs, for each composition. The oxide growth proceeds, up to a certain exposure time, in the field-aided oxidation mode (solid lines in Figure 4.2b), followed by thermal diffusion-

induced growth (dashed lines in Figure 4.2b). The time at which a transition between the two growth modes is observed increases with increasing x, from 70min for $x = 0.12$ to 150min for $x = 0.72$. The coefficients h_1 (which is assumed to be proportional to ΔV) and h_2, and the slopes of the fits in the diffusion controlled time range increase with increasing x as well. This behavior can be explained either by the higher electrochemical potential of aluminum, as compared with gallium, or by a higher mobility of the smaller Al ions, leading in both cases to faster oxide growth. The variations of ΔV and h_2 with x are shown in Figure 4.4. In particular, ΔV varies between 0.17±0.07eV for $x = 0.12$ to 0.51±0.05eV for $x = 0.72$. Note that the GaAs Mott potential was found to be about 1.5eV [126], and should be added to the values found here to find the absolute values of V in $Al_xGa_{1-x}As$.

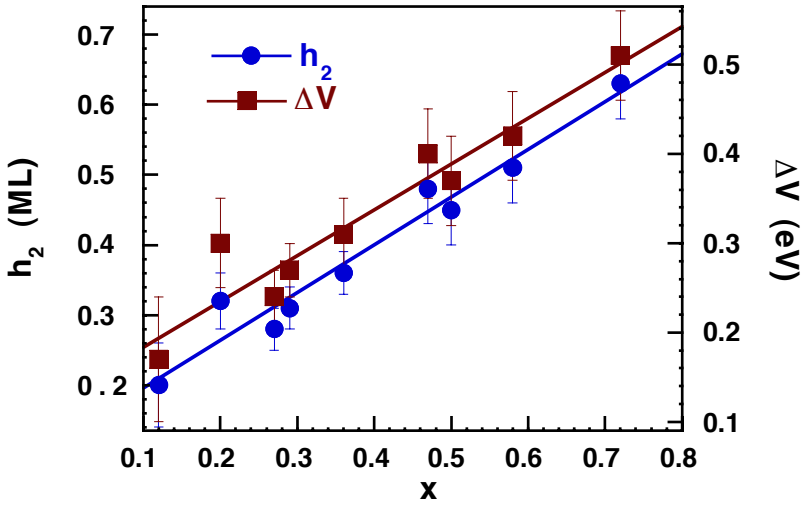

Figure 4.4: Dependence of the fitting parameters ΔV (circles) and h_2 *(squares) from eq. (4.2), as a function of* x*, for the* $Al_xGa_{1-x}As$*/GaAs sample (Figure 4.1b).*

From the discussion above, we conclude that the mode of oxide growth on the cleaved surface of $Al_xGa_{1-x}As$ ($x < 0.7$) proceeds in a way similar to the oxidation of GaAs, differing only quantitatively in the reaction rates. The smooth surface over large areas and the low growth rate of the oxide (< 1nm/h) indicate quasi layer-by-layer formation of these thin films. After 200 min of oxidation, a quasi-stable height profile is reached, which is only slowly changing with time.

4.1.4 Application to the imaging of nanostructures

The height differences between GaAs and $Al_xGa_{1-x}As$ as a function of x and t can be used for inferring the Al concentration from the height profile of a given sample. For Al concentrations in the range $0 < x < 0.72$, we used the difference in height to identify composition and thickness of layers deposited on nonplanar substrates. As an example of this application, we show cross-sectional AFM images of two samples. The first consists of GaAs layers, nominally 60nm thick, separated by 4nm thick $Al_{0.5}Ga_{0.5}As$ markers (Figure 4.5a). The second consists of $Al_{0.5}Ga_{0.5}As$ layers (nominally 50nm thick), separated by 3nm thick GaAs markers (Figure 4.5b). Both samples were grown under similar conditions on V-grooved substrates (see

the figure caption for details). The resulting contrast between the GaAs and AlGaAs regions is sufficient to observe details of the growth front, including faceting, and the formation of GaAs QW layers on the different facets and GaAs QWRs at the bottom of the grooves. A dark (lower) band running through the center of each groove indicates Ga accumulation in that region (VQW). AFM analysis of the VQWs will be presented in section 4.2.2.1. The AlGaAs regions inside the grooves appear darker (lower) than the AlGaAs regions on the (100) planar regions, due to lower (by 10±2%) incorporation rate of Al atoms on the sidewall facets. The quantitative difference in the Al mole fractions cited here were obtained by translating the height difference to *x* values using the data of Figure 4.4. The qualitative difference in the Al content is also evident in TEM cross sections of these structures, but quantification is difficult in that case. (see page 110).

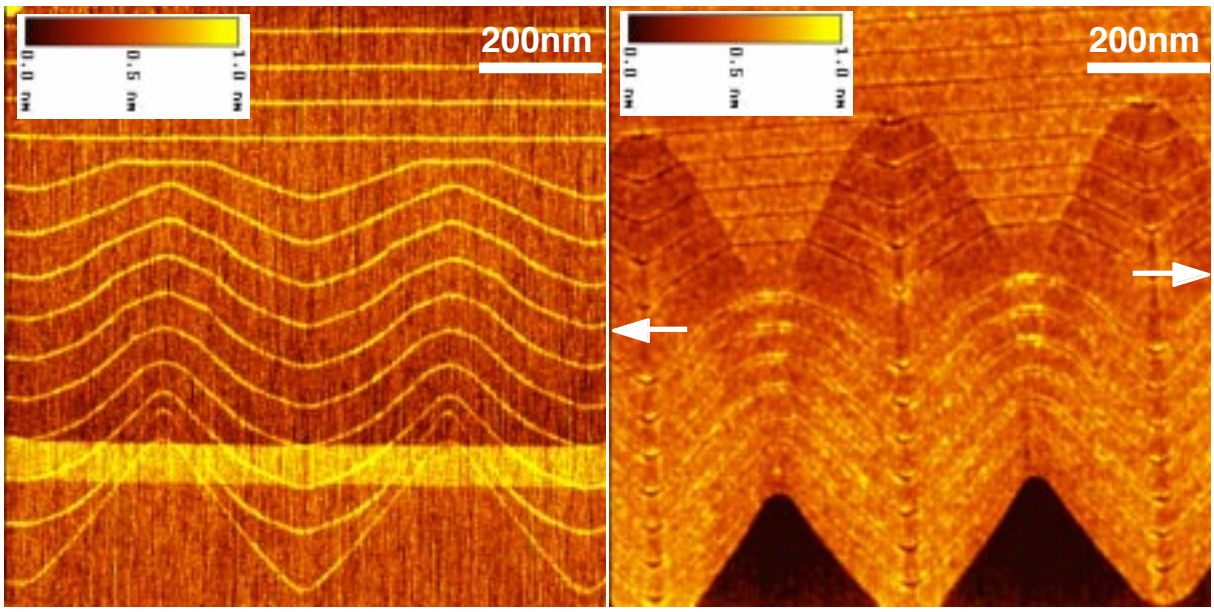

Figure 4.5: a) AFM height image of the cleaved $(01\bar{1})$ surface of a nonplanar GaAs/$A_{0.5}Ga_{0.5}As$ heterostructure after 3h of exposure to air. Several $A1_{0.5}Ga_{0.5}As$ layers of a nominal thickness of 4nm were grown at a temperature of 750°C, sandwiched between nominally 60nm-thick GaAs layers on a nonplanar GaAs substrate, consisting of V-shaped grooves with 0.5µm pitch. The light stripe running horizontally through the structure is due to imperfect cleave. b) AFM height image of the cleaved $(01\bar{1})$ surface of a nonplanar $Al_{0.5}Ga_{0.5}As$/GaAs heterostructure after 3h of exposure to air. Several GaAs layers of a nominal thickness of 2.5nm were sandwiched between 50nm-thick $Al_{0.5}Ga_{0.5}As$ on a nonplanar GaAs substrate, consisting of V-shaped grooves with 0.5µm pitch. The growth temperature for the first seven layers was 750°C and then decreased to 650°C during growth of the 100nm thick $Al_{0.5}Ga_{0.5}As$ layer, indicated by the arrow.

The oxide height difference Δh between the $Al_{0.5}Ga_{0.5}As$ layer and the GaAs substrate is in both cases around 0.5nm, comparable to the height difference obtained after the same period (three hours) of oxidation of the $Al_{0.5}Ga_{0.5}As$/GaAs calibration heterostructure. However, Δh is only 0.12 nm for the thin (~3nm) GaAs QW layers. This is due to the finite size of the AFM tip (about 30nm), which prevents its full penetration into the lower, oxidized GaAs regions. The larger lateral extension of the GaAs QWRs allows the tip to better penetrate, leading to a maximum Δh of 0.51nm, comparable to the step at the $Al_{0.5}Ga_{0.5}As$/GaAs interface of Figure

4.1. A simple model, describing the imaging of a structure (groove or ridge) which is smaller than the diameter of the tip [133], shows that the measured height of a thin ridge should be correct, whereas its width should appear larger, as found in the experiments. In the case of a groove, the depth appears reduced, but the imaged width corresponds to the real value. We compared cross sectional TEM images of the sample shown in Figure 4.5b with the AFM picture and obtained a good agreement for the dimension of the GaAs-layer. The uncertainty in the lateral dimension of the layer was about 1nm, probably determined by lateral oxide growth and the finite tip width.

4.2 Self-ordering of $Al_xGa_{1-x}As$ vertical quantum wells

In the rest of the chapter, we will focus on the compositional self-ordering of $Al_xGa_{1-x}As$ alloys grown on V grooves. We will analyze the $Al_xGa_{1-x}As$ profile composition with AFM, EELS, PL, and CL techniques. All these techniques consistently show evidence for Ga segregation at the bottom of the V grooves, giving rise to a VQW structure. The detailed geometrical structure of the VQWs will be analyzed using cross-sectional and top-view TEM data.

4.2.1 Overview of the VQW structures

All the structures studied here were grown on 3μm-pitch V grooves. Typical layer sequences consist of a multilayer $Al_xGa_{1-x}As$ structure, grown on a short-period $GaAs/Al_{0.45}Ga_{0.55}As$ superlattice (SL) buffer. The AlGaAs structures are composed of a ~500nm-thick $Al_xGa_{1-x}As$ core layer, sandwiched between a ~300nm and a ~150nm-thick $Al_{0.45}Ga_{0.55}As$ barriers. A 10nm-thick GaAs cap was deposited on top of the AlGaAs sequence. We grew a series of different samples with nominal compositions x in the core layers ranging between 0.09 to 0.45, to study the optical properties. Additional samples, with a similar layer structure, were grown with higher Al concentrations, up to $x = 0.89$, for AFM studies.

Figure 4.6 shows an AFM cross section of a typical structure used for luminescence experiments, with $x = 0.3$ in the core region. Since the layers composing the SL buffer are too thin to be resolved with the AFM, the SL appears as a single layer with a contrast corresponding to an average $x \approx 0.2$. In all the subsequent layers, the VQW is visible as a ~20nm-wide darker (i.e., less oxidized) vertical stripe at the bottom of the groove, indicating a region with an Al composition lower than in the surroundings. As observed earlier (Section 2.2), after etching and heat-up, the groove sidewalls in the substrate are initially composed of {111}A sections near the ridges, which smoothly connect to high index facets in the bottom part of the groove. These high index, fast growing facets, forming an angle between them of about 90° expand during growth, until they extend throughout the sidewall area. During further growth, the orientation of these facets remains constant. Note that, as in Figure 2.3, the top profile sharpens up during the initial SL growth. Since the etched profile at the top of the mesa is much sharper than that of Figure 2.3, it can sharpen up until it reaches a self-limiting width, in the 10-20nm range. This is

visible by the lighter vertical stripe in the $Al_{0.45}Ga_{0.55}As$ layer at the top of the ridge, that denotes a region of *lower* Ga content, which we will term *vertical quantum barrier* (VQB). We will analyze the VQBs in more detail in Section 4.2.3.

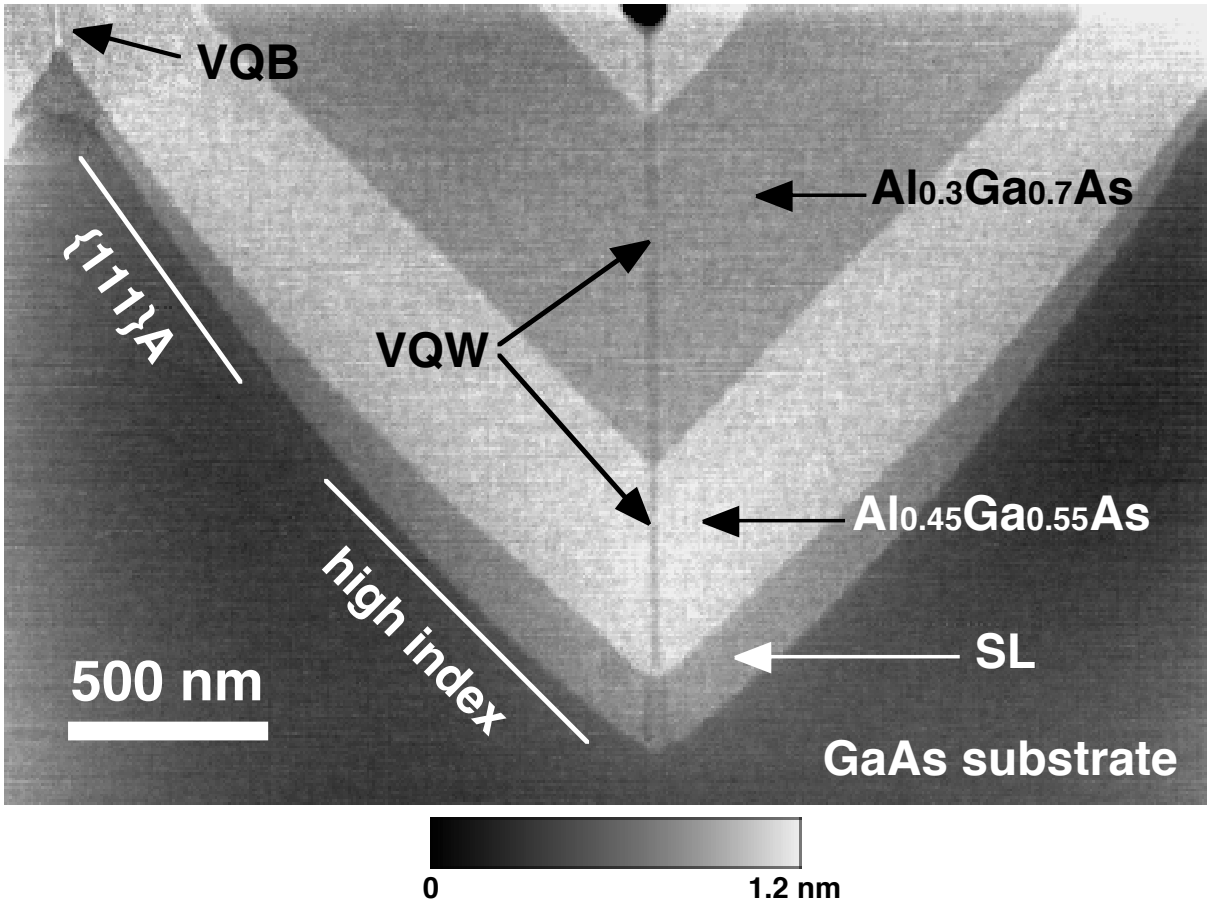

Figure 4.6: AFM cross section of a 3µm-pitch GaAs V groove, on which a multilayer AlGaAs heterostructure was grown by LP-OMCVD. Formation of a bottom VQW and of a ridge VQB is indicated.

4.2.2 Alloy composition in V-grooved structures

4.2.2.1 AFM measurements

Figure 4.7a is an AFM cross section of a VQW formed at the interface between two layers with nominal $x = 0.21$ and 0.49, obtained after 60 min of oxidation in air. Higher Al mole fractions yield a thicker oxide layer and hence correspond to a higher topography in the AFM image. To measure the composition profile across the VQW, we have taken AFM line scans like the one indicated by the line AB in Figure 4.7a. These scans are averaged along the growth direction, within the area defined by the rectangle around the scan line, to reduce effects of scanning noise. This averaging is necessary, since the oxide layer has an inherent random roughness, evident from Figure 4.7a, which increases with the Al concentration and oxidation time. The oxide RMS roughness is typically of the order of half of the VQW height difference, and therefore screens the VQW contrast obtained in a single line scan.

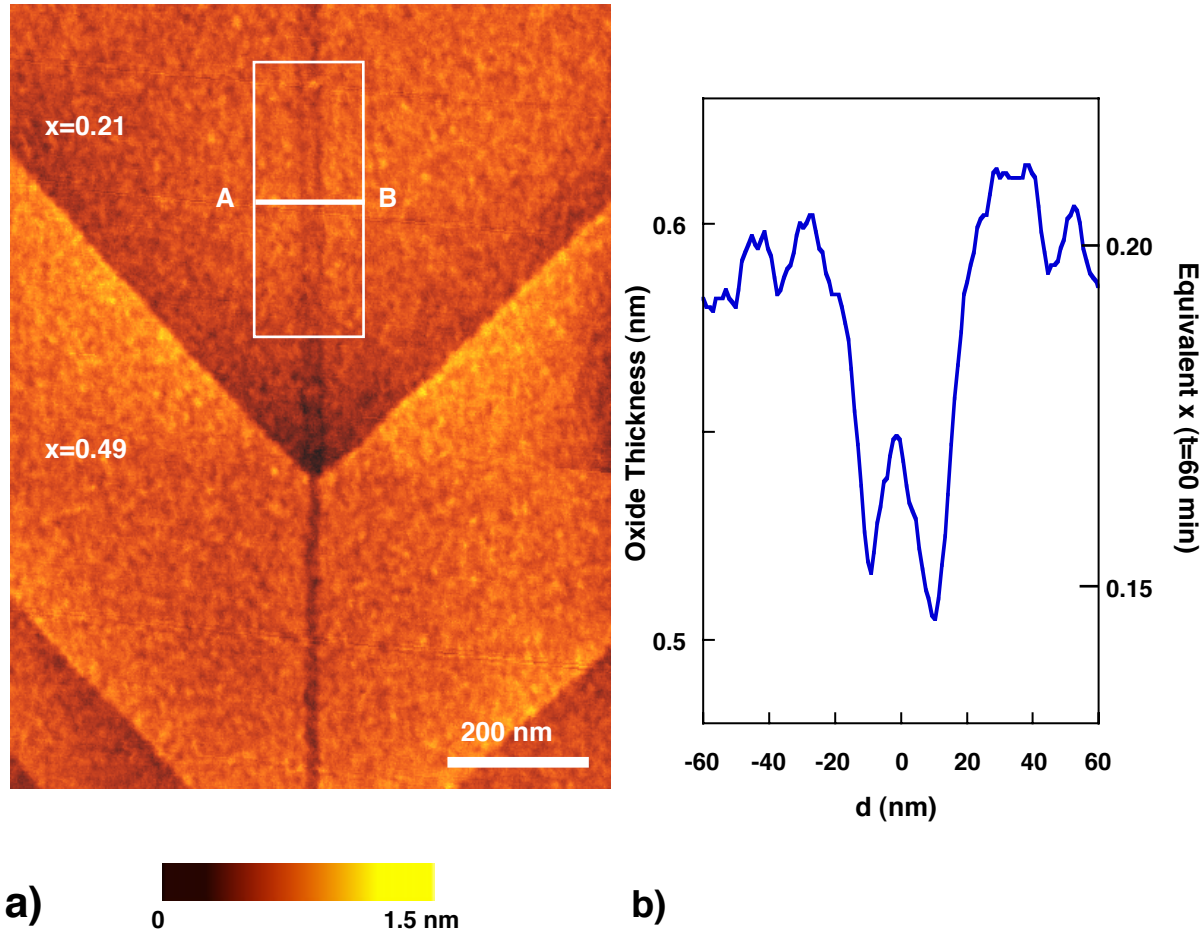

Figure 4.7: a) AFM cross section of the $Al_{0.21}Ga_{0.79}As/Al_{0.49}Ga_{0.51}As$ interface at the bottom of a V groove. b) AFM line scan across the sections AB in Figure 4.7a, averaged along the VQW within the framed region. The line scan was taken after 60 min. oxidation time. The oxide height is shown on the left ordinate, and the equivalent composition on the right ordinate.

An averaged line scan across the VQW structure is shown in Figure 4.7b, and reveals that the VQW is composed of two different branches, each showing an oxide layer height which is lower by about 0.8-0.9Å than the surroundings. Determination of the equivalent Al mole fraction x_b was done by measuring the height difference on line scans taken at different oxidation times, from 5 min after the cleave up to about two hours. Using the calibration curves of Figure 4.4, the right vertical scale converts the measured oxide thickness to the equivalent Al composition, and allows therefore measuring directly x_b. The bowing of the AFM scans introduces an error in the absolute height of the sidewall region, with respect to the GaAs substrate (the substrate lies about 1μm away from the measured region, and two other layers are grown in between). We have chosen, therefore, to estimate the sidewall composition x_s as equal to the nominal one. This assumption is justified by direct measurements by means of EELS, PL and CL, as shown below. The accuracy in the relative concentrations $\Delta x_b = x - x_b$ thus obtained is about ±0.01 to ±0.02, as inferred from the statistical dispersion of the data. For the sample shown here, the height variation between the sidewall and the VQW corresponds to a decrease in Al mole fraction of about 0.07±0.01, yielding $x_b = 0.14 \pm 0.01$.

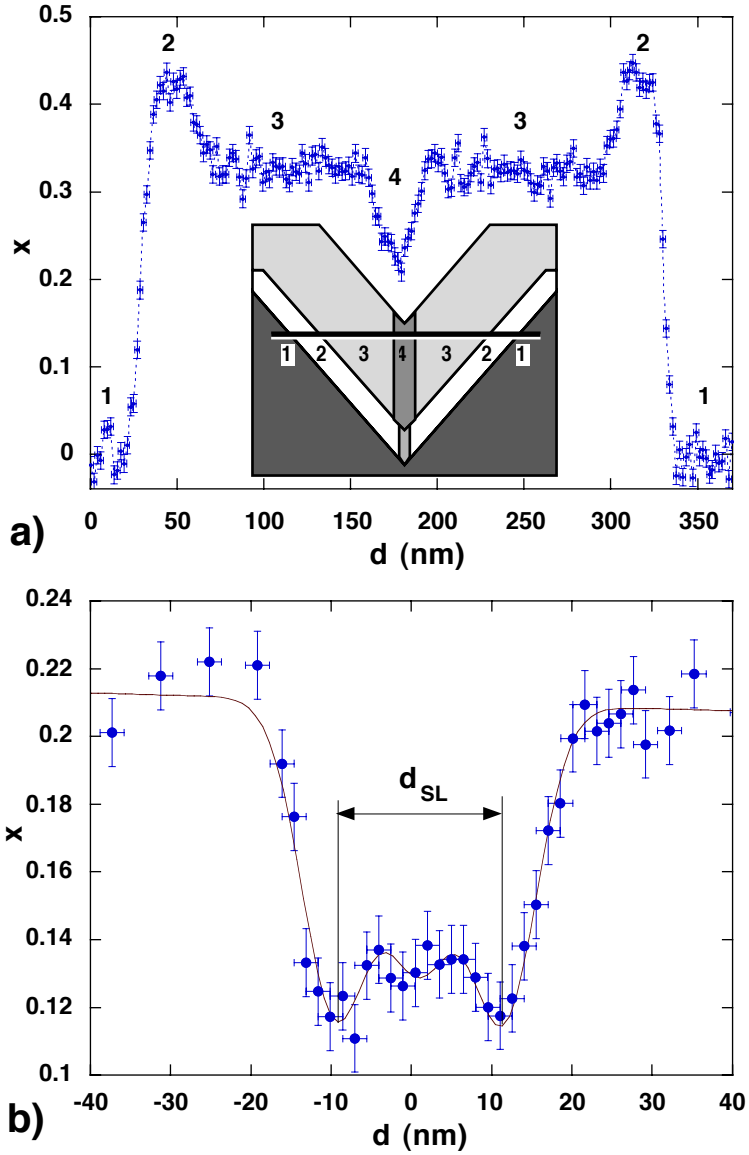

Figure 4.8: a) Cross sectional EELS line scan across a 0.5µm-pitch V groove. Four different regions can be identified: GaAs substrate (1); $Al_{0.42}Ga_{0.58}As$ (2); $Al_{0.32}Ga_{0.68}As$ (3); VQW (4). The inset shows a schematic cross section of the groove and the layer structure, with numbers identifying each region in the EELS scan. b): Cross sectional EELS line scan across the VQW region, in the low-Al concentration layer of the sample in Figure 4.7. The solid line is a triple-gaussian fit of the data.

4.2.2.2 EELS measurements

The Al composition across the VQW was independently determined with higher spatial resolution using EELS in a field emission TEM [134]. For the EELS measurements, the electron probe (FWHM=1.5nm) in a Hitachi HF2000FEG TEM is scanned across the VQWs in a cross sectional sample geometry. At each dwell point of the scan, we acquired an EELS spectrum during 1.5s using a Gatan spectrometer model 666. The Ga and Al L_{23} edges were extracted by extrapolating a power law fit from the pre-edge region to the edges. The concentrations are obtained by comparing the edge intensities to Hartree-Slater cross sections [135]. Using EELS, we can obtain concentration profiles with a precision in the relative and

absolute concentrations of ±0.01 and ±0.02, respectively [135]. The spatial resolution under the experimental conditions used here is typically 1.5-3nm.

A cross sectional EELS line scan across a 0.5μm V groove is shown in Figure 4.8a. The sample was grown at 680°C, and consisted of a 50nm-thick $Al_{0.42}Ga_{0.58}As$ layer, followed by a 100nm-thick $Al_{0.32}Ga_{0.68}As$ layer (values of thicknesses and compositions are the nominal ones). The inset shows a schematic cross section of the groove, with the black line indicating the EELS scan. Four different regions can be identified in the scan, located symmetrically about the bottom of the groove: the GaAs substrate (1), the $Al_{0.42}Ga_{0.58}As$ layer (2), the $Al_{0.32}Ga_{0.68}As$ layer (3) and the VQW in the $Al_{0.32}Ga_{0.68}As$ layer (4). The measured compositions in the different layers are as follows: 0.41±0.02 (region 2), 0.31±0.02 (3), and 0.22±0.02 (4, VQW). In both $Al_xGa_{1-x}As$ layers, therefore, the composition on the sidewalls is equal to the nominal one on a planar (100) substrate, within the experimental errors. The VQW Al mole fraction is about 29% lower than on the sidewalls. Figure 4.8b shows an 80nm-wide line scan of the VQW region in the $Al_{0.21}Ga_{0.89}As$ layer from Figure 4.7. Note that a central branch can be inferred from the scan, between the well-resolved lateral ones. The measured values of x_s and x_b were 0.21±0.02 and 0.12±0.02, respectively. Also in this case, we measured $x_s \cong x$, and the measured value of x_b agrees well with the AFM estimate.

4.2.2.3 Luminescence measurements

Figure 4.9 (solid line) shows the PL spectrum of the sample of Figure 4.7. The spectrum was measured at T = 8K with an argon ion laser beam (488nm), at a power density ~1W/cm^2. The PL spectrum is dominated by luminescence at 1.723eV. The lowest energy peak at 1.698eV is identified as the emission from the VQW; it becomes the dominant PL peak in a selectively etched sample where the {311}A and (100) regions were removed [114] (dotted line spectrum in Fig.3). The emission at 1.723eV originates from the {311}A edge region between the top (100) ridge and the sidewalls, the emission at 1.736eV originates from the narrow (100) ridge region, and the one at 1.767eV is due to recombination at the sidewalls. These peak assignments were confirmed by low-temperature, cross-sectional CL imaging of the emission wavelengths [136]. The linewidth of the VQW transition is 6meV, consistent with the good structural uniformity of the VQW measured along the $[01\bar{1}]$ and the [100] directions (see the TEM analysis discussed later). At temperatures above 80K, the VQW dominates the PL spectra even in the unetched samples, due to the efficient, thermally-activated carrier transfer from the {311}A regions into the VQW. The composition profile across the V-groove facets is hence deduced from the CL and PL spectra: $x_{sw} \geq t_{op\ 100} \geq x_{top\ 311} \geq x_b$. The dashed line is the PL emission detected from the control planar (100) reference sample, and coincides in energy with the emission from the sidewalls, confirming the EELS measurements of the Al content of the sidewalls. The Al composition of the VQW, inferred from the energetic position of the corresponding PL peak is $x_b = 0.125$ (by neglecting quantum confinement effects on the transition energy), in good agreement with AFM and EELS findings.

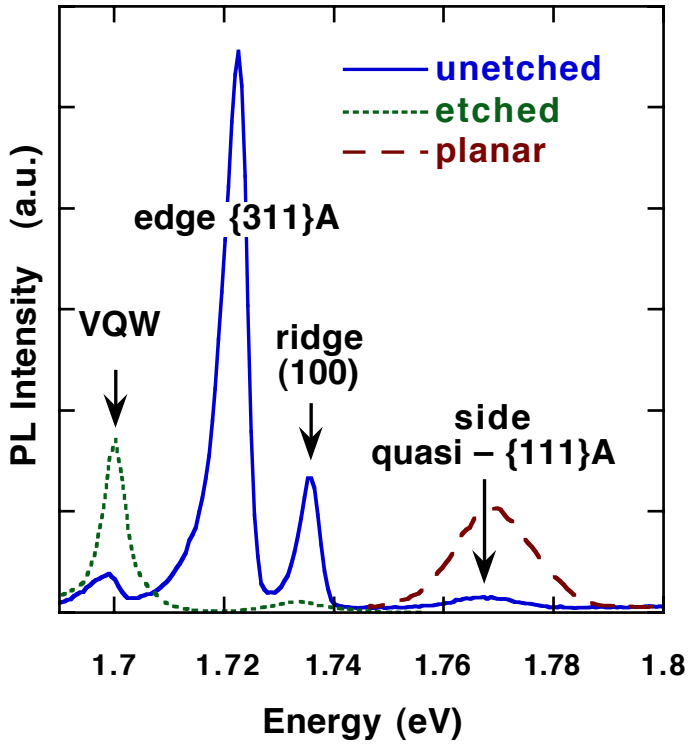

Figure 4.9: Photoluminescence spectra of the VQW sample with background Al composition x= *0.215, at* T= *8 K on an unetched sample (solid line) and at* T= *20 K for a sample where the {311}A edge and (100) ridge regions were removed by selective etching (dotted line). The dashed line indicates PL emission from a (100) planar reference sample.*

4.2.3 Structure of the VQWs

4.2.3.1 General features

AFM and EELS data presented in the previous pages have shown that the Ga segregation in the VQW is modulated across the bottom of the groove. This substructure in the VQW is better imaged by dark-field TEM (the contrast between the VQW and the sidewall is too low to be imaged with high-resolution TEM). Figure 4.10a is a cross section, at the bottom of the groove, of the interface between two AlGaAs layers with different Al composition, in a sample identical to that shown in Figure 4.6, except for the different *x* in the low-Al region (0.23). As seen in Section 2.3.1, the AlGaAs profile appears to be faceted in this region, thanks to the more kinetically-limited nature of LP-OMCVD under these growth conditions [23]. In particular, the interface reveals a central (100) facet, surrounded by two {311}A facets and, further away, by the high-index sidewalls. Associated with this faceting, one can observe the *formation of distinct branches* in the VQW: two lateral branches, corresponding to each of the {311}A facets, and a narrower, central one originating in the (100) facet. Note that the separation and width of the {311}A VQW branches depend on the Al composition, as we will show in more detail in the next section. The branch widths and separations stay constant during the growth of the lower layer and, after a short transition region (≈ 20nm) above the interface, reach another stable, self-limited profile also in the upper layer.

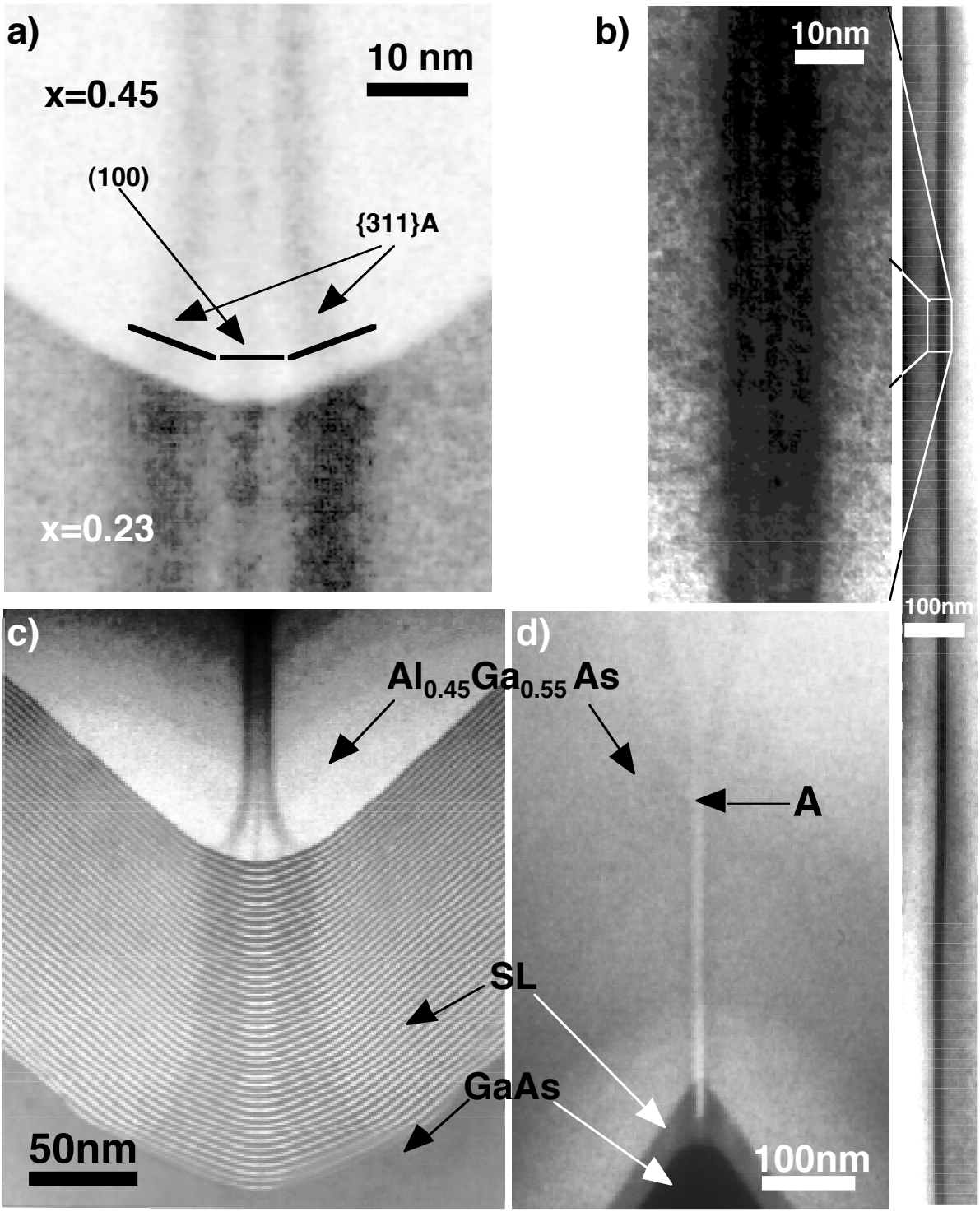

Figure 4.10: Dark-field TEM images of different AlGaAs layer structures grown on V grooves. a): Cross section of the interface between two AlGaAs layers with different Al concentrations at the bottom of a V groove, showing the formation of a (composition dependent) VQW, characterized by three distinct branches of enhanced Ga content. b): Top-view image of a VQW, with two different magnifications. c) Cross section of the bottom of a V groove, in which a GaAs-AlGaAs SL and an AlGaAs layer are grown on a GaAs substrate. d) Cross section of the same layers, at the top of the ridge between two grooves, showing the formation of a self-limiting AlGaAs VQB.

Figure 4.10b is a top-view TEM of a VQW in an $Al_{0.45}Ga_{0.55}As$ layer grown at 700°C. The VQW appears to be straight across the whole image range (2μm), in agreement with top

view AFM observations of AlGaAs and GaAs surfaces, where the bottom of the groove was found to be laterally uniform over several microns (see Section 3.3.5). The magnified view of Figure 4.10b shows that the VQW branching is visible also in the groove direction. The regularity of the profile in the growth direction and along the groove suggests a three-dimensional self-ordering mechanism, giving rise to the formation of a truly 2D VQW.

Figure 4.10c shows the GaAs substrate, the SL and the high x AlGaAs regions at the bottom of the groove, of the sample in Figure 4.6. The faceting is evident in the profiles of the substrate and of the SL layers. The relatively wide profile of the etched substrate (with bottom facets extending laterally over about 150nm) sharpens up during deposition of the SL, and eventually reaches a self-limiting shape, about 60nm wide. The darker contrast in the SL at the bottom of the groove, with respect to the sidewalls, is due both to a thickening of the GaAs layers (see Section 2.3.4.1) and to Ga segregation in the AlGaAs layers. Note that on the {311}A planes the excess Ga is distributed over the entire facets, therefore the width of the VQW branches follows closely that of the facets. Conversely, on the (100), Ga segregates only at the center of the facet and, while the facet width depends on the material and growth conditions, the branch width keeps rather constant.

Figure 4.10d shows a section of an identical sample, taken at the top of the groove. The formation of the self-limiting VQB, imaged by AFM in Figure 4.6, is evident in the TEM image. This metastable self-limiting growth stops however at the point labeled "A" in the figure. From this point, the top region begins to expand via a development of (100) and {311}A facets, leading eventually to the planarization of the sample as growth proceeds. We will explain the growth behavior of this top region in the framework of the diffusion model discussed in Section 5.2.

4.2.3.2 Dependence on the growth conditions

Figure 4.11a shows TEM cross sections of three VQW structures, grown at 700°C, with nominal x equal to 0.65, 0.45 and 0.23, top to bottom, respectively. It can be seen that the three VQW branches tend to approach as x increases, until they become indistinguishable to the eye for $x = 0.65$. In these conditions, the inter-branch separation becomes smaller than the composition gradient in each individual branch, and/or smaller than the TEM spatial resolution. To evaluate quantitatively the geometry of the VQWs, we have fitted TEM line scans of the bottom region, in self-limiting $Al_xGa_{1-x}As$ layers, with three gaussian profiles, corresponding to the branches. Figure 4.11b shows an example of such a fit, for the $x = 0.45$ sample of Figure 4.11a. The lateral size of the VQW can be therefore characterized completely by the separation d_{sl} between the center of the {311}A branches, and by the half width at half maximum of the individual branches w_{100} and w_{311}. Note that the transient of grayscale in the VQW, evident from the line scans, is due both to a real gradient in composition, and to artifacts related to the TEM imaging. These artifacts include effects related to the sample tilt, non-linearity in the grayscale of the TEM negative and non-linearity of the TEM contrast with the composition.

With a tilt angle of the order of 2° and a sample thickness of about 50nm, the apparent broadening of any vertical interface would be of the order of 2nm. This amount corresponds to a non-negligible fraction of the base-to-peak horizontal distance in a typical VQW profile (this value is about 5.5nm in the section of Figure 4.11b).

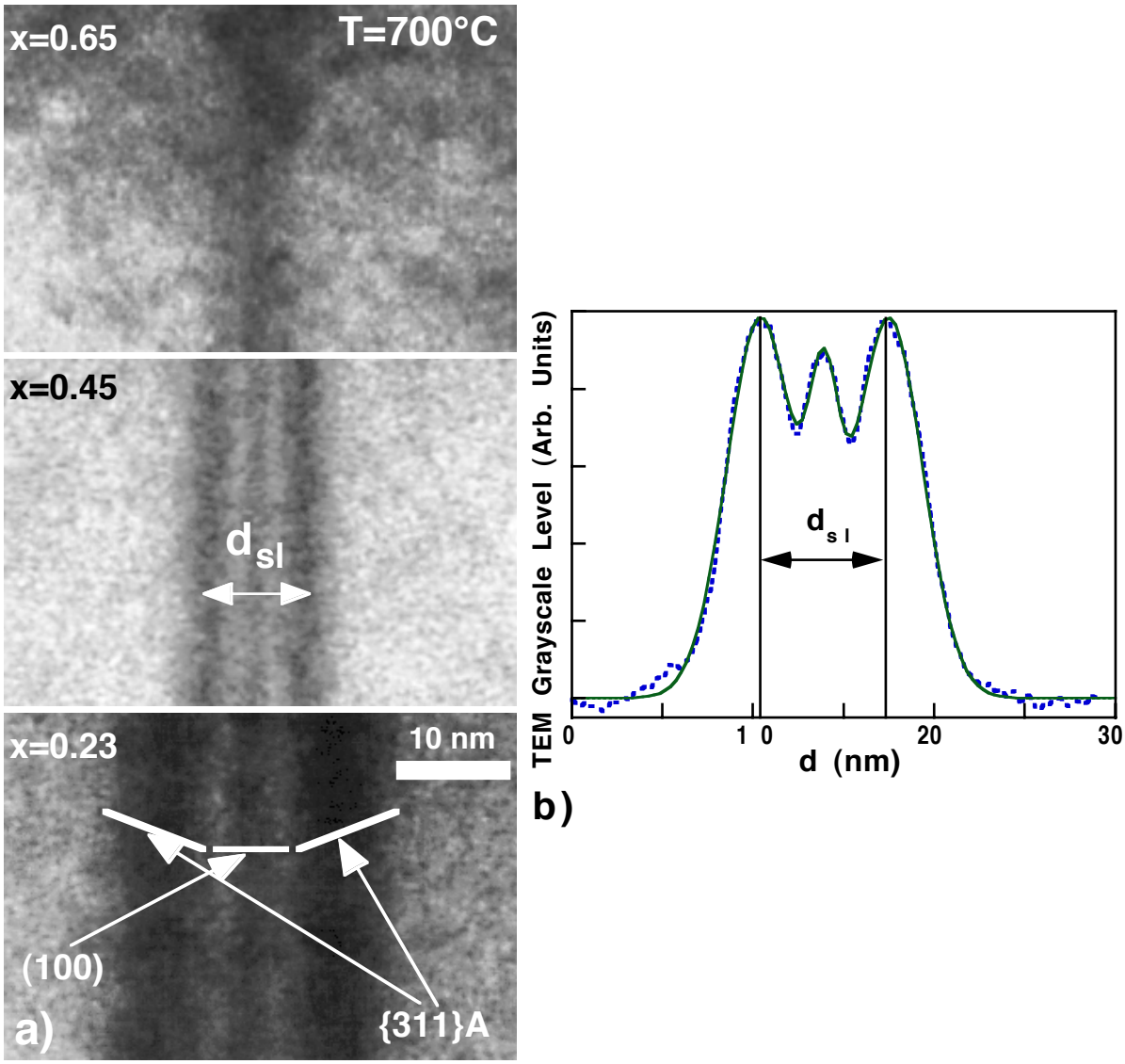

Figure 4.11: a): Dark-field TEM cross sections of three VQW structures grown at 700°C, with nominal x equal to 0.65, 0.45 and 0.23, top to bottom, respectively. b): Line scan of the TEM cross section of the VQW region from the second sample in part (a), (dashed line), fitted with a three-gaussians profile (solid line).

Figure 4.12a shows the measured self-limiting separation d_{sl}, as a function of x, for $T = 700$°C. This distance decreases with increasing nominal Al mole fraction, as a result of a narrowing of the bottom profile (see Section 2.3.3.1); d_{sl} ranges between 28.7nm for $x = 0.13$ to 5.1nm for $x = 0.75$. Typical VQW lateral sizes are therefore smaller than those obtained with higher reactor pressures, that are in the range 20-30nm for similar growth temperatures and Al mole fractions [116, 137]. Figure 4.12b shows the measured values of w_{100} (circles) and w_{311} (squares) in the same samples as in Figure 4.12a. The width w_{311} decreases by about a factor of

three, when x increases from 0.13 to 0.75. A similar reduction is also observed for the lateral width of the {311}A facets, measured under the same growth conditions (see Section 2.3.3.1). This suggests that Ga segregation takes place over most of the {311}A facets. Conversely, the width w_{100} is rather insensitive to variations in the Al mole fraction, while the size of the corresponding (100) facets decreases strongly with increasing x (by about a factor of 4, for an x variation from 0.12 to 0.47). It follows therefore that segregation takes place mainly at the center of the (100) facet, giving rise to regions with higher Al content between the facets, as was discussed in the previous section.

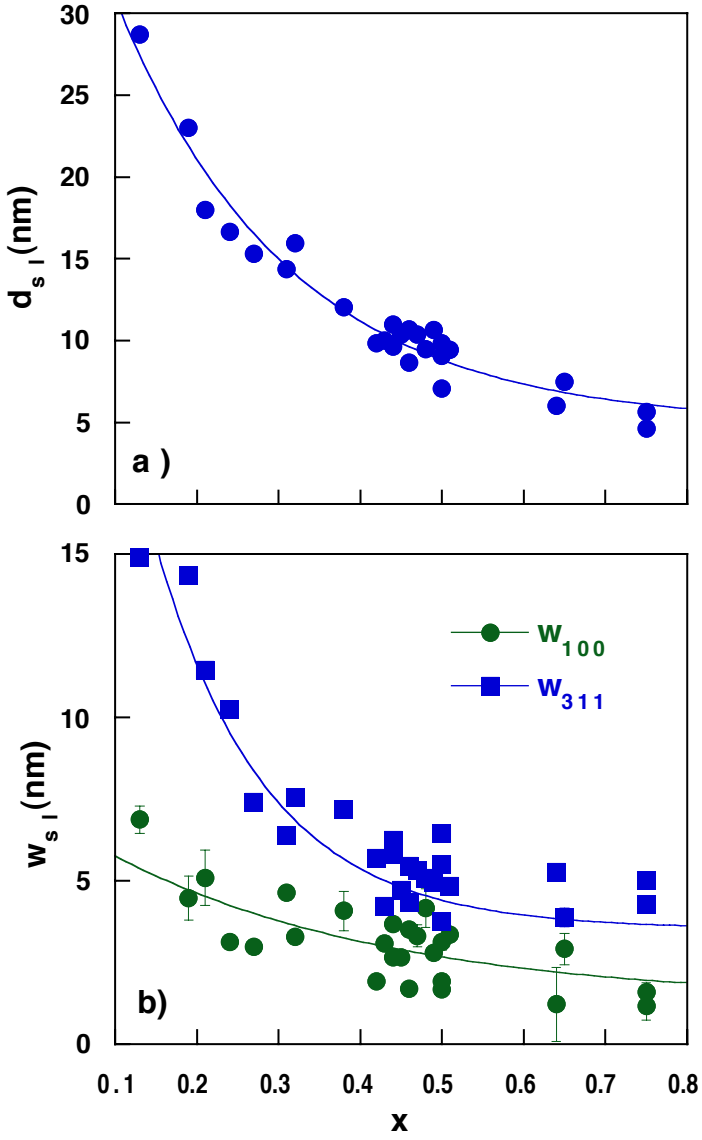

Figure 4.12: a): Self-limiting separation d_{sl} *between the {311}A VQW branches (see Figure 4.10), as a function of the nominal Al content* x, *for* T = 700°C. *b): Self-limiting width of the (100) (circles) and {311}A branches (squares), for the samples of part (a). Solid lines in both plots are guides to the eye.*

Figure 4.13 shows the dependence of d_{sl} on the growth temperature T, presented in the form of an Arrhenius plot, for $x = 0.21$ (circles) and $x = 0.45$ (squares), in samples grown between 650°C and 750°C. Like the corresponding facet widths (Section 2.3.3.1), d_{sl} increases

with T, as a result of increased surface diffusion. In this range of temperatures, the values of d_{sl} change by a factor 2.3 for $x = 0.21$ and a factor 3.0 for $x = 0.45$. The figure shows that the dependence of d_{sl} on T fits well to an Arrhenius plot (solid lines in Figure 4.13). The Arrhenius slopes give activation energies of 0.61±0.07eV for $x = 0.21$ and 0.91±0.06eV for $x = 0.45$. A similar energy (0.93eV) was found for the T dependence of the self-limiting radius of curvature of OMCVD-grown InP [138]. In Section 5.3.2.2 we will give an interpretation of this activation energy as a function of capillarity-induced surface diffusion.

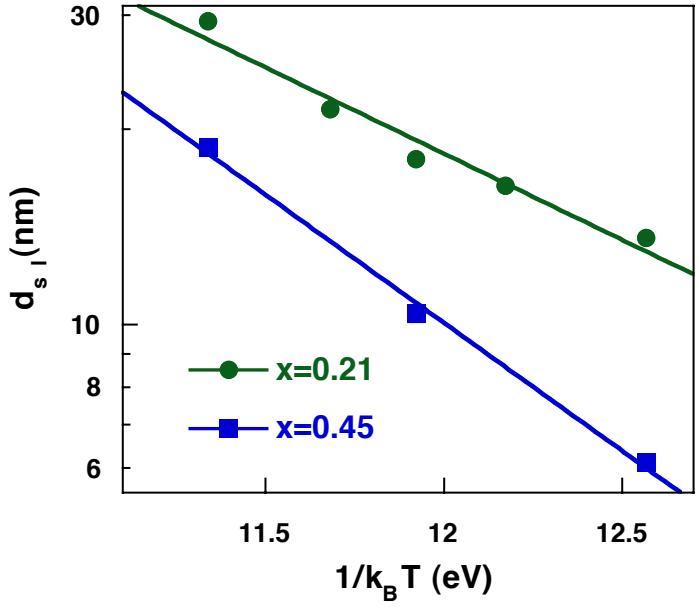

Figure 4.13: Arrhenius plot of the self-limiting separation d_{sl} *between the {311}A VQW branches, for* x = *0.21 (circles) and* x = *0.45 (squares), in the temperature range 650 to 750°C.*

4.2.4 Study of the Ga segregation in the VQWs

Figure 4.14a shows a series of VQW scans, similar to that of Figure 4.7b, performed on different samples grown at 700°C, with different nominal Al mole fractions x, as measured by XRD. The scans were taken after an oxidation period of 60 min. The vertical scale is linear in the equivalent x (left scale), inferred from the oxide thickness (right scale) with the calibration described above. Note the high nonlinearity of the relation between oxide height and equivalent x. Figure 4.14b shows the values of x_b, measured with AFM (diamonds), EELS (circles), and PL (open triangles) as a function of the nominal x, for $T = 700$°C. The agreement among these independent estimates is evident from the plot. The sidewall composition x_s, determined by EELS (squares) and PL (solid triangles) are also shown, and reveal that x_s is approximately equal to the nominal x, within the experimental uncertainty of the techniques. Our data show that the Ga segregation in the VQW approaches zero for $x \rightarrow 0$ and $x \rightarrow 1$, and reaches a maximum (about 0.15 in composition) between $x = 0.55$ and $x = 0.6$. Our measurements of VQW segregation are in agreement with the values of x_b measured by PL on atmospheric-pressure (AP) grown VQWs by Vermeire *et al.*, in the range $x = 0.15$-0.35 [115]

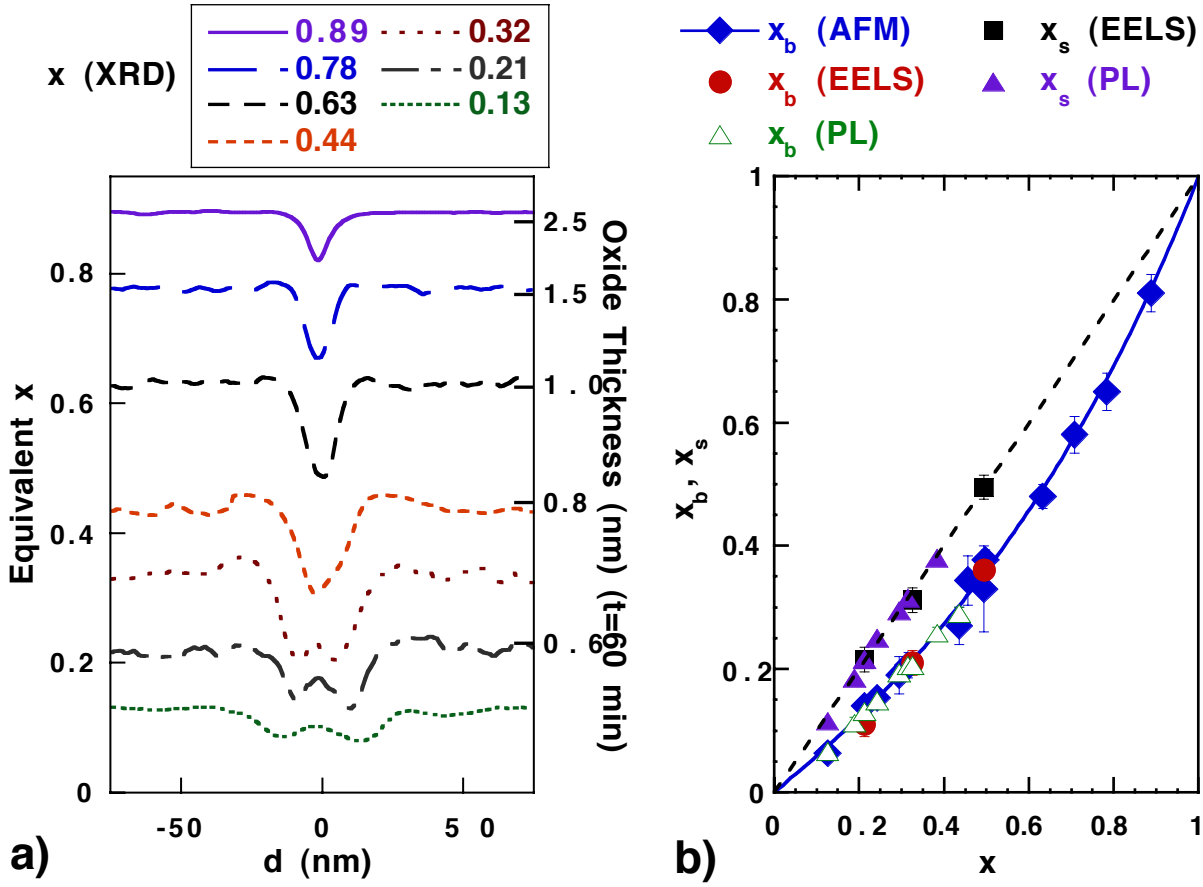

Figure 4.14: a) Series of AFM line scans across sections like AB in Figure 4.7a, averaged along the VQW within framed regions as the one in Figure 4.7a. The line scans correspond to samples, grown at 700°C, with different nominal Al content, and taken after 60 min. oxidation time. The oxide height is shown on the right scale, and the equivalent composition on the left scale. b): Measured values of the VQW composition x_b *as a function of the nominal one,* x. *These values were estimated by AFM (diamonds), EELS (circles), and PL (open triangles). Also shown are the sidewall composition* x_s, *measured by EELS (squares) and PL (solid triangles). The solid line is a fit of* x_b *with eq. (4.3), giving* k = *1.81±0.05. The growth temperature was 700°C for all the samples.*

The dependence of x_b on x can be parameterized with a simple empirical model that assumes an enhanced Ga incorporation in the VQW, with respect to the sidewalls. As seen in Section 1.2.3.1, in our mass-transport limited growth conditions, the solid composition on a *planar* substrate can be written, as a function of the Al and Ga partial pressures, as $x = p^A / (p^A + p^G)$ [23]. On a *non-planar* substrate, surface kinetics become important in determining growth rates and solid compositions, since average decomposition/incorporation times are in general orientation-dependent. The resulting inter-facet migration (stronger for Ga than for Al) can therefore modify the local growth rates and compositions. We can integrate these effects on the VQW composition by assuming that the resulting Ga flux in this region is enhanced by a factor k, with respect to that of Al, giving $x_b = p^A / (p^A + k \cdot p^G)$. We can therefore express x_b in terms of x as

$$\frac{1 - x_b}{x_b} \frac{x}{1 - x} = k \ . \qquad (4.3)$$

From this relation, we can derive the maximum segregation $\Delta x^{max} = (x - x_b)^{max}$, and the corresponding nominal Al composition x^{max}:

$$\Delta x^{max} = \frac{\sqrt{k} - 1}{\sqrt{k} + 1}; \qquad x^{max} = \frac{\sqrt{k}}{\sqrt{k} + 1}. \tag{4.4}$$

The solid line in Figure 4.14b is a fit of the AFM and EELS data with eq. (4.3). The fit shows a good agreement with the experimental values, and yields a Ga incorporation rate enhancement $k = 1.81 \pm 0.05$. With this value of k, we obtain $\Delta x^{max} = 0.147 \pm 0.07$ and $x^{max} = 0.574 \pm 0.03$.

The law of mass action (4.3) is typical of diffusion models involving enthalpic and entropic contributions to diffusion. Phenomena involving eq. (4.3) include segregation at surfaces [123] and grain boundaries [122], and surface diffusion on a lattice with two non-equivalent sites [139]. Eq. (4.3) is formally identical to the classical McLean's equation, originally derived for segregation at grain boundaries [122], provided that $k = \exp(E_s / k_B T)$, where E_s can be interpreted as a VQW segregation energy. For $k = 1.81 \pm 0.05$, we obtain $E_s = 0.051 \pm 0.005$eV. We will see in Section 5.2.4 that this Ga incorporation rate enhancement can be ascribed to a more efficient Ga lateral diffusion from the sidewalls, with respect to Al. The physical mechanism giving rise to this preferential surface diffusion towards the bottom will also be discussed.

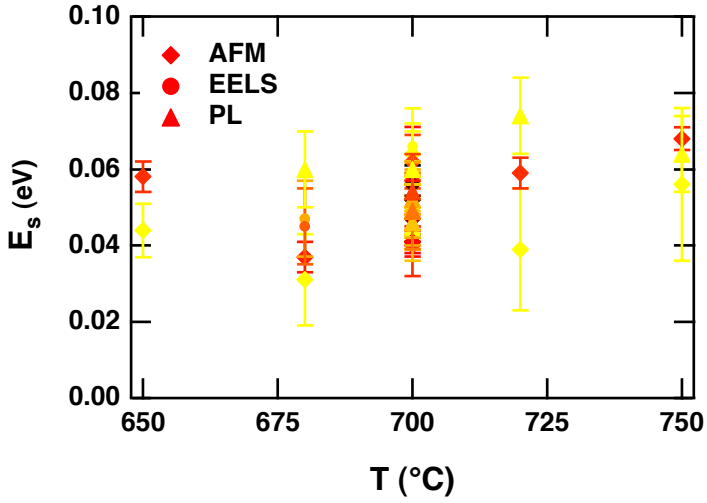

Figure 4.15: VQW segregation energy, given by (4.5), as a function of the growth temperature, measured by AFM (diamonds), EELS (circles) and PL (diamonds). Samples with x *ranging from 0.13 to 0.89 are shown, with darker grayscale corresponding to higher* x.

To study the temperature dependence of the Ga segregation in the VQWs, it is convenient to evaluate the quantity

$$E_s = k_B T \ln\left(\frac{1 - x_b}{x_b}\frac{x}{1 - x}\right), \tag{4.5}$$

which is independent of x. Besides, according to the segregation law, it should be also independent on T. In Figure 4.15 we plot this quantity as a function of T, measured by AFM

(diamonds) and EELS (circles), in the temperature range 625°C to 750°C. The grayscale in the data points corresponds to different x, with the darkest grade relative to the largest x (0.89) and the lightest grade relative to the smallest (0.13). Despite the rather large scattering of the data, the plot shows no evident dependence on T or x, confirming the applicability of the segregation model above to determine the composition of the VQW. The overall average of the values gives $E_s = 0.052 \pm 0.009$eV, in complete agreement with the value determined at 700°C alone.

Measuring the absolute value of x_b, for a given x, did not show any clear trend as a function of T, as reflected by the smallness of E_s. In particular, the VQW composition measured by AFM and PL (Figure 4.15) for $x = 0.23$ varies by less than 0.02, with no systematic temperature dependence. Consistently, the maximum segregation Δx^{max}, according to eq. (4.4), and with the value of E_s found above, is predicted to vary between 16.4 at 625°C and 14.4 at 750°C, with x^{max} practically constant. This independence on T is not in contrast to what was observed at 130mbar by Pan *et al.* [137], who reported a negligible PL energy shift (corresponding to a decrease in x_b as small as 0.01) in two VQW samples grown at 600°C and 650°C, respectively, with $x = 0.33$. On the other hand, Vermeire *et al.* [115] observed a more marked T dependence of the VQW luminescence properties, in samples grown at AP with $x = 0.35$. The decreased PL polarization anisotropy, observed in [115] as T is increased, could be explained by the lateral widening of the VQW (see Figure 4.12). However, the wavelength shift reported in this paper corresponds to a systematic x_b increase of about 0.1, as T is increased from 650 to 760°C, hence in the opposite direction and much stronger than the one observed in [137]. Therefore, it seems that the relative increase of Ga and Al surface mobility with T is reversed by increasing the reactor pressure.

4.3 Summary

In the first part of the chapter, we have introduced a simple and efficient method for imaging III-V heterostructures by cross-sectional AFM. The layer composition was imaged by using the composition dependence of the thin native oxide growth on the cleaved surface. We have investigated the oxidation properties of $Al_xGa_{1-x}As$ in air, finding that the oxidation process follows largely the mechanism proposed by Cabrera and Mott [126, 130]. With this method, the A1 mole fraction can be determined with an accuracy of ±0.02, using calibration curves measured at specific times after cleaving on a reference sample. Our studies demonstrate that AFM imaging of heterostructures in air is capable of detecting GaAs layers, embedded between AlGaAs, with a thickness as small as 1 nm, with an accuracy of ±0.5 nm. GaAs/AlGaAs QWRs and AlGaAs VQWs can be imaged with this technique.

In the second part of the chapter, we have studied systematically the structural properties of self-limiting AlGaAs VQWs, which form spontaneously at the bottom of V-grooved substrates in LP-OMCVD growth. Cross-sectional TEM analysis shows that the VQWs have a substructure composed of three distinct branches, which are associated with the nm-sized facets forming in this region. These branches are highly uniform both in the growth direction and

along the grooves. We have observed that a metastable, self-limiting VQB with a higher Al content can form at the top of the grooves, if the initial etched profiles are sharp enough. The width of the VQWs was found to decrease with increasing nominal Al mole fraction and decreasing growth temperature, suggesting that their formation is governed by surface diffusion mechanisms. The Ga segregation in the wells, studied by AFM, PL and EELS in the range $x = 0.1$ to 0.9 of nominal composition, was found to depend on x, and to be maximal (about 0.15) for $x \cong 0.57$. We observed on the other hand that the segregation does not depend appreciably on the growth temperature, in contrast with results reported earlier at AP [115]. The x and T dependence of the Ga segregation follows the McLean equation predicted by segregation models [122]. The resulting VQW segregation energy was found to be about 0.05eV, which is lower than the one measured for Ga segregation at surfaces in AlGaAs alloys (0.1±0.05eV) [123].

Chapter 5

Modeling of self-ordering on nonplanar surfaces

In this last chapter we will develop an analytic model that explains the phenomenology of self-ordering on nonplanar surfaces, described so far. These phenomena can be ascribed to local variations of the surface chemical potential μ, since this quantity defines the supersaturation, that is the (local, in this case) driving force for epitaxy. It can be shown that μ depends on the surface free energy γ and on the local surface curvature, and becomes lower as the concavity of the surface increases. These general concepts will be presented in Section 5.1. Using such a chemical potential, and a discretized-form of the Nernst-Einstein and continuity equations, in Section 5.2 we will develop a model that can account for the formation of self-limiting profiles, and for the transients between them. Self-ordering results from an interplay among effects of capillarity, growth rate anisotropy and entropy of mixing, in the case of alloys. The general equations developed in this framework will be applied to LP OMCVD growth on V-grooved substrates in Section 5.3, and compared with the experimental results presented so far. A kinetic Monte Carlo simulation of nonplanar growth, which agrees with the general features of the analytic model, will be presented at the end of the chapter.

5.1 Surface relaxation and ordering driven by diffusion

5.1.1 The surface chemical potential

We will first of all introduce the concept of surface chemical potential. This quantity determines both the equilibrium shape of a crystal, and the driving force (supersaturation) for epitaxy. We will see how local variations of the surface affect the chemical potential; in particular we will analyze the effects of surface curvature and tangential stress [1]. This latter term is not present in the case of unstrained systems, like AlGaAs/GaAs. However, its contribution will be briefly discussed, both for reason of generality and because, as we shall see, of analogies

[1] In general, the chemical potential of an interface contains also a contribution due to the influence of the stress normal to the interface on the emission or absorption of atoms at the interface [140]. This term is however not present in the case of free surfaces considered here [37, 141].

with the formalism that we will use for treating evolving surface shapes during nonplanar epitaxy.

5.1.1.1 Chemical potential of a smoothly curved surface

For a rigid solid containing N atoms in a volume V, bound by an arbitrary surface S, the free energy can be expressed as

$$F = \left(\frac{\mu_0}{\Omega_0} - P\right)V + \int y(\mathbf{n})dS\,, \tag{5.1}$$

where μ_0 is the chemical potential of the solid, Ω_0 is the atomic volume ($\Omega_0 = V/N$), P the equilibrium vapor pressure and γ the surface free energy, as defined in section 1.3.1. We can define a chemical potential for a given F as [59]

$$\mu = \frac{\partial}{\partial N}(F + PV)\bigg|_{T,P} = \frac{\partial G}{\partial N}\bigg|_{T,P}\,, \tag{5.2}$$

where G is the Gibbs free energy of the system. To relate μ to μ_0, we calculate the effects on F of an infinitesimal deformation δdS of a surface element dS_0 (see Figure 5.1). To the first order in the thickness of the deformation, the variation of the surface contribution to F is [142]:

$$\delta\int\gamma dS = \int\delta\gamma dS_0 + \int\gamma\delta dS\,.$$

It can be shown [142] that, for a smoothly curved surface (i.e., with no cusp points), the right-hand side terms of the equation above can be written as:

$$\int\delta\gamma dS_0 = \left(\frac{\partial^2\gamma}{\partial\theta_1^2}\frac{1}{R_1} + \frac{\partial^2\gamma}{\partial\theta_2^2}\frac{1}{R_2}\right)\delta V$$

$$\int\gamma\delta dS = \gamma\left(\frac{1}{R_1} + \frac{1}{R_2}\right)\delta V$$

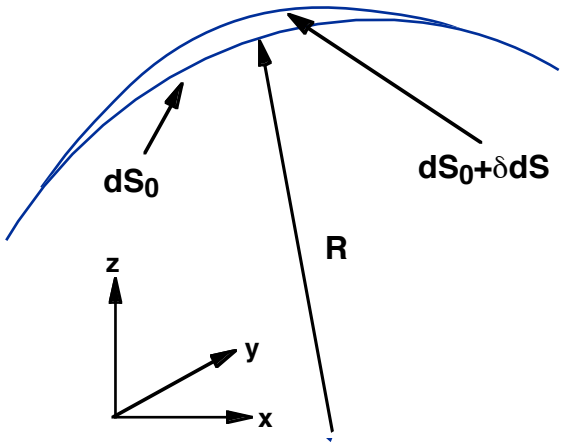

Figure 5.1: Infinitesimal deformation of an element of surface dS_0, *characterized by a radius of curvature* R.

where θ_1 and θ_2 are the angles defining the surface normal **n** along the x and y directions, R_1 and

R_2 are the principal radii of curvature of dS along x and y, and δV is the infinitesimal volume variation caused by the deformation. Therefore, the variation of the free energy (5.1) can be written as

$$\delta F = \left(\frac{\mu_0}{\Omega_0} - P \right) \delta V + \gamma \left(\frac{1}{R_1} + \frac{1}{R_2} \right) \delta V + \left(\frac{\partial^2 \gamma}{\partial \theta_1^2} \frac{1}{R_1} + \frac{\partial^2 \gamma}{\partial \theta_2^2} \frac{1}{R_2} \right) \delta V$$

or, from (5.2),

$$\delta F = \left(\frac{\mu}{\Omega_0} - P \right) \delta V \quad ,$$

where $\delta N = \delta V / \Omega_0$. By equating these two relations, we find the so-called Gibbs-Thomson (GT) equation [142]

$$\mu = \mu_0 + \left[\gamma \left(\kappa_1 + \kappa_2 \right) + \frac{\partial^2 \gamma}{\partial \theta_1^2} \kappa_1 + \frac{\partial^2 \gamma}{\partial \theta_2^2} \kappa_2 \right] \Omega_0 \ , \tag{5.3}$$

where $\kappa_1 = 1 / R_1$ and $\kappa_2 = 1 / R_2$ are the surface curvatures along x and y [2,3].

Since at equilibrium $\mu=\mu_0$, this relation tells that the equilibrium surface will be flat. Any surface with an arbitrary shape, if let to itself, will therefore flatten down until it will planarize.

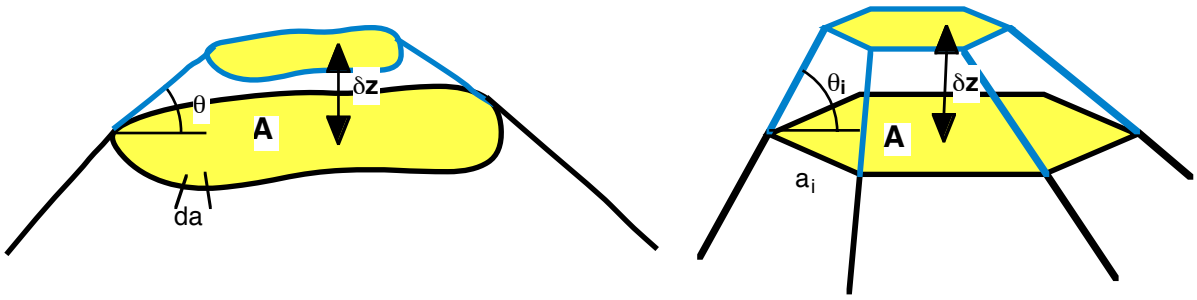

Figure 5.2: Changes of a crystal shape when a layer of constant thickness δz *is added to a flat facet* A *bounded by a smooth (left) or a faceted surface (right).*

---

[2] Note that this expression, in the case of isotropic surface free energy, assumes the simple form, calculated for a spherical liquid droplet of radius R, immersed in its vapor: $\mu = \mu_0 + (2\gamma / R)\, V_l$, where V_l is the molar volume of the liquid phase (see, e.g., [143], pag. 78). As in the liquid, therefore, a curved surface induces an increase in the chemical potential, with respect to the bulk.

[3] Chernov has shown [144] that, as expected, the minimization of γ at constant volume, leading to the Wulff construction (Section 1.3.1), is identical to solving the GT equation for constant μ over the surface. In particular, facets are expected to correspond to the cusps of $\gamma(\theta_1, \theta_2)$, since a zero curvature is required in order to maintain μ finite when $\partial^2\gamma / \partial\theta^2$ diverges (see below).

5.1.1.2 Chemical potential of a faceted surface

If the surface is composed of flat facets separated by sharp corners, the γ-plot defined in Section 1.3.1 contains sharp minima in the directions corresponding to these facets (see Figure 1.11). In these directions, therefore, the terms $\partial^2\gamma/\partial\theta^2$ in the GT equation will diverge. Herring [142, 145] developed an alternative approach to treat the surface energy contributions to the chemical potential in the case of faceted surfaces.

An infinitesimal parallel displacement δz of a flat facet A, with surface free energy γ_0, and bounded by an arbitrary surface profile (Figure 5.2, left), causes an increase of the surface contribution to the free energy in equation (5.1) that is given by [142]:

$$\delta\int\gamma dS = \int\left(\gamma_1\delta z\csc\theta - \gamma_0\delta z\cot\theta\right)da \tag{5.4}$$

where γ_1 is the surface free energy of the surrounding surface (that in general depends on the local surface orientation), θ is the angle between A and the surrounding surface, and the integration on da is extended over the perimeter of the facet A. If the surrounding profile is completely faceted (Figure 5.2, right), the integral in (5.4) is replaced by a sum over the N neighboring facets [145], each forming with A an edge of length a_i:

$$\delta\int\gamma dS = \sum_{i=1}^{N}\left(\gamma_i\delta z\csc\theta_i - \gamma_0\delta z\cot\theta_i\right)a_i\ ,$$

with the symbols defined as above. By following the same procedure as for the case of the smooth surface above, we can express the chemical potential as

$$\mu = \mu_0 + \frac{\Omega_0}{A}\int\left(\gamma_1\csc\theta - \gamma_0\cot\theta\right)da \tag{5.5a}$$

$$\mu = \mu_0 + \frac{\Omega_0}{A}\sum_{i=1}^{N}\left(\gamma_i\csc\theta_i - \gamma_0\cot\theta_i\right)a_i\ , \tag{5.5b}$$

for a smooth or faceted bounding contour, respectively.

5.1.1.3 Chemical potential of a stressed surface

Let us consider now a surface with a negligible curvature, but where a nonuniform strain field is present. This is the situation, for example, created by a strain-induced Stranski-Krastanow island (e.g., InAs in GaAs) on the host material in which it is buried (see Figure 5.3)

According to its definition as the change of free energy associated with the addition or removal of an atom, the chemical potential depends on the local stress, since this free energy changes according to the nature and magnitude of the stress [141]. Taking this effect into account, the chemical potential can be written as [37, 141]

$$\mu = \mu_0 + \frac{\Omega_0}{2E}\left[\sigma_\tau(x,y)\right]^2, \tag{5.6}$$

where σ_τ is the (local) tangential stress and E is the elastic modulus, dependent on the surface orientation.

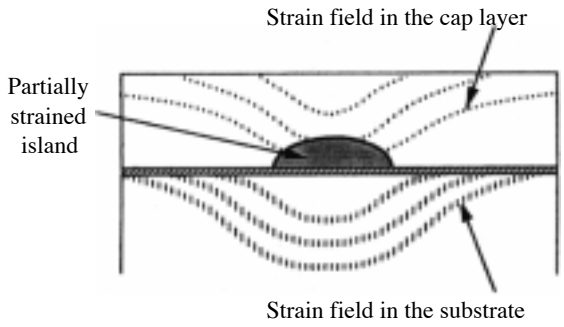

Figure 5.3: Schematic representation of the strain fields induced by a buried InAs island in the GaAs substrate and cap layer [24].

5.1.2 Thermal smoothening of a nonplanar profile

The most extensively studied phenomenon, that depends on local variations of the surface chemical potential, is probably the thermal smoothening of a nonplanar profile, commonly defined as "capillarity". Experimentally, this can be done by creating a periodic profile on an otherwise planar surface, and observing the decaying of its amplitude and changes of its shape as a function of time, upon annealing (for a review of experimental work see, for example, [146] and references therein). Intuitively, this smoothening is associated with a flux of atoms from convex to (energetically more favorable) concave regions, where an atom "can find" more bonds and therefore be incorporated more easily into the crystal. In terms of the surface chemical potential, this translates into a flux from regions with high μ (positive curvature) to regions with low μ (negative curvature), according to the GT equation (5.3). In the rest of this section we will formalize this phenomenon, and examine the difficulties associated with anisotropies in the surface free energies and faceting of the surface profile.

The surface flux j in the presence of a varying chemical potential is given by the Nernst-Einstein relation

$$j = -\frac{nD}{k_B T}\frac{\partial \mu}{\partial s}, \tag{5.7}$$

where n is the surface density of adatoms, D the surface diffusion coefficient and ds an infinitesimal surface arc length. We will limit ourselves to one-dimensional profiles (i.e., a sequence of grooves); we can therefore neglect the surface coordinate parallel to the grooves and write $ds = (dx^2+dz^2)^{1/2}$. In absence of evaporation-condensation[4], the evolution of the profile $z = z(x,t)$ is given by the continuity equation

[4] The treatment of surface smoothening via evaporation-condensation and volume diffusion, based on the original work of Mullins [109], can be found, for example, in [59], pag. 102. The results are qualitatively similar to the diffusion kinetics, but the characteristic decay times depend differently on the pitch Λ of the profile. In practice, at least for metals, diffusion is the dominant process for $\Lambda < 10\mu$m and T< 1000°C [59].

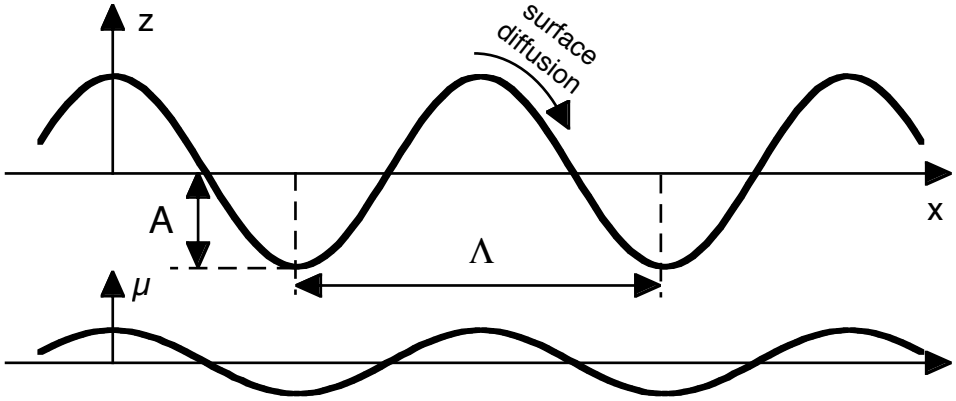

Figure 5.4: Sinusoidal surface profile (top) and corresponding chemical potential, as given by equations (5.9)-(5.10).

$$\frac{\partial z}{\partial t} = -\Omega_0 \frac{\partial j}{\partial x} . \tag{5.8}$$

The chemical potential is given by the GT equation (5.3), that in one dimension becomes

$$\mu = \mu_0 + \left(\gamma + \frac{\partial^2 \gamma}{\partial \theta^2} \right) \Omega_0 \kappa , \tag{5.9}$$

with

$$\kappa(x) = -\frac{d^2 z}{dx^2} \left[1 + \left(\frac{dz}{dx} \right)^2 \right]^{-3/2} . \tag{5.10}$$

The set of three equations (5.7)-(5.9) defines completely the problem.

At temperatures higher than the roughening transition T_r, the surface energy is continuous everywhere, and the term $\partial^2 \gamma / \partial \theta^2$ can be generally considered small, with respect to γ. In the approximation of small slopes ($dz \ll dx \approx ds$), and considering $\gamma \approx$ constant, combining equations (5.7)-(5.9) Mullins found out that the time dependence of the nonplanar height profile is given by [109]

$$\frac{\partial z}{\partial t} \cong -\frac{nD\Omega_0^2 \gamma}{k_B T} \frac{\partial^4 z}{\partial x^4} . \tag{5.11}$$

If the starting surface is a sinusoidal profile $z_0 = A_0 \cos(2\pi x/\Lambda)$ (Figure 5.4), the time-dependent profile will be shape-preserving, i.e., a sinusoidal profile with an amplitude decaying exponentially with time:

$$A = A_0 \exp(-t/\tau)$$

with

$$\tau^{-1} = \frac{(2\pi)^4 nD\Omega_0^2 \gamma}{k_B T \Lambda^4} . \tag{5.12}$$

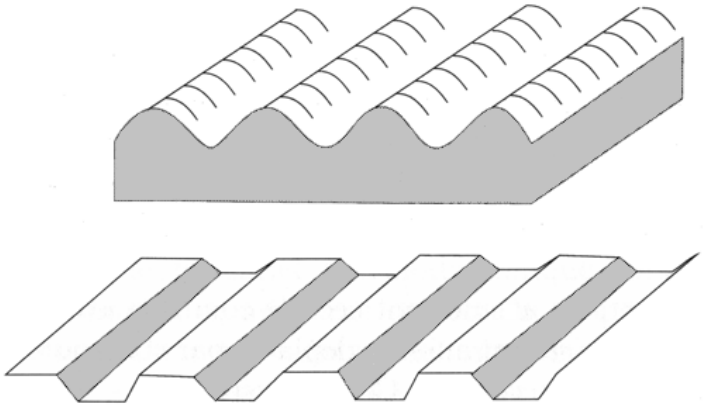

Figure 5.5: Formation of facets upon thermal annealing of a periodic profile with an initial sinusoidal shape [59].

Since any periodic profile can be decomposed into its Fourier components, the linearity of eq. (5.11) and the strong Λ dependence of eq. (5.12) imply that the higher harmonics of the profile decay much faster than the fundamental component. An arbitrary contour will therefore always converge to a decaying sinusoidal profile. By measuring the decay time τ, it is possible to extract an "effective diffusivity" nD (provided the surface free energy is known). This quantity should have an Arrhenius form, since

$$\begin{aligned} n &= a^{-2}\exp\left(-\Delta F_F / k_B T\right) \\ D &= D_0 \exp\left(-E_B / k_B T\right), \end{aligned} \tag{5.13}$$

with a = lattice constant, ΔF_F = free energy of formation of an adatom, and E_B = binding energy to the substrate.

Mullins' theory has the advantage of simplicity, in providing an analytic solution to the problem that can be easily verified experimentally. There are a number of experimental evidences, however, which contradict Mullins' predictions. In particular, measurements on metal [147] and Si surfaces [148] have evidenced the formation of facets in the decaying profile (Figure 5.5). These deviations from Mullins' theory originate in the anisotropic nature of the surface free energy. A first attempt to take into account the anisotropy of γ is due to Bonzel *et al.* [147], who solved numerically the exact form of the continuity equation (5.11) (analytic solutions to this non-linear equation have not been found yet):

$$\frac{\partial z}{\partial t} = \frac{nD\Omega_0^2}{k_B T}\left[1+\left(\frac{\partial z}{\partial x}\right)^2\right]^{-1/2}\left\{\left[1+\left(\frac{\partial z}{\partial x}\right)^2\right]^{-1}\frac{\partial z}{\partial x}\frac{\partial^2 z}{\partial x^2}\frac{\partial}{\partial x}-\frac{\partial^2}{\partial x^2}\right\}\left\{\left[\gamma(\theta)+\frac{\partial^2\gamma}{\partial\theta^2}\right]\left[1+\left(\frac{\partial z}{\partial x}\right)^2\right]^{-3/2}\frac{\partial^2 z}{\partial x^2}\right\}.$$

The solutions to the equation above could well reproduce the faceting observed on Ni(110) patterned surfaces [147]. Below T_r, it became however clear that the surface step structure and the step-step interactions (energetic and entropic) affect in a relevant way the chemical potential. Various authors have examined the morphological evolution of a periodic profile below T_r. Villain [149], by considering a density of surface free energy of the form $G=G_0+G_1\left|\partial z/\partial x\right|+1/3G_3\left|\partial z/\partial x\right|^3+...$, derived an expression for the chemical potential, that

can be written as $\mu=\mu_0-2G_3\Omega_0 \left| \partial z/\partial x \right| \partial^2 z/\partial x^2$. Ozdemir and Zangwill [150] have developed both a continuum theory (based on the above form of μ) and a microscopic model (based on entropic repulsions between parallel steps), finding a time dependence of the type $z(x,t)\sim t^{-1}$. Recently [146], the influence on the chemical potential of step annihilation on the top and bottom terraces via thermal fluctuations was analyzed, both with an analytic model and a MC simulation, resulting in deviations from the classical Mullins' model. The problem is however at present far from being resolved, and contradictions exist among the different models, mainly because of the difficulty in determining the orientation dependence of the surface free energy and the mechanisms of surface diffusion.

5.1.3 Vertical self-organization of strained 3D islands

This section will briefly show an example of how chemical potential-driven surface diffusion can account for self-ordering in strained epitaxy. As seen in section 1.1.2, the size uniformity and spatial correlation are a critical issue for the quantum confinement properties of strained 3D islands. The strain fields created by the islands account for a partial island size equalization, but they propagate also in the cap layer of the host material (see Figure 5.3). Therefore atoms of a second plane of the strained material will find an energetically more favorable situation on top of the islands of the layer below, provided the spacer in between is thin enough to keep a residual strain field on the surface. This is what has been found by Xie *et al.* for the InAs/GaAs system in MBE growth [37], as shown in the TEM micrographs of Figure 5.6 (left).

In terms of the chemical potential, relation (5.6) induces a surface flux of InAs towards the stressed regions, i.e., above the islands of the layer below (see Figure 5.6, right). We will not enter into the details of the model, since we will follow a similar formalism to analyze our self-limiting growth on nonplanar substrates, as described in the next section. This model gives an island pairing probability decreasing with increasing spacer thickness, which fits well to the observed thickness dependence [37].

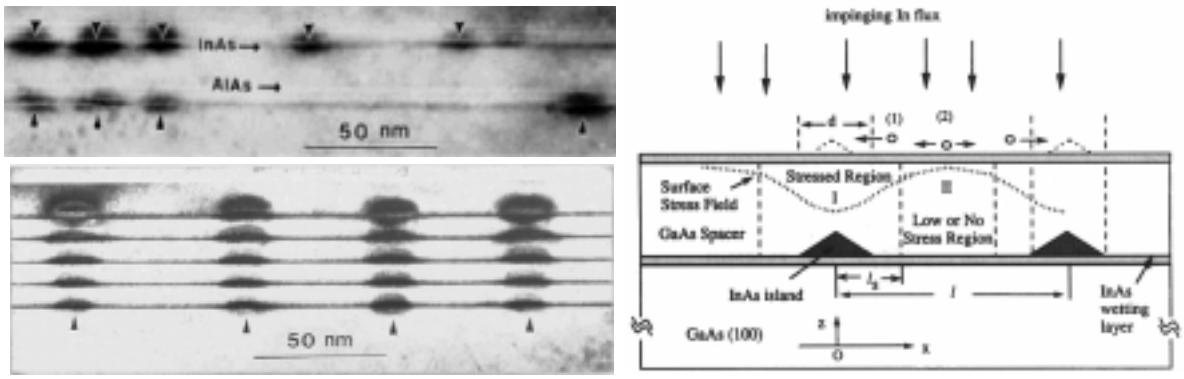

Figure 5.6: Left: TEM cross sections of two InAs layers separated by 92ML GaAs spacers (top), and five InAs layers separated by 36ML spacers (bottom), grown by MBE. Note the increase of the vertical correlation between islands as the spacer gets thinner. Right: schematics of the proposed diffusion model, based on strain-induced chemical potential differences [37].

5.2 Modeling of self-limiting growth on V grooves

In this section, we will use the principles discussed above to develop a model accounting for the self-ordered OMCVD growth on V-grooved substrates, as described phenomenologically in the previous chapters. We will first of all write the equations appropriate to our physical system, and later we will apply this model to the experimental observations of the previous chapters.

5.2.1 General equations

The starting point for the model is to find the equivalent of the basic equations (5.7)-(5.9), appropriate for our system. In particular, two elements must be taken into account, as explained in the following paragraphs.

5.2.1.1 Growth rate anisotropy

Since we are concerned primarily with the evolution of nonplanar profiles *during OMCVD growth*, we must add in eq. (5.8) a growth flux to the lateral diffusion flux. Note that, in absence of growth, no self-limiting nonplanar profile can exist since, according both to the classical Mullins' theory and to the more recent implementations, the surface will always tend to planarize at equilibrium, if left to develop on its own. Furthermore, this will be the situation also if a uniform growth rate is added to eq. (5.8), since its effect will be only a vertical shift of the surface parallel to itself. Therefore, as we will see, the anisotropy of the growth rate, depending on the surface orientation, will be a critical parameter in determining the self-ordering properties of our system.

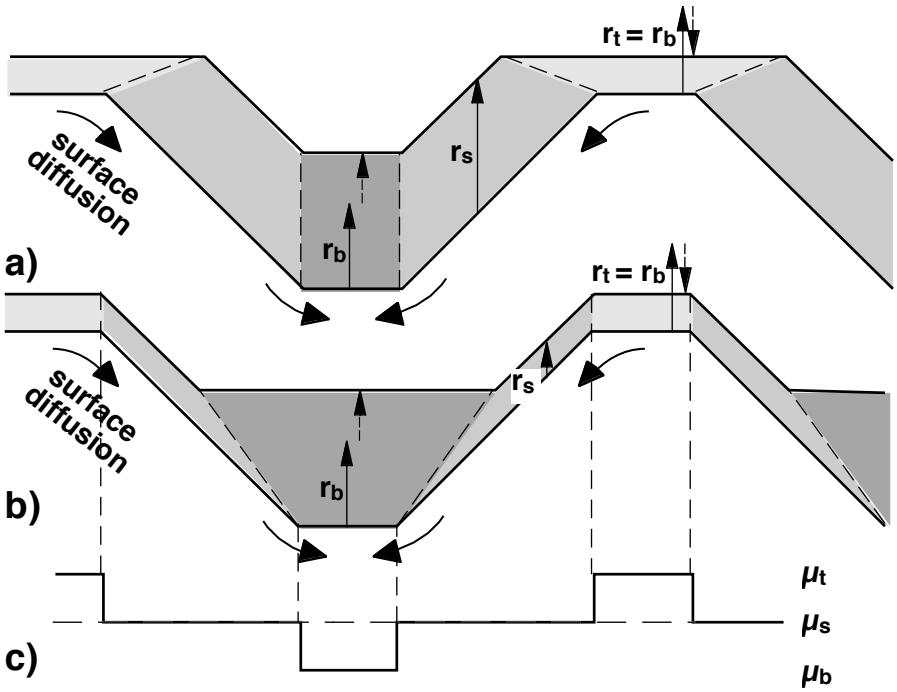

*Figure 5.7: Schematic representations of a groove, composed of a bottom (100) (*b*), a sidewall (*s*) and a top (100) (*t*) facet (not to scale). a) Evolution of the growth front as commonly observed in OMCVD. b) The same for MBE. c) Chemical potential at each facet.*

As we have seen in Section 1.3, the determination of the complete orientation dependence of the growth rates on a nonplanar substrate would require the solution of coupled gas phase and surface diffusion equations, appropriate for the species involved and the geometry of the substrate. We will not tackle this problem in our model, since we are mostly concerned with the effects that growth rate anisotropy has on the self-limiting properties of our systems, and not on the quantitative analysis of its origin. Besides, predictions of such diffusion models are based inevitably on a number of unknown parameters, that must be determined by fitting the observed growth rates. Our treatment of the growth rates on different facets will therefore rely on the qualitative features discussed in section 1.3 and on the experimental observations of section 2.2.2. As a result of the very efficient lateral diffusion of precursors (with diffusion lengths much larger than the groove pitch Λ), no growth rate variations are observed across the sidewalls in going from the top to the bottom of the groove. We can therefore assume that the "intrinsic" growth rate (i.e., in the absence of capillarity) on a facet is uniform, and depends only on the facet orientation. By referring to the polar plot of the growth rates (Figure 2.8), we can express the growth rate (in the growth direction [5]) $R_{\{ijk\}}$ on the facet {ijk} as a function of the nominal growth rate R on a planar reference sample as

$$R_{\{ijk\}} = R \cdot r_{\{ijk\}} , \tag{5.14}$$

with $r_{\{ijk\}}$ a constant typical for the facet.

Since, as seen in Section 2.2.2, $r_s > r_{311} \cong r_{100}$ (with the subscript s = sidewall), in the absence of capillarity the bottom facets would disappear during growth (see eq. (1.10) and Figure 1.13). Moreover, their formation itself would not be justified, according to the construction of Jones et al. [63] (Figure 1.14). The achievement of a self-limiting profile is therefore due to an *interplay between capillarity* (that would tend to expand the bottom facets until planarization) *and growth rate anisotropy* (that would tend to suppress these bottom facets). Note that, according to this picture, a self-limiting state can not be reached at the top of the mesas, since in this region capillarity tends to drive atoms away from the top facets. Therefore, both capillarity and growth rate anisotropy cause an increase of the growth rate on the sidewalls, with respect to the top facets. According to Figure 1.13, this will lead to a planarization of the V groove, as observed in OMCVD. The evolution of the top and bottom facets, for the case where the sidewalls growth rate is higher than the one at the extremities of the groove, is shown in Figure 5.7a.

The different behavior of MBE growth on V-grooved substrates can also be explained qualitatively in terms of growth rates anisotropy. With MBE, nonplanar growth results in general in the formation of exactly oriented {111}A or {111}B sidewalls, depending on the

---

[5] For clarity, we will refer all our space-dependent variables (growth rates, surface densities, diffusion lengths and constants...) and derivatives to a cartesian system with vertical and horizontal coordinates. Values along a facet or its normal are found by scaling by the cosine of the angle between the facet and the horizontal.

orientation of the grooves. Since the growth rate on these planes is lower than on the (100) facets for a large range of growth conditions, effects of capillarity at the bottom of the groove will add up to growth rate anisotropy, causing an indefinite thickening and widening of the bottom of the groove. This would explain the difficulty in obtaining self-limiting growth at the bottom of a V groove with MBE [151]. The opposite situation is realized at the top of the mesas: in this case diffusion of atoms from the top ridges to the sidewalls due to capillarity can be balanced exactly by atom diffusion with opposite sign, due to growth rate anisotropy. This would yield a self-limiting behavior on the ridges, as was experimentally observed [16, 152]. This situation is shown in Figure 5.7b.

5.1.1.2 Faceting of the profile

Since we observed a distinct formation of facets, and we are not dealing with small perturbations with respect to a planar surface, it is evident that the approximations that led to Mullins' equation (5.11) can not be applied in the present situation. Rather, an appropriate form of the chemical potential must be found, that takes into account the anisotropy of surface energy (implied by the marked faceting of our profiles).

Following the procedure of Ozdemir and Zangwill [145], we will suppose that epitaxial growth on periodic profiles exposes a set of facets with fixed orientation; these facets evolve parallel to themselves, and no new facets can appear. These assumptions are justified by experimental observations; the only deviation from this picture is a weak dependence of the orientation of the sidewalls on the growth conditions (x, T). Since these variations of orientation are limited to about 5° for most growth conditions (see Figure 2.5), we will assume that changes of the surface energy associated with these variations can be neglected. Furthermore, growth rates on the sidewalls are constant, within ~10% (see Figure 2.10), depending on the growth conditions and orientation. Our surface will be composed therefore of five different facets (see Figure 5.8, top), as described in Table 5.1. Note that the sets of facets at the top and at the bottom of the groove have the same orientation and crystallographic structure, and therefore the same surface energy. The corresponding chemical potentials can be calculated by using equation (5.5)b, yielding:

Facet	Length	Angle with respect to (100)	Surface energy
top (100)	l_{1t}	0	γ_1
top {311}A	l_{3t}	α=25°	γ_3
sidewall	l_s	$\theta \cong 45°$	γ_s
bottom {311}A	l_{3b}	α=25°	γ_3
bottom (100)	l_{1b}	0	γ_1

Table 5.1: Set of facets considered in the model, with the respective length, angle with respect to the (100) plane and (orientation-dependent) surface free energy (see Figure 5.8).

$$\begin{aligned}
\mu_{1t} &= \mu_0 + \frac{\bar{\gamma}_1 \Omega_0}{l_{1t}} \\
\mu_{3t} &= \mu_0 + \frac{\bar{\gamma}_3 \Omega_0}{l_{3t}} \\
\mu_s &= \mu_0 \\
\mu_{3b} &= \mu_0 - \frac{\bar{\gamma}_3 \Omega_0}{l_{3b}} \\
\mu_{1b} &= \mu_0 - \frac{\bar{\gamma}_1 \Omega_0}{l_{1b}}
\end{aligned} \tag{5.15}$$

where

$$\begin{aligned}
\bar{\gamma}_1 &= 2\left(\gamma_3 \csc\alpha - \gamma_1 \cot\alpha\right) \\
\bar{\gamma}_3 &= \gamma_s \csc(\theta-\alpha) + \gamma_1 \csc\alpha - \gamma_3\left(\cot(\theta-\alpha) + \cot\alpha\right).
\end{aligned} \tag{5.16}$$

Note that $\bar{\gamma}_3$, $\bar{\gamma}_1 > 0$ is required in order to reproduce the physically realistic situation in which the chemical potential decreases monotonically in going from the top of the ridges to the bottom of the grooves, thus providing a positive driving force for adatoms towards the bottom of the groove. In this case, the chemical potential varies across the groove in the way depicted schematically at the bottom of Figure 5.8. Note that μ has a similar qualitative behavior as in the case of a smoothly curved surface (Figure 5.4), but is not continuous, due to the faceted nature of the profile.

To reduce the number of parameters involved in the problem, it is useful to simplify the geometry of the profile, by considering only a "bottom region" of lateral extension $l_b = l_{1b} + 2l_{3b}\cos\alpha$ and a "top region" of lateral extension $l_t = l_{1t} + 2l_{3t}\cos\alpha$, separated by the sidewall. This would allow a more direct testing of the predictions of the model, by comparing the evolution of l_b, as a function of the growth parameters, with the measured values of the total length of the bottom facets, or the related value of the radius of curvature of the bottom. We show in Appendix B the qualitative predictions of a model taking into account the full facet structure of the profile in Figure 5.8. Since the boundary of relevance, even in the simplified picture, is the one between the sidewalls and the {311}A facets, we can still take into account the crystallographic orientation of the latter by assigning a surface energy γ_3 to the bottom and top regions, and consider that the bottom and the sidewalls intersect at an angle $(\theta-\alpha)$. With only three facets, the set of five equations (5.15) reduces to [145]

$$\begin{aligned}
\mu_t &= \mu_0 + \frac{\gamma \Omega_0}{l_t} \\
\mu_s &= \mu_0 \\
\mu_b &= \mu_0 - \frac{\gamma \Omega_0}{l_b}
\end{aligned} \tag{5.17}$$

with

$$\gamma = 2\left(\gamma_s \csc(\theta-\alpha) - \gamma_3 \cot(\theta-\alpha)\right). \tag{5.18}$$

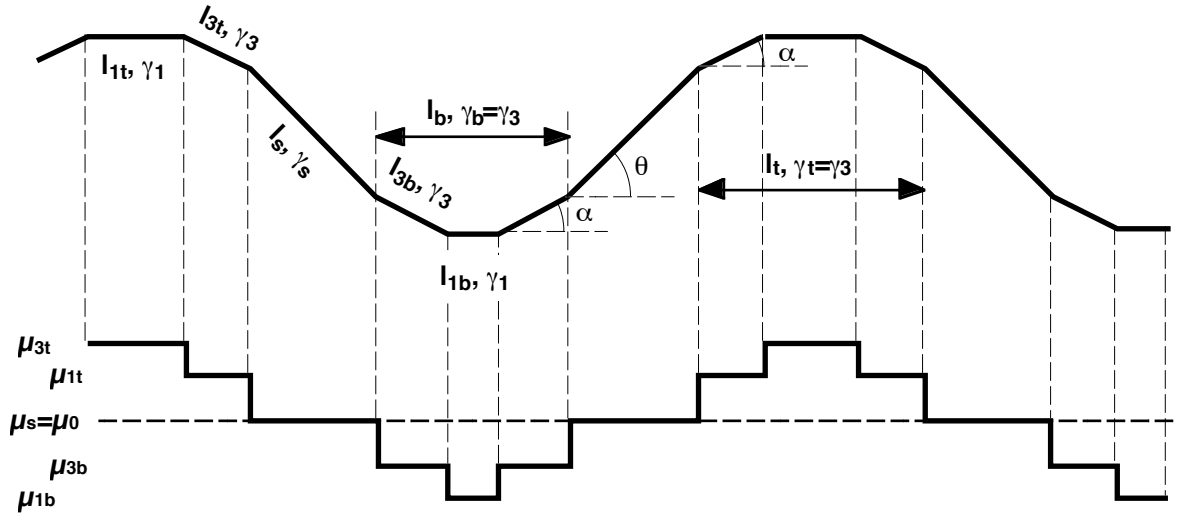

Figure 5.8: Top: schematic cross section of the nonplanar profile used in the model, showing the facets described in Table 5.1. Bottom: corresponding chemical potential. Note the qualitative similarity to the chemical potential at a smoothly curved surface (Figure 5.4).

Note that, in this case, the requirement of monotonic decrease of μ in going from the top ridge to the bottom region, becomes $\gamma_s > \gamma_3 \cos(\theta-\alpha) \cong 0.94\ \gamma_3$. This assumption is reasonable since, according to the Wulff construction, low index facets in the groove are associated with (cusped) minima in the surface energy, while the sidewalls are high index surfaces, therefore associated with a larger value of γ.

Once the chemical potential for this particular geometry is known, we have to find a suitable form of the Nernst-Einstein and continuity equations (5.7)-(5.8) for the discontinuous μ of eq. (5.17), taking in account also a nonuniform growth flux, as discussed previously. Derivatives of the chemical potential and of the diffusion flux should be replaced by discrete variations across neighboring facets. Solving this set of equations will determine in principle the growth rate on each facet, subject to lateral diffusion fluxes due to capillarity effects. To deal with these equations, we will follow the same formalism that Xie *et al.* [37] applied to the case of vertical self-organization if strained InAs islands (see Section 5.1.3). Eq. (5.7) can be discretized by introducing a surface flux from facet *j* to facet *i*:

$$j_{ij} = \frac{nD_j}{k_B T} \frac{\mu_j - \mu_i}{\lambda_{ij}}$$

and a rate of atom transfer K_{ij} from facet *j* to facet *i*, with the dimensions of a speed, defined as

$$K_{ij} = \frac{j_{ij}}{n} = \frac{D_j}{k_B T} \frac{\mu_j - \mu_i}{\lambda_{ij}}\ , \qquad (5.19)$$

where λ_{ij}, in analogy with the case of strain-dependent chemical potential [37], is a distance over which the effects of curvature become negligible. We therefore assume $\lambda_{ij} \sim l_b,\ l_t$. Note that $D_j / k_B T$ is the adatom surface mobility on the facet *j*, and $(\mu_j - \mu_I) / \lambda_{ij}$ is the average driving force for adatom diffusion. By using (5.17), eq. (5.19) becomes, at the interfaces between the sidewall and the top and bottom regions, respectively:

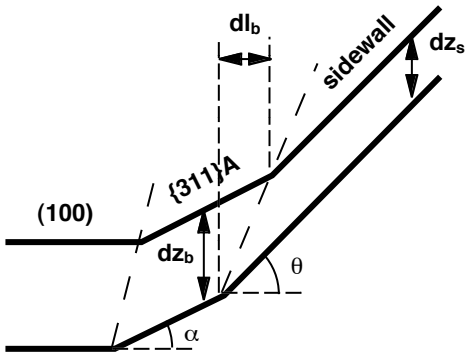

Figure 5.9: Schematics showing the geometrical relation between an infinitesimal height variation of the sidewalls dz_s *and of the bottom facets* dz_b*, and the corresponding variation of the extension of the bottom region* dl_b.

$$K_{ts} = \frac{D_s}{k_B T}\frac{\mu_s - \mu_t}{l_t} = -\frac{D_s \Omega_0 \gamma}{k_B T l_t^2} < 0$$
$$K_{bs} = \frac{D_s}{k_B T}\frac{\mu_s - \mu_b}{l_b} = \frac{D_s \Omega_0 \gamma}{k_B T l_b^2} > 0 \qquad (5.20)$$

The continuity equation (5.8) must now be written for the height $z_j(t)$ above each facet j, bounded by facets i and k, and assumes the form

$$\frac{dz_j}{dt} = R_j + \frac{\Omega_0}{l_j}(n_+ K_{ij} - n_- K_{jk}), \qquad (5.21)$$

where n_+ and n_- are the adatom concentrations at the boundaries with facets i and k, respectively. The set of equations (5.14), (5.17)-(5.21), solved for the different facets, provides the complete evolution of the nonplanar profile, composed of facets with known and stable orientation. In particular, at the top, sidewall and bottom facets, the growth rates become:

$$\frac{dz_t}{dt} = R_b + \frac{2\Omega_0 n_{ts} K_{ts}}{l_t}$$
$$\frac{dz_s}{dt} = R_s + \frac{\Omega_0}{l_s}\left(n_{ts} K_{ts} + n_{bs} K_{bs}\right) \qquad (5.22)$$
$$\frac{dz_b}{dt} = R_b + \frac{2\Omega_0 n_{bs} K_{bs}}{l_b}.$$

In the first and last relations, we take into account the symmetry of the boundaries limiting the top (bottom) facets, that yields $K_{st} = -K_{ts}$ ($K_{sb} = -K_{bs}$) and $n_+ = n_- = n_{ts}$ ($=n_{bs}$), and the crystallographic equivalence between the two regions ($R_t = R_b$).

Finally, the length of the bottom region l_b is related to the growth rate of the bottom and sidewall regions by the geometrical relation (see Figure 5.9):

$$\frac{dl_b}{dt} = p\left(\frac{dz_b}{dt} - \frac{dz_s}{dt}\right); \quad p = \frac{2}{\tan\theta - \tan\alpha} \cong 3.75 \qquad (5.23)$$

if $\theta \approx 45°$ and $\alpha \cong 25°$, where the factor 2 is due to the (symmetric) variations on both sides of the bottom facets. A similar relation holds for l_t, except for a minus sign multiplying the right part of the relation above.

5.1.2 Flattening of the profile in the absence of growth

If no growth flux is present, eq. (5.22) become:

$$\frac{dz_t}{dt} = \frac{2\Omega_0 n K_{ts}}{l_t}$$
$$\frac{dz_s}{dt} = \frac{\Omega_0}{l_s}\left(nK_{ts} + nK_{bs}\right)$$
$$\frac{dz_b}{dt} = \frac{2\Omega_0 n K_{bs}}{l_b},$$

where in this case n is the equilibrium concentration of adatoms. By substituting the values of K_{ts} and K_{bs} from (5.20), we obtain

$$\begin{aligned} &\frac{dz_t}{dt} = -\frac{C}{l_t^3} \\ &\frac{dz_s}{dt} = \frac{C}{2l_s}\left(\frac{1}{l_t^2} - \frac{1}{l_b^2}\right) \\ &\frac{dz_b}{dt} = \frac{C}{l_b^3}, \\ &\text{with} \quad C = \frac{2n\Omega_0^2 D_s \gamma}{k_B T}. \end{aligned} \tag{5.24}$$

We have seen in Chapter 2 that, in conditions close to equilibrium, when surface diffusion processes become dominant over deposition (e.g., at low x, high T, and during extended growth interruptions), the sidewall planes break down into low-index facets, influencing eventually also the shape of the bottom region. We will limit our analysis only to the first phases of the relaxation process, when the evolving contour is still shape-preserving, and no additional faceting takes place on the sidewalls and on the extrema of the groove. Since this faceting appears when the sidewall regions are still extending over the majority of the grooved profile, we can assume that $l_s \gg l_t, l_b$. This implies that in (5.24) $|dz_s/dt| \ll |dz_t/dt|$, $|dz_b/dt|$, therefore (5.23) becomes, for the top and bottom facets, respectively:

$$\frac{dl_{b,t}}{dt} \cong \frac{Cp}{l_{b,t}^3},$$

that can be integrated, yielding

$$\begin{aligned} &l_t = l_{t0}\left(1 + t/\tau_t\right)^{1/4}; \quad \tau_t = l_{t0}^4 / 4Cp \\ &l_b = l_{b0}\left(1 + t/\tau_b\right)^{1/4}; \quad \tau_b = l_{b0}^4 / 4Cp \end{aligned} \tag{5.25}$$

These equations show that both the top and the bottom of the profile tend to widen *ad infinitum* in the absence of a growth flux. Therefore, as expected qualitatively from Mullins' analysis, no nonplanar self-limiting profile can be established in the presence of surface diffusion alone, and the monotonic expansion of the groove extrema will eventually lead to its planarization.

5.1.3 Self-limiting profiles during epitaxial growth

When a growth flux is present, the set of eqs. (5.22) must be used. In this case, the adatom concentration will differ from its equilibrium value, and will not be uniform across the length of a facet. To find the concentrations n_{ts} and n_{bs} at the boundaries between the sidewalls and the top and bottom regions, respectively, we will apply the general formalism of Schwoebel [37, 153] on the sidewall regions. The concentration of adatoms on the sidewalls $n_s(x)$ obeys the continuity equation

$$-D_s \frac{d^2 n_s(x)}{dx^2} = \frac{R_s}{\Omega_0} - \frac{n_s(x)}{\tau_s}, \tag{5.26}$$

whose solutions are

$$n_s(x) = A\cosh\left(x/L_s\right) + B\sinh\left(x/L_s\right) + \frac{R_s\tau_s}{\Omega_0},$$

with boundary conditions

$$K_{bs} n_s\left(-l_s/2\right) = D_s \left.\frac{dn_s(x)}{dx}\right|_{-l_s/2}$$

$$K_{ts} n_s\left(l_s/2\right) = -D_s \left.\frac{dn_s(x)}{dx}\right|_{l_s/2}$$

where τ_s is the lifetime for adatom incorporation on the sidewalls (adatom desorption can be neglected for our growth conditions), and $n_s(-l_s/2) = n_{bs}$, $n_s(l_s/2) = n_{ts}$. $L_s = (D_s\tau_s)^{1/2}$ is the adatom diffusion length. Determination of the constants A, B yields

$$n_{bs,ts} = \frac{R_s\tau_s}{\Omega_0} \frac{2D_s\left(D_s + K_{bs,ts}L_s\tanh Q\right)}{D_s\left(K_{bs}+K_{ts}\right)L_s\left(\tanh Q + \coth Q\right) + 2\left(D_s^2 + K_{bs}K_{ts}L_s^2\right)} \quad , \quad Q = \frac{l_s}{2L_s}.$$

This expression can be strongly simplified, in relation to our geometrical and epitaxial conditions, by noting that:

a. Since $l_s \cong 1.5\mu$m, and $L_s < L_t \approx$ a few 100 nm for GaAs and lower for AlGaAs (see section 3.2.1), we can estimate $Q \gtrsim 2$, therefore we can approximate, with an error at the most of about 5%, $\tanh Q \cong \coth Q \cong 1$;

b. $K_{bs,ts}L_s / D_s = \left(a^2\gamma / k_BT\right)\left(aL_s / l_{b,t}^2\right)$, where a is the GaAs lattice constant. By estimating $a^2\gamma / k_BT \cong 10$ [145] and $L_s \approx l_{b,t}$, and since $a \ll l_{b,t}$, we get $K_{bs,ts}L_s / D_s \ll 1$.

With these approximations, $n_{bs,ts}$ become

$$n_{bs,ts} \cong \frac{R_s\tau_s}{\Omega_0} = \frac{Rr_s\tau_s}{\Omega_0}.$$

This approximation is equivalent to disregarding lateral gradients of $n_s(x)$ in (5.26). The set of eqs. (5.22) becomes therefore:

$$\begin{aligned}
\frac{dz_t}{dt} &= R\left(r_b - r_s\frac{C}{l_t^3}\right)\\
\frac{dz_s}{dt} &\cong Rr_s\left(1-\frac{C}{2l_s}\left(\frac{1}{l_t^2}-\frac{1}{l_b^2}\right)\right)\\
\frac{dz_b}{dt} &= R\left(r_b + r_s\frac{C}{l_b^3}\right)\ ,\\
\text{with}\quad C &= \frac{2\Omega_0 L_s^2\gamma}{k_B T}\ ,
\end{aligned} \tag{5.27}$$

and $r_t = r_b$, since they have the same crystallographic orientation. With the approximation (b) above, and with the condition $l_s \gg l_{b,t}$, like in section 5.2.2, we can neglect the capillarity effects on the sidewalls, and assume $dz_s/dt \cong Rr_s$. Equations (5.27) correctly predict that capillarity tends to attract adatoms towards the concave bottom region, and to drive them away from the convex top region.

The condition for obtaining a self-limiting profile, with vertical propagation of the boundaries between facets, is the vanishing of $dl_{b,t}/dt$ in (5.23). With the relations above, this implies:

$$l_t^{sl} = \left(C\frac{r_s}{-\Delta r}\right)^{1/3} \tag{5.28a}$$

$$l_b^{sl} = \left(C\frac{r_s}{\Delta r}\right)^{1/3}\ , \tag{5.28b}$$

with $\Delta r = r_s - r_b$. These relations show formally what was anticipated in section 5.2.1.1: a self limiting evolution of a concave (convex) profile is possible only if the growth rate on the surrounding facets, in the absence of the positive (negative) capillarity, is larger (smaller) than that on the curved region in question. Relation (5.28)a justifies also the existence of a metastable self-limiting state at the top of the mesas, observable sometimes in our growth (see Figure 4.10d): an exactly oriented {111}A facet is usually present in the upper part of the V groove, exhibiting a very small growth rate (see Figure 2.8). Since this {111}A surface grows more slowly than the vicinal surface developing in the remaining part of the groove, it will be gradually consumed. However, if the top of the mesa has been etched sharply enough (i.e., with a width not much larger than l_t^{sl}), the self-limiting condition (5.28)a can be fulfilled before the disappearance of the {111}A planes. When eventually the fast-growing, high index facets reach the top of the mesa, then $r_s > r_b$, and the top facets begin to expand indefinitely, leading to a gradual planarization of the groove. Relations (5.28) can also explain the fundamental difference in the self-ordering properties of nonplanar OMCVD and MBE. Differing from OMCVD, MBE usually maintains the {111} orientation of the sidewalls, defined by lithography, both for grooves aligned in the $[01\bar{1}]$ and in the [011] direction. The low growth rate and large diffusion length on these {111}A or B facets favors therefore self-limiting growth

on the ridges (vertical arrays of GaAs/AlGaAs ridge QWRs have been formed with this technique [16]). On the contrary, the bottom region can not resharpen, unless AlAs is used as the barrier material, since its growth selectivity is reversed ($\Delta r > 0$), with respect to AlGaAs and GaAs [154].

5.1.4 Self-ordering of alloys: entropic contributions

The simplest way to model self-limiting $Al_xGa_{1-x}As$ growth is to use a mean-field theory, i.e., to approximate this ternary alloy with a binary material whose properties are intermediate between those of its constituents. We can therefore characterize surface diffusion with an average energy barrier that varies linearly between the GaAs one E_B^G and the AlAs one E_B^A (the superscripts *A*, *G* refer to AlAs and GaAs, respectively);

$$E_B(x) = (1-x)E_B^G + xE_B^A \ .$$

The self-limiting alloy profile can therefore be inferred from (5.28)b, by noticing that the adatom diffusion coefficient D_s has an Arrhenius dependence on the growth temperature (see eq. (5.13)): $D_s = D_{s0}\exp(-E_B / k_BT)$. Since, according to (5.28)b, $l_b^{sl} \propto D_s^{1/3}$, in the mean-field approximation l_b^{sl} would depend *exponentially* on the nominal composition:

$$l_b^{sl}(x) = l_{sl}^G \exp\left[x\left(E_b^G - E_b^A\right)/3k_BT\right]. \qquad (5.29)$$

This model, however, even though it has the advantage of simplicity, can not account for the Ga segregation that takes place at the bottom of the groove. To explain this phenomenon, we must make the more realistic assumption of an alloy composed by two different species that can diffuse independently, with two different diffusion lengths. In this picture, the more mobile Ga adatoms will diffuse more efficiently towards the bottom than the Al ones, in response to the same gradient of chemical potential (see (5.20)). As a consequence, a Ga-rich alloy will form in this region, giving rise to a VQW.

However, to fully interpret the experimental results, we must take into account an additional phenomenon. We have seen in Section 2.3.5 that the self-limiting AlGaAs bottom profiles are narrower than those of SLs with the same equivalent composition. A GaAs/AlAs SL shape can be explained by a simple empirical model taking into account the self-ordering behaviors observed in the two binary components, but this model overestimates the self-limiting profile widths of AlGaAs alloys. Therefore, the profile at the bottom of the groove is narrower than what this model predicted. As anticipated, the reason can be found in the entropic and enthalpic interactions between the binary components during alloy growth [60]. If we consider an $Al_xGa_{1-x}As$ as a so-called "regular" solution (in which only the energetic interactions between nearest neighbor atoms are taken into account), the *molar* Gibbs free energy $g^{AG}(p,T,x) = G(p,T,N_A,N_G) / (N_A+N_G)$ can be written as

$$g^{AG} = (1-x)g^G + xg^A + k_BT\left[(1-x)\ln(1-x) + x\ln x\right] + \Omega x(1-x) \ ,$$

where the first two terms are the molar Gibbs free energies the two binaries, the third is due to

the entropy of mixing, and the fourth comes from energetic interactions [60]. Using (5.2) for each component, the chemical potentials for AlAs and GaAs are written, respectively:

$$\mu_A^{AG}(x,T) = \mu^A(T) + k_B T \ln x + \Omega(1-x)^2$$
$$\mu_G^{AG}(x,T) = \mu^G(T) + k_B T \ln(1-x) + \Omega x^2 \qquad (5.30)$$

where $\mu^A(T)$ and $\mu^G(T)$ are the chemical potentials of the two binaries if grown separately, given, for our systems, by the sets of equations (5.15) or (5.17). Due to the similarity of Ga and Al atoms, the last term can be neglected in the equations above (Ref. [23], page 66) (i.e., AlGaAs forms a so-called "ideal" solution). Note that the two additional terms due to the entropy of mixing are negative, and decrease as the mole fraction of the corresponding binary component approaches zero. This means that, wherever a local compositional change takes place, a gradient of chemical potential will tend to contrast this unbalance, through eq. (5.7) [6]. In our V-groove system, such an effect will tend to decrease the Ga segregation in the VQWs and consequently to sharpen up the profiles.

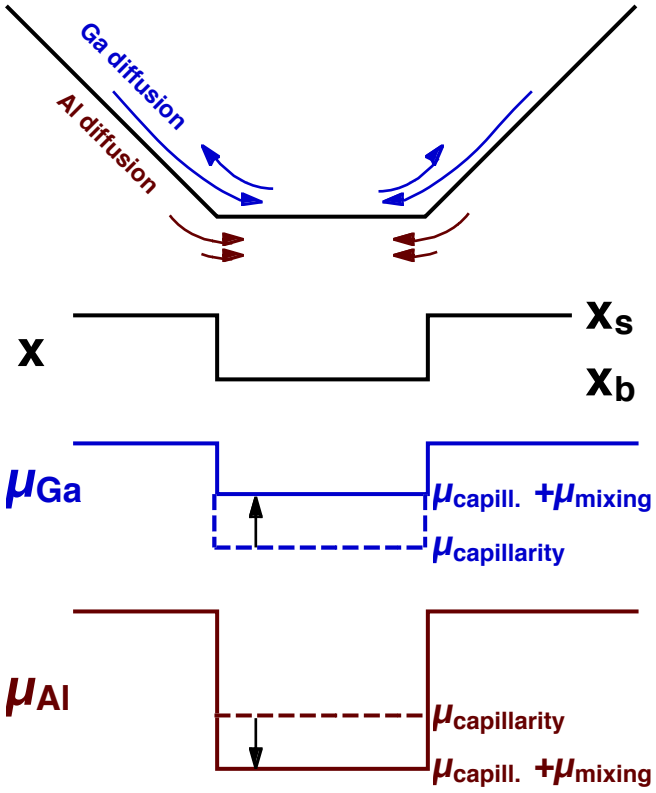

Figure 5.10: Schematics of the surface profile, of the composition and of the Ga and Al chemical potentials at the bottom of the groove for $Al_xGa_{1-x}As$ growth. Corrections to the chemical potentials due to the entropy of mixing are indicated by the vertical arrows, as well as the resulting surface fluxes for Ga (above the profile) and Al (below the profile).

[6] It can be easily shown (see Appendix B) that the entropy of mixing exhibits a maximum when the composition is uniform.

To formalize this principle, we will re-write eq. (5.20) for the bottom profile, with the correction terms (5.30):

$$\begin{aligned} K_{bs}^{A} &= \frac{D_s^A \Omega_0 \gamma}{k_B T l_b^2} + \frac{D_s^A}{l_b} \ln \frac{x}{x_b} \\ K_{bs}^{G} &= \frac{D_s^G \Omega_0 \gamma}{k_B T l_b^2} + \frac{D_s^G}{l_b} \ln \frac{1-x}{1-x_b}, \end{aligned} \tag{5.31}$$

where x_b is the composition at the bottom, that can be expressed as a function of the nominal composition x by using eq. (4.3). Since $x_b < x$, these equations predict correctly that diffusion of Ga (Al) is decreased (increased) by the mixing entropy terms. Figure 5.10 shows schematically how the Ga and Al surface chemical potentials and the consequent diffusion fluxes are modified by the nonuniform entropy of mixing. By using (5.22), and with the definition of the binary self-limiting profiles of 5.2.3, the AlAs and GaAs growth rates at the bottom become, respectively:

$$\begin{aligned} \frac{dz_b^A}{dt} &= R^A \left[r_b^A + \Delta r^A \left(\frac{l_{sl}^A}{l_b} \right)^3 + 2 \left(\frac{L_s^A}{l_b} \right)^2 \ln\left(x(1-k)+k \right) \right] \\ \frac{dz_b^G}{dt} &= R^G \left[r_b^G + \Delta r^G \left(\frac{l_{sl}^G}{l_b} \right)^3 + 2 \left(\frac{L_s^G}{l_b} \right)^2 \ln \frac{x(1-k)+k}{k} \right], \end{aligned} \tag{5.32}$$

with $R^A = x\,R$, $R^G = (1\text{-}x)\,R$. By assuming that the composition on the sidewalls is equal to the nominal one, the equalization of the growth rates on the different facets, leading to a self-limiting bottom profile, yields

$$\frac{dz_b^A}{dt} + \frac{dz_b^G}{dt} = R\left[x r_s^A + (1-x) r_s^G \right].$$

By using the growth rates at the bottom as just defined, this gives a cubic equation in $1/l_b$:

$$\frac{a}{l_b^{sl\,3}} + \frac{b}{l_b^{sl\,2}} = \Delta r(x) \quad \text{, with}$$

$$\begin{cases} a = x \Delta r^A l_{sl}^{A\,3} + (1-x) \Delta r^G l_{sl}^{G\,3} \\ b = 2 \left(x L_s^{A\,2} \ln\left(x(1-k)+k \right) + (1-x) L_s^{G\,2} \ln \dfrac{x(1-k)+k}{k} \right) \\ \Delta r(x) = x \Delta r^A + (1-x) \Delta r^G . \end{cases} \tag{5.33}$$

The self-limiting profile of an alloy is therefore given by the solution of (5.33), which expresses the equilibrium among capillarity (*a*), entropy of mixing (*b*) and growth rate anisotropy ($\Delta r(x)$).

5.1.5 Evolution towards self-limiting profiles

From the last of relations (5.27) and from (5.28)b, the GaAs growth rate at the bottom of the groove, relative to the nominal one, can be written as

$$\frac{dz_b}{dz_n} = r_s + \Delta r\left[\left(\frac{l_b^{sl}}{l_b}\right)^3 - 1\right], \tag{5.34)a}$$

where $dz_n = R\,dt$. Similarly, for $Al_xGa_{1-x}As$, relations (5.32) and (5.33) imply that

$$\frac{dz_b}{dz_n} = r_s(x) + \Delta r(x)\left[\left(\frac{l_b^{sl}}{l_b}\right)^3 - 1\right] + \frac{b}{l_b^3}\left(l_b - l_b^{sl}\right), \tag{5.34)b}$$

where $r_s(x) = x\Delta r^A + (1\text{-}x)\Delta r^G$. With the condition $\Delta r > 0$ (or $\Delta r(x) > 0$, respectively), verified in the case of OMCVD, these relations state that the bottom growth rate

a. diverges for $l_b \ll l_b^{sl}$, since in this limit the (negative) bottom chemical potential and the related surface diffusion fluxes diverge [7] (see (5.17), (5.20) and (5.31));
b. approaches r_s for $l_b \to l_b^{sl}$, determining an uniform growth rate across the bottom faceted profile;
c. approaches r_b for $l_b \gg l_b^{sl}$, since in this limit the capillarity (and entropy of mixing) effects become negligible (see again (5.17), (5.20) and (5.31)).

From (5.34)a, the evolution of the bottom profile (5.23) can be written for GaAs, as a function of the nominal growth thickness:

$$\frac{dl_b}{dz_n} = p\Delta r\left[\left(\frac{l_b^{sl}}{l_b}\right)^3 - 1\right]. \tag{5.35}$$

This equation can be integrated analytically, giving

$$z_n = \frac{l_b^{sl}}{p\Delta r}\left(\arctan\left(\frac{1}{\sqrt{3}}\left(1+2\frac{l_b}{l_b^{sl}}\right)\right) - \arctan\left(\frac{1}{\sqrt{3}}\left(1+2\frac{l_b^0}{l_b^{sl}}\right)\right) + \frac{1}{3}\ln\left(\left(\frac{l_b^{sl2}+l_b^{sl}l_b+l_b^2}{l_b^{sl2}+l_b^{sl}l_b^0+l_b^{02}}\right)^{1/2}\frac{l_b^{sl}-l_b^0}{l_b^{sl}-l_b} + \frac{l_b^0-l_b}{l_b^{sl}}\right)\right) \tag{5.36}$$

For $Al_xGa_{1-x}As$, the evolution of the bottom profile can be obtained with eq. (5.34)b:

$$\frac{dl_b}{dz_n} = p\left\{\Delta r(x)\left[\left(\frac{l_b^{sl}}{l_b}\right)^3 - 1\right] + \frac{b}{l_b^3}\left(l_b - l_b^{sl}\right)\right\}. \tag{5.37}$$

Consistently with the analysis of the bottom growth rates, relations (5.35) and (5.37) show that l_b tends to expand (contract) when its size is smaller (larger) than its self-limiting one. The recovery rate increases as this deviation becomes bigger. Therefore, l_b will always tend towards its self-limiting value, defined only by the material and the growth conditions. In particular, if the initial profile is much smaller than l_b^{sl}, at the first stages of deposition this will determine a very

[7] Note that $b < 0$ (see the comment on pag. 143), therefore in this limit the entropy term has the same (positive) sign as the capillarity one.

large expansion rate, since capillarity increases with decreasing bottom size. Conversely, if the initial profile is much wider than l_b^{sl}, then the profile will contract initially at a rate $\propto \Delta r$ (i.e., the *intrinsic* growth rate anisotropy), since in this limit capillarity and mixing effects are negligible.

Note that the equivalents of eqs. (5.35)-(5.37) for the exponential law (2.2), used to model empirically the profile evolution in Section 2.3.2, would be

$$\frac{dl_b}{dz_n} = \frac{l_b^{sl} - l_b}{\tau}, \text{ and}$$

$$z_n = \tau \ln\left(\frac{l_b^0 - l_b^{sl}}{l_b - l_b^{sl}}\right) .$$

In particular, the first of these two relations can be considered as the first-order series expansion of (5.35) and (5.37) around $l_b = l_b^{sl}$, provided that the typical length for profile recovery is

$$\tau = \frac{l_b^{sl}}{3p\Delta r} \qquad \text{GaAs}$$

$$\tau = \frac{l_b^{sl}}{p\left(3\Delta r(x) - b/l_b^{sl\,2}\right)} \qquad \text{AlGaAs}$$

(note again - see footnote 21 - that $b<0$, therefore $\tau>0$ always, both for GaAs and for $Al_xGa_{1-x}As$). This definition of τ is consistent with the experimental observation that the recovery thickness does not depend on the initial profile, but only on the properties of the material being deposited (see Section 2.3.5). Note that the driving force towards the establishment of a self-limiting profile is stronger as the growth rate anisotropy Δr increases.

It is worth to note that this empirical exponential law would predict, by using (5.23), a *linear* dependence of the bottom growth rate, as a function of l_b:

$$\frac{dz_b}{dz_n} = r_s + \frac{l_b^{sl} - l_b}{p\tau},$$

that can not reproduce correctly the experimental results, and in particular the limits for $l_b \ll l_b^{sl}$ and $l_b \gg l_b^{sl}$ described in the points a. - c. on page 139. The exponential relation (2.2) is therefore a good parameterization to describe empirically the self-ordering behavior not too far from self-limiting conditions, but is missing important physical aspects of the mechanism.

5.3 Application of the diffusion model to nonplanar OMCVD

5.3.1 Flattening of the profile in the absence of growth

To check the thermal relaxation of the nonplanar surface profiles, we have compared the predictions of the model developed in Section 5.2.2 for the bottom of the groove with a series of AlGaAs profiles, for which growth was interrupted for increasing time intervals after deposition

of 100nm-thick AlGaAs layers. The structure and experimental data relative to this set of structures were presented and discussed in Section 2.3.3.3.

We will compare here the results of Figure 2.19 with the prediction of the model. To follow the evolution of the profile it is convenient to plot the inverse of the length l_b, from that figure. This quantity can be regarded as the curvature κ of the bottom of the groove, which should tend to zero following the law

$$\kappa = \frac{\kappa_0}{\left(1 + t/\tau_b\right)^{\alpha}}, \tag{5.38}$$

where $\alpha = 0.25$, according to eq. (5.25). This equation can be easily compared to the experimental values of the inverse of the radius of curvature, measured on the TEM cross sections.

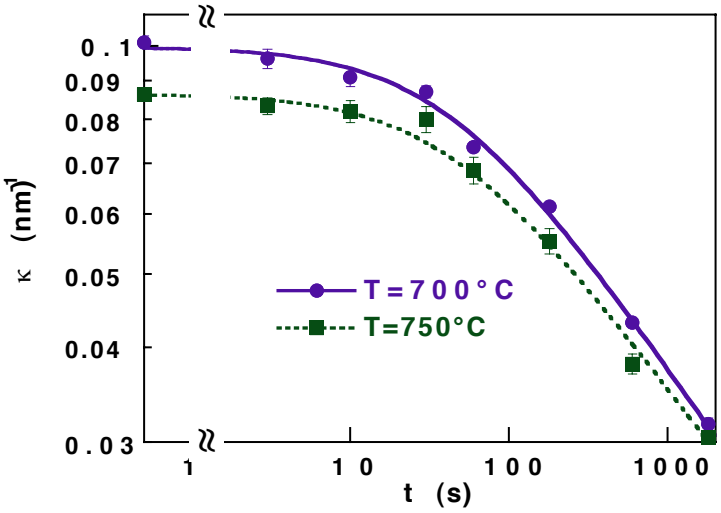

Figure 5.11: Self-limiting curvature κ at the bottom of a V groove in $Al_{0.45}Ga_{0.55}As$ alloys, as a function of the growth interruption time, for T = *700°C (circles) and 750°C (squares). Solid and dashed lines are fits of the experimental data with the function (5.38). The exponent appearing in (5.38) is a parameter of the fit.*

Figure 5.11 shows the values of κ measured on the samples described above, grown at 700°C (circles) and 750°C (squares), as a function of the time t of the growth interruption, in the range 0 to 1800s. The plot is in a log-log scale, to evidence the $t^{-\alpha}$ dependence of the curvature, for $t / \tau_b \gg 1$. The solid and dashed lines are a fit of the data for 700°C and 750°C, respectively, with the function (5.38), in which the fit parameters are τ_b and α, while κ_0 (self-limiting curvature for the given x and T) is fixed to the measured value of κ for $t = 0$. The fit to the two series of data yields values of 0.28±0.02 and 0.27±0.02 for α, and 39±10s and 33±5s for τ_b, at T = 700 and 750°C, respectively. The good match of the value of α with the theoretical value 0.25 shows the validity of the model and of the simplifications assumed. The possible slight decrease of the recovery time τ_b with T can be associated with the Arrhenius dependence on T of n and D_s, to which τ_b is related through relations (5.24) and (5.25).

5.1.2 Self-limiting GaAs and $Al_xGa_{1-x}As$ profiles

5.1.2.1 Dependence on the composition

To model the dependence of self-limiting $Al_xGa_{1-x}As$ profiles on the composition, we will first of all apply the mean-field approximation, defined in section 5.2.4, to the measured $Al_xGa_{1-x}As$ profiles. In Figure 5.12 we fit with eq. (5.29) the experimental data relative to the self-limiting bottom profile width l_b^{sl} of $Al_xGa_{1-x}As$ alloys, as a function of x, for $T = 700°C$. The figure shows that the data can be well fitted with an exponential. The result of the fit yields a difference in the energy barriers $E_B^A - E_B^G = 0.81 \pm 0.03 eV$.

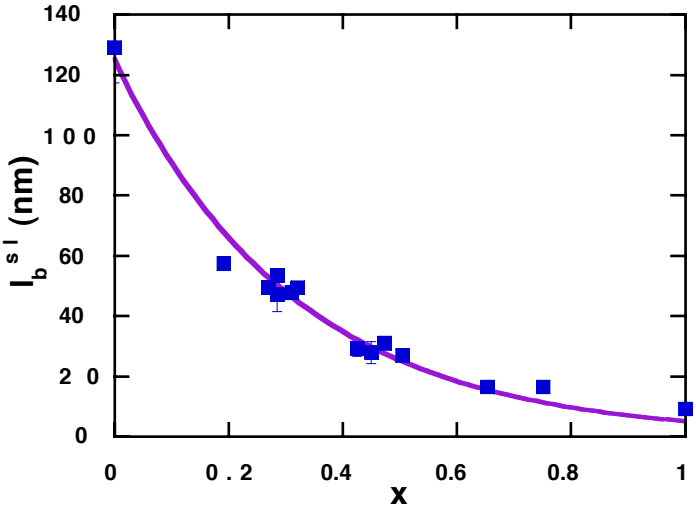

Figure 5.12: Width of the self-limiting $Al_xGa_{1-x}As$ profile, for T = 700°C, fitted with the exponential function defined in (5.29).

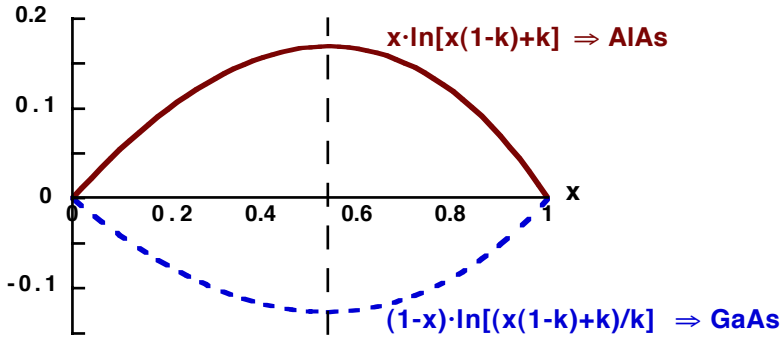

Figure 5.13: Variations, as a function of x, of the AlAs- (solid line) and GaAs- (dashed line) related logarithmic terms in the mixing entropy contribution (b) to the alloy self-limiting profile (eq. (5.33)) for k = 1.81.

As discussed in Section 5.2.4, this simple picture, though reproducing quite well the dependence of the self-limiting profiles on the $Al_xGa_{1-x}As$ composition, can not account for the Ga segregation at the bottom of the grooves. We will apply therefore the full model (defined by eq. (5.33)) to the experimental data, taking into account independent Ga and Al diffusion, and the effects of the entropy of mixing. For typical values of the parameter k ($k = 1.81 \pm 0.05$ for T

= 700°C, see Section 4.2.4), the logarithmic term associated to AlAs, appearing in the parameter b of (5.33), is positive, and the one associated to GaAs is negative. These logarithms are in absolute value smaller than 0.2 and 0.15, respectively, and both vanish for $x = 0$ and $x = 1$ (see Figure 5.13). Since $(L_s^G)^2 \gg (L_s^A)^2$, the AlAs term of b is negligible for the whole composition range, with respect to the GaAs one. We will therefore neglect this AlAs term, thus ascribing any entropy-related compositional variations in the VQW to *Ga diffusion* away from the bottom.

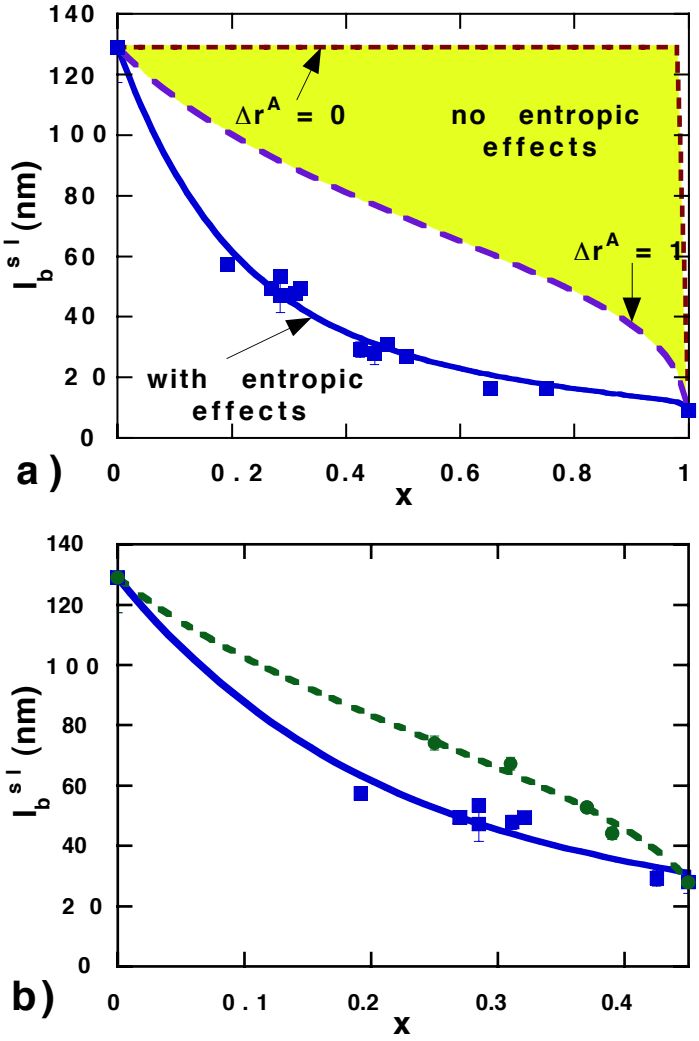

Figure 5.14: a) Measured self-limiting width of the bottom profile l_b^{sl}, as a function of x *for* T = *700°C. The solid line is a fit of the data, with the function defined in (5.33). Long-dashed and short-dashed lines, delimiting the shaded region, represent the hypothetical dependence of l_b^{sl} on* x *by neglecting the entropy of mixing effects (eq. (5.39)), and setting $\Delta r^G = 0.22$ and $\Delta r^A = 1$ or $\Delta r^A \to 0$, respectively (see text for details). b) Squares and solid line: the same data and fit as in a), for $0 < x < 0.45$. Circles: measured self-limiting width of the bottom profile l_b^{sl} in GaAs/$Al_{0.45}Ga_{0.55}As$ V-groove SLs, grown at 700°C, as a function of the equivalent* x. *The dashed line is a fit of the data with eq. (5.39), where "1" (AlAs) is replaced by "0.45" ($Al_{0.45}Ga_{0.55}As$).*

In Figure 5.14a we fit the experimental data of Figure 5.12 (squares), with the solution of (5.33) (solid line). Since the nominal growth rates R are different for different Al compositions, and our model implies a dependence of the profile width on $R^{-1/3}$ (see Section 5.3.2.3 below), we

have normalized the values of l_b^{sl} in Figure 5.14 to the cubic root of the alloy growth rates, relative to the GaAs one. Besides, in the fit we left L_s^G as the only free parameter, as we inferred the other quantities from the experiments: $l_{sl}^G = 129\pm3$nm, $l_{sl}^A = 9.1\pm0.1$nm and $\Delta r^G = 0.22\pm0.05$ (see Section 2.2.2). We have no reliable estimate for Δr^A, however the fit is very insensitive to this parameter: by changing Δr^A from 0 to 1, the corresponding best fit of L_s^G varied only by 7nm, without affecting the quality of the fit. The main source of uncertainty in the fit is the error in Δr^G, that causes a ~10% error in the determination of L_s^G: $L_s^G = 175\pm20$nm. This estimate confirms the assumptions that led to the simplifications at page 135. The Ga diffusion length on the sidewalls is therefore smaller than on the (100) ridges (estimated to be ~400nm at 700°C by AFM measurements - see 3.2.1). This conclusion is consistent with the fact that the sidewalls are high-index planes, with a higher density of steps and kinks, and hence a better incorporation efficiency than the monolayer-smooth (100) facets.

Without the entropy of mixing effects, the solution of (5.33) would reduce to

$$l_b^{sl} = \left(\frac{a}{\Delta r(x)}\right)^{1/3} = \left(\frac{x\left(\Delta r^A/\Delta r^G\right)l_{sl}^{A\,3} + (1-x)l_{sl}^{G\,3}}{x\left(\Delta r^A/\Delta r^G\right) + (1-x)}\right)^{1/3} . \qquad (5.39)$$

We indicated with a shaded region in Figure 5.14a how l_b^{sl} would depend on x, according to the equation above, and setting $\Delta r^G = 0.22$ and $\Delta r^A = 1$ (long-dashed line) or $\Delta r^A \to 0$ (short-dashed line). It is clear that the experimental results could not be reproduced with this simplification (unless one takes unphysically high values of the ratio Δr^A / Δr^G, of the order of 60). In Section 2.3.5, we have shown that self-limiting growth of GaAs/AlGaAs SLs results in a bottom profile that is much wider than that of an AlGaAs alloy, with the same Al mole fraction. In the framework of the model presented here, this can be accounted for by the absence of the entropy of mixing in the SLs, where GaAs and AlAs are deposited alternatively. The circles in Figure 5.14b (squares and solid line are the same as in part a) represent l_b^{sl} for four GaAs/$Al_{0.45}Ga_{0.55}$As V-groove SLs, grown at 700°C. The GaAs nominal thickness was 1.8nm in all samples, while the AlGaAs nominal thickness varied from 2.2 to 11.6nm from left to right. The abscissa of the data points corresponds to the equivalent Al mole fraction over a SL period. Since one of the layers composing the SL is an AlGaAs alloy, the entropy of mixing is only partially reduced, with respect to the one of an alloy with the same equivalent composition. The profile width is therefore intermediate between that of the corresponding alloy (squares, solid line) and the one expected in the total absence of entropy of mixing (dashed lines). We can model tentatively this SL growth by applying an equation equivalent to (5.39), in which we replaced "1" (AlAs) with "0.45" ($Al_{0.45}Ga_{0.55}As$), and by fixing l_{sl}^G and l_{sl}^A to the values measured at $x = 0$ and $x = 0.45$ (129±3nm and 28±2nm). The result is shown by the dashed line in Figure 5.14b, and exhibits a good match to the experimental data.

5.1.1.2 *Dependence on the growth temperature*

Eq. (5.28)b, with the constant C defined in (5.27), shows that l_b^{sl} in a binary compound is proportional to the diffusion length on the sidewalls to the power 2/3. This equation formalizes therefore the qualitative conclusions of section 2.3.3.1, based on the experimental behavior of l_b^{sl} on the growth temperature and the Al mole fraction. Eq. (5.28)b can be written as

$$l_b^{sl} = \left(\frac{r_s}{\Delta r} \frac{2\Omega_0 \gamma}{k_B T} D_s \tau_s \right)^{1/3}, \quad \text{with } D_s = D_{s0} \exp\left(-E_B / k_B T\right). \tag{5.40}$$

If we approximate τ_s as the average time between the arrival of two adatoms on the same site (this can be effectively considered as the upper limit for the migrating adatom lifetime), the temperature dependence of l_b^{sl} (or of the related self-limiting radius of curvature ρ_{sl} [8]) is of the form $\exp(-E_B / 3\, k_B T)$ [9].

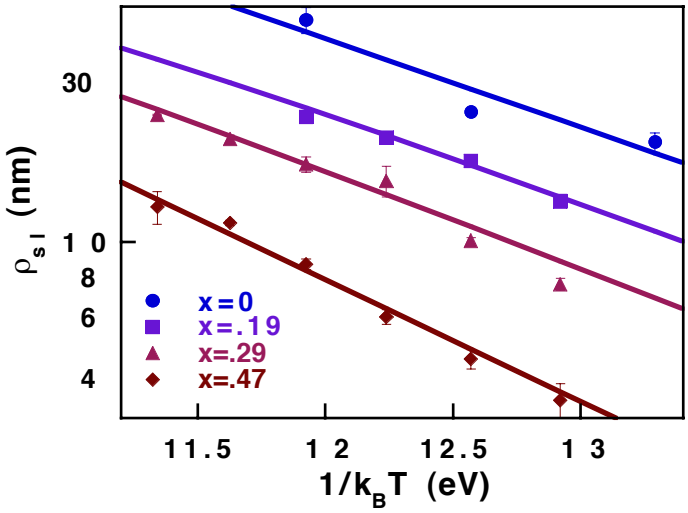

Figure 5.15: Arrhenius plot of ρ_{sl}, for AlGaAs alloys with composition ranging from x = 0 to x = 0.45. Solid lines are fits of the experimental data with eq. (5.40) (GaAs) and (5.33) ($Al_xGa_{1-x}As$).

For $Al_xGa_{1-x}As$, the temperature dependence of l_b^{sl}, given by eq. (5.33), is more complicated, and comes essentially from the Arrhenius form of $l_{sl}^{A,G}$ and $L_s^{A,G}$. We have examined the temperature dependence of the self-limiting profiles for $Al_xGa_{1-x}As$ alloys for $0 < x < 0.45$. Figure 5.15 shows Arrhenius plots of ρ_{sl} for $x = 0$, 0.19, 0.29 and 0.45, for growth

---

[8] We will show in Appendix A that, by approximating the bottom profile with a hyperbola, the radius of curvature at the bottom ρ follows the same self-limiting behavior as l_b.

[9] We will neglect a weak dependence on T coming from the factor $(k_B T)^{-1/3}$ and from the pre-exponential factor of the diffusion coefficient D_{s0}. This latter, in particular, is considered to be virtually temperature-independent, as compared with the exponential term [59].

temperatures ranging from 600°C to 750°C. The Arrhenius fit for GaAs gives E_B^G = 1.9±0.3eV. The GaAs behavior can be plugged into eq. (5.33) to fit the $Al_xGa_{1-x}As$ profiles, as a function of L_s^G only. As before, we have assumed $(L_s^G)^2 \gg (L_s^A)^2$, fixed $\Delta r^G = 0.22\pm0.05$ (this value does not change appreciably with T, in the range considered, as we have seen in Section 2.2.2), and verified the insensitivity of the fit to Δr^A. Least squares fits of the $Al_xGa_{1-x}As$ profiles, shown in, Figure 5.15, are practically indistinguishable from Arrhenius laws and yield, consistently for the three compositions, E_B^A = 2.3±0.2eV. This higher energy is consistent with stronger Al-As bonds, with respect to Ga-As ones [87]. Note that the difference E_B^A - E_B^G is about a half of the one estimated with the mean-field approximation (Figure 5.12). A more quantitative discussion of these values, in comparison to what has been found on (100) surfaces, is however not reliable, due to the wide range of results obtained on this orientation [87].

Finally, we can estimate the order of magnitude of L_s^G and L_s^A. By using eq. (5.40) and, for example, the measured values of l_b^{sl} in GaAs and AlAs layers at 700°C (~100nm and ~10nm, respectively), we obtain $L_s^G \approx$ 150-200nm and $L_s^A \approx$ 5nm. The GaAs value agrees well with the estimation given in the previous section.

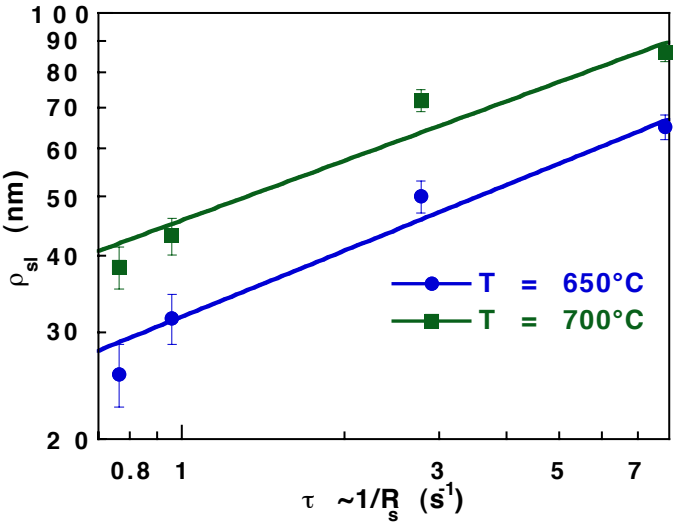

Figure 5.16: Log-log plot of ρ_{sl} in GaAs layers, as a function of the inverse of the growth rate, for T = 650°C *(circles) and 700°C (squares). Solid lines are power fits of the data.*

5.1.1.3 Effects of the growth rate

By decreasing the growth rate R, the self-limiting profile should expand (until it becomes planar in the absence of growth – see Section 5.2.2), since effects of diffusion towards the bottom of the groove become increasingly dominant, with respect to the effects of growth rate anisotropy (that, as we have seen, tend to sharpen the groove). We have verified this hypothesis on self-limiting GaAs profiles, grown at 650 and 700°C, with growth rates ranging between 0.036 and 0.370nm/s (see Figure 2.18a for a description of the structures). Figure 5.16 replots

the data relative to ρ_{sl}, from Figure 2.18b, in a log-log scale, as a function of $1/R$. A marked decrease of the profile width is observed as R increases. With the approximation above for τ_s, taken as the average time between the arrival of two atoms on the same site [73], we can write $\tau_s = 1/R$, if R is expressed in ML/s. From eq. (5.40) therefore we would expect l_b^{sl} (or ρ_{sl}) $\sim (R)^{-1/3}$. A power fit of the data of Figure 5.16 gives an exponent of -0.36±0.05 for T=650°C and -0.32±0.06 for T = 700°C (see solid lines in the figure), showing that this simplifying interpretation of τ_s is able to explain quantitatively the observed dependence of ρ_{sl} on the growth rate. We remark that τ_s is in general lower than $1/R$, since an adatom could re-evaporate before the arrival of another adatom on the same site [155], however, no appreciable group-III adatom re-evaporation is observed for our growth conditions.

5.1.1.4 Effects of the reactor pressure

In Section 2.3.3.4 we showed that increasing the reactor pressure to 1atm yields self-limiting bottom profiles that are more rounded and wider than at 20mbar, for otherwise similar growth conditions. As discussed in the same section, a quantitative comparison of the experimental results in the two cases is not completely justified, due to the influence on the profiles of other, not completely controlled, growth parameters. Therefore, we will limit ourselves to a qualitative discussion of the pressure effects, based on the model developed here. Since changing the reactor pressure does not affect the surface kinetics and thermodynamics, capillarity and entropy of mixing effects should be the same, at LP and AP. The main effect of increasing the reactor pressure is to reduce mass transport of the gas species to the surface through the boundary layer. Therefore, at AP growth is more mass-transport limited than at LP (see Figure 1.10, right). Since mass transport does not depend on the surface orientation, the value of Δr (that results from an interplay between mass transport and surface kinetics) should decrease, as the reactor pressure increases. As a result, the self-limiting bottom profile width (which, according to eq. (5.40), is proportional to $(\Delta r)^{-1/3}$) should be higher at AP than at LP, as the experimental results indeed show.

x	l_b^{sl} **(nm)**		**Δr**	
	T = 650°C	**T = 700°C**	**T = 650°C**	**T = 700°C**
0	67±2	129±3	0.21±0.05	0.22±0.05
0.3	18.1±0.4	31.5±0.7	0.23±0.05	0.19±0.05
0.45	13.6±0.3	17.7±0.4	0.23±0.05	0.21±0.05

Table 5.2: Measured self-limiting extensions of the bottom profiles l_b^{sl} and growth rate anisotropies Δr in GaAs, $Al_{0.3}Ga_{0.7}As$ and $Al_{0.45}Ga_{0.55}As$ at 650 and 700°C.

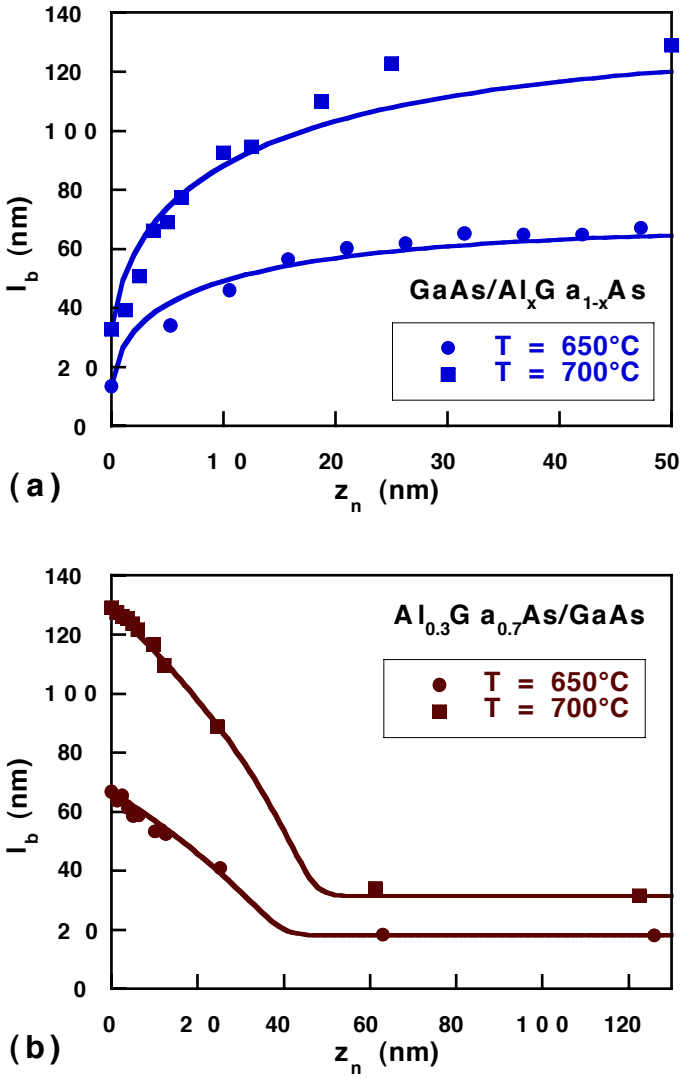

Figure 5.17: a): Measured evolution of the GaAs profile widths l_b towards their self-limiting value l_b^{sl}, as a function of the nominal thickness, for T = 650°C, grown on $Al_{0.45}Ga_{0.55}As$ (circles), and T = 700°C, grown on $A_{l0.3}Ga_{0.7}As$ (squares). Solid lines are theoretical predictions of the profile evolutions (eq. (5.35)), with the parameters l_b^{sl} and Δr fixed as the values determined experimentally (see text). b) Measured evolution of the $Al_{0.3}Ga_{0.7}As$ profile widths l_b towards their self-limiting value l_b^{sl} as a function of the nominal thickness, for T = 650°C (circles), and T = 700°C (squares), both grown on self-limiting GaAs. Solid lines are fits of the data, with the parameters l_b^{sl} and Δr(x) fixed as the values determined experimentally, and the Ga diffusion length on the sidewalls as a fitting parameter (see text).

5.1.3 Self-limiting evolution of GaAs and $Al_xGa_{1-x}As$

We have compared with the experimental results the time evolution of l_b towards its self-limiting value for GaAs, $Al_{0.3}Ga_{0.7}As$ and $Al_{0.45}Ga_{0.55}As$ at 650 and 700°C. The samples consisted of a sequence of layers of increasing thickness, until a self-limiting profile is established, after about 100nm. GaAs layers were grown on self-limiting $Al_xGa_{1-x}As$, and $Al_xGa_{1-x}As$ layers were grown on self-limiting GaAs.

Figure 5.17a shows l_b, as a function of z_n for GaAs grown at 650°C on self-limiting

$Al_{0.3}Ga_{0.7}As$ (circles) and at 700°C on self-limiting $Al_{0.45}Ga_{0.55}As$ (squares). Both profiles evolve towards their self-limiting sizes, as the thickness increases (see Table 5.2). The time evolution of the GaAs profile has been modeled by integrating numerically eq. (5.35). The solid line represents the simulated profile evolution according to this equation, where we have selected the values of l_b^{sl} and Δr measured experimentally (see Table 5.2 and Section 2.2.2). The evolutions of both GaAs profiles are well reproduced by the theoretical curves with our choice of parameters. The self-limiting evolution of $Al_{0.3}Ga_{0.7}As$ and $Al_{0.45}Ga_{0.55}As$ is modeled by integrating numerically eq. (5.37). We have again plugged into the equation the measured values of the self-limiting profile widths and growth rate anisotropies (see Table 5.2 and Section 2.2.2). We have left therefore L_s^G, contained in b, as a fitting parameter. Figure 5.17b shows the experimental points and the results of the fit for $Al_{0.3}Ga_{0.7}As$ at 650°C (circles) and 700°C (squares). Similar behaviors are obtained for $Al_{0.45}Ga_{0.55}As$ (not shown). Least-squares fits of the experimental values at 700°C yielded $L_s^G = 145\pm20$nm from the $Al_{0.3}Ga_{0.7}As$ data and $L_s^G = 130\pm20$nm from the $Al_{0.45}Ga_{0.55}As$ data. These values are consistent between them, and of the same order of the one determined in Figure 5.14a, though about 20-25% lower. At 650°C, we obtained, consistently, $L_s^G = 90\pm10$nm from the $Al_{0.3}Ga_{0.7}As$ data and $L_s^G = 70\pm10$nm from the $Al_{0.45}Ga_{0.55}As$ data. The ratio between the average Ga diffusion lengths at 650 and 700°C, yields $L_s^G(650°C) / L_s^G(700°C) = 0.58\pm0.11$. Since $L_s = (D_s\tau_s)^{1/2}$ and $\tau_s \approx 1/R$, according to (5.40) we have

$$\frac{L_s^G(T_1)}{L_s^G(T_2)} = \exp\left[\frac{E_B^G}{2}\left(\frac{1}{k_B T_2} - \frac{1}{k_B T_1}\right)\right].$$

With $E_B^G = 1.9\pm0.3$eV (see Section 5.3.2.2), this relation gives a diffusion length ratio $L_s^G(650°C) / L_s^G(700°C) = 0.55\pm0.11$, in excellent agreement with the value found from the fits above.

Figure 5.17 shows that the transient size variations to attain the self-limiting profile are qualitatively different, depending whether $l_b^0 < l_b^{sl}$ (a) or $l_b^0 > l_b^{sl}$ (b):

GaAs/$Al_xGa_{1-x}As$ case (a): In the initial stages of profile evolution we have $l_b \ll l_b^{sl}$, therefore the term "-1" can be neglected in (5.35) and the profile will evolve approximately according to the law (5.25). This is due to the fact that, when the profile is very sharp, with respect to the surface diffusion length, lateral capillarity fluxes are dominant over vertical growth fluxes.

$Al_xGa_{1-x}As$/GaAs case (b): In the initial stages of profile evolution, we have $l_b \gg l_b^{sl}$, therefore the capillarity and entropy of mixing terms can be neglected in (5.37). This is equivalent to saying that for very shallow profiles (much wider than the surface diffusion length), lateral fluxes are negligible, and each facet grows with its "intrinsic" growth rate r_i. As a

consequence (see (5.37)), the profile contraction is initially constant, at a rate given by $\Delta r(x)$. This linear profile evolution is well reproduced in Figure 5.17b for $l_b \leq 20$nm.

5.1.4 Formation of quantum-confined nanostructures

The model developed above is useful not only for evaluating the self-limiting characteristics of the growth, but also can be employed to elucidate the self-ordering of several types of quantum nanostructures relying on such self-limiting surface evolution.

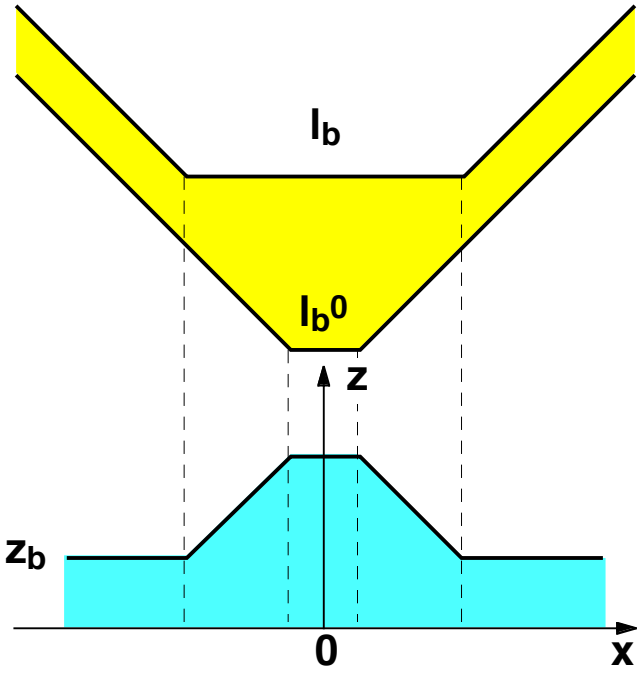

Figure 5.18: Schematics of a QWR, composed of a single bottom facet, and corresponding thickness profile.

- ***$Al_xGa_{1-x}As$ VQWs***. As seen above, the Ga segregation in the VQWs during AlGaAs growth derives directly from the higher mobility of Ga adatoms, with respect to the Al ones, and from the corrections due to entropy of mixing effects. The self-limiting facet widths for AlGaAs alloys give the confinement dimension of VQW structures.
- ***GaAs/$Al_xGa_{1-x}As$ QWRs***. The fact that the self-limiting width increases with increasing diffusion length of the group-III adatoms on the sidewalls explains directly the self-ordering of crescent-shaped QWRs. Thus, growing a low bandgap semiconductor layer (e.g., GaAs), characterized by a longer diffusion length, on a self-limiting, higher bandgap surface (e.g., AlGaAs) leads to the expansion of the bottom facet and the experimentally observed formation of a QWR. The QWR shape can be predicted, as a function of the nominal GaAs thickness and growth conditions, by using eq. (5.35). For the typical QWR thicknesses, we have $l_b \ll l_b^{sl}$; therefore, as discussed on page 150, we can approximate l_b with the analytic formula (5.25), with $\tau = (l_b^0)^4 / [4p\,\Delta r\,(l_b^{sl})^3]$. The QWR thicknesses z_b at the center can be evaluated using (5.23). The thickness profile, as a function of the lateral

coordinate x, can be easily found in the approximation of a single bottom facet (see Figure 5.18):

$$z_b(z_n,x)=\begin{cases} r_s z_n & x<-\dfrac{l_b}{2} \\ r_s z_n+\dfrac{l_b+2x}{p}=r_s z_n+\dfrac{l_b^0}{p}\left[\left(1+\dfrac{z_n}{\tau}\right)^{1/4}+\dfrac{2x}{l_b^0}\right] & -\dfrac{l_b}{2}\le x<-\dfrac{l_b^0}{2} \\ r_s z_n+\dfrac{l_b-l_b^0}{p}=r_s z_n+\dfrac{l_b^0}{p}\left[\left(1+\dfrac{z_n}{\tau}\right)^{1/4}-1\right] & -\dfrac{l_b^0}{2}\le x<\dfrac{l_b^0}{2} \\ r_s z_n+\dfrac{l_b-2x}{p}=r_s z_n+\dfrac{l_b^0}{p}\left[\left(1+\dfrac{z_n}{\tau}\right)^{1/4}-\dfrac{2x}{l_b^0}\right] & \dfrac{l_b^0}{2}\le x<\dfrac{l_b}{2} \\ r_s z_n & x\ge\dfrac{l_b}{2} \end{cases}$$

The equations above define completely the QWR shape (in the single bottom facet approximation), and can be used to calculate the wire quantum confinement potential.

- ***GaAs/Al$_x$Ga$_{1-x}$As QWR SLs.*** We have seen in Section 2.3.5 that these structures can be grown with Al$_x$Ga$_{1-x}$As barriers much thinner than the ones needed to recover the self-limiting Al$_x$Ga$_{1-x}$As profile. A peculiar SL self-limiting state is established, and has been modeled analytically in Section 2.3.5.2 by using empirical evolution laws for the GaAs and Al$_x$Ga$_{1-x}$As profiles. In Figure 5.19 we show the results of the modeling of the SL of Figure 2.25, where we have simulated numerically the SL profile using eqs. (5.34)a and b. The parameters of the simulation were fixed by fitting the self-limiting evolution of GaAs and Al$_{0.45}$Ga$_{0.55}$As at 650°C, determined in Section 5.3.3.

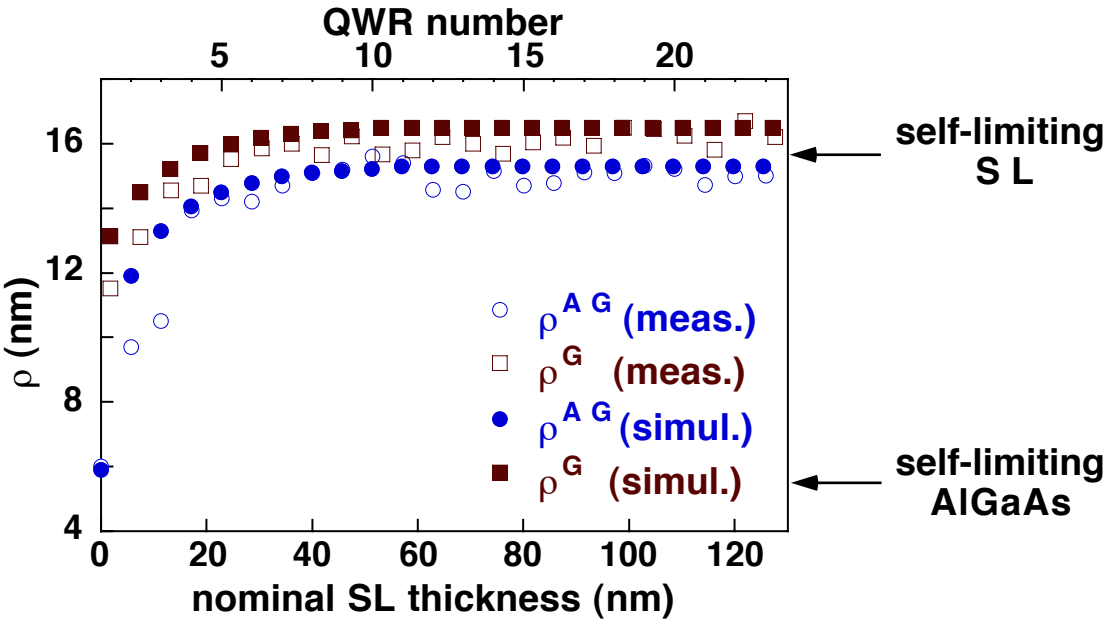

Figure 5.19: Open symbols: measured QWR SL radius of curvature, as a function of the SL thickness, from Figure 2.25a. Full symbols: simulated radius of curvature, using eqs. (5.34)a and b. Circles: upper Al$_{0.45}$Ga$_{0.55}$As profile; squares: upper GaAs profile.

The plot shows that the SL self-limiting growth can be well reproduced with our model. The simulation gave self-limiting SL radii of curvature of 17.9nm, 15.9nm, 13.4nm and 12.0nm for the samples of Table 2.3. The agreement with the experimental values is comparable to that of the empirical model introduced in Section 2.3.5.2, based on the exponential evolution of GaAs and AlGaAs profiles.

- ***$In_xGa_{1-x}As/Al_xGa_{1-x}As$ QWRs.*** Compositional self-ordering takes place also in $In_xGa_{1-x}As$ alloys, in analogy to $Al_xGa_{1-x}As$. This results in the formation of an In-rich VQW at the bottom of the groove (see Section 2.3.4.2). InGaAs self-ordering could be explained by our model, as the diffusion length of In is larger than that of Ga. In this case, however, one should also take into account the effects of strain, when InGaAs is grown on GaAs or AlGaAs buffer layers. This can be done formally by solving the Nernst-Einstein and continuity equations outlined above, with a surface chemical potential that takes into account nonplanarity, entropy of mixing *and* strain, this latter effect being included through eq. (5.6). We will not try to develop analytically the model in this general case. We note however that, since the bottom region is concave, this profile geometry should be unfavorable for a lateral release of the strain, and therefore should reduce In migration to the bottom. The formation of In-rich VQWs indicates therefore that the effects of capillarity (that should widen the bottom of the groove and enhance the In composition in this region) are more important than those of strain.
- ***$Al_xGa_{1-x}As$/GaAs quantum dots on inverted pyramids*** [156]**.** By etching tetrahedral recesses on (111)B-oriented GaAs substrates, self-ordering of $Al_xGa_{1-x}As$ is observed at the bottom of these pyramids by OMCVD. Growth on the side facets of the pyramids is analogous to the one taking place in V grooves: sidewalls with similar quasi-{111}A planes develop, and at their intersection self-ordered GaAs/$Al_xGa_{1-x}As$ QWRs and $Al_xGa_{1-x}As$ VQWs are formed. At the bottom of the pyramids, at the intersection of the three QWRs and VQWs, a GaAs quantum dot and a vertical AlGaAs QWR form, respectively. Our model can be extended to treat two-dimensional lateral diffusion in such a 60° geometry.

5.4 Monte Carlo simulations of nonplanar epitaxy

According to the analytic model presented here, self limiting growth results from the competition between the growth rate anisotropy on the different facets of the groove and the surface diffusion of adatoms. In order to support this assumption and gain understanding of the growth process on the atomic level, we developed a two-dimensional Monte Carlo (MC) simulation based on the solid-on-solid model (see Section 1.3.4). In this kinetic model, the growth is separated into two events: the random arrival of adatoms and their diffusion on the surface. To take into account the growth rate anisotropy Δr, we have assumed that the arrival rate depends not only on the nominal growth rate but also on the local slope of the surface. This assumption should account for the effects of the surface geometry on gas-phase diffusion, precursor decomposition and lateral diffusion of intermediate reaction species [64, 69, 70],

without explicitly simulating them.

Concerning adatom diffusion, only two parameters are introduced: the binding energy to the substrate for the group-III element ($E_s \sim 1.3$-1.7eV) and the binding energy to the in-plane nearest neighbours (E_v =0.2eV) [74]. The cation diffusion is then treated as a sequence of hops between neighboring lattice sites and the presence of anions is included in the effective binding energy parameters. The growth of AlGaAs/GaAs heterostructures is simulated by alternate deposition of layers composed exclusively of only one cation type, i.e. with only one binding energy parameter. For AlGaAs growth, we have adopted a mean-field theory to treat the average cation diffusion as a function of the alloy composition. Thus, the average diffusion barrier energy for adatoms is given by $E_s(x) = (1\text{-}x)\, E_s^G + x\, E_s^A$. By approximating the ternary alloy with a binary material with an equivalent average diffusion, we neglect segregation effects at the bottom, deriving from the difference between Ga and Al mobility.

The typical calculations are done on a 600×30 simple-cubic array of "GaAs sites" (240×12nm) with periodic boundary conditions. The sidewalls of the groove are approximated as {211} surfaces, instead of the ~10° off-{111} and {311} facets geometry observed experimentally. This simplification is justified because the density of steps is very high on these facets so that the {211} surface used in the simulation reproduces quite well the low effective diffusion length of adatoms on the high-index sidewalls.

We studied in detail how the radius of curvature ρ of the simulated profiles is influenced by the two critical parameters of the growth, namely the surface diffusion barrier and the growth rate anisotropy. We show in Figure 5.20a the variation of the simulated ρ as a function of the layer thickness, for $\Delta r = 0.35$, 0.15 and 0, at a given growth temperature and nominal growth rate ($T = 650$°C, $R = 1$ML/s). Starting from a perfectly sharp profile ($\rho = 0$), we ideally "grow" first 50ML of a material with a low diffusion barrier energy (E_s=1.5eV), followed by 50ML of a material with a 0.2eV higher one (E_s=1.7eV). As discussed below, the energy barriers used here correspond to those of $Al_{0.5}Ga_{0.5}As$ and pure AlAs, respectively. The values of ρ_{sl} agree with those observed experimentally for equivalent growth conditions. If $\Delta r > 0$, the simulated ρ stabilizes to a self-limiting value during the deposition of the first layer, and converges to a lower value during the deposition of the second layer, where diffusion is reduced. As Δr decreases, the recovery is slower and the profiles become wider. At the limit $\Delta r = 0$, the profile width still seems to saturate slowly during deposition of the first material, but no resharpening is possible when diffusion is reduced. These simulated behaviors are in agreement with experiments and with the predictions of the analytic model. In particular, as eq. (5.28)b implies, the simulations show that $\Delta r > 0$ is needed in order to have self-limiting growth at the bottom, and that the profile becomes sharper as Δr increases.

Figure 5.20b shows the simulated dependence of ρ_{sl} on E_s, for $T = 650$°C, $R = 1$ML/s, and $\Delta r = 0.85$ (the dimensionless parameter $E_s / k_B T$ is shown in the figure). The figure shows that ρ_{sl} decreases exponentially as the diffusion barrier increases. This behavior agrees with the

analytic model (see eq. (5.40)). We note that no entropy of mixing effects can be deduced from this simulation, since only one diffusing species is considered. Quantitative agreement with experimental results is obtained by putting $E_s = 1.3$eV in GaAs and $E_s = 1.7$eV in AlAs. These values are lower than those of E_B estimated with the analytic model, since they refer only to the binding energy to the substrate. On the contrary, the analytic model provides overall diffusion energies (substrate + lateral binding energies), averaged on a densely stepped sidewall facet. These values are therefore expected to be higher than those of E_s inferred from the simulation.

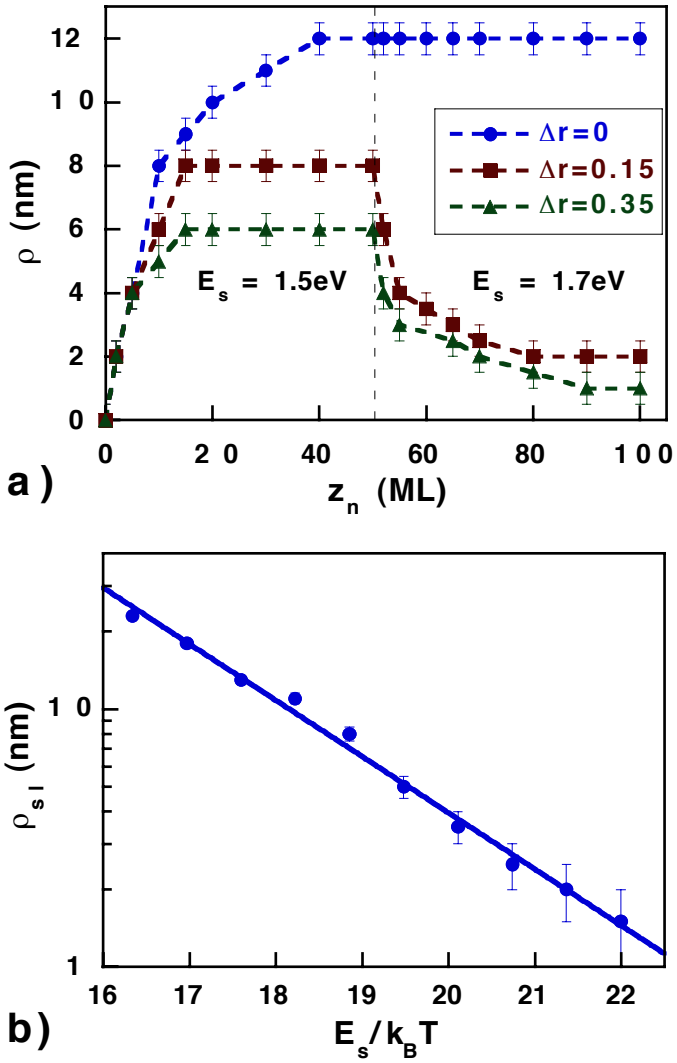

Figure 5.20: a) Simulated evolution of the bottom radius of curvature ρ, for different growth rates anisotropy and diffusion barriers (see text). b) Simulated dependence of ρ_{sl} on the substrate diffusion barrier E_S*, normalized to the growth temperature.*

Figure 5.21 (bottom) shows a simulation of the growth of a 10ML-thick $GaAs/Al_{0.5}Ga_{0.5}As$ QWR structure, similar to the one shown in the TEM cross section at the top of the same figure. We fixed the parameters $T = 680$°C, $R = 1$ML/s, and $\Delta r = 0.1$. In the mean-field theory approximation, the diffusion barrier energies are $E_s(0) = 1.3$eV for GaAs and $E_s(0.5) = 1.5$eV for $Al_{0.5}Ga_{0.5}As$. The simulation gives us a complete overview of the growth front and can reproduce the main features of the actual structure shown above. At the bottom,

self-limiting growth is reached in the lower $Al_{0.5}Ga_{0.5}As$ layer. Deposition of the QWR results in a thickening and expansion of the profile. Subsequent growth of the second barrier layer recovers the $Al_{0.5}Ga_{0.5}As$ self-limiting profile. The roughness of the simulated interfaces on the sidewalls is due to the very low surface diffusion of adatoms on these facets, where the kink density is overestimated as compared to the experimental 10° off-{111} sidewalls. As expected, at the top of the mesa the (100) facet grows slower than the sidewall, leading to a gradual planarization of the groove.

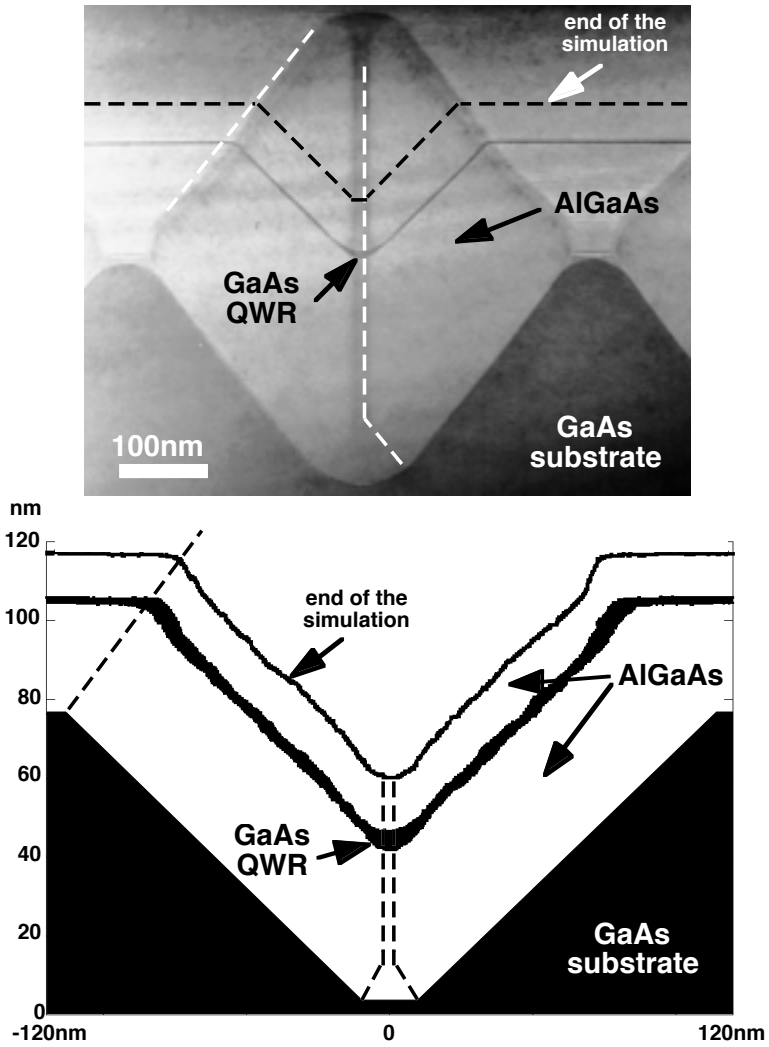

Figure 5.21: Top: Dark-field TEM cross section of a 0.5µm-pitch GaAs V groove, on which an $Al_{0.3}Ga_{0.7}As$/GaAs heterostructure was grown by LP-OMCVD at 680°C. Bottom: Cross-sectional simulated profile of a V-groove GaAs/AlGaAs QWR.

5.5 Summary

We have developed an analytic model that explains self-ordered epitaxy on nonplanar substrates. Self-limiting profiles result from the interplay among three processes:

- The growth rate anisotropy on the different facets composing the groove. According to the sign of this anisotropy, self-limiting growth can be attained at the top of the ridges (like in MBE) or at the bottom of the grooves (like in OMCVD).

- The lateral capillarity fluxes towards the bottom of the grooves, due to curvature-related chemical potential gradients. These fluxes can self-adjust, in order to yield uniform growth rates and therefore self-limiting growth.
- The entropy of mixing-related lateral diffusion, that arises in alloy growth. Gradients of the entropy of mixing are due to the larger concentration of the high-mobility components of the alloy at the bottom of the groove, and tend to contrast this segregation, thus affecting shape and composition of the self-limiting profiles.

A kinetic Monte Carlo simulation supports the main features of the model, and is able to reproduce qualitatively the observed growth features. In this approach, growth rate enhancements at the bottom of the grooves derive from the difficulty for adatoms to diffuse from this region towards the sidewall through the boundary between them, thus creating a net diffusion flux towards the bottom. The effects of this phenomenon are therefore equivalent to those of capillarity, taken into account in the analytic model.

The predictions of the model have been applied to LP-OMCVD growth of GaAs/$Al_xGa_{1-x}As$ nanostructures on V-grooved substrates, and are able to describe with great accuracy the self-ordering phenomena taking place at the bottom of the grooves. This formalism can be extended to describe and design self-limiting growth of novel low-dimensionality confined structures, such as VQWs, QWRs, QWR superlattices and vertical arrays of QDs in inverted pyramids [156].

Chapter 6

Conclusions and future directions

This thesis project was aimed at the understanding of the physics of epitaxial growth of semiconducting materials on corrugated surfaces, and particularly of the low-dimensional quantum nanostructures thus formed. Most of the experimental and theoretical work has been devoted to organometallic chemical vapor deposition (OMCVD) growth of GaAs/$Al_xGa_{1-x}As$ heterostructures on V-shaped substrates. This technique has been long proven to be a suitable method to form uniform arrays of quantum wires (QWRs) [46]. It has soon been recognized that this possibility stems from a *self-ordering mechanism* at the bottom of the V grooves. This mechanism ensures the formation of steady-state profiles, which depend only on the material and growth conditions, and form again after deposition of each QWR. No clear physical reason, however, was identified for such an evolution of the profile at the bottom of the groove, leading to a metastable equilibrium, and for the drastic dependence of this evolution on the growth technique (e.g., MBE versus OMCVD).

An essential phase in our project was a broad and systematic experimental study of self-limiting growth during OMCVD for different materials and growth conditions. This study contributed to improve our understanding of the physics of low-dimensional structures grown on corrugated surfaces in different ways.

- First, it allowed us to gain an *empirical understanding of the self-ordering mechanisms*. We observed that the bottom of the grooves, grown by LP-OMCVD, is composed of a set of nm-sized facets. The dependence of the facet widths on the growth conditions suggests that the self-limiting profile is at least partly determined by surface diffusion. Another evidence for the influence of surface diffusion on self-limiting growth is the observation of vertical quantum wells (VQWs) at the bottom of the grooves. The longer diffusion length of Ga, compared to Al, brings to the formation of three Ga-rich VQW branches, corresponding to the facets at the bottom of the groove. Top surface AFM studies of the profiles showed that the morphology of the planes composing the groove is directly related to the one characteristic of planar substrates with the same orientations. However, the step structure of these planes was modified, with respect to the infinite surfaces, by the presence of boundaries that confine these facets to sizes comparable with, or smaller than the surface

diffusion length.

- On the other hand, our study helped to better understand the *electronic and optical properties* of the low-dimensional structures forming at the bottom of the grooves, and to relate them to their structural features. The very good uniformity and interface definition of VQW structures allowed us to evidence lateral quantum confinement effects, and the determination of the composition profiles by EELS and cross-sectional AFM helped to model the observed intersubband transitions [88]. The establishment of a peculiar self-limiting profile in QWR-SL growth allowed us to recognize a transition from multi-QWR regime to a strongly coupled one, as the barrier thickness decreases and the so-forming SL miniband width becomes larger than the 1D subband splitting [89]. Variations of the profile morphology along the groove axis, evidenced by AFM studies, were identified as the cause for the appearance of sharp (<200μeV) excitonic lines in QWR luminescence spectra [112]. This roughness creates local potential minima for excitonic recombination, and can even quantum confine the excitons into naturally formed QD-like structures.
- Finally, with the knowledge we have acquired, it has been possible to identify the critical factors affecting the *quality of our nanostructures*, in terms of density, uniformity and lateral confinement. Besides, this can be used in the future to predict and optimize quantum-confined nanostructures. For example, lateral confinement in VQWs can be improved by a suitable choice of growth conditions, in order to reduce the lateral branch size and maximize the Ga segregation. Similarly, the QWR cross-sectional shape, that can be approximately related to the 2D confinement properties by an adiabatic model [48], can be optimized by suitable choices of growth temperature, growth rates and Al composition in the AlGaAs barriers. In the same way, one can design the profile of QWR SL structures, once the self-ordering properties of the constituent materials have been determined, as a function of the growth conditions. Finally, improving the QWR uniformity along the groove should reduce the inhomogeneous broadening of the wire luminescence. This should be aimed at in the future mainly by reducing the substrate roughness, with a suitable choice of the etching process and with a study of the effects of the pre-growth heat-up on the nonplanar profiles.

The main goal of this project was however the understanding of the physical processes at the base of self-limiting growth on corrugated substrates. We have developed a model in which self-ordering results from an interplay between three different phenomena:

- The *growth rate anisotropy* among the different facets composing the grooved profile. This anisotropy depends on the growth technique, and leads to a resharpening of the nonplanar profile either at the bottom of the grooves (typically in OMCVD) or at the top of the ridge (typically in MBE).
- The *capillarity fluxes* of adatoms towards the bottom of the groove. These fluxes can self-adjust in order to yield a steady-state propagation of the faceted profile either at the bottom or at the top region, depending on the growth rate anisotropy. The dependence of these

fluxes on the adatom diffusion length determines the self-limiting profile width, as a function of the material and growth conditions.

- The nonuniformity of the *entropy of mixing* in the profile of alloys. The different diffusion length of the alloy components gives rise to segregation of the more mobile species at the bottom of the groove, and of the less mobile at the top of the mesa. However, these variations of the alloy composition give rise to gradients of the entropy of mixing, which tend to re-establish a uniform composition.

With suitable approximations, we were able to apply quantitatively our model to the experimental self-limiting behavior of GaAs/$Al_xGa_{1-x}As$ structures analyzed in this project, and with the results of kinetic Monte Carlo simulations. Besides giving an accurate physical interpretation of self-ordering phenomena in nonplanar epitaxy, this analytic model provided an estimate of some quantities relevant to the epitaxial process, such adatom diffusion lengths and activation energies on the groove sidewalls.

Our model could be further developed in the future to describe self-limiting growth of more complex systems. By including the effects of strain on the surface chemical potential, the model could be extended to lattice-mismatched InGaAs/AlGaAs heteroepitaxy on V grooves [157]. Finally, by writing appropriate two-dimensional diffusion equations, it could be possible to describe self-limiting growth of GaAs/AlGaAs quantum dots grown on (111)B patterned substrates, where the dots form at the intersection of three QWRs at the bottom of an inverted pyramid [156].

Appendix

A Self-ordering model in the hyperbolic approximation

We will show in this Appendix that, by applying the Nernst-Einstein and continuity equations to a continuous, hyperbolic surface profile, the equation defining the self-ordering properties of the radius of curvature at the bottom of the hyperbola are identical (except for a geometrical proportionality factor) to those found in Chapter 5 for a faceted profile.

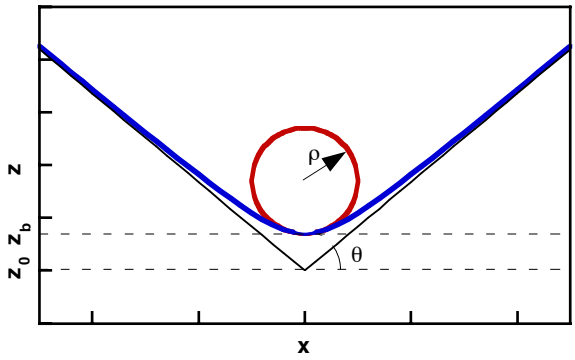

Figure A.1: Schematic plot of a hyperbola.

The hyperbolic profile is defined by the function

$$z(x,t) = z_0(t) + \tan\theta(t)\sqrt{\left(\rho(t)\tan\theta(t)\right)^2 + x^2}\ ,$$

where $z_0(t)$ is the vertical coordinate of the focus, $\theta(t)$ is the angle that the asymptotes form with the horizontal and $\rho(t)$ is the radius of curvature at the bottom (see Figure A.1). The equations defining the bottom ($x = 0$) and the sidewalls ($x \gg \rho$) are, respectively:

$$\begin{aligned} z_b(0,t) &= z_0(t) + \rho(t)\tan^2\theta(t) \\ z_s(x,t) &= z_0(t) + x\tan\theta(t) \end{aligned} \qquad \text{(A.1)}$$

If we assume that the surface free energy $\gamma = \bar{\gamma}$ is isotropic on the curved surface profile, then the solution of the continuous Nernst-Einstein and diffusion equations lead to the relation

$$\frac{\partial z(x,t)}{\partial t} = R\cdot r(x) - \frac{n\Omega_0^2 D_s \bar{\gamma}}{k_B T}\frac{\partial^4 z}{\partial s^4}\ , \qquad \text{(A.2)}$$

where ds is the infinitesimal arc length, $r(x)$ is the incorporation rate with respect to the planar reference substrate (as defined in Section 5.2.1.1), and $n = R\ r(x)\ \tau / \Omega_0$ in the case of growth, or

n = constant in the case of no growth (the other symbols are defined as in Section 5.2.1). Since

$$\frac{\partial^4 z}{\partial s^4} = \frac{\partial^4 z}{\partial x^4} = -\frac{3}{\rho^3 \tan^2\theta} \qquad x = 0 \text{ (bottom)}$$

$$\frac{\partial^4 z}{\partial s^4} = 0 \qquad \text{x >> } \rho \text{ (asymptotes - sidewalls),}$$

at these two points eq. (A.2) becomes, with r_s and r_b having the same meaning as in Section 5.2.3,

$$\frac{\partial z_b}{\partial t} = R \cdot r_b + \frac{3n\Omega_0^2 D_s \bar{\gamma}}{k_B T \tan^2\theta} \frac{1}{\rho^3} \text{ at the bottom;}$$

$$\frac{\partial z_s}{\partial t} = R \cdot r_s \qquad \text{on the sidewalls.}$$

By neglecting temporal variations of the sidewall orientation θ, as was done by treating the case of a faceted profile (Section 5.2.1.2), we can write (see eq. (A.1))

$$\frac{\partial}{\partial t}(z_s - z_b) = \frac{\partial}{\partial t}(x\tan\theta - \rho(t)\tan^2\theta) \cong -\tan^2\theta \frac{\partial \rho}{\partial t}$$

$$\Rightarrow \quad \frac{\partial \rho}{\partial t} = -\frac{R \cdot \Delta r}{\tan^2\theta} + \frac{3n\Omega_0^2 D_s \bar{\gamma}}{k_B T \tan^4\theta} \frac{1}{\rho^3},$$

with $\Delta r = r_s - r_b$.

This general equation allows to predict the self-limiting properties of the bottom of the groove in terms of ρ. As in Section 5.3, we can identify three particular situations:

a. In the case of *no growth* ($R = 0$), by integrating the last equation we obtain

$$\rho(t) = \rho_0 (1 + t/\tau)^{1/4}; \quad \tau = \frac{\rho_0^4 k_B T \tan^4\theta}{12 n \Omega_0^2 D_s \bar{\gamma}},$$

that corresponds to the second of eq. (5.25), upon the substitution

$$\frac{l_0^4}{2p\gamma} \rightarrow \frac{\rho_0^4 \tan^4\theta}{3\bar{\gamma}}.$$

b. *During growth*, the self-limiting condition ($\partial\rho / \partial t = 0$) implies that

$$\rho_{sl} = \left(\frac{r_s}{\Delta r} \frac{3\Omega_0 L_s^2 \bar{\gamma}}{k_B T \tan^2\theta} \right)^{1/3},$$

that corresponds to l_b^{sl} (eq. (5.28)b), provided that $2\gamma \leftrightarrow 3\bar{\gamma} / \tan^2\theta$.

c. Finally, the *evolution* towards the self-limiting profile, as a function of the nominal thickness $dz_n = R\, dt$, is given by

$$\frac{\partial \rho}{\partial z_n} = \frac{\Delta r}{\tan^2\theta} \left[\left(\frac{\rho_{sl}}{\rho} \right)^3 - 1 \right],$$

that is the same as eq. (5.35), upon exchanging $p \leftrightarrow 1 / \tan^2\theta$.

Point b. provides a relation between the "average" surface free energy considered in the hyperbolic approximation, and the facet-dependent one defined in eq. (5.18). By putting $2\gamma = 3\bar{\gamma}/\tan^2\theta$, the relation in a. becomes $l_0^4/p = \rho_0^4 \tan^2\theta$, that expresses now only a geometric proportionality between the facets and hyperbola formalisms, and is consistent with the geometric relation found in c. We can conclude therefore that the equations defined for the evolution of a faceted profile hold also in the case of a continuous one, parameterized with a hyperbola. This will allow us to compare the predictions of the model with experimental data relative either to bottom facet lengths and to the radius of curvature. Finally, the equations above show that our diffusion model can be applied also to cases in which no evident faceting of the profile is observable, as in AP OMCVD.

B Self-ordering model for a three-facets bottom profile

In Chapter 5, we have developed a diffusion model to explain self-limiting growth at the bottom of the grooves, by assuming that this region is composed only of a single facet. This simplification has proven to be very useful for interpreting self-ordering phenomena as a function of a few physical parameters, which can be easily inferred by comparison with experimental results. This picture, however, lacks of a description of the full fine structure of the bottom region. In this appendix we will write the equations of motion for all three facets (central (100) and two lateral {311}A) that are composing the bottom of the groove (see Figure 5.8).

For such a structure, the chemical potential at each facet is given by the set of equations (5.15). According to eq. (5.19), therefore, the atom transfer rates between the sidewalls and the bottom {311}A, and between the bottom {311}A and the bottom (100) are, respectively:

$$K_3 = \frac{D_s \Omega_0 \bar{\gamma}_3}{k_B T l_3^2}$$

$$K_1 = \frac{D_3 \Omega_0}{k_B T l_1}\left(\frac{\bar{\gamma}_1}{l_1} - \frac{\bar{\gamma}_3}{l_3}\right)$$

where the subscripts *s*, 3 and 1 refer to the sidewall, the {311}A and the (100) facets, respectively. The surface free energy differences $\bar{\gamma}_1$ and $\bar{\gamma}_3$ are defined in eq. (5.16). We will assume that the boundaries between the {311}A and the sidewalls evolve also in this case according to eq. (5.35), with $l_b = 2l_3\cos\alpha + l_1$. This assumption is justified by the good agreement of the observed behavior of l_b with the simplified model developed in Chapter 5. According to eq. (5.21), the equation of motion of the central (100) facet can be written as

$$\frac{dz_1}{dt} = R_1 + \frac{2\Omega_0}{l_1} n_1 K_1 \ .$$

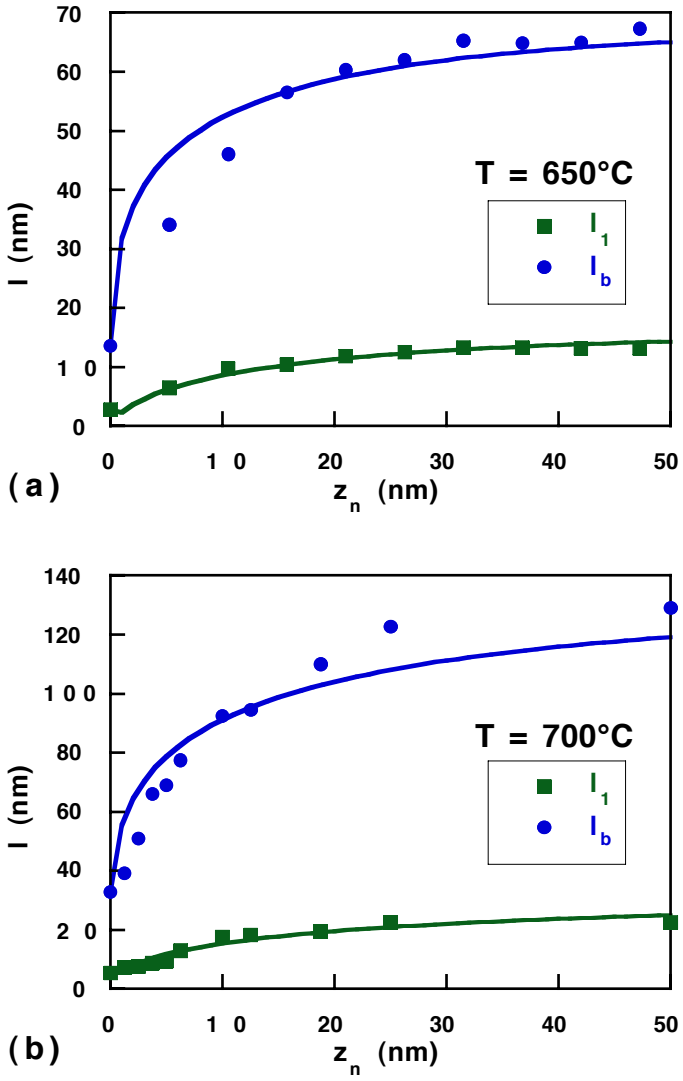

Figure B.1: Measured (symbols) and calculated (lines) evolution of the (100) (circles) and {311}A (squares) boundaries, in GaAs heteroepitaxy on self-limiting Al0.45Ga0.55As at 650°C (a), and on self-limiting Al0.3Ga0.7As at 700°C (b).

The adatom concentrations at the boundaries between the {311}A and the (100) n_1 can be found by applying the same procedure as in Section 5.2.3 to the {311}A facets. The expression for n_1 is complicated in this case by the asymmetry of the {311}A boundaries. After some algebra, and assuming that $\tanh l_3/2L_3 \ll 1$, we obtain

$$n_1 = \frac{R_3}{\Omega_0}\frac{l_3}{K_1 + K_3} .$$

By noticing that $dl_1 = (2/\tan\alpha)\,(dz_1 - dz_3)$, we obtain

$$\frac{dl_1}{dz_n} = \frac{2}{\tan\alpha}\left[r_1 + r_3\left(2\frac{l_3^3}{Al_1^3 + l_1 l_3^2} - 1\right) - (r_s - r_3)\left(\frac{l_b^{sl}}{2l_3\cos\alpha + l_1}\right)^3\right],$$

where $A = (D_s / D_3)\,(\bar{\gamma}_3 / \bar{\gamma}_1)$ and r_i is the relative growth rate of facet i. The equation above and eq. (5.35) define the evolution of the {311}A and (100) boundaries, in the absence of

entropy of mixing effects. We have fitted the evolution of l_1 and l_b for GaAs profiles, at $T = 650°C$ and 700°C (see Figure 5.17a) with the system of equations just described. In Figure B.1 we show the results of such fits, where we have fixed the r_i's to their measured values (Section 2.2.2), and varied the parameter A. A good match to the experimental data is obtained for $A \approx 5$-10 for the two cases here described. Since A is the ratio of quantities that should not differ significantly from facet to facet, it is reasonable to obtain values for A not too far from 1. Thus, the results support the validity of the procedure and of the approximations made above. However, we will not discuss further the numerical value of A found here, since it is not possible to estimate independently the diffusion coefficient and surface energy ratios that appear in this parameter.

C Entropy of mixing for a two-phases, two-components system

We will calculate the entropy of mixing of a system, with total volume V composed by a two-components alloy, with average composition $\bar{x}$ and two regions of volumes V_1 and V_2, with different compositions x_1 and x_2. The system is represented schematically in Figure C.1.

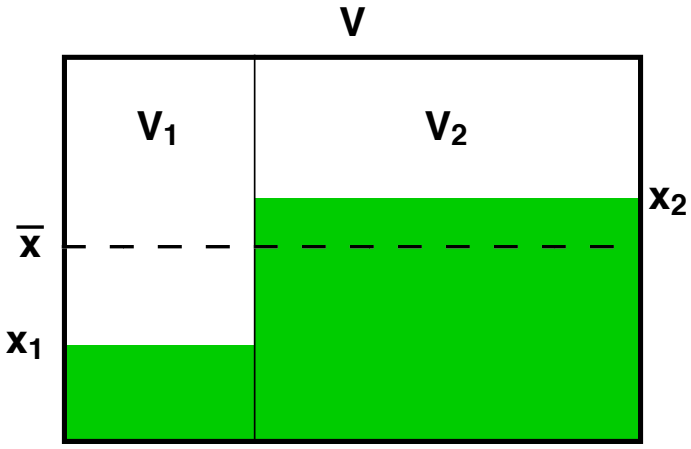

Figure C.1: Schematic representation of a system of volume V, containing a binary alloy of average composition $\bar{x}$, and divided in two parts with volumes $V_{1,2}$ and compositions $x_{1,2}$.

The *local* molar entropy in each region is given by [60]

$$s_{1,2} = k\left[\left(1-x_{1,2}\right)\ln\left(1-x_{1,2}\right) + x_{1,2}\ln x_{1,2}\right],$$

with $V_1 + V_2 = V$, $x_1 V_1 + x_2 V_2 = x V$. By defining $v = V_1 / V$, the *overall* molar entropy, expressed as a function of the variables in the first region, will be

$$\begin{aligned} s &= \left(s_1 V_1 + s_2 V_2\right)/V \\ &= -k\left\{v\left[\left(1-x_1\right)\ln\left(1-x_1\right) + x_1\ln x_1\right] + \left(1-v\right)\left[\left(1-\frac{\bar{x}-x_1 v}{1-v}\right)\ln\left(1-\frac{\bar{x}-x_1 v}{1-v}\right) + \frac{\bar{x}-x_1 v}{1-v}\ln\frac{\bar{x}-x_1 v}{1-v}\right]\right\}. \end{aligned}$$

As expected, this function has a maximum for $x_1 = \bar{x}$, corresponding to the state of maximum disorder:

$$s = -k\left[(1-\bar{x})\ln(1-\bar{x}) + \bar{x}\ln\bar{x}\right].$$

The dependence of the normalized molar entropy *s/k*, as a function of x_1 is shown in Figure C.2, for different values of $\bar{x}$ and *v*.

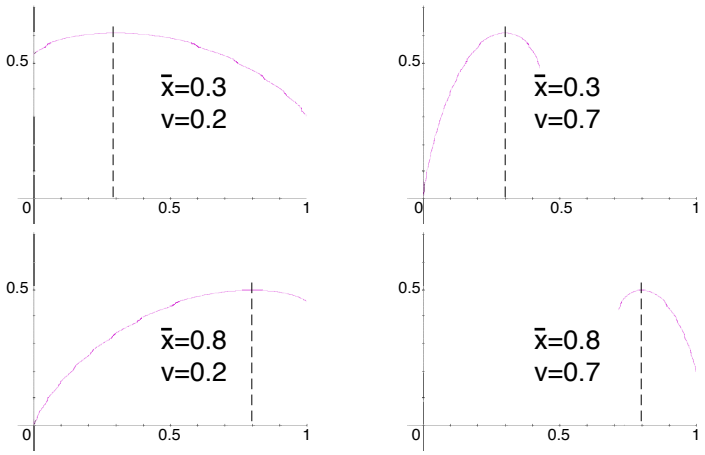

Figure C.2: Normalized variations of the overall molar entropy s/k, as a function of x_1, for different values of $\bar{x}$ and v.

Bibliography

1. H. J. Bremmermann, in *On self-organization: an interdisciplinary search for a unifying principle*, edited by R. K. Mishra, D. Maass and E. Zwierlein (Springer, Berlin ; New York, 1994), Vol. 61, p. 5.
2. K. Gurney, *An Introduction to Neural Networks* (Taylor and Francis Incorporated, Bristol, 1997).
3. F. Hinterberger, in *On self-organization : an interdisciplinary search for a unifying principle*, edited by R. K. Mishra, D. Maass and E. Zwierlein (Springer, Berlin ; New York, 1994), Vol. 61, p. 35.
4. *McGraw-Hill multimedia encyclopedia of science and technology* (McGraw-Hill, 1994).
5. G. Bastard, *Wave Mechanics Applied to Semiconductor Heterostructures* (John Wiley and Sons, New York, 1988).
6. E. Kapon, in *Epitaxial Microstructures*, edited by A. C. Gossard (Academic Press, Boston, 1994), Vol. 40, p. 259.
7. D. M. Eigler and E. K. Schweizer, *Nature **344**, 524 (1990).*
8. H. Drexler, D. Leonard, W. Hansen, J. P. Kotthaus, and P. M. Petroff, *Phys. Rev. Lett. **73**, 2252 (1994).*
9. J. Oshinowo, M. Nishioka, S. Ishida, and Y. Arakawa, *Appl. Phys. Lett. **65**, 1421 (1994).*
10. J.-Y. Marzin, J.-M. Gérard, A. Izraël, D. Barrier, and G. Bastard, *Phys. Rev. Lett. **73**, 716 (1994).*
11. S. Fafard, D. Leonard, J. L. Merz, and P. M. Petroff, *Appl. Phys. Lett. **65**, 1388 (1994).*
12. W. T. Tsang and A. Y. Cho, *Appl. Phys. Lett. **30**, 293 (1977).*
13. D. L. Miller, *Appl. Phys. Lett. **47**, 1309 (1985).*
14. E. Kapon, M. C. Tamargo, and D. M. Hwang, *Appl. Phys. Lett. **50**, 347 (1987).*
15. H. P. Meier, E. V. Gieson, W. Ealter, and C. Harder, *Appl. Phys. Lett. **54**, 433 (1989).*
16. S. Koshiba, T. Noda, H. Noge, Y. Nakamura, H. Ichinose, T. Shitara, D. D. Vvedensky, and H. Sakaki, *J. Cryst. Growth **150**, 322 (1995).*
17. C. Weisbuch and B. Vinter, *Quantum Semiconductor Structures* (Academic Press, Boston, 1991).
18. E. Kapon, *Proc. IEEE **80**, 398 (1992).*
19. P. C. Sercel and K. J. Vahala, *Phys. Rev. B **42**, 3690 (1990).*
20. A. Yariv, *Appl. Phys. Lett. **53**, 1033 (1988).*
21. C. Fall, Diploma thesis, EPFL (Lausanne, 1995).
22. M. A. Herman and H. Sitter, *Molecular beam epitaxy : fundamentals and current status* (Springer, Berlin, 1996).
23. G. B. Stringfellow, *Organometallic vapor phase epitaxy : theory and practice* (Academic Press, Boston, 1989).
24. A. Madhukar, *J. Cryst. Growth **163**, 149 (1996).*
25. K. Kash, A. Scherer, J. M. Worlok, H. G. Craighead, and M. C. Tamargo, *Appl. Phys. Lett. **49**, 1043 (1986).*
26. J. Y. Marzin, A. Izrael, L. Birotheau, B. Sermage, N. Roy, R. Azoulay, D. Robein, J.-L. Benchimol, L.

Henry, V. Thierry-Mieg, F. R. Ladan, and L. Taylor, *Surf. Sci.* ***267****, 253 (1992).*

27. W. D. Laidig, N. H. Jr., M. D. Camras, K. Hess, J. J. Coleman, D. P. Dapkus, and J. Bardeen, *Appl. Phys. Lett.* ***38****, 776 (1981).*
28. J. Cibert, P. M. Petroff, G. J. Dolan, S. J. Pearton, A. C. Gossard, and J. H. English, *Appl. Phys. Lett.* ***49****, 1275 (1986).*
29. E. Kapon, N. G. Stoffel, E. A. Dobisz, and R. Bhat, *Appl. Phys. Lett.* ***52****, 351 (1988).*
30. K. Kash, R. Bhat, D. D. Mahoney, P. S. D. Lin, A. Scherer, J. M. Vorlock, B. P. V. d. Gaag, M. Koza, and P. Grabbe, *Appl. Phys. Lett.* ***55****, 681 (1989).*
31. L. Pfeiffer, K. W. West, H. L. Stormer, J. P. Eisenstein, K. W. Baldwin, D. Gershoni, and J. Spector, *Appl. Phys. Lett.* ***56****, 1697 (1990).*
32. W. Wegscheider, G. Schedelbeck, G. Abstreiter, M. Rother, and M. Bichler, *Phys. Rev. Lett.* ***79****, 1917 (1997).*
33. T. Fukui and H. Saito, *Appl. Phys. Lett.* ***50****, 824 (1987).*
34. M. Tsuchiya, P. M. Petroff, and L. A. Coldren, *Appl. Phys. Lett.* ***54****, 1690 (1989).*
35. M. S. Miller, H. Weman, C. E. Pryor, M. Krishnamurthy, P. M. Petroff, H. Kroemer, and J. L. Merz, *Phys. Rev. Lett.* ***68****, 3464 (1992).*
36. C. Giannini, L. Tapfer, Y. Zhuang, L. D. Caro, T. Marschner, and W. Stolz, *Phys. Rev. B* ***55****, 5276 (1997).*
37. Q. Xie, A. Madhukar, P. Chen, and N. P. Kobayashi, *Phys. Rev. Lett.* ***75****, 2542 (1995).*
38. J. Tersoff, C. Teichert, and M. G. Lagally, *Phys. Rev. Lett.* ***76****, 1675 (1996).*
39. C. Teichert, M. G. Lagally, L. J. Peticolas, J. C. Bean, and J. Tersoff, *Phys. Rev. B* ***53****, 16334 (1996).*
40. G. Solomon, J. Trezza, A. Marshall, and J. Harris, *Phys. Rev. Lett.* ***76****, 952 (1996).*
41. M. K. Zundel, P. Specht, K. Eberl, N. Y. Jin-Phillipp, and F. Phillipp, *Appl. Phys. Lett.* ***71****, 2972 (1997).*
42. A. Y. Cho and W. C. Ballamy, *J. Appl. Phys* ***46****, 783 (1975).*
43. K. Kamon, S. Takagishi, and H. Mori, *J. Cryst. Growth* ***73****, 73 (1985).*
44. J. A. Lebens, C. S. Tsai, K. J. Vahala, and T. F. Kuech, *Appl. Phys. Lett.* ***56****, 2642 (1990).*
45. T. Fukui, S. Ando, Y. Kokura, and T. Toriyama, *Appl. Phys. Lett.* ***58****, 2018 (1991).*
46. E. Kapon, D. M. Hwang, and R. Bhat, *Phys. Rev. Lett.* ***63****, 430 (1989).*
47. C. J. Fall, M. A. Dupertuis, and E. Kapon, *IEEE J. Quant. Electron. (to be published).*
48. E. Kapon, G. Biasiol, D. M. Hwang, M. Walther, and E. Colas, *Solid State Electronics* ***40****, 1 (1996).*
49. R. L. Moon and Y.-M. Houng, in *Chemical vapor deposition - Principles and applications*, edited by M. L. Hitchman and K. F. Jensen (Academic Press, London, 1993).
50. I. Kamiya, L. Mantese, D. E. Aspnes, D. W. Kisker, P. H. Fuoss, G. B. Stephenson, and S. Brennan, *J. Cryst. Growth* ***163****, 67 (1996).*
51. L. Vescan, in *Handbook of thin film process technology*, edited by D. A. Glocker and S. I. Shah (Institute of Physics Publishing, Bristol, 1995), p. B1.4:1.
52. S. Berkman, V. S. Ban, and N. Goldsmith, in *Heteroepitaxial semiconductors for electronic devices*, edited by G. W. Cullen and C. C. Wang (Springer-Verlag, Berlin, 1979).

53. D. W. Kisker and T. F. Kuech, in *Handbook of crystal growth*, edited by D. T. J. Hurle (Elsevier Science, Amsterdam, 1994), Vol. 3, p. 93.
54. I. Kamiya, D. E. Aspnes, H. Tanaka, L. T. Florez, J. P. Harbison, and R. Bhat, *Phys. Rev. Lett.* ***68****, 627 (1992).*
55. I. Kamiya, H. Tanaka, D. E. Aspnes, M. Koza, and R. Bhat, *Appl. Phys. Lett.* ***63****, 3206 (1993).*
56. G. Wulff, *Z. Krist.* ***34****, 449 (1901).*
57. C. Herring, *Phys. Rev.* ***82****, 87 (1951).*
58. A. F. Andreev, *Sov. Phys. JETP* ***53****, 1063 (1982).*
59. J. Villain and A. Pimpinelli, *Physique de la croissance cristalline* (Ed. Eyrolles, Collection Aléa Saclay, Paris, 1995).
60. J. Y. Tsao, *Material Fundamentals of Molecular Beam Epitaxy* (Academic Press, Inc., Boston, 1993).
61. N. Moll, A. Kley, E. Pehlke, and M. Scheffler, *Phys. Rev. B* ***54****, 8844 (1996).*
62. J. S. Smith, P. L. Derry, S. Margalit, and A. Yariv, *Appl. Phys. Lett.* ***47****, 712 (1985).*
63. S. H. Jones, L. K. Seidel, K. M. Lau, and M. Harold, *J. Cryst. Growth* ***108****, 73 (1991).*
64. S. H. Jones, L. S. Salinas, J. R. Jones, and K. Mayer, *J. Electron. Mater.* ***24****, 5 (1995).*
65. K. M. Dzurko, E. P. Menu, and P. D. Dapkus, *Inst. Phys. Conf. Ser.* ***96, chap. 3****, 147 (1989).*
66. P. Demeester, P. V. Daele, and R. Baets, *J. Appl. Phys* ***63****, 2284 (1988).*
67. Y. Ueta, N. Wada, S. Sakai, and Y. Shintani, *J. Electron. Mater.* ***21****, 355 (1992).*
68. L. Buydens, P. Demeester, M. V. Ackere, A. Ackaert, and P. V. Daele, *J. Electron. Mater.* ***19****, 317 (1990).*
69. D. G. Coronell and K. F. Jensen, *J. Cryst. Growth* ***114****, 581 (1991).*
70. M. J. Anders, M. M. G. Bongers, P. L. Bastos, and L. J. Giling, *J. Cryst. Growth* ***154****, 240 (1995).*
71. A. Hartmann, Ph.D. thesis, Rheinisch-Westfälischen Technischen Hochschule (Aachen, 1996).
72. D. Vvedensky and S. Clarke, *Surf. Sci.* ***225****, 373 (1990).*
73. J. D. Weeks and G. H. Gilmer, *Adv. Chem. Phys.* ***40****, 157 (1979).*
74. T. Shitara, D. D. Vvedensky, M. R. Wilby, J. Zhang, J. H. Neave, and B. A. Joyce, *Phys. Rev. B* ***46****, 6815 (1992).*
75. D. D. Vvedensky, N. Haider, T. Shitara, and P. Smilauer, *Phil. Trans. Roy. Soc. London A* ***344****, 493 (1993).*
76. T. Shitara, T. Kaneko, and D. D. Vvedensky, *Appl. Phys. Lett.* ***63****, 3321 (1993).*
77. Y. N. Makarov, M. S. Ramm, E. A. Subashieva, and A. I. Zhmakin, *J. Cryst. Growth* ***145****, 271 (1994).*
78. N. Haider, M. R. Wilby, and D. D. Vvedensky, *Appl. Phys. Lett.* ***62****, 3108 (1993).*
79. B. Dwir, F. Reinhardt, H. Wehman, A. Gustafsson, and E. Kapon, *Microelectronic Engineering* ***35****, 269 (1997).*
80. C. Ratsch and A. Zangwill, *Appl. Phys. Lett.* ***58****, 403 (1991).*
81. A. Hartmann, M. Bongartz, M. Hollfelder, H. Hardtdegen, C. Dieker, and H. Luth, *J. Cryst. Growth* ***170****, 605 (1997).*
82. M. Grundmann, V. Tuerck, J. Christen, E. Kapon, D. M. Hwang, C. Caneau, R. Bhat, and D. Bimberg, *Solid-State Electron.* ***37****, 1097 (1994).*
83. A. Hartmann, C. Dieker, M. Hollfelder, H. Hardtdegen, A. Förster, and H. Lüth, *Appl. Surf. Sci.*

***123/124**, 704 (1998).*

84. J.-S. Lee, H. Isshiki, T. Sugano, and Y. Aoyagi, *J. Cryst. Growth **183**, 43 (1998).*
85. T. Shitara, J. H. Neave, and B. A. Joyce, *Appl. Phys. Lett. **62**, 1658 (1993).*
86. S. Koshiba, Y. Nakamura, M. Tsuchiya, H. Noge, H. Kano, Y. Nagamune, T. Noda, and H. Sakaki, *J. Appl. Phys **76**, 4138 (1994)1 Oct. p.*
87. A. Kley, P. Ruggerone, and M. Scheffler, *Phys. Rev. Lett. **79**, 5278 (1997) and references therein.*
88. E. Martinet, A. Gustafsson, G. Biasiol, F. Reinhardt, E. Kapon, and K. Leifer, *Phys. Rev. B **56**, R7096 (1997).*
89. Y. Ducommun, E. Martinet, H. Weman, G. Biasiol, A. Gustafsson, and E. Kapon, *Physica E (1998).*
90. C. C. Hsu, T. K. S. Wong, and I. H. Wilson, *Appl. Phys. Lett. **63**, 1839 (1993).*
91. M. Shinohara, M. Tanimoto, H. Yokoyama, and N. Inoue, *Appl. Phys. Lett. **65**, 1418 (1994).*
92. M. Kasu and N. Kobayashi, *J. Cryst. Growth **145**, 120 (1994).*
93. R. Nötzel, J. Temmyo, and T. Tamamura, *Appl. Phys. Lett. **64**, 3557 (1994).*
94. G. Binnig, C. F. Quate, and C. Gerber, *Phys. Rev. Lett. **56**, 930 (1986).*
95. E. Meyer, *Progress in Surface Science **41**, 3 (1992).*
96. Q. Zhong, D. Inniss, K. Kjoller, and V. B. Elings, *Surf. Sci. **290**, 1 (1993).*
97. TappingMode ™ and MultiMode™ are trademarks of Digital Instruments, Santa Barbara, CA. NanoScope® is a registered trademark of Digital Instruments, Santa Barbara, CA.
98. D. N. Butcher and B. J. Sealy, *J. Phys. D: Appl. Phys. **11**, 1451 (1978).*
99. F. Reinhardt, W. Richter, A. B. Muller, D. Gutsche, P. Kurpas, K. Ploska, K. Rose, and M. Zorn, *J. Vac. Sci. Technol. B **11**, 1427 (1993).*
100. M. Kasu, N. Kobayashi, and H. Yamaguchi, *Appl. Phys. Lett. **63**, 678 (1993).*
101. D. W. Kisker, G. B. Stephenson, P. H. Fuoss, F. J. Lamelas, S. Brennan, and P. Imperatori, *J. Cryst. Growth **124**, 1 (1992).*
102. J. E. Epler and H. P. Schweizer, *Appl. Phys. Lett. **65**, 1839 (1993).*
103. H. Asai, *J. Cryst. Growth **80**, 425 (1987).*
104. D. W. Kisker, G. B. Stephenson, J. Tersoff, P. H. Fuoss, and S. Brennan, *J. Cryst. Growth **163**, 54 (1996).*
105. Y. W. Mo and M. G. Lagally, *Surf. Sci. **248**, 313 (1991).*
106. M. Wassermeier, J. Sudijono, M. D. Johnson, K. T. Leung, B. G. Orr, L. Däweritz, and K. Ploog, *Phys. Rev. B **51**, 14721 (1995).*
107. S. Fuke, M. Umemura, N. Yamada, K. Kuwahara, and T. Imai, *J. Appl. Phys **68**, 97 (1990).*
108. H. Heinecke, E. Veuhoff, N. Pütz, M. Heyen, and P. Balk, *J. Electron. Mater. **13**, 815 (1984).*
109. W. W. Mullins, *J. Appl. Phys **28**, 333 (1957).*
110. E. Kapon, in *Optical spectroscopy of low dimensional semiconductors*, edited by G. Abstreiter, A. Aydinli and J. P. Leburton (Kluwer Academic Publishers, Dordrecht ; Boston, 1997), Vol. 344, p. 99.
111. F. Vouilloz, D. Y. Oberli, M. A. Dupertuis, A. Gustafsson, F. Reinhardt, and E. Kapon, *Phys. Rev. Lett. **78**, 1580 (1997).*
112. F. Vouilloz, D. Y. Oberli, S. Wiesendanger, B. Dwir, F. Reinhardt, and E. Kapon, *Physica Status Solidi A*

***164**, 259 (1997).*

113. G. Biasiol, F. Reinhardt, A. Gustafsson, E. Martinet, and E. Kapon, *Appl. Phys. Lett.* ***69**, 2710 (1996).*
114. M. Walther, E. Kapon, J. Christen, D. M. Hwang, and R. Bhat, *Appl. Phys. Lett.* ***60**, 521 (1992).*
115. G. Vermeire, Z. Q. Yu, F. Vermaerke, L. Buydens, P. Van Daele, and P. Demeester, *J. Cryst. Growth* ***124**, 1 (1992).*
116. A. Gustafsson, L. Samuelson, J. O. Malm, G. Vermeire, and P. Demeester, *Appl. Phys. Lett.* ***64**, 695 (1994).*
117. W. Pan, H. Yaguchi, K. Onabe, R. Ito, and Y. Shiraki, *Appl. Phys. Lett.* ***67**, 959 (1995).*
118. V. Berger, G. Vermeire, P. Demeester, and C. Weisbuch, *Appl. Phys. Lett.* ***66**, 218 (1995).*
119. E. Kapon, B. Dwir, H. Pier, A. Gustafsson, J. M. Bonard, D. M. Hwang, and E. Colas, in *Conference on Lasers and Electro-Optics / Quantum Electronics and Laser Science Conference*, Baltimore, MA (USA), May 1995).
120. N. Usami, W. Pan, H. Yaguchi, R. Ito, K. Onabe, H. Akiyama, and Y. Shiraki, *Appl. Phys. Lett.* ***68**, 3221 (1996).*
121. X.-L. Wang, M. Ogura, and H. Matsuhata, *Appl. Phys. Lett.* ***67**, 804 (1995).*
122. D. McLean, *Grain boundaries in metals* (Clarendon Press, Oxford, 1957).
123. J. M. Moison, C. Guille, F. Houzay, F. Barthe, and M. V. Rompay, *Phys. Rev. B* ***40**, 6149 (1989).*
124. M. B. Johnson, U. Maier, H. P. Meier, and H. W. M. Salemink, *Appl. Phys. Lett.* ***63**, 1273 (1993).*
125. R. M. Silver, J. A. Dagata, W. Tseng, and W. Monch, *J. Appl. Phys* ***76**, 5122 (1994).*
126. W. Mönch, *Semiconductor Surfaces and Interfaces* (Springer, Berlin, 1995).
127. W. Mönch, *Surf. Sci.* ***168**, 577 (1986)March p.577-93.*
128. K. A. Bertness, J.-J. Yeh, D. J. Friedman, P. H. Mahowald, A. K. Wahi, T. Kendelewicz, and W. E. Spicer, *Phys. Rev. B* ***38**, 5406 (1988).*
129. C. D. Thurmond, G. P. Schwartz, G. W. Kammlott, and B. Schwartz, *J. Electrochem. Soc.* ***127**, 1366 (1980).*
130. F. Cabrera and N. F. Mott, *Rep. Progr. Phys.* ***12**, 163 (1948).*
131. J. Stöhr, R. S. Bauer, J. McMenamin, L. Johansson, and S. Brennan, *JVST* ***16**, 1195 (1979).*
132. A. T. Fromhold, *Theory of metal oxidation* (North-Holland, Amsterdam, 1976).
133. B. Dwir, F. Reinhardt, G. Biasiol, and E. Kapon, *Materials Science & Engineering B* ***37**, 83 (1996).*
134. K. Leifer, Ph.D. Thesis, EPFL (Lausanne, 1997).
135. K. Leifer and B. A. Buffat, *Inst. Phys. Conf. Ser.* ***157**, 381 (1997).*
136. A. Gustafsson, G. Biasiol, B. Dwir, F. Reinhardt, and E. Kapon, *Inst. Phys. Conf. Ser.* ***157**, 373 (1997).*
137. W. Pan, H. Yaguchi, K. Onabe, Y. Shiraki, and R. Ito, *J. Cryst. Growth* ***158**, 205 (1996).*
138. P. Bönsch, D. Wüllner, T. Schrimpf, H.-H. Wehmann, and A. Schlachetzki, in *7th European Workshop on Metal Organic Vapour Phase Epitaxy and Related Growth Techniques*, edited by W. Richter, Berlin, Germany, June 1997).
139. Z. Chvoj, H. Conrad, and V. Cháb, *Surf. Sci.* ***376**, 205 (1997).*
140. C. Herring, *J. Appl. Phys* ***21**, 437 (1950).*
141. D. J. Srolovitz, *Acta Metall.* ***37**, 621 (1989).*

142. C. Herring, in *The Physics of Powder Metallurgy*, edited by W. E. Kingston (McGraw-Hill, New York, 1951), p. 143.

143. J. B. Hudson, *Surface Science: an Introduction* (Butterworth-Heinemann, Boston, 1991).

144. A. A. Chernov, *Sov. Phys. Uspekhi* ***4****, 116 (1961).*

145. M. Ozdemir and A. Zangwill, *J. of Vac. Sci. Technol. A* ***10****, 684 (1992).*

146. J. D. Erlebacher and M. J. Aziz, *Surf. Sci.* ***374****, 427 (1997).*

147. H. P. Bonzel, E. Preuss, and B. Steffen, *Appl. Phys. A* ***35****, 1 (1984).*

148. C. C. Umbach, M. E. Keeffe, and J. M. Blakely, *J. of Vac. Sci. Technol. A* ***11****, 1830 (1993).*

149. J. Villain and F. Lançon, *C. R. Acad. Sci. Paris, Série II* ***309****, 647 (1989).*

150. M. Ozdemir and A. Zangwill, *Phys. Rev. B* ***42****, 5013 (1990).*

151. X. Q. Shen, M. Tanaka, K. Wada, and T. Nishinaga, *J. Cryst. Growth* ***135****, 85 (1994).*

152. S. Koshiba, H. Noge, H. Akiyama, T. Inoshita, Y. Nakamura, A. Shimizu, Y. Nagamune, M. Tsuchiya, H. Kano, H. Sakaki, and K. Wada, *Appl. Phys. Lett.* ***64****, 363 (1994).*

153. R. J. Schwoebel, *J. Appl. Phys* ***40****, 614 (1969).*

154. X. Q. Shen, M. Tanaka, and T. Nishinaga, *J. Cryst. Growth* ***127****, 932 (1993).*

155. T. Nishinaga, in *Handbook of crystal growth*, edited by D. T. J. Hurle (North-Holland, Amsterdam ; New York, 1994), Vol. 3b, p. 665.

156. A. Hartmann, L. Loubies, F. Reinhardt, and E. Kapon, *Appl. Phys. Lett.* ***71****, 1314 (1997).*

157. E. Martinet, F. Reinhardt, A. Gustafsson, G. Biasiol, and E. Kapon, *Appl. Phys. Lett.* ***72****, 701 (1998).*

Curriculum Vitae

- Name: **Giorgio Biasiol**
- Born: Gorizia, Italy, December 12, 1967
- Address: Av. de Préfaully 25C, 1022 Chavannes (Switzerland)
- E-mail: Giorgio.Biasiol@epfl.ch
- Citizenship: Italian

Education:

1992 Laurea Summa cum Laude, Dipartimento di Fisica, Universita` di Trieste, Trieste, Italy. Advisors: Professors A. Franciosi and R. Rosei.
Thesis title: Heterovalent Semiconductor Heterojunctions: Molecular Beam Epitaxy Synthesis of Ge/III-V and III-V/Ge Heterostructures.

1986 Scientific high school diploma, Liceo Scientifico "Michelangelo Buonarroti", Monfalcone, Italy.

Occupations:

8/1994-present: Graduate student-assistant, Institut de Micro- et Optoélectronique, École Polytechnique Fédérale, Lausanne (Switzerland).

8/1992-7/1994: Research Specialist, Department of Chemical Engineering and Materials Science, University of Minnesota, Minneapolis, MN (USA).

11/1990-12/1990: High School teacher, Liceo Scientifico Statale "Michelangelo Buonarroti", Monfalcone , Go (Italy).

Awards, achievements:

- Young Author Best Paper Award, 24th International Conference on the Physics of Semiconductors, Jerusalem (Israel), August 2-7, 1998
- Biography included in “Marquis Who’s Who in the World”, 16th Edition (1999).

Publications

1992-1995

1. G. Bratina, L. Sorba, A. Antonini, G. Biasiol, and A. Franciosi, "AlAs-GaAs Heterojunction Engineering by Means of Group IV Elemental Interface Layers", *Phys. Rev. B Rap. Comm.* ***45*** *(8), 4528 (1992).*
2. G. Bratina, L. Sorba, G. Biasiol, L. Vanzetti, and A. Fanciosi, "AlAs-GaAs Heterojunction Engineering by Means of Group IV Interface Layers", *MRS Proceedings* ***240****, 603 (1992).*
3. G. Biasiol, L. Sorba, G. Bratina, R. Nicolini, A. Fanciosi, M. Peressi, S. Baroni, R. Resta, and A. Baldereschi, "Microscopic Capacitors and Neutral Interfaces in III-V/IV/III-V Semiconductor Heterostructures", *Phys. Rev. Lett.* ***69*** *(8), 1283 (1992).*
4. L. Sorba, G. Biasiol, G. Bratina, R. Nicolini, and A. Fanciosi, "Charged Versus Neutral Interfaces in III-V/Ge Quantum Wells", *J. Cryst. Growth* ***127****, 93 (1993).*
5. A. Franciosi, L. Sorba, G. Bratina, and G. Biasiol, "Modification of Heterojunction Band Offsets at III-V/IV/III-V Interfaces" *J. Vac. Sci. Technol. B* ***11*** *(4), 1628 (1993).*
6. X. Yu, A. Raisanen, G. Haugstad, N. Troullier, G. Biasiol, and A. Franciosi, "Nonmagnetic/semimagnetic Semiconductor Heterostructures: Ge/$Cd_{1-x}Mn_xTe$(110)", *Phys. Rev. B* ***48*** *(7), 4545 (1993).*
7. G. Bratina, L. Sorba, A. Antonini, G. Ceccone, R. Nicolini, G. Biasiol, A. Franciosi, J. E. Angelo, and W. W. Gerberich, "Band Offsets and Strain in CdTe-GaAs Heterostructures", *Phys. Rev. B* ***48*** *(12), 8899 (1993).*
8. G. Biasiol, L. Sorba, G. Bratina, R. Nicolini, and A. Fanciosi, "Modification of Heterojunction Band Offsets at III-V/IV/III-V Interfaces" in *Physical Concepts and Materials for Novel Optoelectronic Device Applications II,* F. Beltram and E. Gornik, Eds., *Proc. SPIE,* ***1985****, 92 (1993).*
9. A. Franciosi, L. Sorba, G. Bratina, L. Vanzetti, Guido Mula, G. Biasiol, and R. Nicolini, "Novel Materials for Optoelectronics", *Alta Frequenza (Italy)* ***5*** *(4), 214 (1993).*
10. L. Sorba, G. Bratina, G. Biasiol and A. Franciosi, "Microscopic Control of Band Offsets in Semiconductor Heterostructures", in *Formation of Semiconductor Interfaces*, B. Lengeler, H. Lüth, W. Mönch, and J. Pollmann, eds. (World Scientific, Singapore, 1994), pp. 589-596.
11. M. Cantile, L. Sorba, S. Yildirim, P. Faraci, G. Biasiol, A. Franciosi, T. J. Miller, and M. I. Nathan, "Silicon-Induced Local Interface Dipole in Al/GaAs(001) Schottky Diodes", *Appl. Phys. Lett.* ***64*** *(8), 988 (1994).*
12. M. Cantile, L. Sorba, P. Faraci, G. Biasiol, G. Bratina, A. Franciosi, T. J. Miller, M. I. Nathan, and L. Tapfer: "Modification of Al/GaAs(001) Schottky Barriers by Means of Heterovalent Interface Layers", *J. Vac. Sci. Technol. B* ***12*** *(4), 2653 (1994).*
13. G. Bratina, L. Vanzetti, L. Sorba, G. Biasiol, A. Franciosi, M. Peressi, and S. Baroni: "Lack of Band-Offset Transitivity for Semiconductor Heterojunctions with Polar Orientation: ZnSe-Ge(001), Ge-GaAs(001), and ZnSe-GaAs(001)", *Phys. Rev. B* ***50*** *(16), 11723 (1994).*
14. A. Franciosi, L. Vanzetti, A. Bonanni, L. Sorba, G. Bratina, and G. Biasiol, "Interfacial Engineering in Blue Laser Structures", in *II-VI Blue/Green Laser Diodes*, R.L. Gunshor and A.V. Nurmikko, Eds., *Proc. SPIE* ***2346****, 100 (1994).*
15. G. Bratina, G. Biasiol, L. Vanzetti, A. Bonanni, L. Sorba, and A. Franciosi, "Nanosize Stress Concentrators at Facets in Zn1-xCdxSe/ZnSe Multiple Quantum Well Laser Structures", in *II-VI Blue/Green Laser Diodes*, R.L. Gunshor and A.V. Nurmikko, Eds., *Proc. SPIE* ***2346****, 180 (1994).*
16. L. Sorba, L. Vanzetti, G. Biasiol, G. Bratina, A. Franciosi, T.J. Miller, and M.I. Nathan,

"1eV-wide Tunability of Schottky Barriers in Al/Si/GaAs(001) Junctions", in *Proceedings 22th Int. Conf. on the Physics of Semiconductors*, D.J. Lockwood, Ed. (World Scientific, Singapore, 1995), 584-587.

1995-present

1. E. Kapon, G. Biasiol, D. M. Hwang, and E. Colas, "Seeded Self Ordering of Low-Dimensional Quantum Structures by Nonplanar Epitaxy", in *Low Dimensional Structures Prepared by Epitaxial Growth or Regrowth on Patterned Semiconductor Substrates*, K. Eberl, P. M. Petroff, and P. Demeester, Eds., *NATO ASI Series E, Applied sciences* ***298****, 291* (Kluwer Academic Publishers, Dordrecht, The Netherlands, 1995).
2. A. Gustafsson, F. Reinhardt, G. Biasiol, and E. Kapon, "Low-Pressure Organometallic Chemical Vapour Deposition of Quantum Wires on V-Grooved Substrates", *Appl. Phys. Lett.* ***67****, 3673 (1995).*
3. E. Kapon, G. Biasiol, D. M. Hwang, and E. Colas, "Seeded Self Ordering of GaAs/AlGaAs Quantum Wires on Nonplanar Substrates", *Microelectron. J.* ***26****, 881 (1995).*
4. A. Gustafsson, B. Dwir, F. Reinhardt, G. Biasiol, J.-M. Bonard, and E. Kapon, "Microscopy Characterization of Quantum Wires Grown on Grooved Substrates", *Institute of Physics Conference Series* ***146****, 375 (1995).*
5. E. Kapon, G. Biasiol, D.M. Hwang, M. Walther, and E. Colas, "Self-Ordering Mechanism of Quantum Wires Grown on Nonplanar Substrates", *Sol. St. Electron.* ***40****, 815 (1996).*
6. B. Dwir, F. Reinhardt, G. Biasiol, and E. Kapon, "Cross-Sectional Atomic Force Imaging of Semiconductor Heterostructures", *Mat. Sci. Engin.* ***B37****, 83 (1996).*
7. G. Biasiol, F. Reinhardt, A. Gustafsson, E. Martinet, and E. Kapon, "Structure and Formation Mechanisms of AlGaAs V-Groove Vertical Quantum Wells Grown by Low Pressure Organometallic Chemical Vapor Deposition", *Appl. Phys. Lett.* ***69****, 2710 (1996).*
8. F. Reinhardt, B. Dwir, G. Biasiol, and E. Kapon, "Atomic Force Microscopy of III-V Nanostructures in Air", *Appl. Surf. Sci.* ***104/105****, 529 (1996).*
9. G. Biasiol, E. Martinet, F. Reinhardt, A. Gustafsson, and E. Kapon, "Low-Pressure OMCVD Growth of AlGaAs Vertical Quantum Wells on Nonplanar Substrates", *J. Cryst. Growth* ***170****, 600 (1997)* [Addendum: *Ibid.* ***181****, 318 (1997)*].
10. F. Reinhardt, B. Dwir, G. Biasiol, and E. Kapon, "Step Ordering during OMCVD Growth on Non-Planar Substrates", *J. Cryst. Growth* ***170****, 689 (1997).*
11. E. Martinet, A. Gustafsson, G. Biasiol, F. Reinhardt, E. Kapon, and K. Leifer, "Carrier Quantum Confinement in Self-Ordered AlGaAs V-Groove Quantum Wells", *Phys. Rev. B Rap. Comm.* ***56****, 7096 (1997).*
12. G. Biasiol, F. Reinhardt, A. Gustafsson, and E. Kapon, "Self-Limiting Growth of GaAs Surfaces on Non-Planar Substrates", *Appl. Phys. Lett.* ***71****, 1831 (1997).*
13. G. Biasiol, F. Reinhardt, A. Gustafsson, and E. Kapon, "Self-Limiting Growth of GaAs on V-Grooved Substrates with Application to InGaAs/GaAs Quantum Wires", *J. Electron. Mat* ***26****, 1194 (1997).*
14. A. Gustafsson, G. Biasiol, B. Dwir, F. Reinhardt, and E. Kapon, "Electron Microscopy Characterization of Low-Dimensional Semiconductor Structures Grown on V-Grooved Substrates", *Inst. Phys. Conf. Ser.* ***157****, 373 (1997).*
15. E. Martinet, F. Reinhardt, A. Gustafsson, C. Constantin, G. Biasiol, and E. Kapon, "Self-ordering and Confinement in Strained InGaAs/AlGaAs V-Groove Quantum Wires Grown by Low-Pressure Organometallic Chemical Vapor Deposition", *Appl. Phys. Lett.* ***72****, 702 (1998).*
16. E. Kapon, F. Reinhardt, G. Biasiol, and A. Gustafsson, "Surface and Interface Properties of

Quantum Nanostructures Grown on Nonplanar Substrates", *Appl. Surf. Sci.* ***123/124****, 674 (1998).*

17. G. Biasiol, E. Kapon, Y. Ducommun, and A, Gustafsson, "Self Ordering of Quantum Wire Superlattices on V-Grooved Substrates", *Phys. Rev. B. Rap. Comm* ***57****, 9416 (1998).*
18. Y. Ducommun, E. Martinet, H. Weman, G. Biasiol, A. Gustafsson, and E. Kapon, "Structure and Optical Properties of V-Groove Quantum Wire Superlattices", *Physica E* ***2****, 954 (1998).*
19. G. Biasiol and E. Kapon, " Mechanisms of self-ordering of quantum nanostructures grown on nonplanar surfaces", *Phys. Rev. Lett.* ***81****, 2962 (1998).*
20. G. Biasiol, F. Lelarge, K. Leifer, and E. Kapon, "Mechanisms of self-ordering of nanostructures in nonplanar OMCVD growth", *J. Cryst. Growth* (in print).
21. E. Martinet, C. Constantin, G. Biasiol, K. Leifer, A. Rudra, F. Reinhardt, and E. Kapon, "Self-ordering and quantum confinement in InGaAs/(Al)GaAs V-groove quantum wires", *J. Electron. Mat* (accepted).
22. G. Biasiol, E. Martinet, A. Gustafsson, H. Weman, Y. Ducommun, F. Reinhardt, and E. Kapon, "Self-ordered AlGaAs vertical quantum wells: formation mechanisms, structure and optical properties", *J. Electron. Mat* (accepted).
23. G. Biasiol, F. Lelarge, K. Leifer, and E. Kapon, "Mechanisms of self-ordering of nanostructures on corrugated substrates",, in *Proceedings 24th Int. Conf. on the Physics of Semiconductors*, (World Scientific, Singapore, accepted).
24. Y. Ducommun, M.-A. Dupertuis, E. Martinet, H. Weman, G. Biasiol, A. Gustafsson, and E. Kapon, "Valence band mixing and 1D-miniband formation in V-groove quantum wire superlattices", in *Proceedings 24th Int. Conf. on the Physics of Semiconductors*, (World Scientific, Singapore, accepted).
25. G. Biasiol and E. Kapon, "Mechanism of self-limiting epitaxial growth on nonplanar substrates", *J. Cryst. Growth* (submitted).
26. F. Lelarge, G. Biasiol, A. Rudra, A. Condo, and E. Kapon, "Self-ordered nanostructures grown by OMCVD on V-grooved substrates: experiments and Monte-Carlo simulations", *Microelectron. J.* (submitted).

Conference presentations

1992-1994

1. G. Biasiol, L. Sorba, G. Bratina, R. Nicolini, L. Vanzetti, and A. Franciosi, "Modification of Heterojunction Band Offsets Within III-V/IV/III-V Heterostructures", 7th European Workshop on Molecular Beam Epitaxy, Bardonecchia (Italy), March 7-10, 1993.
2. G. Biasiol, L. Sorba, G. Bratina, R. Nicolini, and A. Franciosi, "Modification of Heterojunction Band Offsets Within III-V/IV/III-V Heterostructures", International Symposium *Physical Concepts and Materials for Novel Optoelectronic Device Applications II*, European Optical Society and International Society for Optical Engineering, Trieste (Italy), May 24-27, 1993.
3. G. Biasiol, G. Bratina, L. Vanzetti, T. Ozzello, F. Bassani, L. Sorba, and A. Franciosi, "Growth and *In-situ* Characterization of ZnSe-GaAs Heterostructures", 25th Annual Synchrotron Radiation Users Group Conference, Stoughton, WI (USA), October 18-19, 1993.

1995-present

1. G. Biasiol, F. Reinhardt, A. Gustafsson, B. Dwir, and E. Kapon, "Self-Ordering Mechanism in Low Pressure OMCVD Growth of Quantum Wires on Nonplanar Substrates", 6th European Workshop on Metal-Organic Vapour Phase Epitaxy and Related Growth Techniques, Gent (Belgium), June 25-28, 1995.
2. G. Biasiol, E. Martinet, F. Reinhardt, A. Gustafsson, and E. Kapon, "Low-Pressure OMCVD Growth of AlGaAs Vertical Quantum Wells on Nonplanar Substrates", 8th International Conference on Metal Organic Vapour Phase Epitaxy, Cardiff (UK), June 9-13, 1996.
3. G. Biasiol, F. Reinhardt, A. Gustafsson, and E. Kapon, "Low Pressure OMCVD Growth of V-Shaped Quantum Wires", International Workshop on Growth, Characterization and Exploitation of Epitaxial Compound Semiconductors on Novel Index Surfaces", Lyon (France), October 7-9, 1996.
4. G. Biasiol, F. Reinhardt, A. Gustafsson, and E. Kapon, "OMCVD Growth of V-Shaped GaAs/AlGaAs Quantum Wires by Seeded Self-Ordering", 2nd Hasliberg Workshop on Nanoscience, Hasliberg (Switzerland), October 14-18, 1996.
5. G. Biasiol, F. Reinhardt, A. Gustafsson, and E. Kapon, "Self-Limiting Growth of GaAs on V-Grooved Substrates with Application to InGaAs/GaAs Quantum Wires", 8th Biennial Workshop on Organometallic Vapor Phase Epitaxy, Dana Point, CA (USA), April 13-17, 1997.
6. G. Biasiol, Y. Ducommun, A. Rudra, F. Reinhardt, A. Gustafsson, and E. Kapon, "Self-limiting OMCVD growth of quantum wire superlattices on nonplanar substrates", 7th European Workshop on Metal-Organic Vapour Phase Epitaxy and Related Growth Techniques, Berlin (Germany), June 8-11, 1997.
7. G. Biasiol and E. Kapon, "Mechanisms of self-ordering of OMCVD-grown V-groove quantum wires", 10th International Winterschool on New Developments in Solid State Physics, Mauterndorf (Austria), February 23-27, 1998.
8. G. Biasiol, F. Lelarge, K. Leifer, and E. Kapon, "Mechanisms of Self-Ordering of Nanostructures in Nonplanar OMCVD Growth", 9th International Conference on Metal Organic Vapor Phase Epitaxy, La Jolla, CA (USA), May 30 - June 4, 1998.
9. G. Biasiol, E. Martinet, A. Gustafsson, H. Weman, Y. Ducommun, F. Reinhardt, and E. Kapon, "Self-ordered AlGaAs vertical quantum wells: formation mechanisms, structure and optical properties", 40th Electronic Materials Conference, Charlottesville, VA (USA), June 24-26, 1998.
10. G. Biasiol, F. Lelarge, K. Leifer, and E. Kapon, "Mechanisms of self-ordering of nanostructures on corrugated substrates", 24th International Conference on the Physics of Semiconductors, Jerusalem (Israel), August 2-7, 1998.
11. G. Biasiol, F. Lelarge, K. Leifer, and E. Kapon, "Mechanism of nm-size self ordering in nonplanar epitaxy", 10th International Conference on Molecular Beam Epitaxy, Cannes (France), August 31 - September 4, 1998.

Acknowledgments

My most sincere gratitude goes to Professor Eli Kapon, who gave me the opportunity to join his newly formed Group of Nanostructures at EPFL, and supervised my research activity with enthusiastic interest in these four years.

In this period, the whole Group of Nanostructures has created a friendly and stimulating atmosphere, which helped me in my thesis project. There are some people, however, who I wish to thank in a particular way. Among these, I would like to mention Frank Reinhardt for introducing me to the world of OMCVD, and for his dynamic presence in my first three years of study.

Transmission electron microscopy has been an indispensable activity for my research. I want to acknowledge Anders Gustafsson for his precious contribution in the first two years of my studies, in terms of quantity and quality. TEM activity was continued afterwards with equal success by Klaus Leifer and Adriana Condo.

I acknowledge with pleasure many useful discussions on the physics of epitaxial growth with François Lelarge and Arno Hartmann, who gave me helpful inputs in the formulation of my model. Monte Carlo simulations were also performed by François.

I want to mention my sincere gratitude for Amy Ils, for her valuable and patient activity in the clean rooms.

The activities and publications on atomic force microscopy, vertical quantum wells and quantum wire superlattices would not have been possible without the participation and help of Benjamin Dwir, Eric Martinet, Alok Rudra and Yann Ducommun.

I would like also to express my acknowledgement to the Group of Quantum Electronics of Professor Hans Melchior at ETHZ for hosting our OMCVD activity. In particular, I want to mention the indispensable help and availability of Emilio Gini and Raimond Bauknecht.

I want as well to take the opportunity to mention my former advisor, Professor Alfonso Franciosi, for addressing me to the Group of Nanostructures at EPFL.

A special thanks goes to Prof. Matthias Scheffler, Prof. Klaus Kern, Dr. Peter Roentgen and Prof. Benoit Deveaud-Pledran, for accepting to be members of my thesis jury.

I could not miss to express my love and gratitude for the people who are in my heart: my parents, who have always supported and encouraged me in all my choices, and Ivana, whose presence in my life is making all the hardest things become easy.